

PLASMA HEATING WITH BEATING ELECTROSTATIC WAVES

BENJAMIN JORNS

A DISSERTATION
PRESENTED TO THE FACULTY
OF PRINCETON UNIVERSITY
IN CANDIDACY FOR THE DEGREE
OF DOCTOR OF PHILOSOPHY

RECOMMENDED FOR ACCEPTANCE
BY THE DEPARTMENT OF
MECHANICAL AND AEROSPACE ENGINEERING
ADVISER: PROFESSOR EDGAR Y. CHOUERI

NOVEMBER 2012

© Copyright by Benjamin Jorns, 2012.

All Rights Reserved

Abstract

The heating of ions in a magnetized plasma with two electrostatic waves whose frequencies differ by the ion cyclotron frequency is analytically, numerically, and experimentally characterized. This process, denoted beating electrostatic wave (BEW) heating, is of particular interest since its ability to non-resonantly accelerate low energy ions suggests that it may be more effective at ion energization than the traditional, resonant heating produced by a single electrostatic wave (SEW). To explore this possibility, the BEW and SEW mechanisms were examined through an analysis of single particle orbits as well as the average power absorbed by an ion ensemble. Using the total input energy density of the waves as a metric, it was found that there are three distinct regimes for comparing the two processes: (I) for low energy density, there is a criterion for the onset of heating that depends on the wave parameters, and this criterion is satisfied for a lower input energy density with BEW; (II) at intermediate energy density, once heating has onset for both processes, SEW heating is superior; and (III) at high energy density above a threshold value that depends both on the wave parameters and background plasma, the BEW heating process is predicted to lead to higher heating levels. These analytical conclusions were tested in a low-temperature experimental setup by examining the increase in ion temperature produced by SEW and BEW as a function of total input energy density and fraction of energy in each wave. The experimental results were found to correspond to within error to the theoretical trends predicted for the first regime (I) and qualitative agreement was found for the second regime (II). Saturation effects combined with a limited available energy density to the experiment precluded a systematic investigation of the third energy density regime.

Acknowledgements

There are a number of individuals I would like to acknowledge who have helped me as I have worked toward completing this milestone. First of all, I would like to thank my advisor, Professor Edgar Choueiri. On my first day at Princeton, you told me to call you “Eddie” since you thought of your graduate students as colleagues. I’ve spent the past five years trying to earn this distinction. Thank you for the advice, insight, opportunities, and most importantly, the appreciation you have imbued in me for ~~card tricks~~ a first-principle approach to research. I also owe a great deal to Bob Sorenson. There may not be a transmission line long enough to move us to the same side of the political Smith chart, but the fact that I can use this metaphor is entirely thanks to you. You have always been very patient with me, and I appreciate all of the help you’ve given me with building, testing, and fixing (and fixing and fixing) my equipment.

To the many teachers and mentors I have had in my graduate career, thank you. I especially want to acknowledge Prof. Robert Jahn, Dr. Cynthia Phillips, and Dr. Rich Hofer. Prof. Jahn, I have always appreciated your feedback on my research—especially your ability to distinguish the important from the trivial. Cynthia, I owe my fascination with plasma waves and instabilities primarily to you. In spite of your busy schedule, I truly appreciate the fact that you have always been willing to take the time to answer questions, give career advice, or just talk plasma. Rich, you came through for me with a NASA opportunity in my last year of graduate study—we had never met but you were willing to give my proposal a try. Thanks for this and for your patience with me—a waves-guy who thought he might have something to say about an argon Hall thruster.

To my labmates, Luke, Ashley, Danny, Justin, Matt, and Matthew, you of all people can appreciate the fact that it’s not easy to spend every day in a windowless lab with harsh fluorescent lighting and vintage red walls. Somehow or other, though, we helped each other through it. To Danny and Justin especially, the people I spent the most time with in grad school, we’ve had some fun adventures together, and I truly am sorry for making you endure four years of my sense of humor. A number of undergraduates also have assisted me with my doctoral work: Julia Ling, Stacey Guo, Kunal Nayyar, and Buddy Gardineer. A special thanks to all of you.

To the many good friends I have made at Princeton during my graduate career, most of us gravitated to each other as acquaintances in our first year looking for kindred (and fun) spirits. Over the past five years, these casual friendships have grown into bonds that I hope will last a lifetime. You have been my support and my safety valve. I would not have reached this point without you.

To my family, I want to thank you for always having faith in me—particularly in my times of self-doubt—and for occasionally letting me stay up past bedtime to watch another episode of Star Trek. At some time or other, all of you have told me that I should never lose sight of my dreams. I may not be building warp engines (for now), but thanks to you, I’m doing the next best thing.

Finally, I want to acknowledge my Jenna. I came to grad school expecting to

learn, to face new challenges, and to better myself as a scientist. I did not expect to meet my better half. Yet, here you are, and you have made these years my happiest. I could write an entirely separate thesis detailing the ways in which you have helped me through this experience (and tolerated the thousands of sheets covered with scratched out equations that have littered our home), but suffice it to say, thank you.

This work was supported by research grants from the Air Force Office of Scientific Research, the National Science Foundation, the NASA Jet Propulsion Laboratory, and the Program in Plasma Science and Technology, Princeton Plasma Physics Laboratory. This dissertation carries T-3261T in the records of the Department of Mechanical and Aerospace Engineering

Contents

| | |
|--|-----------|
| Abstract | iii |
| Acknowledgements | iv |
| Nomenclature | x |
| 1 Introduction | 1 |
| 1.1 Background and motivation | 1 |
| 1.2 Dissertation objective | 7 |
| 1.3 Review of previous theoretical work | 8 |
| 1.3.1 Kinetic analysis | 8 |
| 1.3.2 Single particle analysis | 11 |
| 1.4 Previous laboratory experiments | 15 |
| 1.5 Dissertation outline and approach | 17 |
| 2 Heating onset | 19 |
| 2.1 Equations of motions | 21 |
| 2.2 Web structure | 23 |
| 2.3 Stochastic onset | 26 |
| 2.3.1 Resonances | 26 |
| 2.3.2 Parameter for stochastic onset | 29 |
| 2.4 Numerical analysis | 32 |
| 2.5 Comparison between SEW, BEW, and non-beating waves | 39 |

| | | |
|----------|---|-----------|
| 2.6 | Oblique propagation | 42 |
| 2.7 | Chapter discussion and summary | 43 |
| 3 | Ensemble heating | 45 |
| 3.1 | Average kinetic energy | 46 |
| 3.1.1 | Numerical investigation | 48 |
| 3.1.2 | Analytical formulation | 49 |
| 3.1.3 | Heating model from the Poincaré cross-section | 52 |
| 3.1.4 | Second-order estimate for heating | 55 |
| 3.1.5 | Conclusions and limitations | 60 |
| 3.2 | Power absorption | 62 |
| 3.2.1 | Oscillation center formulation | 64 |
| 3.2.2 | First and second-order components of the oscillation-center Hamiltonian | 67 |
| 3.2.3 | First and second-order contributions to the oscillation-center density distribution | 70 |
| 3.2.4 | Fourth-order expression for power absorption | 71 |
| 3.2.5 | Coarse grain analysis | 75 |
| 3.2.6 | Interpretation of terms | 78 |
| 3.2.7 | Limit of perpendicular propagation | 80 |
| 3.3 | Comparing descriptions | 83 |
| 3.4 | Dispersion relation | 85 |
| 3.5 | Condition for superiority of BEWH | 86 |
| 3.6 | Chapter summary | 90 |
| 4 | Experimental setup and diagnostics | 92 |
| 4.1 | Vacuum chamber and solenoid | 92 |
| 4.2 | Plasma source | 93 |

| | | |
|----------|---|------------|
| 4.3 | Antenna | 98 |
| 4.4 | Variable dual-frequency wave launcher | 99 |
| 4.5 | Diagnostics | 112 |
| 4.5.1 | Double Langmuir probe array | 112 |
| 4.5.2 | Laser induced fluorescence | 118 |
| 4.6 | Conclusion | 132 |
| 5 | Experimental results and analysis | 133 |
| 5.1 | SEW results | 133 |
| 5.1.1 | Dispersion relation | 133 |
| 5.1.2 | Frequency dependence of heating | 134 |
| 5.2 | BEW heating onset | 137 |
| 5.3 | BEW power absorption after onset | 144 |
| 5.4 | Chapter summary | 148 |
| 6 | Conclusions | 150 |
| 6.1 | Summary of major findings | 151 |
| 6.1.1 | Analytical findings | 151 |
| 6.1.2 | Experimental findings | 152 |
| 6.2 | Recommendations for future work | 152 |
| A | Derivation of the Hamiltonian | 155 |
| A.1 | Single particle Hamiltonian | 155 |
| A.2 | Ensemble Hamiltonian | 157 |
| B | Lie transform analysis | 159 |
| B.1 | General theory | 159 |
| B.2 | Hamiltonian in Eq. 2.2 | 161 |
| B.3 | Analysis in Sec. 3.1 | 162 |

| | | |
|----------|---|------------|
| B.4 | Analysis in Sec. 3.2 | 164 |
| C | Simplification of terms from Chapter 2 | 166 |
| C.1 | Simplification of F | 166 |
| C.2 | Completing the square | 169 |
| D | Estimating the maximum Lyapunov exponent | 171 |
| E | Electrostatic dispersion relation | 175 |
| F | Fourth-order beating contribution | 177 |
| F.1 | Unshielded term | 177 |
| F.2 | Shielded term | 179 |
| G | LIF broadening effects for BWX II | 184 |

Nomenclature

| | |
|---|--|
| \perp | Perpendicular to applied magnetic field |
| \parallel | Parallel to magnetic field |
| $J_n(z)$ | Bessel function of the first kind |
| $H_n^{(1)}$ | Hankel function of the first kind |
| $I_n(\lambda)$ | Modified Bessel function of the first kind |
| m_e | Mass of electron |
| m_i | Mass of ion |
| q | Elementary charge |
| n_0 | Plasma density |
| ϵ_0 | Permittivity of free space |
| T_i | Ion temperature in units of energy |
| T_e | Electron temperature in units of energy |
| E | Electric field |
| B | Magnetic field |
| ω_j | Frequency of j^{th} wave |
| Ω_i | Ion cyclotron frequency |
| Ω_e | Electron cyclotron frequency |
| ω_{pi} | Ion plasma frequency |
| ω_{pe} | Electron plasma frequency |
| v_{ti} | Ion thermal velocity |
| v_{te} | Electron thermal velocity |
| v_{di} | Ion parallel drift velocity |
| v_{de} | Electron parallel drift velocity |
| $f_0(\mathbf{v})$ | Background density distribution |
| Φ_j | Potential amplitude of j^{th} wave |
| $\mathbf{k}_j = (k_{jx}, k_{jz}, k_{jz})$ | Wave vector for the j^{th} wave |

| | |
|--|--|
| \bar{r}_L | Average thermal Larmor radius |
| θ | Angle of Larmor precession |
| $\nu_j = \omega_j/\Omega_i$ | Wave frequency normalized by ion cyclotron frequency |
| ν_c | Lowest common frequency of the two waves |
| $\kappa_j = k_{jx}/k_{1x}$ | Perpendicular component of wavevector normalized by reference wavevector |
| $\kappa_{jz} = k_{jz}/k_{1x}$ | Parallel component of wavevector normalized by reference wavevector |
| I | Normalized ion kinetic energy |
| ρ | Normalized Larmor radius |
| $\bar{\kappa}_j = k_{jx}\bar{r}_L$ | Perpendicular component of wavevector normalized by thermal Larmor radius |
| $\bar{\kappa}_{jz} = k_{jz}\bar{r}_L$ | Parallel component of wavevector normalized by thermal Larmor radius |
| $\varepsilon_j = qk_{1x}^2\Phi_j/m_i\Omega_i^2$ | Normalized potential amplitude of j^{th} wave for single wave analysis |
| $\bar{\varepsilon}_j = q\Phi_j/m_i\bar{r}_L^2\Omega_i^2$ | Normalized potential amplitude of j^{th} wave for ensemble analysis |
| $\bar{\xi}_j = qk_{jx}\Phi_j/m_i\bar{r}_L\Omega_i^2$ | Normalized electric field amplitude of j^{th} wave for ensemble analysis |
| $\tau = \Omega_i t$ | Normalized time |
| H, K | Hamiltonians |
| W_j | Energy density of the j^{th} wave |
| $\eta = W_1/W_T$ | Fraction of total energy density in the first mode |
| W_0 | Threshold in total energy density for stochastic onset with beating electrostatic waves |
| W_T^* | Threshold in total energy density for stochastic onset |

| | |
|------------------|---|
| | with a single electrostatic wave |
| \overline{W}_T | Value of total energy density where BEWH becomes superior to SEWH |
| λ | Maximum Lyapunov exponent |
| Z_T | Impedance of Variable Dual-frequency Wave Launcher |
| β | Normalized magnetic flux density |
| A_p | Area of Langmuir probe tip |
| ν_L | Doppler-shifted laser frequency |
| ν_0 | Rest frame frequency of the LIF transition |
| c | Speed of light |
| $I(\nu)$ | Intensity of fluoresced signal |

Chapter 1

Introduction

1.1 Background and motivation

The heating of a plasma with externally-coupled radiofrequency (RF) waves is a process that is widely employed in both industrial and scientific applications. The ability of these RF waves to introduce energy without directly contacting the plasma particularly recommends this mechanism when efficiency and material erosion are of paramount importance. Indeed, over the latter half of the last century, the RF heating of plasmas has become an indispensable tool for research ranging from the largest of fusion experiments [1] to small-scale industrial plasma sources [2]. Even more recently, RF waves have found a place in the field of plasma propulsion where thruster lifetime is largely limited by the erosion of the materials exposed to the plasma. By employing inductively coupled modes to either heat or directly accelerate the ions of the plasma [3, 4, 5, 6], this electrodeless mechanism is a promising method for producing continuous thrust for in-space propulsion systems.

Given the near ubiquity of RF heating in the field of plasma physics, there is an ongoing effort to identify and understand the ways in which excited waves exchange energy with the plasma (cf. Swanson [7]). Among these studies, the need to achieve

particle confinement for many plasma applications has motivated particular interest in the power absorption processes that occur in the presence of strong magnetic fields. Moreover, a subset of these power absorption processes that has merited significant attention is the coupling of energy to ions and electrons through electrostatic (ES) waves. This is because electrostatic waves, so-called since the time-dependent changes in magnetic field induced by these modes as they propagate in a plasma are negligible, can be launched in a plasma with a relatively simple antenna configuration [8], they propagate across magnetic field lines, and there is a subset of these ES modes that exists within the range of the ion cyclotron frequency, which facilitates a direct energy exchange with the ions (c.f. Ono's review on ion Bernstein wave research [9]). In light of these advantages, we choose to focus in this thesis on ES wave power absorption processes in a magnetized plasma.

The way an obliquely-propagating ES wave transfers energy to ions in a magnetized plasma is traditionally represented through the process of ion cyclotron damping (cf. [7, 10]). This physically intuitive mechanism can be understood through a simple zeroth order analysis of single ion orbits. We show in Fig. 1.1 an ion undergoing Larmor precession where the magnetic field is oriented in the \hat{z} direction such that the ion parallel velocity is v_z and the ion cyclotron precession occurs in the $\hat{x} - \hat{y}$ plane with perpendicular velocity v_\perp , Larmor angle θ , and ion cyclotron frequency $\Omega_i = qB_0/m_i$ where B_0 denotes the magnitude of the magnetic field, q is the charge, and m_i is the ion mass. We also show an obliquely-propagating ES wave where we have oriented the transverse component of the electrostatic wave in the \hat{x} direction. Since this is an electrostatic mode, the wave vector and electric field are parallel $\mathbf{E} \parallel \mathbf{k}$ and the wave's electric field in the laboratory frame of reference is given by

$$\mathbf{E} = (E_x \hat{x} + E_z \hat{z}) \cos(k_x x + k_z z - \omega t). \quad (1.1)$$

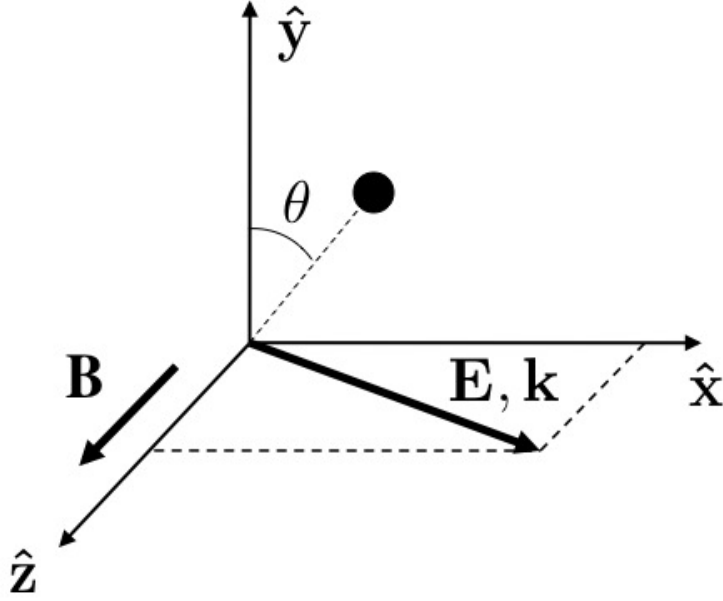


Figure 1.1: A single ion in a constant magnetic field $\mathbf{B} = B_0 \hat{z}$ is subject to an obliquely-propagating electrostatic wave. The electrostatic wave ($\mathbf{E}||\mathbf{k}$) is assumed without loss of generality to have $k_y = 0$.

The position of the unperturbed particle, on the other hand, is

$$\begin{aligned}
 x &= \frac{v_{\perp}}{\Omega_i} \sin \theta \\
 y &= \frac{v_{\perp}}{\Omega_i} \cos \theta \\
 \theta &= \Omega_i t \\
 z &= v_z t,
 \end{aligned} \tag{1.2}$$

where $(x, y, \theta, z) = (0, v_{\perp}/\Omega_i, 0, 0)$ at $t = 0$.

We can substitute these zeroth order orbits into Eq. 1.1 in order to estimate the electric field \mathbf{E}^p the ion sees in its frame of reference:

$$\begin{aligned}
 \mathbf{E}^p &= (E_x \hat{x} + E_z \hat{z}) \cos \left(\frac{k_x}{\Omega_i} v_{\perp} \sin(\Omega_i t) + k_z v_z t - \omega t \right) \\
 &= (E_x \hat{x} + E_z \hat{z}) \sum_{m=-\infty}^{\infty} J_m \left(\frac{k_x}{\Omega_i} v_{\perp} \right) \cos([m\Omega_i + k_z v_z - \omega] t),
 \end{aligned} \tag{1.3}$$

where we have used an apt identity [11] to express the field in terms of a series expansion of J_m , the Bessel function of the first kind.

It is immediately evident from this result that ions with parallel velocity that satisfy the so-called ion cyclotron resonant condition [7, 10], $\omega - k_z v_z - m\Omega_i = 0$, encounter on average a constant electric field in their frame of reference. This can lead to significant energy exchange with the ion. Alternatively, ions with velocities outside the resonant condition experience time-dependent electric fields that average to zero—thus imparting no energy. The perpendicular velocity has a part to play too since we see that when the ion cyclotron condition on the parallel velocity is satisfied, the magnitude of the electric field in the particle’s reference frame is proportional to $J_m(k_x v_\perp / \Omega_i)$ where $m = (\omega - k_z v_z) / \Omega_i$. Since the magnitude of the Bessel function has a peak value that depends monotonically on the index [11], the ion’s perpendicular velocity also must satisfy a resonant condition, $v_\perp \approx \omega / k_x - (k_z / k_x) v_z$, in order to achieve significant acceleration.

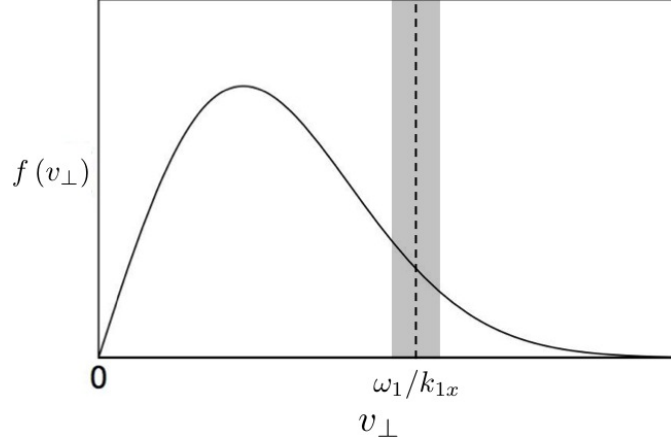
In translating this single particle description to the heating of an ensemble of ions, the resonant conditions in the parallel and perpendicular directions become non-trivial requirements since the frequencies and wavenumbers of the modes that propagate in a plasma are limited by an electrostatic wave dispersion relation, $D(\omega, \mathbf{k}) = 0$ [10]. In particular, the situation may arise for relatively low temperature plasmas where the phase velocity of the wave in both directions is significantly larger than the average thermal velocity of the ensemble, $v_{ti} \ll \omega / k_z, \omega / k_x$. The parallel resonant condition in this case is only satisfied for waves that are *on-resonance*, i.e. with a frequency that is an integer multiple of the ion cyclotron frequency, $\omega \approx m\Omega_i$. The perpendicular resonant condition similarly collapses to $v_\perp \approx \omega / k_x$ such that only a few ions in the tail of the thermalized ensemble distribution satisfy the perpendicular resonant condition. We illustrate this case in Figs 1.2 (a) and (b) where we show a Maxwellian distribution of the perpendicular component of the ion velocity along with the perpendicular phase

velocities of two different modes. We include a small range around the phase velocities denoted by the shaded region to indicate qualitatively that finite amplitude effects can bring slightly off-resonant ions into the resonant condition [12]. It is evident from these figures that for a single electrostatic wave (SEW) with a large phase velocity relative to the thermal velocity, the energy exchange with the ion distribution is confined to a small number of particles. In some cases, it is possible to overcome this limitation by employing a wave with a lower perpendicular phase velocity relative to the thermal velocity. This procedure is only effective to a point, however, since the dispersion relation for ES waves in a plasma frequently places a lower bound on the wave phase velocity. For example, in the acoustic limit of the low-frequency neutralized ion Bernstein wave, denoted the electrostatic ion cyclotron mode [13, 10], this lower bound is given approximately by the acoustic velocity $\omega/k_x > \sqrt{T_e/m_i}$ where T_e is the electron temperature in units of energy and m_i is the ion mass. Since for many low temperature plasmas $T_i \ll T_e$, it is evident that $\omega/k_x \gg v_{ti}$ and thus the resonant condition on the phase velocity of the wave prevents significant energy exchange with the plasma ions.

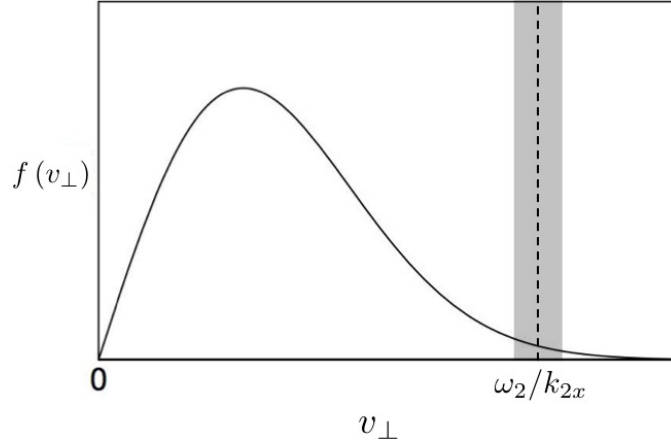
We thus are forced to turn to nonlinear processes in an effort to target the low energy ions outside the resonant condition. A promising and elegant nonlinear method for achieving this end is to employ two electrostatic waves with frequencies that satisfy the so-called beat criterion [14, 15, 16, 17]:

$$\omega_2 - \omega_1 = n\Omega_i, \tag{1.4}$$

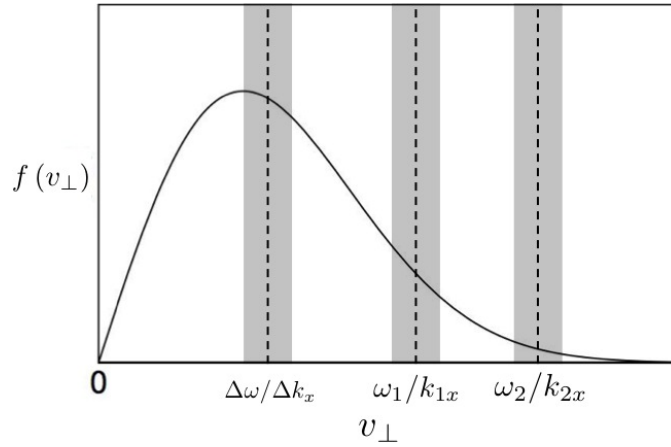
where n is an integer. The interaction of the two modes is illustrated in Fig. 1.2c where we see that the beating of the individual waves can be approximated as a virtual mode at the difference frequency $\Delta\omega = \omega_2 - \omega_1$ with wavenumber $\Delta\mathbf{k} = \mathbf{k}_2 - \mathbf{k}_1$. The resonant condition for this beat mode in the parallel direction is given



(a)



(b)



(c)

Figure 1.2: Maxwellian distribution of the perpendicular ion velocity. a) Perpendicular phase velocity of the wave couples to a small number of particles in the distribution. b) The second mode targets even fewer ions. c) The beat mode at $\Delta\omega$ and Δk_x has a lower phase velocity and is capable of targeting more of the thermally distributed ions. Grey regions denote resonance broadening due to finite amplitude effects.

by $\Delta\omega - \Delta k_z v_z - p\Omega_i = 0$ and in the perpendicular direction by $\Delta\omega/\Delta k_x \approx v_\perp$. Given the beat condition for the two frequencies, we see that this driven mode is already on-resonance such that the resonant condition is satisfied for arbitrarily low energy ions in the parallel direction $v_z \rightarrow 0$. Similarly, depending on the frequencies and wavenumbers of the electrostatic modes, the beat mode also can have a lower perpendicular phase velocity than the individual SEW, $\Delta\omega/\Delta k_x < \omega_1/k_{1x}, \omega_2/k_{2x}$. There is no lower bound on phase velocity for this difference mode imposed by the dispersion relation since it is not a natural plasma wave. Rather, it is locally driven by the beat oscillations in amplitude produced by the superposition of the two naturally propagating waves [18]. The beating electrostatic waves (BEW) therefore can be tailored in some cases to couple energy to ions whose initial velocities do not satisfy the resonant condition for the individual waves. This possibility of enhanced heating recommends the BEWH process for the many magnetized plasma applications we have outlined above.

1.2 Dissertation objective

In light of the advantages of BEW heating we have motivated qualitatively in the previous section, a large body of work has risen to investigate the BEW acceleration process [14, 15, 19, 16, 20, 17, 21, 22, 23, 24, 25]. Yet, in spite of all of the insight provided by these studies into the means by which BEW accelerate individual ions, a central question of both practical and academic importance remains: *is BEW heating (BEWH) superior to SEW heating (SEWH)?* The goal of this thesis is to answer this question by first analytically and experimentally characterizing BEWH and SEWH and then using these results to determine the conditions for when BEWH is the superior process.

1.3 Review of previous theoretical work

The BEW effect is inherently nonlinear since it results from the second-order effect of the slow variations in the wave amplitude that occur at the beat frequency. This nonlinearity leads to complicated behavior for both the acceleration of individual ions as well as the heating of an ion ensemble in the presence of the beating waves, and as consequence, we invariably find that any attempt to characterize this process requires a perturbative approach that uses the wave amplitudes as the expanding parameter.

These perturbation analyses have proceeded on two fronts—separated both by time and approach. The first falls within the realm of weak turbulence theory where the BEW can be identified as a subset of a process termed nonlinear Landau damping. The advantage of this analysis is that it provides a framework for determining how the waves effect macroscopically relevant parameters of the plasma, e.g. temperature and power absorption. On the other hand, this technique inherently averages over the ensemble of ions—washing out some of the telling dynamical effects associated with single ion acceleration. As an alternative, a second and more recent perturbative method, the method of Lie transforms, examines the dynamics of a single ion subject to BEW. The beat effect—especially the slow acceleration that results from the amplitude variation at the cyclotron frequency—can be explicitly seen with this technique. Both methods provide unique insight into the problem, and we employ each in measure in our analysis of the efficacy of BEW. In the present discussion, we review the work that has been done from each perspective.

1.3.1 Kinetic analysis

Sagdeev and Galeev in their classic text on plasma-wave interactions make the observation that “nonlinear plasma theory is usually referred to as the theory of weak turbulence” (p. 1 [18]), a formalism where the nonlinear electrostatic wave interactions

are examined through a perturbation analysis of the Vlasov and Poisson equations. The nonlinear interactions in this context fall into three categories: quasilinear wave-particle interactions, nonlinear wave-wave interactions, and nonlinear wave-particle interactions. SEW plasma heating is an example of a quasilinear particle interaction where particles at the resonant condition are subject to energy exchange with the wave. This is commonly referred to as Landau damping or in the case of magnetized plasmas, cyclotron damping. Nonlinear wave-wave interactions result when three waves with ω_1, \mathbf{k}_1 , ω_2, \mathbf{k}_2 and the difference frequency and wave vector $\Delta\omega, \Delta\mathbf{k}$ exchange energy by means of the background plasma. A condition for this coupling is that all the waves are natural modes of the plasma, i.e. they all satisfy the dispersion relation. The nonlinear wave-particle interaction, on the other hand, is a two-wave process with a driven mode at the difference frequency $\Delta\omega$ and wavevector $\Delta\mathbf{k}$ that is not included in the plasma's dispersion relation. This driven mode acts like a virtual wave, and in directly analogy to the way a single wave resonantly delivers energy to particles through a quasilinear interaction, it imparts energy directly to the plasma species through a resonant exchange at its difference frequency and wavevector. Given the nonlinear nature of the damping of the driven mode, this process is commonly referred to as nonlinear Landau damping or nonlinear cyclotron damping (NICD) when a magnetic field is present.

Rosenbluth and Coppi [14] first examined NICD for the special case of purely perpendicularly-propagating electrostatic waves. The authors of this study employed a combination of perturbation analysis and a dressed particle treatment to derive a kinetic wave equation for the damping of the individual wave amplitudes in the presence of nonlinear wave-particle coupling. Porkolab and Chang [15] in the 1970s extended this analysis to the case of two, obliquely-propagating modes in a magnetized plasma by examining the Vlasov and Poisson equations to fourth order. In an elegant Hamiltonian formulation that relied on a transformation to an oscillation

center coordinate system, Johnston et al. [19] successfully reproduced Porkolab and Chang’s result. This approach was unique, however, in that the wave damping was inferred by first estimating the power absorbed by the particles subject to nonlinear Landau damping.

The work of Porkolab and Chang as well as Johnston was particularly useful for explaining anomalous heating at the half-harmonics of the ion cyclotron frequency that had been observed in fusion experiments [26, 27, 28]. Indeed, the nonlinear self-interaction of an electrostatic wave with itself occurs at $\Delta\omega = 2\omega$ such that at the half-harmonics, the nonlinear coupling is on-resonance (at a harmonic of the cyclotron frequency). This can lead to substantial energy exchange. Additional studies have delved more in depth into this nonlinear process [29, 30, 31] through a combination of analytical and numerical results—most of which draw upon the conclusions of Porkolab and Chang. These works have lent an additional component of self-consistency in that they allow for the evolution of the background distribution of ions when subject to the nonlinear damping. This is in contrast to the original work by Porkolab and Chang who assumed the plasma was sufficiently lossy that the background distribution of ions remained at a constant temperature.

In the context of kinetic theory, the BEW interaction is an example of NICD where instead of relying on the self-interaction of a single mode, two waves that satisfy the beat criterion are launched into the plasma. The advantage of analyzing this interaction through the lens of weak turbulence and the methods outlined above is that it leads directly to approximations for the power absorbed by a background species of an ion population when subject to BEW. This power absorption is the metric we ultimately adopt for contrasting the BEW and SEW processes. On the other hand, one of the most significant disadvantages of the weak turbulence theory is that in solving the Vlasov equation for the power absorption of the ions subject to BEW, we average over the individual particle orbits. This averaging procedure

assumes the existence of a randomizing element to destroy the phase coherence of the particle orbits, and while typically a small spread in the spectrum of the waves or weak collisionality are employed to justify this random assumption, in the presence of monochromatic waves with small collisionality, this procedure may not be correct. Examining the problem from a single particle perspective therefore is a necessary step to determine if particles orbits can be approximated as random.

1.3.2 Single particle analysis

In an effort that has evolved largely independently of NICD research, a number of studies have examined the BEW effect from the single particle perspective. These analyses, which are based on formulating a Hamiltonian for the motion of a single ion subject to externally imposed electrostatic waves, were first inspired by a need to explain anomalous acceleration of ions in regions of the earth’s ionosphere known as Lower Hybrid Solitary Structures (LHSS) [32]. Sounding rocket studies of the LHSS revealed that oxygen and hydrogen ions undergo prodigious acceleration in the direction perpendicular to the earth’s magnetic field (see Ref. [33] for a review) and that these acceleration zones are typically characterized by a broad spectrum of perpendicularly-propagating electrostatic waves. Given the correlation between these two phenomena, there have been a number of analytical attempts to link the ion acceleration to an interaction with these electrostatic modes.

Traditional quasilinear cyclotron damping cannot explain the observed energization since this process does not allow for power absorption in the limit of perpendicular propagation [34]. Karney et al. [35, 12, 36] (for the case of an off-resonance wave) and Fukuyama [37] (for the case of on-resonance), on the other hand, showed from a single particle perspective that for sufficiently large amplitude waves, particle orbits in the presence of a perpendicularly-propagating electrostatic can become stochastic—thereby leading to a random walk of the particle in velocity phase space and a net

increase in energy. The only caveat is that this process occurs primarily for particles with velocities near the resonant condition, $v_{\perp} = \omega/k_x$ —ions with velocities outside of this zone have relatively unperturbed orbits. Thus, while the amplitudes of the electrostatic waves in the ionosphere are sufficiently large to allow for this stochastic acceleration, Ram et al. [16] showed that the initial velocity of the ions were too different from the phase velocities of the propagating modes in the ionosphere to undergo energy exchange. This is illustrated in Fig. 1.3.

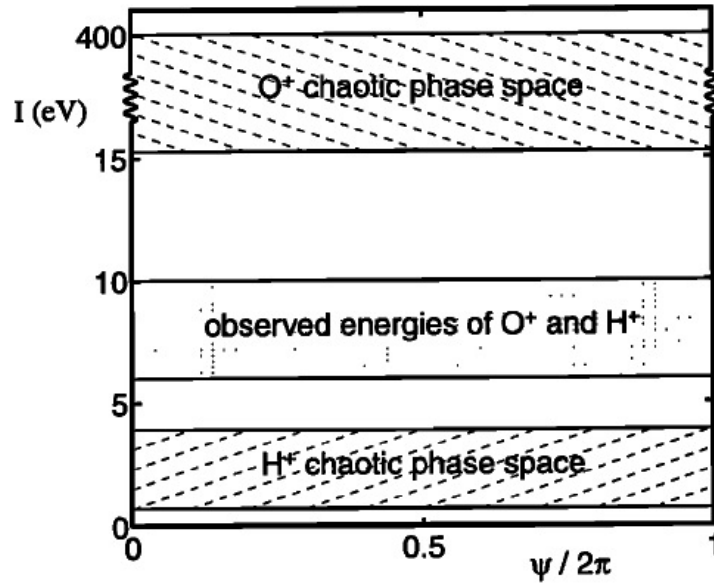


Figure 1.3: Figure from Ref. [16] that shows the observed initial energy of ions in the LHSS and the predicted regions where energy exchange with the waves can occur.

Given the failure of single wave theory to explain the anomalous acceleration, Ram et al. performed a numerical simulation to solve the equations of motion for a single ion subject to two electrostatic waves. Through a parametric investigation of frequency combinations, they demonstrated that when two waves satisfy the beat criterion, $\omega_2 - \omega_1 = n\Omega_i$, some low energy ions with velocities significantly different from the phase velocities of the individual waves are subject to a slow, coherent acceleration. This process energizes an ion until its velocity reaches the SEW resonant condition. Stochastic acceleration then becomes the dominant effect. Ram et al.

proposed that in the spectrum of propagating modes of the LHSS, some of the waves could satisfy the beat criterion. They then demonstrated through the same simple, non-self-consistent numerical model that given the reported experimental data, this process could explain the anomalous acceleration of ions.

Interestingly, in a more recent review of the LHSS structure in 2003, Schuck et al. [32] pointed out that the data set used by Ram et al. to perform their analysis contained significant errors in the estimates for the electrostatic wavelengths. In light of this, these authors demonstrated that Ram et al.'s simulations did not in fact predict the correct levels of acceleration observed in the ionosphere. This ruled out the BEW as a likely explanation for the anomalous acceleration.

Ram et al.'s work was still significant, however, in that they had identified a non-resonant mechanism for particle acceleration. A number of studies correspondingly have been devoted to understanding this interaction. In particular, Chia et al. [20] actually predate Ram et al. in attempting to characterize the underlying coherent acceleration that results when multiple waves are present that satisfy the beating wave criterion. Benisti et al. [17, 21] similarly published a detailed analytical and numerical analysis of single particle dynamics when subject to two externally imposed, perpendicularly-propagating electrostatic waves. They ultimately demonstrated that the beating condition is a necessary criterion to couple energy to low energy ions outside the resonant zones of the individual waves.

Strozzi et al. [22] were the first to examine the BEW effect on individual ion orbits for the more general case of oblique propagation. They demonstrated that coherent acceleration persists provided the difference in the parallel wavenumbers is small, and they also showed that the coherent acceleration characteristic of BEW will only accelerate ions up to the resonant velocity if the initial Hamiltonian of the ion falls within a certain range of values. This finding was a precursor to the more rigorous but specialized investigation performed by Spektor and Choueiri [23], who

in 2004 returned to the case of perpendicularly-propagating modes and demonstrated through an analysis of the single particle Hamiltonian that for the special case of two waves with equal amplitudes and equal perpendicular wavenumbers, the beating criterion is only a necessary condition for acceleration. There is in fact an additional requirement on the initial Hamiltonian of the ions in order for coherent acceleration to occur.

The culmination of this work is shown in Fig. 1.4 where we have a Poincaré cross-section [38] defined at the least common time period of the two beating waves. This portrait [23, 24], which shows the ion velocity as a function of Larmor angle, concisely depicts the types of dynamical behavior that ions will encounter when subject to two transversely-propagating BEW with equal wave amplitudes and wavenumbers. The three classes of trajectories are dictated by fixed points in the plane, H_H, H_E with the hyperbolic fixed point H_H corresponding to the phase velocity of the lower frequency wave. Particles near the elliptic point H_E are in the forbidden region and are only subject to sinusoidal changes in their perpendicular velocity with no net change in energy. On the other hand, ions in the stochastic region are sufficiently close to the phase velocity of the wave that they undergo SEW stochastic acceleration. Indeed, the SEW Poincaré cross-section is similar to the one shown in Fig. 1.4 where the entire area below the phase velocity becomes the forbidden region. The BEW effect occurs in the third, regular acceleration region where ions are subject to slow, coherent BEW acceleration until they reach the resonant condition. At this point they undergo stochastic acceleration.

From this portrait, the advantage of a single wave analysis becomes clear. We immediately can identify the nonlinear effect of the beating waves (the slow coherent acceleration) as well as the stochastic effect brought on by the individual SEW. For sparse, non-thermalized plasmas where individual acceleration is important and the waves can be approximated as externally imposed, the single particle analysis thus

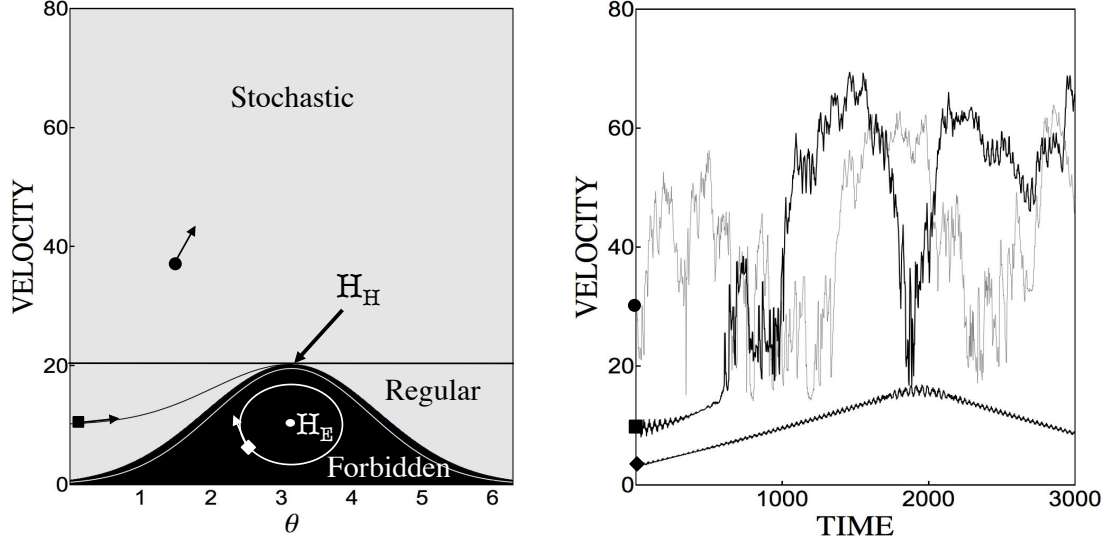


Figure 1.4: Left: Poincaré figure adapted from Spektor and Choueiri [23] that illustrates the necessary and sufficient conditions for coherent acceleration to occur for the case of two BEW with equal amplitudes and wavenumbers. The wave frequencies are $\omega_1 = 20.2\Omega_i, \omega_2 = 21.2\Omega_i$. The phase velocity of the lower frequency wave is denoted by the solid line. Right: sample trajectories in time for ions in each region of the Poincaré cross-section.

is the most apt for describing the dynamical system. On the other hand, when trying to characterize the heating of an ensemble of ions, single particle analysis has significant shortcomings – not only due to its lack of self-consistency but because of the fundamental difficulty of translating the inherently deterministic orbits predicted by the single ion Hamiltonian to the randomization of energy that is characteristic of ensemble heating. In the context of plasma heating then, single particle analysis best serves as a complement to the kinetic analysis from the previous section in that it indicates when the use of the random phase approximation is appropriate.

1.4 Previous laboratory experiments

A number of experiments have focused on NICD with the goal of explaining half-harmonic heating in magnetically confined fusion plasmas. These studies [26, 28, 39, 40] have experimentally demonstrated that nonlinear damping on both particle

species does in fact occur in magnetically confined fusion plasmas for SEW with sufficiently large wave amplitudes. As for the case of the BEW process where the nonlinear interaction arises from two externally imposed waves, there have been significantly fewer investigations. The first experimental work was performed by Porkolab and Chang [41, 42] who investigated the electron equivalent of NICD, nonlinear electron cyclotron damping (NECD), by examining wave damping and amplification in the presence of two nearly perpendicularly-propagating beating electron Bernstein modes. They confirmed to within an order of magnitude their predictive model for the nonlinear damping of electron modes and thus illustrated for the first time the reality of the nonlinear process for two externally-coupled waves. More recently, Spektor [43, 44, 24] constructed the first Beating Waves Experiment to explicitly compare the ion heating levels produced by SEW when compared to BEW. In this configuration, electrostatic ion cyclotron waves were launched in a magnetically confined argon plasma by means of a small plate antenna situated in the plasma, and the ion temperature increase was monitored with a laser induced fluorescence (LIF) system. The results from this setup indicated the superiority of BEW at the only set of wave frequencies and antenna power that were investigated.

While this study set the stage for more detailed investigations of nonlinear ion heating BEW, we note here that a few issues cast the results of this investigation into doubt. In particular, while there was an effort made to maintain equal input power to the antenna for both the SEW and BEW cases, the antenna coupling to the plasma from the individual waves was not taken into account. It therefore is possible that the second mode coupled to the plasma more efficiently by virtue of its higher frequency and longer parallel wavenumber. In this event, the total power carried into the plasma would have been greater than the SEWH case—even though the input power from the wave amplifier was the same. Thus, while the absorption of BEW could in fact have been the more efficient mechanism, the uncertainty about

the input power in this experiment precluded a direct comparison between processes. Additionally, the observed discrepancy between heating levels barely exceeded error bars such that the conclusion that the BEW heating was superior to SEW heating is suspect. Thus, while this study laid the ground work for more detailed investigations of the BEW plasma heating process, given the limited scope and limited statistical significance of results of this investigation, the work's conclusions are tenuous. BEW heating consequently has yet to be systematically compared with the SEW process.

1.5 Dissertation outline and approach

From previous theoretical, experimental, and numerical work, several aspects of the BEW mechanism have been examined. The ultimate goal of this dissertation is to build on these previous results with the purpose of answering the fundamental question: is the BEW process superior to SEW heating? To this end, we use in this thesis a common metric, the total input energy density to the waves, to compare the efficacy of the two processes in heating the plasma. We proceed by

1. Determining analytically the threshold for the onset of heating as a function of input energy density.
2. Comparing analytically and numerically SEWH and BEWH once the onset of heating has occurred.
3. Predicting analytically the criteria for the superiority of BEWH over SEWH.
4. Presenting experimental results to support our analytical findings.

In Chapter 2, we accomplish the first aim by employing a single particle description for BEW ion acceleration to predict the onset of stochastic particle orbits. This section largely follows the treatment of Karney et al. [36] who performed a similar analysis in determining the threshold for the onset of stochasticity in the presence of

a SEW. In Chapter 3, we present two models for BEW and SEW heating of an ion ensemble. The first connects directly to the single particle description outlined by Spektor and Choueiri [23] while the second is a kinetic model for power absorption that is largely inspired by Johnston’s Hamiltonian treatment for the same problem [19]. We use this second description to determine a criterion in terms of energy density for when BEWH is the superior process to SEWH. In Chapter 4, we describe our experimental setup, methods, and diagnostics for investigating the BEWH and SEWH in the second generation of the Beating Waves Experiment. In Chapter 5, we present our experimental results for a parametric investigation of the BEWH and SEWH processes and discuss these in context of our analytical predictions. Finally, in Chapter 6, we outline the implications of our work for future applications of BEWH as well as suggest additional avenues of research.

Chapter 2

Heating onset

From a single ion description it has been demonstrated that when two electrostatic waves satisfy the so-called beat criterion, $\omega_2 - \omega_1 = n\Omega_i$ where ω_1, ω_2 are the wave frequencies, Ω_i is the ion cyclotron frequency, and n is an integer, ions with initial velocity below the SEW phase velocity can experience significant acceleration through a two-stage process. First, the ions are coherently accelerated by the slowly varying beat envelope at the difference frequency $\omega_2 - \omega_1$ of the BEW. Second, after these ions have been accelerated to the phase velocities of the individual waves that comprise the BEW, the much faster stochastic effects characteristic of SEW dominate and ions are accelerated to higher energies through a random walk in velocity space.

The coherent acceleration of the low energy ions characteristic of the two-stage BEW process has been the subject of a number of theoretical and numerical studies [20, 16, 17, 21, 22, 23, 45, 25]. These investigations have not only predicted analytically the orbits followed by the low energy and coherently accelerated ions subject to BEW [17, 21, 22] but also—for a special case of wave parameters—the necessary and sufficient conditions for this acceleration to occur [23].

Most of these single ion results are valid only for velocities below the SEW resonant conditions of each wave, however, and with the exception of a first-order on-resonance

analysis done by Benisti et al. [21] and a numerical argument presented by Sheng et al. [45], the full extent of acceleration for ions after they reach this resonant condition is unknown. Indeed, the stochastic acceleration produced by BEW is not well understood, and to date it simply has been assumed without proof that these high energy orbits follow the well-established trends of stochasticity for SEW ion acceleration [22, 17, 25]. This is a critical oversight given the two-fold importance of stochastic effects to the BEW acceleration process. First, without decorrelation of particle orbits to supplement the coherent acceleration provided by BEW, the increase in ion energy can be significantly limited [20, 21]. Second, in addition to the coherent acceleration provided by the BEW, the existence of the beat resonance between the two waves suggests that for equal wave energy density, the onset of stochasticity for BEW should be lower than the SEW case [45]. Since the loss of phase information produced by this stochastic effect can lead to efficient power absorption of the waves, we anticipate enhanced heating for lower input energy with the BEW case—even when the coherent beat acceleration of low energy ions is suppressed (when extreme collisionality, for example, is dominant).

Stochasticity is thus an important consideration for the BEW process, and the need is apparent for a systematic evaluation of this effect. The goal of this chapter is to achieve this end by deriving an expression that indicates three critical aspects of the stochasticity: the threshold wave amplitudes for the onset of stochasticity; the lower bound in ion velocity at which this stochastic effect occurs; and the upper bound in ion velocity for particles subject to stochasticity.

In the first section, we begin with the case of perpendicular propagation and review the relevant equations of motion for the interaction of a single ion with BEW. In the second part, we examine analytically and numerically the particle dynamics through the use of the Poincaré cross-section. We also demonstrate in that section trends for the onset of stochasticity and its boundaries in phase space. In the third section, we

derive an analytical condition for the onset of stochasticity, which we subsequently verify numerically in the fourth section through an analysis of the maximum Lyapunov exponents. For the fifth part, we use our analytically derived condition to compare the onset of stochasticity for the SEW, BEW, and two non-beating waves. In the last section, we extend our results from the perpendicularly-propagating case to allow for a finite parallel wavenumber and derive a modified form of the stochasticity parameter.

2.1 Equations of motions

The equation of motion for an ion subject to two, perpendicularly-propagating electrostatic waves in a uniform magnetic field is given by [22]

$$m_i \frac{d^2 \mathbf{x}}{dt^2} = q \sum_{j=1}^2 \Phi_j k_{jx} \sin(k_{jx}x - \omega_j t + \alpha_j) + q \mathbf{v} \times \mathbf{B}, \quad (2.1)$$

where m_i denotes the ion mass, q is the charge, Φ_j is the potential amplitude, k_{jx} is the wave vector where we have denoted the direction of propagation as \hat{x} , ω_j is the wave frequency, $\mathbf{B} = B_0 \hat{z}$ denotes the background magnetic field, and α_j is the phase of the wave.

We can express this dynamical system in a normalized, action-angle formulation that is more easily analyzed by perturbation methods (Appendix A). This yields

$$H = I + \sum_{i=1}^2 \varepsilon_j \cos(\kappa_j \rho \sin \theta - \nu_j \tau + \varphi_j), \quad (2.2)$$

where capitalized letters denote normalized quantities, $I = \frac{1}{2} (V_x^2 + V_y^2)$ is the kinetic energy of the particle, $\nu_j = \omega_j / \Omega_i$, $\rho = \sqrt{2I}$, $\varepsilon_j = (q k_{1x}^2 \Phi_j / m_i \Omega_i^2)$, $\kappa_j = k_{jx} / k_{1x}$, θ is the angle of cyclotron precession measured from the \hat{y} direction, and $\tau = \Omega_i t$. In this system, lengths have been normalized by the wavelength k_{1x}^{-1} and velocities have been normalized by the term Ω_i / k_{1x} .

It should be noted that in this formulation, the definition of the normalized wave amplitude ε_j differs from those in related references [17, 23] by a factor of k_{1x}/Ω_i . This stems from our anticipated need to accommodate obliquely propagating waves with respect to the background magnetic field. Further implicit in this derivation is the result that the guiding center of motion in the \hat{x} direction is a constant of motion. This allows for the elimination of a degree of freedom in the problem.

We now see that the equations of motion can easily be separated into an action $H_0 = I$ that is modified by a phase- and time-dependent term $H_1(I, \theta, \tau)$. This form lends itself to perturbation analysis techniques that we employ in different measure throughout our investigation. Specifically, we can transform Eq. 2.2 to a more tractable form K by employing a second-order (in amplitudes $\varepsilon_1, \varepsilon_2$) canonical transformation derived with the method of Lie transforms (Appendix B) in Ref. [17]:

$$K = \tilde{I} + \sum_{j=1}^2 \varepsilon_j^2 S_1^{\nu_j}(\tilde{\rho}) + \varepsilon_1 \varepsilon_2 \cos \left[(\nu_1 - \nu_2) (\tilde{\theta} - \tau) + \varphi_1 - \varphi_2 \right] S_6(\tilde{\rho}), \quad (2.3)$$

where $\tilde{\theta}, \tilde{I}$ denote the transformed coordinates and we have

$$\begin{aligned} S_1^{\nu_j}(\tilde{\rho}) &= \sum_m \frac{m J_m(\kappa_j \tilde{\rho}) J'_m(\kappa_j \tilde{\rho})}{2\tilde{\rho}(\nu_j - m)} \\ S_6(\tilde{\rho}) &= \sum_m \frac{m J_m(\kappa_1 \tilde{\rho}) J'_{m+1}(\kappa_2 \tilde{\rho})}{2\tilde{\rho}(\nu_1 - m)} + \frac{m J_m(\kappa_2 \tilde{\rho}) J'_{m-1}(\kappa_1 \tilde{\rho})}{2\tilde{\rho}(\nu_2 - m)}. \end{aligned} \quad (2.4)$$

The summation is over all integer m , and J_m denotes the Bessel function of the first kind. This transformation was derived for the so-called off-resonance case where $\nu_2 - \nu_1 = 1$ and for $\nu_1 \neq n$, and $2\nu_1 \neq n$ where n is an integer. However, as we will demonstrate in the following sections, the threshold for stochasticity we find from this expression is numerically validated even for these exceptional cases. Additionally, the relationship between the canonical and the transformed variables is a first order transformation $I = \tilde{I} + O(\varepsilon_j), \theta = \tilde{\theta} + O(\varepsilon_j)$ [17]. For our purposes, we follow

the precedent of Refs. [17, 21, 22, 23] in adopting the small perturbation limit such that the transformation of coordinates is of order unity. We therefore drop the tilde coordinates in our subsequent analysis and allow $K \rightarrow H$.

2.2 Web structure

In order to illustrate the dynamics governed by Eq. 2.2, we employ the Poincaré cross-section (PC)—alternatively known as the surface of sections method [38]. We follow the previously established convention for BEW investigations [23] in defining our PC with respect to time. Numerical solutions are plotted in this case by integrating the equations of motion from Eq. 2.2 for a number of initial conditions, (θ, ρ) at $\tau = 0$, and sampling these values at a fixed time interval equal to the least common period of the two waves, τ_c .

We show a series of these PC in Fig. 2.1 for the representative parameters $\nu_1 = 24.2, \nu_2 = 25.2; \kappa_1 = \kappa_2 = 1; \varphi_1 = \varphi_2 = 0$; and increasing values of the perturbation ε where we have let $\varepsilon_1 = \varepsilon_2$ and defined $\varepsilon = \varepsilon_1$. The initial conditions in each plot are the same; however, the time of integration is larger for smaller wave amplitudes in order to account for the slower orbit frequency around islands in the PC. It is evident from these results that in the case of small perturbation strength ($\varepsilon = 0.1$), the beat effect produces a web structure in phase space characterized by a series of islands with intervening separatrices around which particle trajectories orbit. This island-populated phase space is well documented [21, 23] and can be predicted analytically by using a generating function of the second kind, $F_2 = J[\theta - \tau]$ [46], to canonically transform Eq. 2.3 to an autonomous form:

$$\hat{H} = \sum_{i=1}^2 \varepsilon_i^2 S_1^{\nu_i}(\rho) + \varepsilon_1 \varepsilon_2 \cos[\psi + \Delta\varphi] S_6(\rho), \quad (2.5)$$

where we have used $J = I$, $\psi = \theta - \tau$, $\Delta\varphi = \varphi_2 - \varphi_1$, and we have invoked the

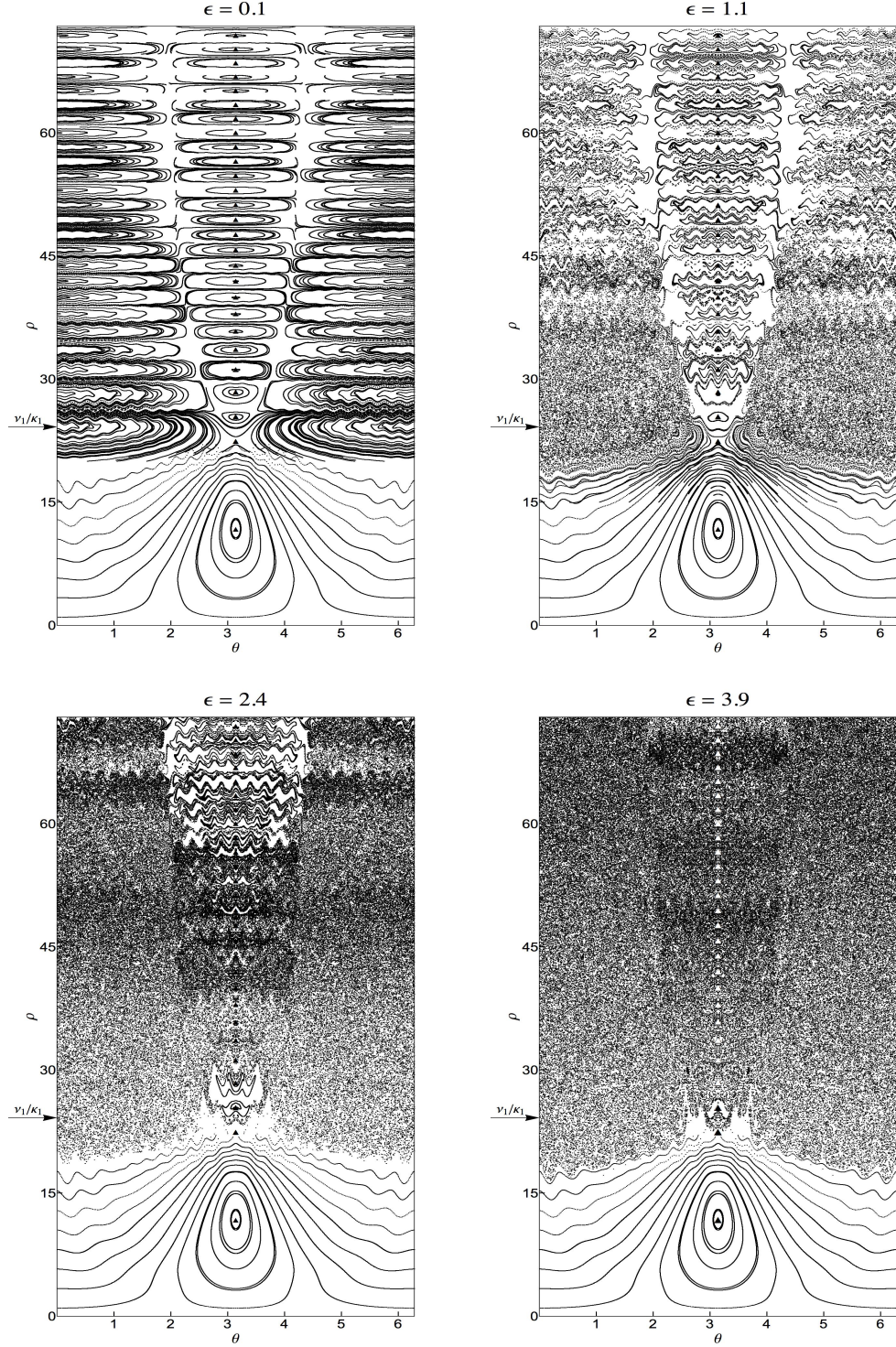


Figure 2.1: Poincaré cross sections in time defined at the least common period of the two waves, ν_1, ν_2 . The same initial conditions are used in all plots with the common wave parameters $\nu_1 = 24.2, \nu_2 = 25.2; \kappa_1 = \kappa_2 = 1; \varphi_1 = \varphi_2 = 0$. The wave amplitudes are also set equal such that $\varepsilon_1 = \varepsilon_2 = \varepsilon$. The markers ($\blacktriangle, \triangle$) indicate the locations of the analytically predicted elliptic points.

beating wave criterion, $\nu_2 - \nu_1 = 1$. In this form, lines of constant \hat{H} describe particle trajectories in the PC, and therefore, the islands and elliptic points should appear at the fixed points of the autonomous Hamiltonian, i.e. where

$$\begin{aligned}\dot{\psi} = 0 &= \sum_{i=1}^2 \varepsilon_i^2 \frac{1}{\rho} \frac{\partial S_1^{\nu_i}(\rho)}{\partial \rho} + \varepsilon_1 \varepsilon_2 \cos[\psi + \Delta\varphi] \frac{1}{\rho} \frac{\partial S_6(\rho)}{\partial \rho} \\ \dot{I} = 0 &= \varepsilon_1 \varepsilon_2 \sin[\psi + \Delta\varphi] S_6(\rho).\end{aligned}\tag{2.6}$$

We denote the location of the analytically predicted elliptic points from this result as markers in Fig. 2.1 where good agreement is observed with the particle orbits over the plotted phase space. This correspondence helps establish the validity of the second-order approach in the small amplitude limit. Furthermore, we note that the web structure predicted from Eqs. 2.5 and 2.6 persists with increasing values of ε for trajectories below the SEW resonant velocity, $\kappa_1 \rho = \nu_1$. This observation permits the continued use of Eq. 2.6 in characterizing this region of phase space for large wave amplitudes, and it is in part because of this expedient result that the coherent acceleration has been the primary focus of previous BEW investigations.

On the other hand, the analysis for trajectories above the SEW resonant conditions $\kappa_j \rho > \nu_j$ is significantly complicated for wave amplitudes where the second-order description begins to break down. Indeed, as can be seen from Fig. 2.1, with increasing perturbation strength the predicted web structure gives way to chaotic orbits. The stochasticity first appears with increasing ε for particles close to the resonant condition and near initial cyclotron phase $\theta \approx 0$ where they are in phase with the two waves. Ions with initial cyclotron angle out of phase with the waves $\theta \approx \pi$ remain in trapped orbits until sufficiently large amplitudes are reached ($\varepsilon = 3.9$). For intermediate values of perturbation strength ($\varepsilon = 1.1, 2.4$), the second-order prediction for the elliptic points remains approximately correct near the trapped orbits, and as already noted, below $\kappa_1 \rho \approx \nu_1$ the web structure persists for all cases. We also observe

that the stochastic region exhibits an upper bound above which the web structure persists and that the lower bound actually extends below the approximation $\kappa_1\rho \approx \nu_1$ for increasing values of ε .

These finite amplitude effects which are inherently tied to stochastic acceleration cannot be predicted by the second-order description in Eq. 2.5 since the integrability of this expression precludes stochastic dynamics. Spektor and Choueiri [23] circumvented this problem in part for the special case of equal wave amplitudes and wavenumbers $\varepsilon_1 = \varepsilon_2, \kappa_1 = \kappa_2$ by identifying—as we have done here through a visual inspection of the PC—the location of the lower bound with the lowest analytical predicted hyperbolic point from Eq. 2.6. They thus recovered $\kappa_1\rho \approx \nu_1$. A similar analysis can be followed from the work of Strozzi et al. [22] whose derivation of the autonomous Hamiltonian in the case of obliquely propagating waves allows for a similar (though numerical) calculation of critical points. These estimates for the lower bounds are only approximations, however, in that they do not take into account the root of the stochasticity in phase space. It is for the same reason that these studies do not provide general predictions for the upper bound of the stochastic region or a threshold condition for the onset of stochasticity. The need is thus apparent to give special attention to the chaotic orbits in the system, and in the following section we motivate a description of the dynamics that accounts for these effects.

2.3 Stochastic onset

2.3.1 Resonances

One commonly employed method to establish the onset of stochasticity for a dynamical system is the so-called Chirikov condition [47], which states that stochasticity occurs when the separation between resonances in phase space becomes smaller than their average frequency half-widths. The physical reason behind this criterion stems

from the frequency mixing produced by the overlap of resonances, which in turn can lead to the decorrelation of particle orbits.

For our dynamical system, we expect to see two classes of resonances: 1) those associated with the SEW resonance between cyclotron motion and the individual wave frequencies such that $\langle \dot{\theta} \rangle / \nu_i = m/n$ where $\langle \rangle$ denotes the time average and n, m are integers and 2) those associated with the BEW resonance between the cyclotron motion and the beat frequency of the waves, $\langle \dot{\theta} \rangle / (\nu_2 - \nu_1) = 1$. Both of these resonances—when they exist—will appear as fixed points in the PC we defined in the previous section. This can be seen explicitly by considering the criterion for the formation of fixed points in this PC:

$$\frac{\nu_c}{\langle \dot{\theta} \rangle} = \frac{p}{s}, \quad (2.7)$$

where s, p are positive integers, $\nu_c = 1/\tau_c$ is the frequency of the common period of ν_1, ν_2 , $\dot{\theta}$ is derived from the non-autonomous Hamiltonian, and $\langle \cdot \rangle$ here denotes the average over p periods of the sampling time, τ_c . We can see from this prescription that BEW resonance corresponds to first-degree islands where $p = 1$, i.e. island chains that only exhibit a single fixed point in the PC. This is exactly the web structure shown in the $\varepsilon = 0.1$ case of Fig. 2.1 and predicted from the autonomous Hamiltonian in Eq. 2.5. On the other hand, we anticipate the islands from interactions with the SEW resonances first to occur where $\langle \dot{\theta} \rangle = \nu_i / \|\nu_i\|$ [35, 12] ($\|\cdot\|$ denotes the nearest integer function). This suggests that these resonances should appear as $p = \|\nu_i\|$ fixed points in the cross-section, and indeed, the effects of these islands can be observed as the periodic ripples in the first degree island orbits.

We have noted from the analytical work in the previous section that the islands due to the BEW effect ($p = 1$) persist for arbitrarily small wave amplitudes. However, as can be seen qualitatively from Fig. 2.1, the resonances associated with in-

dividual waves, ν_1, ν_2 , exist exclusively near the SEW resonant velocities in phase space $\rho = \nu_j/\kappa_j$. It is only with increasing perturbation strength that these higher degree islands expand into higher velocities, i.e. larger values of ρ . This can be explained by considering the source of these respective resonances. In the BEW case, the resonances arise from the difference frequency of the two waves—a fixed parameter—which is inherent to the system. On the other hand, SEW resonances require nonlinear perturbations in the average frequency of cyclotron precession $\langle \dot{\theta} \rangle$ in order to be satisfied. This distinction between resonances is important, for even though the BEW islands exist for small amplitudes, we can see from a qualitative inspection of Fig. 2.1 that it is the SEW resonances and their overlap with the inherent BEW resonances that lead to stochasticity.

In order to demonstrate this overlap analytically from the Chirikov criterion it is necessary to identify the location of these resonances as well as the perturbation-dependent width. We can analytically do the former through a second-order perturbation analysis. Characterizing the widths, however, in a global and analytical way is significantly more difficult: while there is an established method [47] for determining island widths, the linearity of $H_0 = I$ in our system precludes the necessary step in this prescription of approximating the motion as a non-linear pendulum.

In light of this limitation, we are forced to turn in the following section to a numerical analysis to complement our investigation. In a technique inspired by Karney and Bers [35, 12] we start by identifying analytically a perturbation-dependent term that predicts the existence of the higher degree SEW resonances and assume that the onset of stochasticity scales with it. We then use this scaling term in conjunction with a numerical investigation of the PC to derive a quasi-analytical condition for the onset of stochasticity.

2.3.2 Parameter for stochastic onset

We begin by referring to the non-autonomous, second-order Hamiltonian from Eq. 2.3 to derive a condition for the formation of SEW islands. As we have noted previously, this integrable Hamiltonian cannot map out stochastic orbits. We therefore only use it to predict the appearance of higher degree, integrable islands in phase space. The stochastic overlap of these islands is reserved for the numerical discussion.

With this in mind, we first determine the equations of motion from Eq. 2.3:

$$\begin{aligned}\dot{\theta} &= 1 + \sum_{j=1}^2 \varepsilon_j^2 \frac{1}{\rho} \frac{\partial S_1^{\nu_j}(\rho)}{\partial \rho} + \varepsilon_1 \varepsilon_2 \cos[\theta - \tau + \Delta\varphi] \frac{1}{\rho} \frac{\partial S_6(\rho)}{\partial \rho} \\ \dot{I} &= \varepsilon_1 \varepsilon_2 \sin[\theta - \tau + \Delta\varphi] S_6(\rho).\end{aligned}\tag{2.8}$$

From the first line of this expression, we can infer that $\theta \approx \tau + \theta_0 + O(\varepsilon_j^2)$ where θ_0 denotes an initial Larmor angle. For our analysis, we let this initial condition satisfy $\theta_0 + \Delta\varphi = 0$ since we have already pointed out from the plots in Fig. 2.1 that this relative phase with respect to the BEW waves is the most favorable for the onset of stochasticity. For small potential amplitudes, we consequently see that $\langle \dot{I} \rangle \sim O(\varepsilon_j^4)$, which allows us to assume constancy to second order for the action in our estimates. We further use the approximation $\theta \approx \tau + \theta_0 + O(\varepsilon_j^2)$ to assert the periodic term in $\dot{\theta}$ is constant when taking the average indicated in Eq. 2.7. This yields

$$\langle \dot{\theta} \rangle \approx 1 + \sum_{j=1}^2 \varepsilon_j^2 \frac{1}{\rho} \frac{\partial S_1^{\nu_j}(\rho)}{\partial \rho} + \varepsilon_1 \varepsilon_2 \frac{1}{\rho} \frac{\partial S_6(\rho)}{\partial \rho}.\tag{2.9}$$

With this expression, we first consider the resonances produced by the lower frequency wave: $\langle \dot{\theta} \rangle / \nu_1 = n/m$ where n and m are integers. For different values of n, m , we follow a treatment similar to that of Karney in defining a parameter

$R = \|\nu_1\| \langle \dot{\theta} \rangle - \nu_1$ such that from Eq. 2.9

$$R = -\delta + \|\nu_1\| \left[\sum_{i=1}^2 \varepsilon_i^2 \frac{1}{\rho} \frac{\partial S_1^{\nu_i}(\rho)}{\partial \rho} + \varepsilon_1 \varepsilon_2 \frac{1}{\rho} \frac{\partial S_6(\rho)}{\partial \rho} \right]. \quad (2.10)$$

where $\delta = \nu_1 - \|\nu_1\|$. Large values of $|R|$ correspond to the onset of additional resonances and islands in the BEW PC. Indeed, $R = 0$ corresponds to the first onset of islands where $n = 1, m = \|\nu_1\|$, while deviations from $R = 0$ indicate the formation of increasingly non-linear $\langle \dot{\theta} \rangle \neq 1$ resonances. This suggests an appropriate scaling term for the onset of stochasticity:

$$F_1 = f(\delta) \|\nu_1\| \left[\sum_{j=1}^2 \varepsilon_j^2 \frac{1}{\rho} \frac{\partial S_1^{\nu_j}(\rho)}{\partial \rho} + \varepsilon_1 \varepsilon_2 \frac{1}{\rho} \frac{\partial S_6(\rho)}{\partial \rho} \right], \quad (2.11)$$

where we have collapsed the dependence on δ into a function $f(\delta)$. We find a similar result for the onset of islands around the resonances of the second wave:

$$F_2 = f(\delta) \|\nu_2\| \left[\sum_{i=1}^2 \varepsilon_i^2 \frac{1}{\rho} \frac{\partial S_1^{\nu_i}(\rho)}{\partial \rho} + \varepsilon_1 \varepsilon_2 \frac{1}{\rho} \frac{\partial S_6(\rho)}{\partial \rho} \right]. \quad (2.12)$$

In the case of large $\nu_1 \gg 1$, these results converge to a global parameter for island overlap at the resonances of each wave. For the remainder of the discussion then, we invoke this large frequency assumption in Eq. 2.11 by defining $F = F_1 \rightarrow F_2$ and similarly $\|\nu_j\| \rightarrow \nu_j$. We note here that solving this term for the case where $F = 0$ corresponds to calculating the location of the elliptic points in the ν_c cross-section from Eq. 2.5. This is not surprising since following the same treatment above for the BEW resonance (substituting $\nu_1 \rightarrow 1; n = m = 1$) should produce a condition for the formation of $p = 1$ islands in the PC.

For higher-order resonances and $F \neq 0$, however, we seek a simpler form of Eq. 2.11. In the limit of large $\kappa_j \rho > \nu_j + (\frac{1}{2}\nu_j)^{1/3}$, we see that this term can be

expressed as (Appendix C):

$$F = f(\delta) \frac{\nu_1^2 \pi}{2 \sin(\pi \delta)} \left[(\varepsilon_1 A_1(\rho) \sin \alpha_1 + A_2(\rho) \varepsilon_2 \sin \alpha_2)^2 - \varepsilon_1 \varepsilon_2 \frac{(A_1^4(\rho) + A_2^4(\rho))}{A_1(\rho) A_2(\rho)} \cos \alpha_1 \cos \alpha_2 - (\varepsilon_1 A_1(\rho) \cos \alpha_1)^2 - (\varepsilon_2 A_2(\rho) \cos \alpha_2)^2 \right], \quad (2.13)$$

where we have defined

$$A_i(\rho) = \frac{|H_{\nu_i}^{1'}(\kappa_i \rho)|}{\rho} \quad (2.14)$$

$$\alpha_i = \left[((\kappa_i \rho)^2 - \nu_i^2)^{1/2} - \nu_i \cos^{-1} \left(\frac{\nu_i}{\kappa_i \rho} \right) - \frac{\pi}{4} (1 - 2\delta) \right].$$

Here $H_{\nu_i}^1$ denotes the Hankel function of the first kind and the derivative is with respect to ρ . In order to simplify this result further, it is desirable to find a method for factoring the additional terms. With this purpose in mind, we show in Appendix C that in the large velocity limit ($\kappa_2 \rho, \kappa_1 \rho \gg \nu_2, \nu_1$) and assuming $\kappa_2 \sim \kappa_1$, we can reduce the second term to

$$\frac{\nu_1^2 \pi}{2 \sin(\pi \delta)} (\varepsilon_1 A_1(\rho) \cos \alpha_1 + A_2(\rho) \varepsilon_2 \cos \alpha_2)^2, \quad (2.15)$$

such that the total expression for the scaling parameter is given by

$$F = f(\delta) \frac{\nu_1^2 \pi}{2 \sin(\pi \delta)} \times \left[(\varepsilon_1 A_1(\rho) \sin \alpha_1 + \varepsilon_2 A_2(\rho) \sin \alpha_2)^2 - (\varepsilon_1 A_1(\rho) \cos \alpha_1 + \varepsilon_2 A_2(\rho) \cos \alpha_2)^2 \right]. \quad (2.16)$$

Finally, we note that since both α_1 and α_2 are rapidly varying functions of ρ , we need only retain the amplitudes of the scaling terms. This suggests that the correct

parameter for the onset of stochasticity is given by

$$F = f(\delta) G(\nu_1, \varepsilon_1, \varepsilon_2, \kappa_1, \kappa_2, \rho), \quad (2.17)$$

where we have folded the constants into the function $f(\delta)$ and defined

$$G(\nu_1, \varepsilon_1, \varepsilon_2, \kappa_1, \kappa_2, \rho) = \nu_1 (\varepsilon_1 A_1(\rho) + \varepsilon_2 A_2(\rho)) \quad (2.18)$$

This final expression provides a simple term for the onset of stochasticity in the case of perpendicularly-propagating BEW that is valid for ion velocities greater than the wave velocity and for normalized wavenumbers that satisfy $\kappa_2 \sim \kappa_1$. It is of particular importance that we were able to factor this result since this form suggests that the BEW effect has a lower threshold for stochasticity than the case with two non-beating waves. We postpone this discussion for the moment, however, in order to numerically verify Eq. 2.17 and determine the appropriate form of $f(\delta)$. To this end, in the following section we use a numerically calculated criterion—the maximum Lyapunov exponent—for stochasticity in phase space.

2.4 Numerical analysis

For dynamical systems, the maximum Lyapunov exponent λ provides a measure of the separation $|\mathbf{Z}|$ in phase space of two particle trajectories as it depends on the small initial separation, $|\mathbf{Z}_0|$ [38]:

$$|\mathbf{Z}| = |\mathbf{Z}_0| e^{\lambda\tau}. \quad (2.19)$$

Since a positive λ corresponds to exponentially diverging trajectories, this parameter can serve as a metric for the degree of stochasticity in a local region of phase space. For

our system, we used a prescribed algorithm (Appendix D) to numerically estimate the maximum Lyapunov exponents (MLE) of Eq. 2.2 as a function of initial conditions, (θ, ρ) at $\tau = 0$. This method yielded values of λ that converged for $\tau < 150$ in all cases considered. Additionally, in order to approximate this stochastic parameter as a function strictly of ρ , we selected five equally spaced initial values of θ for a fixed ρ and averaged them to find $\bar{\lambda}(\rho) = \frac{1}{5} \sum_{n=1}^5 \lambda(n2\pi/5, \rho)$.

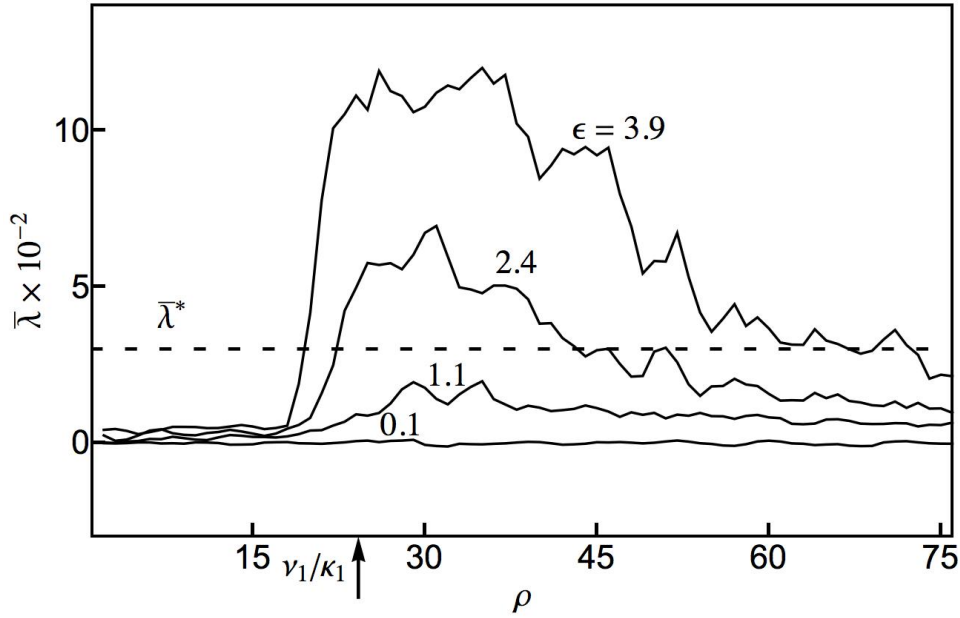


Figure 2.2: The angle-averaged maximum Lyapunov exponent as a function of normalized velocity for the same wave parameters as in Fig. 2.1. The dashed line represents the stochastic value of MLE where the majority of orbits in phase space of the corresponding PC are chaotic.

We show $\bar{\lambda}(\rho)$ in Fig. 2.2 for the same wave parameters as the four cases in Fig. 2.1. Based on the criterion that $\bar{\lambda} > 0$ corresponds to the appearance of non-integrable, diverging orbits, we see that the average MLE accurately predicts the trends depicted in the BEW PCs. For the non-stochastic case in Fig. 2.1 ($\epsilon = 0.1$), the value of the average MLE is $\bar{\lambda} \approx 0$ for the entire range of phase space. On the other hand, the MLE becomes finite with increasing perturbation strength. This

occurs first in the vicinity of the SEW resonant condition $\kappa_1\rho = \nu_1$, which as can be seen from the $\varepsilon = 1.1$ case of Fig. 2.1 is where stochasticity first appears in the PC. As the normalized amplitude becomes even larger, the region of stochasticity extends to a wider range of velocities around the resonant SEW velocity. This trend reflects the orbits shown in the corresponding PC where stochasticity is most prevalent near the SEW resonant condition but gives way to the BEW web structure away from this velocity. A more detailed visual inspection of these PCs reveals that while non-zero, finite values of the MLE indicate the first appearance of stochastic orbits, the phase space becomes dominated by chaotic orbits above a finite threshold value that we denote $\bar{\lambda}^* \approx 3 \times 10^{-2}$. We adopt this numerical estimate as a local metric for stochasticity in the following discussion.

Armed with this criterion for stochasticity, we now can investigate the validity of the analytically derived term in Eq. 2.17 by examining the dependence of the average MLE on the stochasticity parameter. In particular, since larger values of F correspond to increased stochasticity, we anticipate a monotonic relationship between F and $\bar{\lambda}$ where at a threshold value F^* stochasticity will occur, i.e. $\bar{\lambda}(F^*) = \bar{\lambda}^*$. The term $f(\delta)$, however, is an unknown function, which bars us from explicitly examining the impact of the stochastic parameter, F . To overcome this limitation, we make the *a priori* assumption that $f(\delta)$ is approximately constant for our analysis, and we instead plot $\bar{\lambda}$ as a function of the defined parameter $G(\nu_1, \varepsilon_1, \varepsilon_2, \kappa_1, \kappa_2, \rho)$ in Fig. 2.3.

We made our numerical investigation of this term comprehensive by generating values of G from a wide range of possible parameters. This was accomplished by randomly selecting 1000 sets of values $(\varepsilon_1, \varepsilon_2, \nu_1, \kappa_1, \kappa_2, \rho)$ that satisfied $G < 0.4$ from the parameter space defined by $\varepsilon_1 \in (1, 20)$, $\varepsilon_2 \in (1, 20)$, $\nu_1 \in (10, 100)$, $\kappa_2 \in (0.7, 1.2)$, and $\rho \in (1, 100)$. On-resonance values $\nu_1 = n$ where n is an integer were included in this range, but since $\kappa_1 = 1$ by virtue of our normalization scheme, it was not necessary to vary this parameter. Using these 1000 values, we then determined

numerically the corresponding phase-averaged MLE, $\bar{\lambda}$. The mean trend from this calculation for $G(\lambda)$ is shown in Fig. 2.3 along with confidence intervals, denoted by the shaded range, where 93% of the 1000 selected points fell.

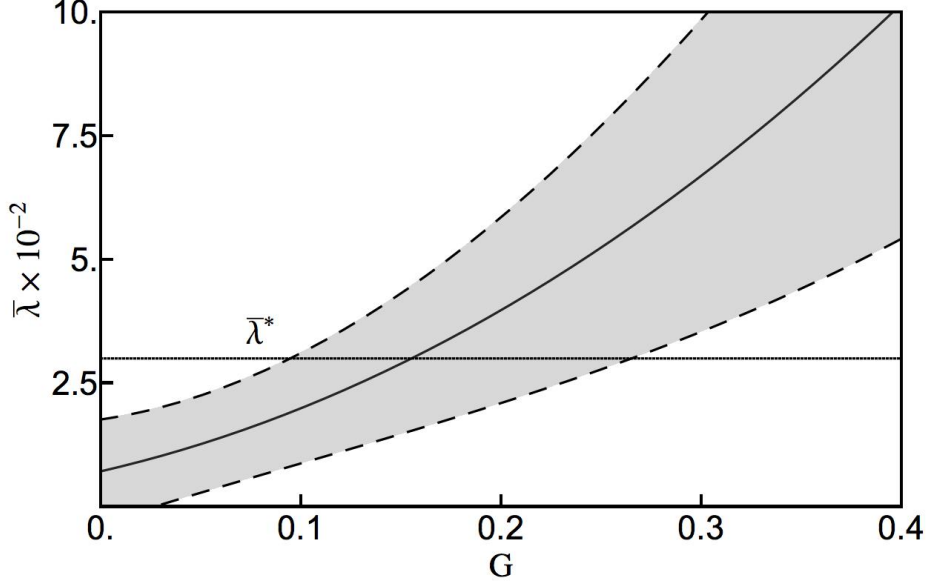


Figure 2.3: The average MLE plotted as a function of the stochastic parameter, G . The solid line indicates the mean trend while the gray region marks the 93% confidence interval for the numerically calculated values. The stochastic condition $\bar{\lambda}^*$ is also shown as a horizontal line.

In spite of the wide range of initial conditions, we see the anticipated monotonically increasing trend of $\bar{\lambda}$ with G . This dependence serves to validate our derivation of G as a correct scaling parameter for the local stochastic state of phase space—even when $\nu_1 = \|\nu_1\|$ where our analytical derivation is not strictly valid. Moreover, we can use our threshold value $\bar{\lambda}^* = 3 \times 10^{-2}$ to estimate from Eq. 2.17 that phase space is stochastic when $G > 0.1 - 0.27$. Our assumption that $f(\delta)$ is approximately constant is thus borne out with an appropriate range of values given by $f(\delta) = 3.7 - 10$. It is important to note that this spread in value persists even when the above investigation is repeated only allowing for a constant off-resonance condition that satisfies $\delta \neq 0$. This suggests that the uncertainty in $f(\delta)$ is not a result of the breakdown in the

validity of Eq. 2.17 in the on-resonance case. Rather, this variance likely stems from small differences in the dynamical orbits brought about by the widely different wave parameters we considered.

We note here that for the SEW case ($\varepsilon_2 \rightarrow 0$) Karney [12] numerically found $f(\delta) = 4$ while Fukuyama [37] with a less stringent condition of stochasticity found $f(\delta) = 6.7$. Both of these investigations were limited in scope, however, in that the numerical analyses were performed for one value of $\|\nu_1\|$ and a small range of ρ values. An analysis over a wider range of parameters introduces less certainty for the estimate of $f(\delta)$. We can confirm this explicitly by investigating our BEW result, $F = f(\delta)G$, in the SEW limit ($\varepsilon_2 = 0$) where our expression converges to the criteria for stochasticity derived in these previously cited studies. With this term, we have repeated the above analysis in the SEW limit over the same range of wave variables to find $f(\delta) = 5 - 10$. This range lies just above the value reported by Karney—a difference that likely stems from the definition for when phase space is primarily stochastic. The more important insight from this result, however, is that the precision of the previously reported SEW case is an artifact of the small range of values that were numerically investigated.

With this in mind, our above analysis allows us to assert the final, linear result for the stochastic parameter in the BEW case:

$$\alpha < \nu_1 (\varepsilon_1 A_1 + \varepsilon_2 A_2), \quad (2.20)$$

where $\alpha = 0.1 - 0.27$. This simplified form incorporates the effects of both waves while it reduces to the previously derived SEW stochasticity limit for small $\varepsilon_2 \rightarrow 0$. This expression also provides a means for characterizing the upper bound of stochasticity in the BEW system for a fixed set of wave parameters. Indeed, for finite $\varepsilon_1, \varepsilon_2$, we see the upper bound in stochastic space occurs where ρ is sufficiently large that Eq. 2.20

is violated. This is shown in Fig. 2.4 where we have plotted the analytical result for $\varepsilon = \varepsilon_1 = \varepsilon_2$ along with the numerically calculated upper bound. The parameter $\alpha = 0.27$ yielded the best fit line in this case.

A similar calculation for the lower bound in phase space is precluded by the underlying assumptions we made in deriving $A_1(\rho), A_2(\rho)$ in Eq. 2.14. Specifically, the Hankel functions are approximations for the amplitude of the Bessel function that are only valid in the limit $\rho\kappa_i > \nu_i + (\frac{1}{2}\nu_i)^{1/3}$, and while these functions diverge at $\rho \rightarrow 0$, we anticipate from our numerical observations of phase space that the coefficients $A_1(\rho), A_2(\rho)$ should in fact approach 0. We therefore are forced to search for an approximate form of the coefficients in the small ρ limit. A reasonable choice is to infer that $A_i(\rho)$ will continue to scale with the amplitude $J'(\kappa_i\rho)$. This is expedient since it not only approaches 0 for small ρ but monotonically increases in the prescribed range until exhibiting a local maximum near $\rho \approx \nu_i/\kappa_i$. Given these considerations then, we can recover an approximate form for these coefficients by extending the definition of A_1, A_2 to encompass the lower values of ρ :

$$A_i(\rho) = \frac{1}{\rho} [\text{envl}(J'_{\nu_i}(\kappa_i\rho))], \quad (2.21)$$

where in order to ensure continuity we have defined envl as a fourth degree interpolating polynomial that satisfies

$$\text{envl}(\rho) = \begin{cases} |H_{\nu_i}^{1'}(\kappa_i\rho)| & \text{for } \kappa_i\rho \geq \nu_i + (\frac{1}{2}\nu_i)^{1/3} \\ J'_{\nu_i}(\kappa_i\rho) & \text{for } \kappa_i\rho < \nu_i. \end{cases}$$

From this result, we plot the predicted lower bound of the stochastic region as a function of ε in Fig. 2.4 along with the numerically observed values. We see general agreement in spite of the approximations we made in deriving this term. In particular, the lower bound is characterized by the phase velocity of the slower wave $\rho = \nu_i/\kappa_i$ with a weak dependence on the perturbation strength— a similar result to that previously reported for SEW [12] and a special case of BEW [23].

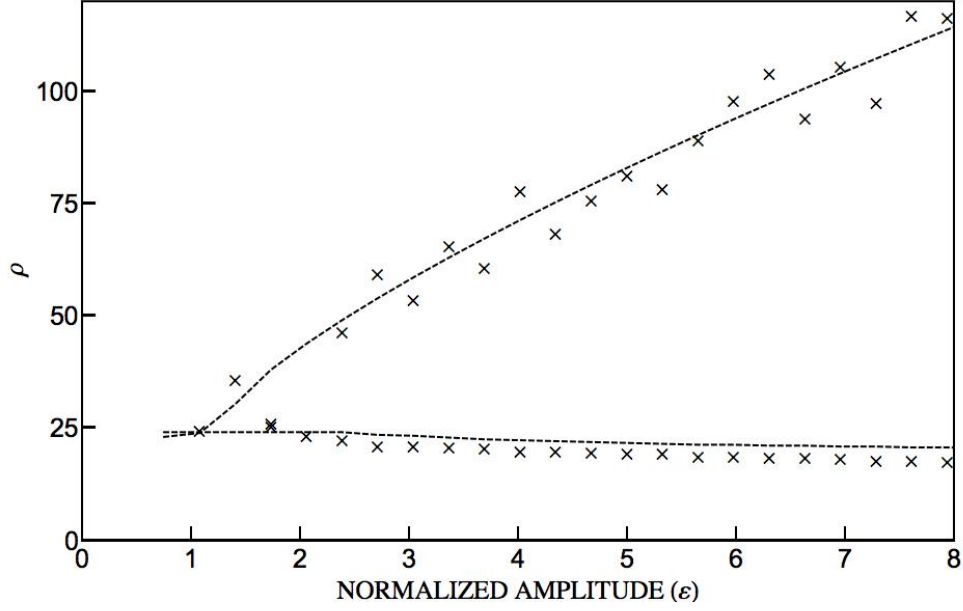


Figure 2.4: Upper and lower bounds of stochastic region as a function of normalized wave amplitude. The markers represent numerically calculated values for the same wave parameters as Fig. 2.1 with $\varepsilon = \varepsilon_1 = \varepsilon_2$. The dashed lines are the analytically derived bounds for $\alpha = 0.27$.

The modified definitions of $A_1(\rho)$ and $A_2(\rho)$ allow us to determine the full extent of phase space that is stochastic, and in some special cases, they can be used in conjunction with Eq. 2.20 to identify analytically the minimum set of wave amplitudes $\varepsilon_1, \varepsilon_2$ for when stochasticity first appears. Specifically, when $\nu_1 > 1$ and $\nu_1/\kappa_1 \approx \nu_2/\kappa_2$, such as may be found in acoustic modes, we see that both coefficients exhibit maxima at $\rho \approx \nu_1/\kappa_1$. At this maximum value and in the limit of large normalized frequency, we see that the Bessel functions can be simplified to $J'_x(x) \approx x^{-2/3}$ [11] such that the coefficients become $A_i(\rho) = \kappa_i^2 \nu_i^{-5/3}$. We substitute this into the above criterion to find the threshold condition for the onset of stochasticity:

$$\alpha = \kappa_1^2 \nu_1^{-1} \left(\varepsilon_1 \nu_1^{1/3} + \varepsilon_2 \nu_2^{1/3} \right). \quad (2.22)$$

This concise form, which is applicable to perpendicularly-propagating acoustic modes,

shows explicitly that the condition for onset depends linearly on perturbation strength where the amplitude of each mode is weighted by the frequency. Of course, the validity of this expression is violated for waves with greater dispersion, but even in this limit, it still can serve as a first test for stochasticity. More generally, this linear dependence is an important consideration for the next section where we demonstrate how stochasticity can be achieved with BEW for lower input energy densities of the exciting waves than with the SEW and non-BEW two-wave systems.

2.5 Comparison between SEW, BEW, and non-beating waves

By comparing the SEW limiting case of Eq. 2.20 to the full expression, we see that stochasticity can be achieved with BEW for lower individual wave amplitude values. A more important question when comparing the efficiency of the two processes, however, is whether stochastic onset occurs for a lower total energy density in the BEW case. To consider this possibility, we first note that the total energy density of each electrostatic wave depends quadratically on the potential [10] such that

$$W = \bar{\beta}_1 \varepsilon_1^2 + \bar{\beta}_2 \varepsilon_2^2, \quad (2.23)$$

where W is the total energy density and $\bar{\beta}_1, \bar{\beta}_2$ are two constants that depend on the individual wave parameters, ν_i, κ_i . Let us denote $\eta = \bar{\beta}_1 \varepsilon_1^2 / W$, i.e. the fractional energy density in the first mode. The threshold for stochasticity in the BEW case then becomes

$$\nu_1 \sqrt{W_{BEW}} \left[A_1(\rho) \bar{\beta}_1^{-1/2} \sqrt{\eta} + A_2(\rho) \bar{\beta}_2^{-1/2} \sqrt{1 - \eta} \right] = \alpha. \quad (2.24)$$

Similarly, the thresholds for the individual SEW are

$$\begin{aligned}\nu_1 (W_{1(SEW)}/\bar{\beta}_1)^{1/2} A_1(\rho) &= \alpha \\ \nu_2 (W_{2(SEW)}/\bar{\beta}_2)^{1/2} A_2(\rho) &= \alpha,\end{aligned}\tag{2.25}$$

where we have assumed the total energy density is concentrated in each mode. The ratio of the required energy density for the onset of stochasticity of BEW compared to that required for the onset of stochasticity for each SEW is thus given by

$$\begin{aligned}\left(\frac{W_{1(SEW)}}{W_{BEW}}\right)^{1/2} &= \left[\sqrt{\eta} + \gamma\sqrt{1-\eta}\right] \\ \left(\frac{W_{2(SEW)}}{W_{BEW}}\right)^{1/2} &= \left[\gamma^{-1}\sqrt{\eta} + \sqrt{1-\eta}\right],\end{aligned}\tag{2.26}$$

where we have denoted $\gamma = (A_2/A_1) (\bar{\beta}_1/\bar{\beta}_2)^{1/2}$ and made the simplifying assumption that $\nu_2/\nu_1 \approx 1$. The BEW process has a lower energy density threshold for the onset of stochasticity if there exists $\eta \in (0, 1)$ when both expressions are greater than 1. It is evident from Eq. 2.26 that this condition is only satisfied provided $\gamma \neq 0, \infty$. These limiting cases can be discounted, however, as they represent the non-physical scenarios where the energy content of one of the BEW is 0.

BEW—subject to the assumptions outlined above—thus will produce stochasticity for lower energy densities than a SEW. This is a significant result as the onset of stochasticity has been shown to coincide with a threshold for plasma heating [48, 49]. The onset of heating therefore may occur for lower levels of energy density with BEW, though of course once this threshold has been exceeded, the level of heating is dependent on the self-consistent exchange of energy of both the SEW and BEW processes. An analysis of this is reserved for the following chapter.

For a final comparison, we examine the case for when there are two waves that *do not* satisfy the beating criterion, i.e. there is no beat resonance. The second-order cross term in Eq. 2.3 that is proportional to $\varepsilon_1 \varepsilon_2$ consequently disappears in the

derivation outlined in Sec. 2.3.2 such that the threshold for the onset of stochasticity becomes

$$\alpha = \nu_1 \left([\varepsilon_1 A_1(\rho)]^2 + [\varepsilon_2 A_2(\rho)]^2 \right)^{1/2}, \quad (2.27)$$

where we have assumed the same range for α . Comparing this result with the BEW case, we immediately see that without the benefit of the beat effect, the onset condition for stochasticity is higher for a given energy density. This stems mathematically from the missing cross-term in the threshold and physically from the loss of the additional resonances in phase space.

Moreover, without the beat effect, the two waves do not appear to offer any energy-saving advantage over SEW stochasticity. We can see this explicitly by expressing Eq. 2.27 in terms of energy densities:

$$\nu_1 \sqrt{W_{nBEW}} \left[A_1^2(\rho) \bar{\beta}_1^{-1} \eta + A_2^2(\rho) \bar{\beta}_2^{-1} (1 - \eta) \right]^{1/2} = \alpha, \quad (2.28)$$

where we have denoted the total energy density of the non-beating waves as W_{nBEW} . When we compare the cases for the energy density for the onset of stochasticity with the SEW case, we find

$$\begin{aligned} \frac{W_{1(SEW)}}{W_{nBEW}} &= \eta + \gamma^2 (1 - \eta) \\ \frac{W_{2(SEW)}}{W_{nBEW}} &= \gamma^{-2} \eta + (1 - \eta). \end{aligned} \quad (2.29)$$

Again, the condition for when the non-BEW process is superior to the SEW occurs when there is some value η such that $W_{1(SEW)}/W_{nBEW}, W_{2(SEW)}/W_{nBEW} > 1$. Solving from the above equations, we see this condition cannot be satisfied for $\eta \in (0, 1)$. Therefore, we must conclude that in the non-BEW case, even though lower individual wave amplitudes are required to produce onset of stochasticity, this two-wave process is not superior to the SEW case when examined in the context of

total wave energy density.

2.6 Oblique propagation

The above findings have applications for physically realizable cases where collinear, perpendicularly-propagating modes are employed. However, in order to extend this discussion to encompass situations where oblique propagation is allowed, we consider briefly in this section the impact of a finite parallel wavenumber.

When including the effects of parallel wave propagation, the Hamiltonian from Eq. 2.2 becomes (Appendix A)

$$H = I + \frac{1}{2}P_z^2 + \sum_{j=1}^2 \varepsilon_j \cos(\kappa_j \rho \sin \theta + \kappa_{jz} Z - \nu_i \tau + \varphi_i), \quad (2.30)$$

where κ_{jz} denotes the normalized wavenumber in the parallel direction and P_z is the normalized velocity in the parallel direction. It is evident from this form that the investigation of stochasticity is complicated by the necessity of examining a large range of cyclotron resonances at $m + \kappa_{jz}P_z - \nu_j = 0$ where m is an integer. We can avoid this difficulty, however, by exploiting the fact that in many physically realizable experiments, the parallel wavenumber of the electrostatic modes coupled into the plasma is dictated by the geometry of the antenna that launches the waves. This allows us to make the approximation that regardless of frequency, the parallel wavenumber is constant, i.e. $\kappa_z = \kappa_{1z} = \kappa_{2z}$.

In this special case of equal parallel wavenumbers, Strozzi et al.[22] demonstrated from a second-order perturbation analysis that to second order P_z is a constant of motion. As a consequence, we can infer that $Z = P_z \tau$ where initial conditions are incorporated into the phases φ_i . These two observations allow us to convert Eq. 2.2

into the more general form of Eq. 2.30 through the following substitutions:

$$H \rightarrow H - \frac{1}{2}P_z^2 \qquad \nu_j \rightarrow \nu_j - \kappa_z P_z. \qquad (2.31)$$

We can apply this same transformation to Eq. 2.20 to yield the limit for the onset of stochasticity in the case where the parallel wavenumbers in the parallel direction are equal:

$$\alpha < \nu_1 \left(\varepsilon_1 \tilde{A}_1(\rho) + \varepsilon_2 \tilde{A}_2(\rho) \right), \qquad (2.32)$$

where we have defined $\tilde{A}_i = A_i(\nu_i \rightarrow \nu_i - \kappa_z P_z)$. This criterion reduces to the previously derived result [12] in the SEW limit ($\varepsilon_2 \rightarrow 0$).

2.7 Chapter discussion and summary

Through a combination of perturbation theory and numerical analysis, we have arrived at an expression for the onset and bounds in phase space of stochasticity for the case of two beating electrostatic waves. We have verified our expression numerically—even in the case of on-resonance $\nu_1 = \|\nu_1\|$ which was not explicitly accounted for in our analytical derivations—and our result has been shown to converge in the single wave case onto the SEW threshold previously derived by Karney and Fukuyama.

The above results offer a number of new insights into the BEW process. For example, while it has been pointed out in previous work [21] that BEW can lead to ion acceleration without stochasticity, only particles subject to the appropriate initial conditions will experience significant acceleration along the separatrices of the BEW web structure. The rest remain trapped in coherent orbits around the first degree BEW islands. It is only when a region of the web becomes stochastic that the coherently accelerated ions can reach even higher energies by a random walk through chaotic phase space. Our new understanding of when and how this stochastic onset

occurs therefore allows for improved estimates of single particle energization through BEW.

The onset of stochasticity has additional bearing on the heating of a plasma with BEW. Indeed, the decorrelation in particles orbits allows us to model the interaction of the waves with the plasma as a random phase process. This critical assumption, which we invoke in the next chapter, provides a link from our discussion of the acceleration of a single particle to the interaction of the waves with an ensemble of ions.

Finally, since the linear dependence of this threshold on wave amplitude suggests that BEW stochasticity occurs for lower energy densities than with SEW or two non-beating waves, we anticipate that the onset of heating should occur for lower energy densities with BEW when compared to SEW heating. In other words, in the regime of low energy densities, BEWH should be the superior process. This is a result we investigate experimentally in Chapter 5.

Chapter 3

Ensemble heating

In the previous chapter, we examined the BEW problem from the single particle perspective in an effort to derive the criterion for when particle orbits first become stochastic. We then conjectured that the appearance of stochasticity, by virtue of its randomizing effect, should lead to the onset of heating in an ensemble of ions. Once this onset has occurred, however, the single particle treatment is no longer appropriate for describing the degree of heating for a collection of ions. Extending our analysis from the *acceleration of a single ion* to the *heating of an ensemble of ions* is therefore both fundamental and of practical importance to understanding plasma heating. In this chapter we carry out this extension numerically and analytically in an effort to answer the following questions: Once heating has onset for both processes, does BEWH outperform SEWH for equal wave energy densities? Is it always the superior process? And if yes, given experimental constraints, can we predict the performance of BEWH?

We attempt to address these questions in the following analysis by developing an accurate model for both types of heating. This is a particularly challenging task for BEWH since individual particles in the ensemble exhibit two significantly different types of motion: stochastic orbits near the resonant condition and integrable trajec-

tories that coherently accelerate particles up to the resonant velocity. Any model we develop to compare BEWH to SEWH must approximate the average of both behaviors. In the following discussion, we present two approaches to achieve this end. First, we make a direct connection to the single particle description by deriving a second-order expression for the increase in kinetic energy of an ion ensemble subject to perpendicularly-propagating BEW. We invoke the stochastic condition in this case to justify a time average while the beating wave effect is introduced through an analysis of the Poincaré cross-section. For our second approach, we derive a self-consistent expression for the power absorbed by an ion ensemble subject to obliquely-propagating BEW. The onset of stochasticity is used in this case as a justification for a random phase approximation while the beat effect appears explicitly as a fourth-order term.

In this chapter, we adopt a different normalization scheme than the one employed in the single particle discussion from Chapter 2. In the previous treatment, the most logical treatment was to normalize to the characteristic length scale of the waves, k_{1x} . However, since we now investigate the impact of ensemble heating, we choose instead to normalize lengths and velocities to the characteristic length and velocity of an initially thermalized, ion ensemble, i.e. $\bar{r}_L = v_{ti}/\Omega_i$ the thermal Larmor radius in the initial ensemble, and $v_{ti} = \sqrt{T_i/m_i}$ the initial thermal velocity where T_i is expressed in units of energy.

3.1 Average kinetic energy

In this section, we begin with the simple case of pure perpendicular propagation of the waves ($k_z = 0$) where we further assume that the modes are collinear. These restrictions significantly simplify our analysis by reducing the problem to two dimensions. We proceed by constructing a model for the average increase in the perpendicular kinetic ion energy for an ensemble by following Gibelli et. al. [50] in assuming the

ions are collisionless and the waves are uninfluenced by the ion dynamics. The first assumption restricts our analysis to plasmas where heating timescales are faster than collisions. The second assumption limits our scope to small perturbations as it precludes self-consistent effects that would inherently limit the maximum amplitude of the waves [51]. In spite of these restrictions, assuming the waves are uninfluenced by the particle dynamics still allows an approximation for the average result of the stochastic energization of an ensemble [50]. Moreover, this assumption enables us to examine BEWH and SEWH in the most general sense: while a self-consistent simulation requires we specify plasma characteristics such as the dielectric response, assuming the waves are uninfluenced by ion dynamics results in a Hamiltonian formulation where the wave parameters are independent variables. We thus can generally compare SEWH and BEWH over all wave parameter space without having to specify a plasma mode.

With this in mind, we formulate the problem in terms of the normalized Vlasov equation with electrostatic waves propagating perpendicularly to a uniform magnetic field:

$$0 = \frac{\partial f}{\partial \tau} + V_X \left[\frac{\partial f}{\partial X} - \frac{\partial f}{\partial V_Y} \right] + \frac{\partial f}{\partial V_X} \left[V_Y + \sum_{j=1,2} \bar{\xi}_j \cos(\bar{\kappa}_j X - \nu_j \tau) \right], \quad (3.1)$$

where $X = x/\bar{r}_L$, $V_{X,Y} = v_{x,y}/v_{ti}$, $\nu_j = \omega_j/\Omega_i$, $\tau = \Omega_i t$, $\bar{\xi}_j = (qE_j)/(m_i \bar{r}_L \Omega_i^2)$, $\bar{\kappa}_j = k_{jx} \bar{r}_L$, and $\tau = \Omega_i t$. Here E_j is the electric field amplitude of the j^{th} wave, and we have neglected the phase of the wave α_j for simplicity. In the summation above, we define $\nu_1 = \nu$ for SEWH and $\nu_1 = \nu$, $\nu_2 = \nu + 1$ for BEWH as this was found [17] to yield the greatest single ion acceleration. In order to approximate equal energy densities for each case, we define $\bar{\xi}_1 = \bar{\xi}_0$, and $\bar{\xi}_2 = 0$ for SEWH and $\bar{\xi}_1 = \bar{\xi}_2 = \bar{\xi}_0/\sqrt{2}$ for BEWH. This is valid under the assumption that the waves are dispersionless. Finally, we note that for two waves, $\bar{\kappa}_1 \neq \bar{\kappa}_2$ has been shown to have

an impact on the level of single ion energization [17, 21]. However, it is also evident from previous studies that if $|\bar{\kappa}_2 - \bar{\kappa}_1|/\bar{\kappa}_1 \ll 1$ – a restriction valid for large group velocities – the resulting acceleration is on par with $\bar{\kappa}_1 = \bar{\kappa}_2$. In order to simplify our analysis then and invoke the results of previous BEW single ion work [52, 23], we define $\bar{\kappa}_1 = \bar{\kappa}_2 = \bar{\kappa}$.

3.1.1 Numerical investigation

With the constraints of the previous section in mind, we first solve Eq. 3.1 using a Monte Carlo particle method [53, 54, 50] where we select particles from the initial distribution function and integrate the equations of motion along the characteristics of Eq. 3.1. We then construct the spatially averaged function $f(V_X, V_Y, \tau)$ at time τ from the discrete velocity distribution of the particles. The initial velocity distribution we adopt for this technique is a two-dimensional Maxwellian:

$$f(V_X^0, V_Y^0, X_0, Y_0, 0) = \frac{1}{2\pi} e^{-\frac{1}{2}[(V_X^0)^2 + (V_Y^0)^2]}. \quad (3.2)$$

The characteristics are the solutions to the Hamiltonian

$$h = \frac{1}{2} [P_X^2 + (P_Y - X)^2] + \sum \frac{\bar{\xi}_j}{\bar{\kappa}} \cos(\bar{\kappa}X - \nu_j\tau), \quad (3.3)$$

where $V_X = P_X$, $V_Y = P_Y - X$, and P_Y is a constant of motion. For our numerical integration, 1000 particles were uniformly spaced in the interval $-\pi/\bar{\kappa} < X < \pi/\bar{\kappa}$ with initial velocities randomly selected from the Maxwellian distribution with the Box-Muller method [55]. The equations of motion were solved using a symplectic solver algorithm [56].

Since the collisionless ion ensemble evolves without thermal equilibration, we followed the convention of Sheng et al. [45] in using the average kinetic energy $K(\tau)$ in the direction perpendicular to the magnetic field instead of temperature to gauge

the energization of the ensemble:

$$K(\tau) = \frac{1}{2} \int \langle (V_X^2 + V_Y^2) f(V_X, V_Y, X, Y, \tau) \rangle_{X,Y} dV_X dV_Y. \quad (3.4)$$

where $\langle .. \rangle_{X,Y}$ denotes the spatial average with respect to X and Y . With our numerical solution for $f(\tau)$, we calculated $K(\tau)$ for a wide range of the wave parameters, $\bar{\xi}_0$, $\bar{\kappa}$ and ν . In each case, this quantity equilibrated to a steady state value, K_{eq} , although as predicted from single ion energization considerations [22], the heating timescale decreased with $\bar{\xi}_0$. We show in the top of Fig. 3.1 plots of the magnitude of K_{eq} for $\bar{\xi}_0 = 5$.

These results serve to illustrate for this special case that BEWH does produce equal or greater heating than SEWH over a wide range of wave parameters. In order to identify exactly why this is the case and ultimately to see if we can establish BEWH superiority beyond the numerically investigated range, we now use these numerical plots as both a guideline and validation in deriving an analytical expression for heating.

3.1.2 Analytical formulation

Given the periodicity of the exciting waves in the X direction, $f(V_X, V_Y, -\pi/\bar{\kappa}, Y, \tau) = f(V_X, V_Y, \pi/\bar{\kappa}, Y, \tau)$, and the absence of Y in the equations of motion, we can re-write Eq. 3.4 as

$$K(\tau) = \frac{\bar{\kappa}}{2\pi} \int (V_X^2 + V_Y^2) f(V_X, V_Y, X, \tau) dX dV_X dV_Y. \quad (3.5)$$

We then can examine this expression in greater detail by performing a change of coordinates to an action-angle formulation by means of a generating function of the first kind similar to the ones employed by Karney [12] and Chia [20] : $F_1(X, Y, \theta_1, \theta_2) =$

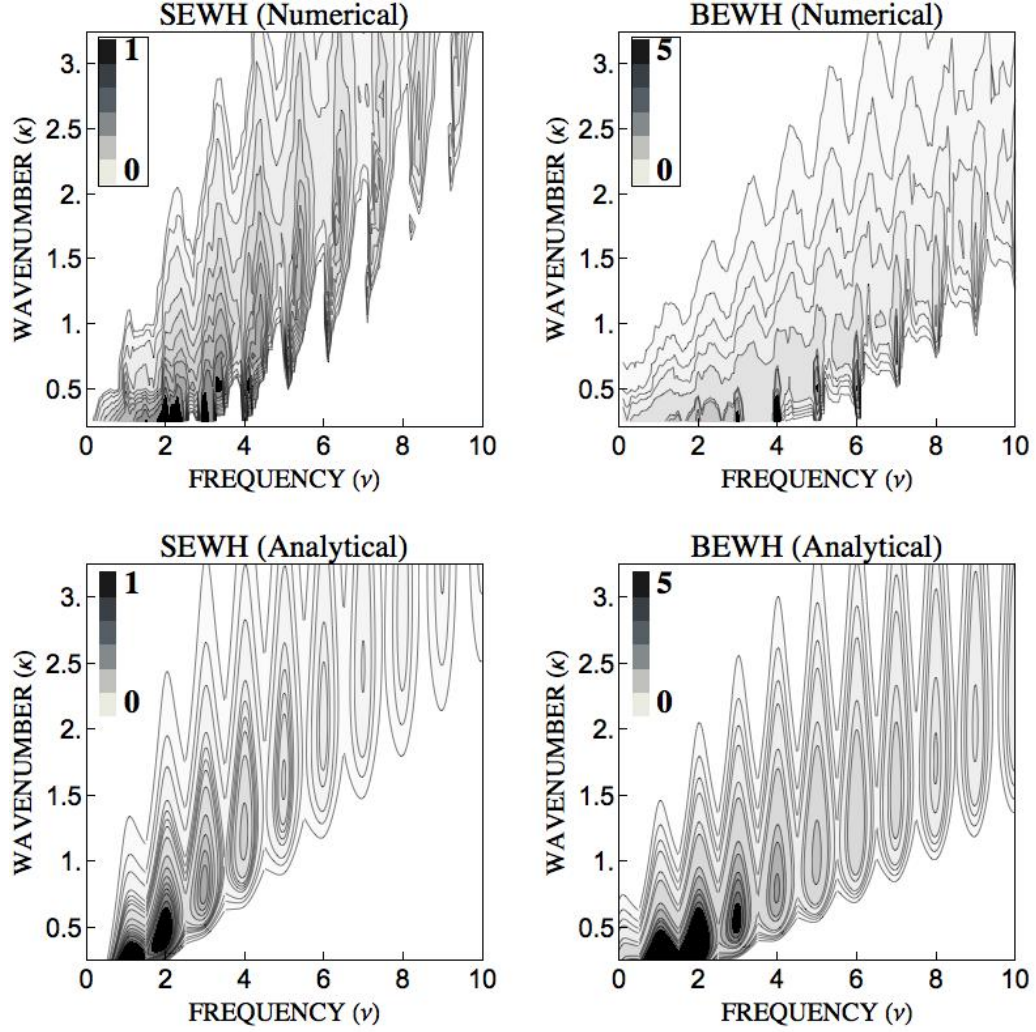


Figure 3.1: Numerical and analytical contour plots of equilibrated kinetic energy, K_{eq} for both SEWH and BEWH as a function of wave parameters $\bar{\kappa}$ and ν : $\bar{\xi}_0 = 5$ in all cases and $\delta_c = 0.25$ for analytical results. Each set of plots is normalized to the maximum SEWH value in the shown domain.

$1/2 (X - \theta_2)^2 \cot \theta_1 + Y \theta_2$. This yields the transformed Hamiltonian (Appendix A):

$$H = I_1 + \sum_{j=1,2} \frac{\bar{\xi}_j}{\bar{\kappa}} \cos(\bar{\kappa} \sqrt{2I_1} \sin \theta_1 + \bar{\kappa} \theta_2 - \nu_j \tau), \quad (3.6)$$

where the coordinate and momenta transformations are given by $X = \sqrt{2I_1} \sin \theta_1 + \theta_2$, $Y = \sqrt{2I_1} \sin \theta_1 - I_2$, $V_X = \dot{X} = \sqrt{2I_1} \cos \theta_1$, and $V_Y = \dot{Y} = -\sqrt{2I_1} \sin \theta_1$. In this case, $I_1 = (V_X^2 + V_Y^2)/2$ is the normalized kinetic energy of an ion, θ_1 is the angle of Larmor precession, θ_2 is the position of the guiding center in the X direction, and $-I_2$ is the position of the guiding center in the Y direction. Since I_1 represents the particle kinetic energy, we can perform a change of coordinates from the cartesian formulation in Eq. 3.5 to the action-angle coordinates to find a simplified form for $K(\tau)$ given by

$$K(\tau) = \frac{\bar{\kappa}}{2\pi} \int I_1 \bar{f}(I_1, \theta_1, \theta_2, \tau) dI_1 d\theta_1 d\theta_2, \quad (3.7)$$

where we have denoted the density distribution expressed as a function of action-angle coordinates as \bar{f} . Since the ion dynamics are Hamiltonian, we can invoke Liouville's theorem to yield the result consistent with the above Vlasov formulation that \bar{f} is constant along the characteristics: $\bar{f}(I_1, \theta_1, \theta_2, \tau) = \bar{f}(I_1^0, \theta_1^0, \theta_2^0, 0)$ where $\bar{f}(I_1^0, \theta_1^0, \theta_2^0, 0) = (2\pi)^{-1} e^{-I_1^0}$. Coupled with the conservation of phase space, this allows us to express Eq. 3.7 as

$$K(\tau) = \int \langle I_1(I_1^0, \theta_1^0, \theta_2^0, \tau) \rangle_{\theta^0} e^{-I_1^0} dI_1^0, \quad (3.8)$$

where $\langle \dots \rangle_{\theta^0}$ denotes the average over the angles $0 < \theta_1^0 < 2\pi$ and $-\pi/\bar{\kappa} < \theta_2^0 < \pi/\bar{\kappa}$. The leading factor $\bar{\kappa}/2\pi$ has been folded into the definition of the average over angles.

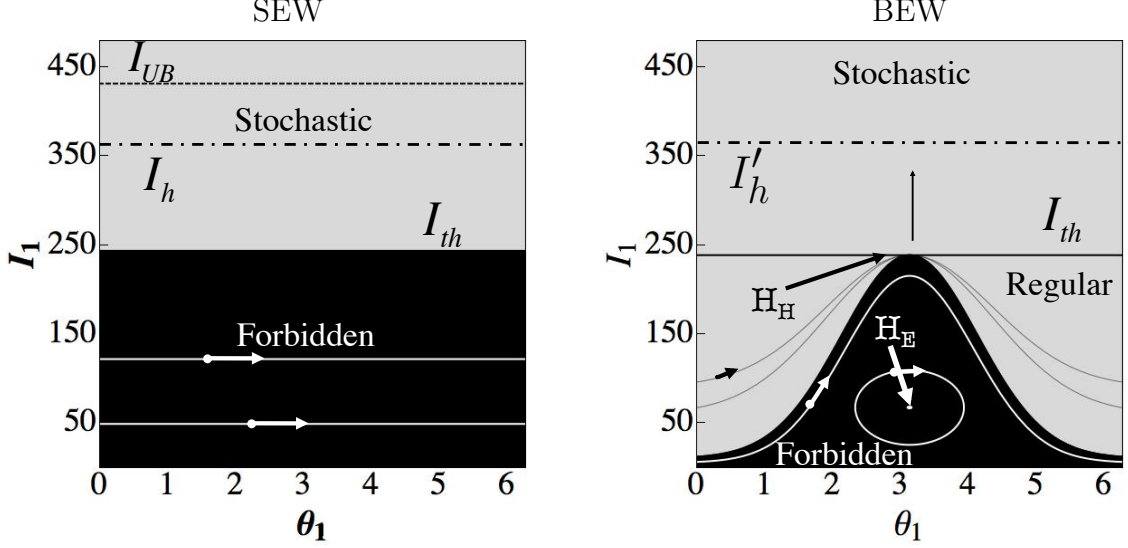


Figure 3.2: Figure adapted from Ref. [23]. Poincaré section for the off-resonance case of an ion subject to SEW (left) and BEW (right). The section is a projection into the coordinate plane of ion orbits at fixed time interval τ_c corresponding to the lowest common period of ν and $\nu + 1$. Typical trajectories for varying initial conditions are shown.

3.1.3 Heating model from the Poincaré cross-section

With the recasting of Eq. 3.5 in the coordinates of Eq. 3.8, an evaluation of the equilibrated kinetic energy requires a careful consideration of $(I_1^0, \theta_1^0, \theta_2^0, \tau)_{\theta^0}$. Before we proceed with an analytical estimate for this term, however, we first use Poincaré cross-sections (PCs) for single particle acceleration to motivate the forms we anticipate K_{eq} to take for BEWH and SEWH. To this end, we show in Fig. 3.2 PCs (adapted from Spektor and Choueiri [23]) that are generalizations to energy space of the plots we generated in Fig. 2.1. These PC are defined for fixed $\bar{\kappa}$ and $\tau = N\tau_c$ where $N = 0, 1, 2, \dots$ and τ_c is the least common period of the exciting waves. They depict the trajectories of individual ions in action-angle coordinates for different initial conditions and serve to illustrate the acceleration regions characteristic of each process. The upper and lower bounds of the stochastic regions are denoted as I_{UB} and I_{th} in these plots and are related to the solutions of Eq. 2.20, ρ'_{th}, ρ'_{UB} , by the transformation $I = [\rho' / (\bar{\tau}_L k_{1x})]^2 / 2$.

We summarize briefly the behavior depicted by these dynamical plots. On one hand, SEW acceleration is a resonance-broadened process where only ions with initial velocity close to the wave phase velocity, $v_{\perp} = \omega/k_x$, are stochastically accelerated. The range of initial actions that satisfy this condition is bounded in phase space by the stochastic threshold [35], I_{th} , and the upper bound, I_{UB} . Ions with initial action outside this resonance zone, i.e. in the forbidden region, are not accelerated. The particle orbits in the marked BEW forbidden and stochastic acceleration regions exhibit approximately the same behavior as their counterparts in the SEW case; however, the fundamental difference for the BEW mechanism—wherein lies its potential for superiority over the SEW process—is that it accelerates a number of ions *outside* the resonance zone to the stochastic regime. This effect occurs in the regular acceleration region, defined by the elliptic point $H_E = (I_1, \theta_1) = ([\nu/\bar{\kappa} - \sqrt{\bar{\xi}_0/\bar{\kappa}}]^2/8, \pi)$, and the hyperbolic point, $H_H = ([\nu/\bar{\kappa} - \sqrt{\bar{\xi}_0/\bar{\kappa}}]^2/2, \pi)$, that intersects the separatrix between regular and forbidden regions [23].

Since θ_1^0 and θ_2^0 are isotropic and the Hamiltonian is independent of I_2^0 , we see from Fig. 3.2 that particles in the SEW forbidden region will have $\langle I_{1(eq)}(I_1^0) \rangle_{\theta^0} = I_1^0$, i.e. the average value of the equilibrated action is constant. On the other hand, particles in the stochastic region, averaged over initial angles, equilibrate to some value $I_{th} < I_h(\bar{\xi}_0, \nu, \bar{\kappa}) < I_{UB}$. Assuming $I_{UB} \gg 1$, we see that all ions in an initial Maxwellian with $I_1^0 > I_{th}$ will be in the stochastic region while the remainder will be in the forbidden region. Therefore, Eq. 3.5 yields for the SEW equilibrated kinetic energy:

$$K_{eq(S)} = 1 + \langle I_{eff} \rangle e^{-[\nu/\bar{\kappa} - \sqrt{\bar{\xi}_0/\bar{\kappa}}]^2/2}, \quad (3.9)$$

where $\langle I_{eff}(\bar{\xi}_0, \nu, \bar{\kappa}) \rangle = I_h - I_{th} - 1$ and $\langle I_1^0 \rangle = 1$ corresponds to the initial average action of the ensemble. We note here that for simplicity we have approximated the solution for the lower bound solution to Eq. 2.20 with an expression that is consistent

with previous analytical work on the BEW problem [23]: $I_{th} \approx \left(\nu/\bar{\kappa} - \sqrt{\bar{\xi}_0/\bar{\kappa}} \right)^2 / 2$, a result that exhibits the same weak dependence on wave amplitude that appears in Fig. 2.4. With this approximation, we can see explicitly from Eq. 3.9 that $\langle I_{eff} \rangle$ indicates ions in the stochastic region gain more energy with increasing frequency due to the widening of stochastic phase space while in opposition to this, the term $e^{-[\nu/\bar{\kappa} - \sqrt{\bar{\xi}_0/\bar{\kappa}}]^2 / 2}$ shows that more of the initial distribution falls in the forbidden region with increasing frequency ν .

We use a similar approach as in Eq. 3.9 to estimate $K_{eq(B)}$ for BEWH. In order to account for the slow coherent acceleration of particles that results from the beat effect, we define a new effective threshold $I'_{th} = [\nu/\bar{\kappa} - (\bar{\xi}_0/\sqrt{2\bar{\kappa}})^{1/2}]^2 / 8$ at the elliptic point. This corrective term accounts for the ultimate depletion of the regular acceleration region by particles as they transition to the stochastic region. This occurs over a long time scale $\tau > 1000$ but is a valid estimate under our simplified, collisionless assumption where non-interacting particles follow their single particle trajectories indefinitely. For simplicity, we further assume that all of the initially stochastic particles as well as those that enter the stochastic region through the beat effect ultimately equilibrate to the same value I'_h . The modified Eq. 3.9 is thus

$$\langle I \rangle_{eq} = 1 + \langle I'_{eff} \rangle e^{-\left[\nu/\bar{\kappa} - (\bar{\xi}_0/[\sqrt{2\bar{\kappa}}])^{1/2} \right]^2 / 8}, \quad (3.10)$$

where $\langle I'_{eff} \rangle = I'_h - I'_{th} - 1$.

Both Eqs. 3.9 and 3.10 are based on the analysis of a Poincaré cross-section valid only for off-resonance frequencies ($\nu \neq \text{integer}$). However, as we have seen from the previous chapter, on-resonance effects only have a small impact on the boundary of the stochastic region. The significant difference in the on-resonance case is the appearance of an enhanced web structure in the stochastic region that leads to acceleration beyond the maximum, I_{UB} [17, 21]. This suggests that Eqs. 3.9 and 3.10 can be universally

applied provided the on-resonance effects are folded into I_{eff} and I'_{eff} .

Eqs. 3.9 and 3.10 are simple, physically intuitive models for the forms of SEWH and BEWH that we have evaluated from a simple inspection of the Poincaré cross-section. While these models lack detail—particularly the forms of I_{eff} and I'_{eff} —they offer qualitative insight into the heating process. Of particular importance is our estimation of the BEW effect, which as we will see is a necessary approximation when the analysis is truncated to second-order. In the next section, we justify these models and provide more detail into the heating mechanism by explicitly evaluating Eq. 3.8.

3.1.4 Second-order estimate for heating

Since the nonlinearity of Eq. 3.6 precludes a closed form solution for $I_1(I_1^0, \theta_1^0, \theta_2^0, \tau)$, we again invoke the results of Lie transform theory [57]. For small amplitude ($\bar{\xi}_0 < 1$) and our appropriately conditioned Hamiltonian, we see that (Appendix B)

$$\langle I_1(\tau)_2 \rangle_{\theta^0} = \langle I_1^0 \rangle_{\theta^0} + \frac{1}{2} \partial_{I_1^0} \left\langle \left[\partial_{\theta_0^1} w_1 \partial_{\theta_0^1} w_1 \right] \right\rangle_{\theta^0}, \quad (3.11)$$

where $w_1 = -\int_0^\tau d\tau H_1$ is the first-order generating function, H_1 is the first-order term in $\bar{\xi}_i$ from Eq. 3.6, the subscript 2 denotes second-order quantities, and the integral is performed over the orbits in phase space pertaining to the solution of the unperturbed Hamiltonian, $H_0 = I_1$. This expression is valid provided the generating functions up to second order from the Lie transform of Eq. 3.6 are periodic with respect to phase angle and the transformed Hamiltonian is independent of the phase angles. These criteria are satisfied for small $\bar{\xi}_0$ and in the *off-resonance* case, $\nu \neq \text{integer}$, such that

Eq. 3.11 becomes

$$\begin{aligned} \langle I_1(\tau)_2 \rangle_{\theta^0} = I_0 + \sum_{\substack{m=-\infty \\ i,j=1,2}}^{\infty} \frac{\bar{\xi}_i \bar{\xi}_j}{\bar{\kappa}^2} \left[m^2 J_m(\bar{\kappa} \sqrt{2I_1^0})^2 \right] \times \\ \frac{\cos[(\nu_i - \nu_j)(\tau - \tau_0)] - \cos[(m - \nu_i)(\tau - \tau_0)] - \cos[(m - \nu_j)(\tau - \tau_0)] + 1}{4(\nu_i - m)(\nu_j - m)}, \end{aligned} \quad (3.12)$$

where τ_0 denotes the initial time. We derived this result from a second-order integrable approximation of the Hamiltonian dynamics, and as such, it does not explicitly incorporate the stochasticity we observed from our numerical analysis in Chapter 2. Rather, we can interpret this expression in the context of small orbit perturbations in response to the waves. For fixed I_1^0 , the interaction with the waves produces a forced oscillation of the ions around an equilibrium point. We can see this quivering in the non-stochastic regions of Fig. 2.1 where the complex BEW web structure is the result of non-resonant interactions with the beat mode (the first order island) as well as the individual waves (higher order oscillations). Averaging over all of these forced oscillators with respect to initial phase leads to the result shown in Eq. 3.12 where the aggregate effect is to produce coherent variations about the fixed points $I' = 1/[4(\nu_i - m)(\nu_j - m)] \left[m^2 J_m(\bar{\kappa} \sqrt{2I_1^0})^2 \right]$. The dominant terms are the slowly varying contributions close to the frequencies of the SEW $m = \|\nu_i\|$ (where $\|\cdot\|$ denotes the nearest integer function) as well as that of the beat mode at $\nu_2 - \nu_1 = 1$.

Since our result stems from an integrable approximation for the Hamiltonian, it is evident that over a sufficiently long time period, our expression for the average kinetic energy for a fixed initial action will be periodic. There is a net increase in energy in so much as the formation of equilibrium points shifts more particles of the monotonically decreasing background distribution from lower energies to higher values than it shifts higher energy particles to lower values. However, in light of the stochastic nature of the orbits which occur for the full solution of the single particle Hamiltonian, the

oscillatory motion about these fixed points in the stochastic region seems unphysical. In order to approximate the effects of this randomizing motion then, we invoke the results from the previous chapter to suggest that the decorrelation of particle orbits allows for the deconstructive interference of the time dependent terms in Eq. 3.12. Consequently, within the stochastic region, $I_{th} < I_1^0 < I_{UB}$, there is a net, steady-state increase in the average kinetic energy for ions that begin with the same initial velocity:

$$\langle I_1(\tau)_2 \rangle_{\theta^0} = I_0 + \sum_{\substack{m=-\infty \\ i,j=1,2}}^{\infty} \frac{\bar{\xi}_i \bar{\xi}_j}{\bar{\kappa}^2} \frac{[m^2 J_m(\bar{\kappa} \sqrt{2I_1^0})^2]}{2(\nu_i - m)(\nu_j - m)}. \quad (3.13)$$

Under the assumption of sufficiently large wave amplitude, $I_{UB} \gg 1$, Eq. 3.8 thus is given by

$$K(\tau)_2 = 1 + \sum_{\substack{m=-\infty \\ i,j=1,2}}^{\infty} \frac{\bar{\xi}_i \bar{\xi}_j m^2}{2\bar{\kappa}^2(\nu_i - m)(\nu_j - m)} \left[\int_0^\infty \frac{\partial}{\partial I_1^0} \left[J_m(\bar{\kappa} \sqrt{2I_1^0})^2 \right] e^{-I_1^0} dI_1^0 \right] \quad (3.14)$$

$$+ \frac{1}{2} \int_0^{I_{th}} \frac{\partial}{\partial I_1^0} \left[J_m(\bar{\kappa} \sqrt{2I_1^0})^2 \right] e^{-I_1^0} dI_1^0 \\ \times ((1 - \delta_{ij}) \cos[(\nu_i - \nu_j)\tau] - \cos[(m - \nu_i)\tau] - \cos[(m - \nu_j)\tau]), \quad (3.15)$$

where δ_{ij} denotes the Kroenecker delta and we have split the integral in order to incorporate the stochastic effects at $I_1^0 > I_{th}$ while retaining the oscillatory motion at lower energy values.

From this result, we see that the beat frequency $\nu_2 - \nu_1$ is averaged out by stochastic effects above the threshold value. This same second-order beat mode does have a slowly varying effect on the ions in the regular acceleration region where $I_1^0 < I_{th}$, but it is evident that this oscillation in average kinetic energy does not capture what we have observed from our single particle analysis. That is, this time-varying term does not reflect the loss of ions in the regular acceleration zone to the stochastic

zone. This is to be expected from an inspection of the PC shown in the first plot of Fig. 2.1. For low perturbation strengths where stochasticity has not occurred, there is no connection between the regular acceleration region and the higher energy orbits—a consequence of the integrability of our second-order approximation. Without this connection, the contribution of the time-varying term can be ignored.

We can see this explicitly by considering that the dominant contributions to Eq. 3.14 stem from the slowly varying terms at $\nu_2 - \nu_1 = 1$ and $m = \|\nu_i\|$. But since $J_m^2(\bar{\kappa}\sqrt{2I_1^0})/J_m^2(m) \ll 1$ as $I_1^0 \rightarrow 0$, the regular acceleration integral must be small compared to the stochastic contribution such that we can approximate

$$K_{eq} \approx 1 + \frac{1}{2} \sum_{j=1,2} \frac{1}{(\|\nu\| - \nu)^2 + \delta_c^2} \frac{\bar{\xi}_j^2}{\bar{\kappa}^2} \int_0^\infty \frac{\partial}{\partial I_0} \left[\|\nu_i\|^2 J_{\|\nu_i\|}(\bar{\kappa}\sqrt{2I_0})^2 \right] e^{-I_0} dI_0, \quad (3.16)$$

where we have dropped the second-order subscript, simplified the infinite summation over m by retaining only the dominant $m = \|\nu_i\|$ terms and introduced the constant $\delta_c^2 \ll 1$ in order to remove the non-physical singularity at on-resonance ($\nu = \|\nu\|$). With this justified neglect of the time-dependent terms, it is even more readily apparent that while our second-order expression captures the stochastic effects of the BEW and SEW waves, the slow connection between BEW acceleration and SEW stochasticity is absent.

Eq. 3.16 is quite close to our qualitatively motivated model from Sec. 3.1.3, which we can see explicitly by evaluating the expression with Weber's second exponential integral identity (Watson [58], p. 395)

$$K_{eq} = 1 + \frac{e^{-\bar{\kappa}^2}}{2 [(\|\nu\| - \nu)^2 + \delta_c^2]} \sum_{i=1,2} \left(\frac{\bar{\xi}_i \|\nu_i\|}{\bar{\kappa}} \right)^2 I_{\|\nu_i\|}(\bar{\kappa}^2), \quad (3.17)$$

where $I_{\|\nu_i\|}(\bar{\kappa}^2)$ is the modified Bessel function of the first kind. In the $\nu/\bar{\kappa} > 1$ limit,

we can expand out the Bessel function to find

$$K_{eq} = 1 + \frac{1}{2\sqrt{2\pi} [(\|\nu\| - \nu)^2 + \delta_c^2]} \sum_{j=1,2} \left(\frac{\bar{\xi}_j \|\nu_j\|}{\bar{\kappa}^{3/2}} \right)^2 e^{-\frac{1}{2} \left(\frac{\|\nu_j\|}{\bar{\kappa}} \right)^2}. \quad (3.18)$$

From this result, we see that the exponential terms in Eq. 3.9 and Eq. 3.18 are almost identical where $\|\nu_j\|$ has replaced ν_j and in our small $\bar{\xi}_0$ analysis the amplitude dependent term $\sqrt{\bar{\xi}_0/\bar{\kappa}}$ is absent. This result thus implies that to second order $\langle I_{eff} \rangle \approx (\|\nu\| - \nu)^2 + \delta_c^2)^{-1} \left(\frac{(\bar{\xi}_0 \|\nu\|)}{\bar{\kappa}^{3/2}} \right)^2$, which we use in conjunction with Eqs. 3.9 and 3.18 to find an approximation for SEWH:

$$K_{eq(S)} = 1 + \frac{1}{2\sqrt{2\pi} [(\|\nu\| - \nu)^2 + \delta_c^2]} \left(\frac{\bar{\xi}_0 \|\nu\|}{\bar{\kappa}^{3/2}} \right)^2 e^{-\frac{(\nu/\bar{\kappa} - \sqrt{\bar{\xi}_0/\bar{\kappa}})^2}{2}}. \quad (3.19)$$

This expression was derived under the assumption $\bar{\xi}_0 < 1$; however, we have found it to accurately predict the correct trends (though not magnitude of energy increase) over the numerically investigated range $0.5 < \bar{\xi}_0 < 10$. This is illustrated by Fig. 3.1 where we see that a normalized plot of Eq. 3.19 corresponds quite well to the numerically indicated data.

Turning to the case of BEWH, we now can see by comparing Eq. 3.10 and Eq. 3.18, that our second-order expression for $K_{eq(B)}$ is not accurate. The discrepancy in the exponential term in Eq. 3.18 for the BEWH case reflects the fact that our approximation for the Hamiltonian fails to capture the connection between the regular acceleration regime and the stochastic region. This failing leaves us with two choices. On one hand, we can continue this formulation to higher order in $\bar{\xi}$, though such an approach requires an estimation of the higher order generating functions w_2, w_3 whose evaluation become prohibitively complicated. As an alternative, we can assume that our qualitative description for the fraction of ions connected to the regular acceleration region, i.e the exponential term in Eq. 3.10, is correct since it stems from a detailed

analysis of the PC. We then can estimate the energization term with the simplifying assumption (consistent with Ref. [17]) that once the stochastic region has formed, the effectively randomized particle trajectories remain qualitatively the same for both the BEW and SEW processes. This enables us to approximate $\langle I'_{eff} \rangle = \langle I_{eff} \rangle$ such that our expression for BEWH is

$$K_{eq(B)} = 1 + \frac{1}{2\sqrt{2\pi}(\|\nu\| - \nu)^2 + \delta_c^2} \left(\frac{\bar{\xi}_0 \|\nu\|}{\bar{\kappa}^{3/2}} \right)^2 e^{-\frac{(\nu/\bar{\kappa} - \sqrt{\epsilon_0/2\bar{\kappa}})^2}{8}}. \quad (3.20)$$

By comparing Eq. 3.20 with numerical results for the investigated range of $\bar{\xi}_0$ in Fig. 3.1, we see this expression successfully describes BEWH without expanding to fourth order. Eq. 3.20 thus generalizes our numerical results and subsequently permits a direct *analytical* comparison between SEWH and BEWH for arbitrary wave parameters. This comparison reveals that under the condition of our simplifying assumptions, for all positive values of $\bar{\kappa}$, ν , and $\bar{\xi}_0$, BEWH is always greater than or equal to SEWH. Furthermore, the good agreement of our results with numerical work provides strong support for our supposition in the above derivations that the major difference between BEWH and SEWH lies in the fraction of particles subject to acceleration (as indicated by the different exponential terms in Eqs. 3.19 and 3.20). We thus confirm the physically intuitive result that BEWH's superiority stems from its ability to energize more of an ion ensemble concurrently for a given wave energy density.

3.1.5 Conclusions and limitations

In the above formulation we solved the equations of motion for individual particles, used a thermal distribution as an initial condition, and then averaged the energy of all the particles as they followed their non-interacting trajectories. While this procedure required that we approximate the ion dynamics as integrable, we incorporated the

effects of stochasticity by averaging out the time dependent terms. Similarly, we estimated the connection between the coherent acceleration of the BEW and the stochastic region by introducing a correction motivated by the Poincaré cross-section.

Our result compared favorably to a non self-consistent, collisionless numerical simulation, and it has offered insight into the nature of the BEWH process. In spite of these advantages, however, there are a number of limitations on the applicability of this model. From a strictly physical perspective, our analysis does not allow for oblique propagation nor does it permit unequal perpendicular wavenumbers—both of these assumptions are violated for most real plasma waves. Additionally, the model is not self-consistent in that arbitrary waves are imposed upon the system rather than determined from the Poisson equation and the dielectric response of the plasma. This can be an advantage—as we have already noted—since it permits a general exploration of parameter space; however, when we examine a real plasma, it is necessary to re-incorporate an element of self-consistency. We can do this by substituting a known dispersion relation, $D(\nu, \bar{\kappa}) = 0$, into Eq. 3.20. But ultimately, this relation must be assumed—the above formulation does not provide a mechanism for determining $D(\nu, \bar{\kappa})$. This lack of self-consistency also is problematic when we consider that in our model an initial Maxwellian distribution is allowed to evolve to an extremely non-thermalized state since the individual ions are non-interacting and governed only by the single-particle equation of motion. In most real plasmas of interest, saturation effects (such as found with BGK solutions [59] or trapping effects [60]), particle collisions, or other loss processes will prevent this unhindered evolution of the distribution function.

The unchecked evolution of the velocity distribution also calls into question the validity of the ad hoc term we introduced to account for the BEW acceleration. Indeed, the slow acceleration in this region occurs over several cyclotron periods, and it is only by virtue of our assumption that the distribution evolves uninterrupted to

its non-Maxwellian steady state that we can assume the regular acceleration region is depleted at equilibrium. The good agreement with numerical results stems from the fact that the simulated particles also were allowed to evolve independently of each other to an equilibrium state. Thus, while this collisionless and non self-consistent model permits us to estimate the BEW effect without expanding to higher order terms, we must recognize that the assumed evolution of the distribution—particularly the full depletion of the regular acceleration region— probably will not be realized in an actual plasma.

In light of the limited applicability of the average kinetic energy model, it is desirable to find a more physically relevant way to characterize the heating effectiveness of both the BEWH and SEWH processes. To achieve this end, we approach the problem from the other limit in time. Instead of estimating the long-term equilibrated kinetic energy, in the next section we self-consistently investigate the instantaneous power absorbed by a thermalized ion ensemble.

3.2 Power absorption

In order to evaluate the power absorbed by a thermalized ion ensemble subject to BEW, we consider a steady-state system with unchanging, local electric field amplitudes. This is the situation we encounter in most plasmas with externally driven waves where an equilibrium is reached between introduced power from the waves and absorption by the plasma ions. The evolution of the density distribution of collisionless particles in such a system is governed by the Vlasov equation:

$$\frac{\partial f}{\partial t} + \mathbf{v} \cdot \frac{\partial f}{\partial \mathbf{x}} + \mathbf{a} \cdot \frac{\partial f}{\partial \mathbf{v}} = 0, \quad (3.21)$$

where f denotes the density distribution function and \mathbf{a} is the acceleration that contains terms from both electrostatic waves as well as the magnetic field:

$$\mathbf{a} = \frac{q}{m_i} \left[\sum_{i=1}^2 \mathbf{k}_j \Phi_j \sin(\mathbf{k}_j \cdot \mathbf{x} - \omega_j t + \alpha_j) + \Delta \mathbf{k} \Phi_{nl} \sin(\Delta \mathbf{k} \cdot \mathbf{x} - \Delta \omega t + \Delta \alpha) + \mathbf{v} \times \mathbf{B} \right]. \quad (3.22)$$

Here m_i denotes the ion mass, Φ_j is the potential amplitude of the wave, $\mathbf{B} = B_0 \hat{z}$, $\mathbf{k}_j = k_{jx} \hat{x} + k_{jz} \hat{z}$, α_j is a constant phase, and $\Delta \mathbf{k} = \mathbf{k}_2 - \mathbf{k}_1$, $\Delta \omega = \omega_2 - \omega_1$. We implicitly assume in this formulation that the plasma density is homogenous and the waves are collinear in the perpendicular direction (denoted x). We also have included for completeness an unspecified, second-order term Φ_{nl} to account for the dielectric response of the plasma to the driven beat mode of the two waves. Mode-mode coupling terms are not included since we assume the beat wave is not a natural mode of the plasma [19].

In the average kinetic energy formulation in the previous section, we used a single particle Hamiltonian to estimate the phase-averaged kinetic energy as a function of the initial conditions and time. This required an integral over the initial coordinates at $\tau = 0$ and the initial velocity distribution function f_0 . For this analysis, however, we instead focus on the time evolution of the distribution function f . In particular, we are interested in the quantity

$$\frac{\partial W}{\partial \tau} = \frac{1}{2} \frac{\partial}{\partial \tau} \int (v_\perp^2 + v_z^2) \langle f \rangle d^3 \mathbf{v}, \quad (3.23)$$

which represents the spatially-averaged power density absorbed by the ions. In order to evaluate Eq. 3.23, it is necessary to solve for the phase-averaged, time evolution of the density distribution, f . The goal of the following discussion is to arrive at an approximation for this through a fourth-order perturbation analysis of the Vlasov equation, Eq. 3.21.

3.2.1 Oscillation center formulation

While there are a number of methods available to self-consistently solve the Vlasov equation in the presence of wave-wave and nonlinear wave-particle interactions [18, 61], these analyses in large part depend on a lengthy perturbation analysis of Eq. 3.21 and the Poisson equation expanded to fourth order [15]. In contrast, it was pointed out by Johnston [19] that we can arrive at an approximation for the power absorption due to nonlinear effects through a less complicated perturbation analysis of a Hamiltonian formulation of the Vlasov equation. Johnston's formulation relied on a transformation of Eq. 3.21 to an oscillation center coordinate system where the slowly varying terms that represent energy exchange with the waves are isolated and the rapidly varying contributions that carry the energy of the waves are transformed away. The system Johnston employed to achieve this transformation was developed to first order by Dewar [62], which Johnston then expanded to second order. For our perturbation analysis, we choose to follow a similar technique, but we instead adopt the more formulaic Lie transform analysis [63, 64, 65]. This technique, which is outlined in Appendix B, has been used to estimate the second-order ponderomotive force produced by a single wave in a plasma [66], and in our formulation, it provides a systematic way to identify the resonant terms responsible for absorption.

As a first step for applying this perturbation technique, it is necessary to express Eq. 3.21 in a simplified Hamiltonian formulation. To this end, we rewrite this expression in terms of a governing, normalized Hamiltonian (Appendix A)

$$\frac{\partial f}{\partial \tau} + \left\{ f, \tilde{H} \right\} = 0, \quad (3.24)$$

where $\{..\}$ denotes the Poisson bracket and we define

$$\begin{aligned} \tilde{H} = & \frac{1}{2} [P_X^2 + (P_Y - X)^2] + \frac{1}{2} P_Z^2 + \sum_{j=1}^2 \bar{\varepsilon}_j \cos(\bar{\kappa}_j X + \bar{\kappa}_{jz} Z - \nu_j \tau + \alpha_j) \\ & + \bar{\varepsilon}_{nl} \cos(\Delta \bar{\kappa} X + \Delta \bar{\kappa}_{jz} Z - \Delta \nu \tau + \Delta \alpha). \end{aligned} \quad (3.25)$$

Here we have employed the same normalization scheme we introduced in the previous section along with the definition $\bar{\kappa}_{jz} = k_{jz} \bar{r}_L$. We note that in contrast to our analysis for the average kinetic energy where electric field amplitude is employed, this expression is a function of the normalized potential amplitude $\bar{\varepsilon}_j = (q\Phi_j/m_i \bar{r}_L^2 \Omega_i^2)$. The reason for this discrepancy is that in the case of oblique, electrostatic propagation, the electric field with its multiple components can no longer be treated as a scalar. The relationship between $\bar{\xi}_j$ and $\bar{\varepsilon}_j$ is given by $\bar{\xi}_j = \bar{\varepsilon}_j \bar{\kappa}_j$.

We next perform the same action-angle transformation to this Hamiltonian discussed in the previous section such that the Z dependent terms remain unchanged [22]:

$$\begin{aligned} H = & I + \frac{1}{2} P_z^2 + \sum_{i=1}^2 \bar{\varepsilon}_i \cos(\bar{\kappa}_i \rho \sin \theta + \bar{\kappa}_{iz} Z - \nu_i \tau + \bar{\varphi}_i) \\ & + \bar{\varepsilon}_{nl} \cos(\Delta \bar{\kappa} \rho \sin \theta + \Delta \bar{\kappa}_z Z - \Delta \nu \tau + \Delta \bar{\varphi}), \end{aligned} \quad (3.26)$$

where we have let $I = I_1$, $\theta = \theta_1$, and we have defined $\bar{\varphi}_i = \alpha_i + \bar{\kappa}_i \theta_2$, the guiding center correction to the phase. From this formulation, we immediately note that the symmetry in Y has eliminated the dependence of the Hamiltonian on I_2 . As a consequence, we find that θ_2 is a constant of motion—the guiding center in the x direction is unchanged by the particle dynamics—and we similarly can neglect the degree of freedom I_2 in our formulation. The Vlasov equation in action-angle

coordinates is thus given by

$$\frac{\partial f}{\partial \tau} + \{f, H\} = 0, \quad (3.27)$$

where the Poisson bracket is defined only with respect to the coordinates θ and Z and their conjugate momenta. In this simplified formulation, Eq. 3.27 dictates the evolution of the velocity density distribution of the ions as perturbed by two-electrostatic waves in a uniform magnetic field. The normalized expression for power absorbed by the ions subsequently is given by

$$\frac{\partial W}{\partial \tau} = 2\pi \int H_0 \langle \frac{\partial f}{\partial \tau} \rangle_{\theta} dI dP_Z, \quad (3.28)$$

where $H_0 = I + P_Z^2/2$ and $\langle \rangle_{\theta}$ denotes the average over the guiding center θ_2 as well as θ and Z .

In this normalized system, Eq. 3.28 still requires that we evaluate f as a function of time, and we are still hindered by the intractability of the nonlinear Hamiltonian governing the equations of motion. However, in the new form, Eq. 3.26 can be analyzed through the aforementioned Lie transform analysis. In particular, we make a canonical transformation to an oscillation-center coordinate system where F is the density distribution of the oscillation centers and the two quantities are related to fourth order by (Appendix B)

$$f = F - \{w_1, F\} + \frac{1}{2} \{w_1, \{w_1, F\}\} - \frac{1}{2} \{w_2, F\} + \frac{1}{8} \{w_2, \{w_2, F_0\}\}, \quad (3.29)$$

where w_1, w_2 denote generating functions given from the Lie transformation as

$$\begin{aligned} \frac{\partial w_1}{\partial t} + \{w_1, H_0\} &= K_1 - H_1 \\ \frac{\partial w_2}{\partial t} + \{w_2, H_0\} &= 2(K_2 - H_2) - L_1(K_1 + H_1). \end{aligned} \quad (3.30)$$

where $L_1 = \{w_1, \dots\}$. In this expression K_1, K_2 are the first and second order elements of the transformed Hamiltonian, and the H components refer to the unperturbed and higher order elements of the untransformed Hamiltonian:

$$\begin{aligned} H_0 &= I + \frac{1}{2}P_z^2 \\ H_1 &= \frac{1}{2} \sum_{i=1}^2 \sum_n \bar{\epsilon}_j J_n(z_j) \exp [i(n\theta + \bar{\kappa}_{jz}Z - \nu_j\tau + \bar{\varphi}_j)] + \text{c.c.} \\ H_2 &= \frac{\bar{\epsilon}_{nl}}{2} \sum_p J_p(\Delta z) \exp [i(p\theta + \Delta\bar{\kappa}_z Z - \Delta\nu\tau + \Delta\bar{\varphi})] + \text{c.c.}, \end{aligned} \quad (3.31)$$

where $z_j = \bar{\kappa}_j\sqrt{2I}$, $\Delta z = \Delta\bar{\kappa}\sqrt{2I}$, the summation is over all integer n and p , and we have assumed the self-consistent term is second-order in amplitude. Since this is a canonical transformation, the equations of motion for the oscillation center distribution are also governed by the transformed Hamiltonian formulation of the Vlasov equation:

$$\frac{\partial F}{\partial \tau} + \{F, K\} = 0. \quad (3.32)$$

We have not yet specified the form of the transformed Hamiltonian, but we can see from Eq. 3.32 that with the appropriate choice of K , the evolution of the new density distribution can be significantly simplified. In the next section, we calculate K_1 and K_2 and the generating functions w_1 and w_2 for our system.

3.2.2 First and second-order components of the oscillation-center Hamiltonian

The typical procedure [65] for determining K is to identify the components from H that contribute secular terms to the generating functions, w_1 and w_2 , and to relegate these to the transformed Hamiltonian. This prescription physically translates to

isolating the wave components that contribute to irreversible energy exchange with the ions (the so-called oscillation center contributions) while neglecting the quickly-varying perturbations of the actual particle motion that do not introduce preferential acceleration in the system.

Following this procedure, we identify from Eq. 3.30 the first-order contribution to K :

$$K_1 = \frac{1}{2} \sum_{j=1}^2 \sum_n \bar{\varepsilon}_j \mathfrak{D}(\nu_j - n - \bar{\kappa}_{jz} P_Z) J_n(z) g_j(\tau) + \text{c.c.} \quad (3.33)$$

Here we have defined \mathfrak{D} as a narrow filter [19] that picks out the resonant terms at $\nu_j - n - \bar{\kappa}_{jz} P_Z$, which we approximate as

$$\mathfrak{D}(x) = \lim_{k \rightarrow \infty} \square \left(k \left[\frac{1}{2} - x \right] \right), \quad (3.34)$$

where \square denotes the Boxcar function. The time dependent terms in Eq. 3.33 have been folded into

$$g_j(\tau) = \exp \left[i \left(-\nu_j \tau + \bar{\kappa}_{jz} Z + n\theta + \bar{\varphi}_j \right) \right]. \quad (3.35)$$

The first-order generating function on the other hand is given by

$$\begin{aligned} w_1 = & \frac{i}{2} \sum_{j=1}^2 \sum_n \bar{\varepsilon}_j [1 - \mathfrak{D}(\nu_j - n - \bar{\kappa}_{jz} P_Z)] J_n(z_j) \\ & \times \frac{g_j(\tau) [\exp[-i(\tau - \tau_0)(n - \nu_j + \bar{\kappa}_{jz} P_Z)] - 1]}{\nu_j - n - \bar{\kappa}_{jz} P_Z} + \text{c.c.}, \end{aligned} \quad (3.36)$$

where τ_0 denotes an initial time and we have solved for w_1 by employing the method of characteristics in Eq. 3.30. We note that in the limit $\tau_0 \rightarrow -\infty$ and assuming a slight damping element in ν_j in order preserve causality, the result for w_1 reduces to the generating function employed in Refs. [17, 23, 22]. We, however, retain the

initial condition for the time being in order to investigate the decorrelating effect stochasticity has on the orbits. Physically, this corresponds to assuming the trajectories follow zeroth order motion for small increments until being randomized by a stochastic effect.

For the second-order contribution to the transformed Hamiltonian, we only include the beat terms in our evaluation from Eq. 3.30 since we are interested primarily in this driven mode:

$$K_2 = \sum_p \mathfrak{D}(\Delta\nu - p - \Delta\bar{\kappa}P_Z) \left(\bar{\varepsilon}_{nl}^{(p)} + \bar{\varepsilon}_b^{(p)} \right) \exp[i(p\theta - \Delta\nu\tau + \Delta\bar{\kappa}_z P_Z + \Delta\bar{\varphi})], \quad (3.37)$$

where we have grouped the self-consistent shielding of the plasma into $\bar{\varepsilon}_{nl}^{(p)}$ and the beat term due to the second-order interaction of the waves into $\bar{\varepsilon}_b^{(p)}$. From Eq. 3.30, we use this second-order transformed Hamiltonian to calculate the form of the second-order generating function:

$$w_2 = \frac{i}{2} \sum_p [1 - \mathfrak{D}(\Delta\nu - p - \Delta\bar{\kappa}P_Z)] \left(\bar{\varepsilon}_{nl}^{(p)} + \bar{\varepsilon}_b^{(p)} \right) \times \frac{g_\Delta(\tau) [\exp[-i(\tau - \tau_0)(p - \Delta\nu + \Delta\bar{\kappa}_z P_Z)] - 1]}{\Delta\nu - p - \Delta\bar{\kappa}_z P_Z} + \text{c.c.}, \quad (3.38)$$

where we have defined

$$g_\Delta(\tau) = \exp[i(-\Delta\nu\tau + \Delta\bar{\kappa}_z Z + p\theta + \Delta\bar{\varphi})]. \quad (3.39)$$

This expression along with the first-order generating function, w_1 , carries non-resonant contributions that are necessary for transforming from F to the cartesian density distribution f . The transformed Hamiltonian K , on the other hand, only contains components that are resonant with the two SEW and the driven beat wave, i.e. the wave components that contribute to resonant energy exchange with the ions. In light

of Eq. 3.32 and the transformed K , we thus see that the oscillation center density distribution will carry information on the net energy gained by the ions.

3.2.3 First and second-order contributions to the oscillation-center density distribution

In order to evaluate the first and second-order contributions to the oscillation-center density distribution, we begin by expanding $F = F_0 + F_1 + F_2$ where $F_0 = f_0$, the background ion velocity distribution. We then substitute into the modified Vlasov equation from Eq. 3.32 to find to first order

$$\frac{\partial F_1}{\partial \tau} + \frac{\partial F_1}{\partial \theta} + P_Z \frac{\partial F_1}{\partial P_Z} = -\{F_0, K_1\}. \quad (3.40)$$

Integrating via the method of characteristics yields

$$\begin{aligned} F_1 = & \frac{1}{2} \sum_{i=1}^2 \sum_n \bar{\varepsilon}_j \mathfrak{D}_j^n J_n(z_j) \left(\bar{\kappa}_{jz} \frac{\partial F_0}{\partial P_Z} + n \frac{\partial F_0}{\partial I} \right) \\ & \times \frac{g_j(\tau) [\exp[-i(\tau - \tau_0)(n - \nu_j + \bar{\kappa}_{jz} P_Z)] - 1]}{\nu_j - n - \bar{\kappa}_{jz} P_Z} + \text{c.c.}, \end{aligned} \quad (3.41)$$

where we have condensed the filter function into $\mathfrak{D}_j^n = \mathfrak{D}(\nu_j - n - \bar{\kappa}_{jz} P_Z)$. We follow a similar technique for the F_2 contribution,

$$\begin{aligned} F_2 = & \frac{1}{2} \sum_p \left(\bar{\varepsilon}_{nl}^{(p)} + \bar{\varepsilon}_b^{(p)} \right) \mathfrak{D}_\Delta^p \left(\Delta \bar{\kappa}_z \frac{\partial F_0}{\partial P_Z} + p \frac{\partial F_0}{\partial I} \right) \\ & \times \frac{g_\Delta(\tau) [\exp[-i(\tau - \tau_0)(p - \Delta\nu + \Delta \bar{\kappa}_z P_Z)] - 1]}{\Delta\nu - p - P_Z \Delta \bar{\kappa}} + \text{c.c.}, \end{aligned} \quad (3.42)$$

where $\mathfrak{D}_\Delta^p = \mathfrak{D}(p + P_Z \Delta \bar{\kappa} - \Delta\nu)$.

Taken together, F_1 and F_2 represent the kinetic response of the oscillation centers to the perturbing waves. With these simplified forms, we proceed in the next section to evaluate the power absorption by ions in the plasma.

3.2.4 Fourth-order expression for power absorption

From the previous discussion, we see that the first and second order components of the distribution functions as well as the generating functions are periodic with respect to the generalized coordinates—a property we assume to be the case for the higher order corrections as well. This periodicity significantly simplifies our calculation of the change in the phase averaged energy density in Eq. 3.28. In particular, after averaging with respect to these coordinates, we can see from Eq. 3.29 that the expression for $\langle f \rangle_{\theta}$ is given to fourth order by

$$\begin{aligned} \langle f \rangle_{\theta} = & F_0 - \langle \{w_1, F_1\} \rangle_{\theta} + \frac{1}{2} \langle \{w_1, \{w_1, F_0\}\} \rangle_{\theta} \\ & + \frac{1}{2} \langle \{w_2, F_2\} \rangle_{\theta} + \frac{1}{8} \langle \{w_2, \{w_2, F_0\}\} \rangle_{\theta}, \end{aligned} \quad (3.43)$$

where we have specified that $F_0 = F_0(I, P_Z)$ is independent of phase. We immediately see that the product of the filter functions between w_1 and F_1 and between w_2 and F_2 allows us to neglect the contributions $\langle \{w_1, F_1\} \rangle_{\theta} = \langle \{w_2, F_2\} \rangle_{\theta} = 0$. Eq. 3.28 thus becomes

$$\begin{aligned} 2\pi \frac{\partial}{\partial \tau} \int \langle H_0 f \rangle_{\theta} dI = & 2\pi \int dI dP_Z \left(I + \frac{1}{2} P_Z^2 \right) \left[\partial_{\tau} F_0 + \frac{1}{2} \partial_{\tau} \langle \{w_1, \{w_1, F_0\}\} \rangle_{\theta} \right. \\ & \left. + \frac{1}{8} \partial_{\tau} \langle \{w_2, \{w_2, F_0\}\} \rangle_{\theta} \right]. \end{aligned} \quad (3.44)$$

In order to evaluate this expression, we begin with the first term on the right, which contains the traditional quasilinear and nonlinear Landau damping terms for power dissipation. By averaging the modified Vlasov equation Eq. 3.32 to fourth order with respect to the generalized coordinates, we find the time dependence of the background distribution F_0 is

$$\frac{\partial}{\partial \tau} F_0 = -\langle \{F_1, K_1\} \rangle_{\theta} - \langle \{F_2, K_2\} \rangle_{\theta}. \quad (3.45)$$

Exploiting the periodicity with respect to the coordinates, we integrate by parts to

find

$$\langle \{F_1, K_1\} \rangle_{\theta} = - \left\langle \frac{\partial}{\partial I} \left[F_1 \frac{\partial K_1}{\partial \theta} \right] + \frac{\partial}{\partial P_Z} \left[F_1 \frac{\partial K_1}{\partial Z} \right] \right\rangle_{\theta} \quad (3.46)$$

$$\langle \{F_2, K_2\} \rangle_{\theta} = - \left\langle \frac{\partial}{\partial I} \left[F_2 \frac{\partial K_2}{\partial \theta} \right] + \frac{\partial}{\partial P_Z} \left[F_2 \frac{\partial K_2}{\partial Z} \right] \right\rangle_{\theta}.$$

Substituting these results into Eq. 3.44 and integrating by parts over the action yields

$$2\pi \int dI dP_Z H_0 \frac{\partial}{\partial \tau} F_0 = P_{QL} + P_{NL} \quad (3.47)$$

where we have defined

$$P_{QL} = -2\pi \text{Im} \sum_{j=1}^2 \sum_m \bar{\varepsilon}_j^2 \int dI dP_Z \mathfrak{D}_j^n (1 - \cos[(\nu_j - \kappa_{jz} P_z - n)(\tau - \tau_0)]) \times \frac{J_n^2(z_j) \left(\bar{\kappa}_{jz} \frac{\partial F_0}{\partial P_Z} + n \frac{\partial F_0}{\partial I} \right) (n + P_Z \bar{\kappa}_{jz})}{2(n + P_Z \bar{\kappa}_{jz} - \nu_j)} \quad (3.48)$$

$$P_{NL} = -2\pi \text{Im} \sum_p \int dI dP_Z \mathfrak{D}_{\Delta}^p (1 - \cos[(\Delta \nu - \Delta \bar{\kappa}_z P_Z - p)(\tau - \tau_0)]) \times \frac{\left(\bar{\varepsilon}_{nl}^{(p)} + \bar{\varepsilon}_b^{(p)} \right)^2 \left(\Delta \bar{\kappa}_z \frac{\partial F_0}{\partial P_Z} + p \frac{\partial F_0}{\partial I} \right) (p + P_Z \Delta \bar{\kappa}_z)}{2(p + P_Z \Delta \bar{\kappa}_z - \Delta \nu)}. \quad (3.49)$$

We have chosen the nomenclature QL and NL for these expressions since both terms contain the traditional quasilinear (QL) diffusion and nonlinear Landau (NL) damping effects. We show this explicitly in the next section when we take into consideration the decorrelation produced by stochastic onset. The remaining terms in Eq. 3.44 represent polarization corrections that arise from transforming from the oscillation center coordinate system to the particle frame of reference. Indeed, while there is only a small subset of the ion density distribution that is subject to irreversible energy exchange with the electrostatic waves, which is represented by the diffusion of the oscillation centers in F , the remaining particles adiabatically carry the energy

of the waves as they propagate across the plasma [10]. These polarization terms, commonly referred to both as a mass renormalization [19] and fake diffusion [18, 66], represent this non-resonant energy.

We can see this explicitly through a calculation of the first-order polarization contribution. Integrating by parts with respect to the generalized coordinates and then with respect to the action yields

$$2\pi \frac{\partial}{\partial \tau} \int dIdP_Z H_0 \langle \frac{1}{2} \{w_1, \{w_1, F_0\}\} \rangle_{\theta} = \frac{\partial}{\partial \tau} W_w + P_S, \quad (3.50)$$

where we have divided the expression into two terms. The first term on the left is given by

$$W_w = 2\pi \sum_{j=1}^2 \bar{\varepsilon}_j^2 \sum_n \text{Re} \int dIdP_Z J_n^2(z_j) (n + P_Z \bar{\kappa}_{jz}) \frac{\left(\bar{\kappa}_{jz} \frac{\partial F_0}{\partial P_Z} + n \frac{\partial F_0}{\partial I} \right)}{2(n + P_Z \bar{\kappa}_{jz} - \nu_j)^2}, \quad (3.51)$$

where we have eliminated the filter term \mathfrak{D}_j^n in light of the fact that taking the real component of this expression yields the principle value. This term corresponds to the particle contribution to the energy density of propagating electrostatic modes (c.f. Chapter 10 of Stix [10]) and thus is the so-called fake diffusion that represents the wave energy carried by the non-resonant particles. Under the assumption of steady state, the local wave energy density remains constant such that the contribution of this term to the power absorption is 0.

On the other hand, the second term in Eq. 3.50 does not necessarily cancel as it depends explicitly on the initial condition τ_0 :

$$P_S = -\pi \sum_{j=1}^2 \bar{\varepsilon}_j^2 \sum_n \int dIdP_Z (1 - \mathfrak{D}_j^n) J_n^2(z_j) (n + P_Z \bar{\kappa}_{jz}) \left(\bar{\kappa}_{jz} \frac{\partial F_0}{\partial P_Z} + n \frac{\partial F_0}{\partial I} \right) \times \frac{\sin[(n + P_Z \bar{\kappa}_{jz} - \nu_j)(\tau - \tau_0)]}{(n + P_Z \bar{\kappa}_{jz} - \nu_j)}. \quad (3.52)$$

As we will discuss in the next section, in the short decorrelation limit and case of near perpendicular propagation, this term can lead to a power absorption that arises from stochastic effects; however, in the long term limit, it disappears—relegating energy

deposition to the quasilinear effects.

The higher order polarization contributions have analogous contributions to W_w and P_s that are given by

$$2\pi \frac{\partial}{\partial \tau} \int dI dP_Z H_0 \langle \frac{1}{8} \{w_2, \{w_2, F_0\}\} \rangle_{\theta} = \frac{\partial}{\partial \tau} W_{BEW} + P_{SBEW}, \quad (3.53)$$

where we have defined

$$W_{BEW} = \frac{\pi}{4} \sum_{j=1}^2 \sum_p \text{Re} \int dI dP_Z \left(\bar{\varepsilon}_{nl}^{(p)} + \bar{\varepsilon}_b^{(p)} \right)^2 (p + P_Z \Delta \bar{\kappa}_z) \times \frac{\left(\Delta \bar{\kappa}_z \frac{\partial F_0}{\partial P_Z} + p \frac{\partial F_0}{\partial I} \right)}{(p + P_Z \Delta \bar{\kappa}_z - \Delta \nu)^2}. \quad (3.54)$$

This term is an approximation for the energy density of the beat mode where again under the assumption of a steady-state wave, we neglect its contribution to the power absorption. On the other hand, the finite-time contribution to the diffusion produced by the beat mode is given by

$$P_{SBEW} = -\frac{\pi}{4} \sum_{j=1}^2 \sum_p \int dI dP_Z (1 - \mathfrak{D}_{\Delta}^p) \left(\Delta \bar{\kappa}_z \frac{\partial F_0}{\partial P_Z} + p \frac{\partial F_0}{\partial I} \right) (p + P_Z \Delta \bar{\kappa}_z) \times \left(\bar{\varepsilon}_{nl}^{(p)} + \bar{\varepsilon}_b^{(p)} \right)^2 \frac{\sin [(p + P_Z \Delta \bar{\kappa}_z - \Delta \nu) (\tau - \tau_0)]}{(p + P_Z \Delta \bar{\kappa}_z - \Delta \nu)}. \quad (3.55)$$

This term represents the fourth-order contribution to stochastic damping in the limit of short decorrelation times.

Taken together with the other contributions from Eqs. 3.48, 3.49, and 3.52, we thus find the final expression for total power absorbed by the BEW process:

$$P_d = P_{QL} + P_{NL} + P_S + P_{SBEW}. \quad (3.56)$$

In contrast to the investigation of the average kinetic energy we presented in Sec. 3.1 where the BEW effect was introduced in an ad hoc manner, the BEW effect explicitly appears in Eq. 3.56 as fourth-order contributions in P_{SBEW} and P_{NL} . On the other hand, just as we found in our approach in Sec. 3.1, we note that the sinusoidal time dependence of the power absorption terms is a direct result of our use of an integrable approximation to the governing Hamiltonian. In the next section, we introduce the

effect of stochasticity and employ it as a means to eliminate this unphysical time dependence.

3.2.5 Coarse grain analysis

The onset of stochasticity leads to the loss of phase information for particles with respect to the wave and ultimately irreversible behavior. In the previous discussion of the average, equilibrated kinetic energy, we used this fact to justify that on a sufficiently long time scale, phase mixing should result in the deconstructive interference of the time dependent terms. We were able to make this simplification since we were investigating the final state of the distribution after an arbitrarily long time period:

$$K_{eq} = \lim_{\Delta\tau \rightarrow \infty} \langle \Delta TE \rangle, \quad (3.57)$$

where $\langle TE \rangle$ denotes kinetic energy of the ensemble averaged over phase and action.

Applying a similar argument to the power absorption is problematic since this quantity represents the instantaneous change in kinetic energy. And while the effect of the stochasticity is to randomize the particle orbits over a characteristic time τ_{ac} , denoted the autocorrelation time, our integrable expression assumes the ion ensemble begins in an initial state at time τ_0 which then evolves uninterrupted according to the second-order, integrable Hamiltonian. In order to account for the initial condition at τ_0 as well as the missing stochastic effects in our description, we apply the concept of coarse graining to our expression for power absorption. In effect, we discretize the time in our problem into intervals of length $\Delta\tau$ such that we can approximate the power absorption as

$$P_d(\tau) \approx \frac{1}{\Delta\tau} \int_0^{\Delta\tau} d\tau' P_d(\tau'), \quad (3.58)$$

where $\tau' = \tau - \tau_0$. In other words, we approximate the instantaneous power absorption as the change in kinetic energy divided by the characteristic time.

The decorrelation of particle orbits leads to the decay of the time coherent terms in

Eq. 3.56 such that we can introduce an effective damping term $e^{-\tau'/\tau_{ac}}$ (characteristic of a Markovian process though we do not prove that here [67, 68]) in front of the time-dependent terms. We then choose $\Delta\tau > \tau_{ac}$ such that on the coarse-grained time scale, the time dependent terms evaluate to 0. This damping is implicitly assumed in the traditional derivation of the nonlinear power absorption terms [15, 19], and in light of Eq. 3.58, the decay of the time dependent terms similarly allows us to simplify Eq. 3.56 to

$$P_d = \bar{P}_{QL} + \bar{P}_{NL}, \quad (3.59)$$

where we have denoted

$$\bar{P}_{QL} = -2\pi\text{Im} \sum_{j=1}^2 \sum_m \bar{\varepsilon}_j^2 \int dIdP_Z \mathfrak{D}_j^n \frac{J_n^2(z_j) \left(\bar{\kappa}_{jz} \frac{\partial F_0}{\partial P_Z} + n \frac{\partial F_0}{\partial I} \right) (n + P_Z \bar{\kappa}_{jz})}{2(n + P_Z \bar{\kappa}_{jz} - \nu_j)} \quad (3.60)$$

$$\bar{P}_{NL} = -2\pi\text{Im} \sum_p \int dIdP_Z \mathfrak{D}_\Delta^p \frac{\left(\bar{\varepsilon}_{nl}^{(p)} + \bar{\varepsilon}_b^{(p)} \right)^2 \left(\Delta \bar{\kappa}_z \frac{\partial F_0}{\partial P_Z} + p \frac{\partial F_0}{\partial I} \right) (p + P_Z \Delta \bar{\kappa}_z)}{2(p + P_Z \Delta \bar{\kappa}_z - \Delta\nu)}. \quad (3.61)$$

The reason for the nomenclature QL now becomes apparent since in this limit of short decorrelation time, the linear absorption associated with the individual waves \bar{P}_{QL} is the traditional quasilinear term for power absorbed by an electrostatic wave in a magnetic field [10]. Similarly, the \bar{P}_{NL} term is comparable to the nonlinear Landau damping terms previously derived by Porkolab and Chang [15] and Johnston [19].

We note here that the validity of Eq. 3.59 depends on the existence of a mechanism to effectively destroy the phase information of orbits over all areas of phase space where particles in the plasma velocity distribution exist. This effect can stem, for example, from weak collisions in the plasma or the phase mixing that arises when a small band of frequencies is excited around the central wave frequency [69]. For our collisionless model where the two waves are monochromatic, however, we assume the

onset of stochasticity is the decorrelating process. In particular, while we have already investigated in Chapter 2 stochastic onset, we now assume that the wave amplitudes are sufficiently large that the stochastic condition is satisfied for the entire thermalized ensemble we investigate.

With this assumption in mind, we continue to employ the power absorption terms in Eqs. 3.60 and 3.61 and simplify them by invoking the Plemelj formula [70] to perform the velocity integrals in the parallel direction:

$$\text{Im} \left[(n + P_Z \bar{\kappa}_{jz} - \nu_j)^{-1} \right] \rightarrow \pi \delta (n + P_Z \bar{\kappa}_{jz} - \nu_j), \quad (3.62)$$

where δ denotes the Dirac delta function. With this relation, our expressions reduce to

$$\begin{aligned} \bar{P}_{QL} = & -\pi^2 \sum_{j=1}^2 \sum_m \bar{\varepsilon}_j^2 \int dI dP_Z J_n^2(z_j) \left(\bar{\kappa}_{jz} \frac{\partial F_0}{\partial P_Z} + n \frac{\partial F_0}{\partial I} \right) \\ & \times (n + P_Z \bar{\kappa}_{jz}) \delta (n + P_Z \bar{\kappa}_{jz} - \nu_j) \end{aligned} \quad (3.63)$$

$$\begin{aligned} \bar{P}_{NL} = & -\pi^2 \sum_p \int dI dP_Z \left(\bar{\varepsilon}_{nl}^{(p)} + \bar{\varepsilon}_b^{(p)} \right)^2 \left(\Delta \bar{\kappa}_z \frac{\partial F_0}{\partial P_Z} + p \frac{\partial F_0}{\partial I} \right) \\ & \times (p + P_Z \Delta \bar{\kappa}_z) \delta (p + P_Z \Delta \bar{\kappa}_z - \Delta \nu), \end{aligned} \quad (3.64)$$

where we have eliminated the filter function in favor of the Dirac delta. Next, we assume a thermally isotropic Maxwellian distribution with a parallel drift V_d :

$$f(I, P_Z) = (2\pi)^{-3/2} e^{-I} e^{-\frac{1}{2}(P_Z - V_d)^2}. \quad (3.65)$$

Substituting this into Eq. 3.63 yields the simplified result for the quasilinear term

$$\bar{P}_{QL} = \frac{\pi^{1/2}}{2\sqrt{2}} \sum_{j=1}^2 \frac{1}{\bar{\kappa}_{jz}} \sum_m e^{-\frac{1}{2} \left(\frac{\nu_j - m - V_d \bar{\kappa}_{jz}}{\bar{\kappa}_{jz}} \right)^2} \bar{\varepsilon}_j^2 \nu_j (\nu_j - \bar{\kappa}_j V_d) \int dI e^{-I} J_m^2(z_j). \quad (3.66)$$

We then employ Watson's identify for Bessel functions [58] to find the reduced form

$$\bar{P}_{QL} = \frac{\pi^{1/2}}{2\sqrt{2}} \sum_{j=1}^2 \frac{1}{\bar{\kappa}_{jz}} \sum_m e^{-\frac{1}{2} \left(\frac{\nu_j - m - V_d \bar{\kappa}_{jz}}{\bar{\kappa}_{jz}} \right)^2} \bar{\varepsilon}_j^2 \nu_j (\nu_j - \bar{\kappa}_j V_d) e^{-\bar{\kappa}_j^2} I_m(\bar{\kappa}_j^2), \quad (3.67)$$

where I_n denotes the modified Bessel function of the first kind.

As for the nonlinear term, we substitute the Maxwellian distribution into Eq. 3.64 to find

$$\begin{aligned} \overline{P}_{NL} &= \frac{\pi^{1/2}}{2\sqrt{2}} \sum_p \frac{1}{\Delta\bar{\kappa}_z} e^{-\frac{1}{2}\left(\frac{\Delta\nu - p - V_d\Delta\bar{\kappa}_z}{\Delta\bar{\kappa}_z}\right)^2} \Delta\nu (\Delta\nu - \Delta\bar{\kappa}V_d) \\ &\times \int dIdP_Z \left(\bar{\varepsilon}_{nl}^{(p)} + \bar{\varepsilon}_b^{(p)} \right)^2 e^{-I} \delta(p + P_Z\Delta\bar{\kappa}_z - \Delta\nu), \end{aligned} \quad (3.68)$$

where we have retained the δ function in P_{NL} since the nonlinear amplitude is a function of the parallel velocity. In particular, the non-shielded amplitude of the beat wave in Eq. 3.64 is given by (Appendix F.1)

$$\begin{aligned} \bar{\varepsilon}_b^{(p)} &= \frac{\bar{\varepsilon}_1\bar{\varepsilon}_2}{4} \sum_m \left[m \left(J_m(z_1) J'_{p+m}(z_2) \left[\frac{1 - \mathfrak{D}_1^m}{\nu_1 - m - P_Z\bar{\kappa}_{1z}} + \frac{1 - \mathfrak{D}_2^{p+m}}{\nu_2 - (p+m) - P_Z\bar{\kappa}_{2z}} \right] \right. \right. \\ &\quad \left. \left. + J_m(z_2) J'_{m-p}(z_1) \left[\frac{1 - \mathfrak{D}_2^m}{\nu_2 - m - P_Z\bar{\kappa}_{2z}} + \frac{1 - \mathfrak{D}_1^{m-p}}{\nu_1 - (m-p) - P_Z\bar{\kappa}_{1z}} \right] \right) \right. \\ &\quad \left. + \bar{\kappa}_{1z}\bar{\kappa}_{2z} J_m(z_1) J_{m+p}(z_k) \left(\frac{1 - \mathfrak{D}_1^m}{(m + P_Z\bar{\kappa}_{1z} - \nu_1)^2} + \frac{1 - \mathfrak{D}_2^{m+p}}{(m + p + P_Z\bar{\kappa}_{2z} - \nu_2)^2} \right) \right], \end{aligned} \quad (3.69)$$

where the filter functions \mathfrak{D}_j^n serve to illustrate that this prescription is only valid for ion velocities that do not satisfy the resonant conditions for individual waves. This term represents the amplitude of the beat mode driven by the two waves. We similarly denote $\bar{\varepsilon}_{nl}^{(p)} = \bar{\varepsilon}_{nl} J_p(\Delta z)$ with $\bar{\varepsilon}_{nl} = q\Phi_{nl}/(m_i\bar{r}_L^2\Omega_i^2)$ where Φ_{nl} is given by Eq. F.26 in Appendix F. This term is the dielectric response of the plasma to the driven mode, which serves to shield the beat wave but is typically smaller in magnitude than $\bar{\varepsilon}_b^{(p)}$.

3.2.6 Interpretation of terms

For the special case of an isotropically thermal Maxwellian distribution, we are now in a position to assign physical significance to the terms in Eq. 3.59. P_{QL} contains the power absorption from the individual modes that occurs through the classic quasilinear process of ion cyclotron harmonic damping (c.f. [7, 10]). It is the rigorous form for power absorption of an ion ensemble that we motivated through a simple single

particle argument in the introduction. As such, we anticipate that the qualitatively motivated conclusions from the single particle description should generalize to the ensemble case. Indeed, we see the cyclotron resonant condition for the ensemble in the parallel direction is manifest in the leading exponential term in Eq. 3.67 where we require $|\nu_j - m - \bar{\kappa}_{jz}V_d| \ll 1$ in order for significant power absorption to occur. In the case of a small drift velocity, $V_d \rightarrow 0$, this condition indicates that maximal heating occurs where $m \approx \|\nu_j\|$. In turn, the maximum contribution at $m = \|\nu_j\|$ to the power absorption from the terms dependent on the perpendicular wavenumber $\bar{\kappa}_j$ is given by $\bar{\kappa}_j \approx \|\nu_j\|$, which translates to the perpendicular resonant condition $\nu_j/\bar{\kappa}_j \approx 1$. In physical coordinates, this is simply $\omega_j/k_{jx} = v_{ti}$, the phase velocity of the wave in the perpendicular direction is equal to the average, thermal velocity of the ions. We thus recover the macroscopic resonant conditions for power absorption of an ion ensemble that we motivated qualitatively in Chapter 1: on-resonance frequencies with perpendicular phase velocity close to the thermal velocity lead to the greatest heating. When these conditions are not satisfied, the power absorbed can be significantly reduced.

Turning to the nonlinear term, Eq. 3.68, we can see that this contribution has a similar form to the quasilinear result, and indeed, we can interpret the effect of this mode partly in the context of quasilinear theory. Specifically, the beat mode generated at the difference frequency $\Delta\omega$ with wavenumber $\Delta\bar{\kappa}$ has a nonlinear (quadratic in potential) amplitude. Since the quasilinear damping of a mode depends on the square of its amplitude, we thus anticipate that the power absorption from this virtual mode should be the fourth order exhibited in Eq. 3.69. Similarly, in direct analogy to the QL case, the cyclotron resonant condition in the parallel direction for the nonlinear term is evident from the exponential term in Eq. 3.68. This is where one of the advantages of the beating criterion becomes immediately evident since waves that satisfy $\nu_2 - \nu_1 = 1$ automatically produce a beat mode in ion cyclotron

resonance at $p = 1$. The interpretation of the perpendicular resonant condition, on the other hand, is more complicated due to the intricacy of the nonlinear amplitude Eq. 3.69. However, we note that in contrast to the quasilinear result of single wave where we require $\nu_j/\bar{\kappa}_j = 1$ for significant power absorption, $\bar{\varepsilon}_b^1$ (the resonant $p = 1$ contribution) exhibits a number of terms that are significant even when this condition is not satisfied. The NL power absorption term thus reflects the ability of BEW to target low energy ions—both in the parallel and perpendicular directions—and in so doing it more rigorously captures the regular acceleration that we described with a qualitative model in our average energy description from Sec. 3.1.

3.2.7 Limit of perpendicular propagation

Stochastic contribution to power absorption

While our description from Eq. 3.59 seems general, we find that in the limit of perpendicular propagation, $\bar{\kappa}_{1z} = \bar{\kappa}_{2z} = 0$, this term is ill-defined. This was first pointed out by Baldwin [34] for the case of single wave propagation where he noted that in the absence of parallel resonances, the classical derivation for single electrostatic modes indicates that these waves do not deliver any power to the plasma. This can be seen explicitly by considering Eq. 3.60 when $\bar{\kappa}_{jz} \rightarrow 0$:

$$\tilde{P}_{QL} = -2\pi\text{Im} \sum_{j=1}^2 \sum_m \bar{\varepsilon}_j^2 \int dI dP_Z \mathfrak{D}_j^n \frac{n^2 J_n^2(z_j)}{2(n - \nu_j)} \frac{\partial F_0}{\partial I}, \quad (3.70)$$

where \tilde{P}_{QL} denotes the limit of perpendicular propagation. Since there are no poles with respect to P_Z , there are no imaginary components to contribute to power absorption. This is a paradoxical conclusion given the results of our simulations and discussion of the average kinetic energy where we have seen that perpendicular waves can exchange energy with the ions. The key to resolving this apparent contradiction, as first pointed out by Baldwin, is that power absorption can occur provided there is some decorrelation mechanism to destroy the phase coherence of the ions on the time

scale of the ion cyclotron frequency.

We can see this explicitly from our formulation by examining the single wave power absorption terms we derived before coarse graining in the limit of perpendicular propagation:

$$\tilde{P}_{QL} = -2\pi \text{Im} \sum_{j=1}^2 \bar{\varepsilon}_j^2 \sum_n \int dI \tilde{\mathfrak{D}}_j^n (1 - \cos[(\nu_j - n)(\tau - \tau_0)]) \frac{n^2 J_n^2(z_j)}{2(n - \nu_j)} \frac{\partial F_0}{\partial I} \quad (3.71)$$

$$\tilde{P}_S = -\pi \sum_{j=1}^2 \bar{\varepsilon}_j^2 \sum_n \int dI \left(1 - \tilde{\mathfrak{D}}_j^n\right) J_n^2(z_j) n^2 \frac{\sin[(n - \nu_j)(\tau - \tau_0)]}{(n - \nu_j)} \frac{\partial F_0}{\partial I}. \quad (3.72)$$

In this limit, decorrelation of orbits can happen on the time scale $\tau_{ac} = \tau - \tau_0 < 2\pi$ [12]. We therefore anticipate that the stochastic effects will effectively destroy all time dependent terms in this limit with the exception of those where $|(\nu_j - m)\tau_{ac}| < 2\pi$. Expanding the above terms in this limit, we only retain $n = \|\nu_j\|$ to find

$$\tilde{P}_{QL} = -\frac{\pi}{2} \text{Im} \sum_{j=1}^2 \bar{\varepsilon}_j^2 \int_{I_{th}}^{\infty} dI \tilde{\mathfrak{D}}_j^{\|\nu_j\|} \tau_{ac}^2 (\nu_j - \|\nu_j\|) \nu_j^2 J_{\nu_j}^2(z_j) \frac{\partial F_0}{\partial I} \quad (3.73)$$

$$\tilde{P}_S = -\pi \tau_{ac} \left(1 - \frac{(\tau_{ac}\delta)^2}{6}\right) \sum_{j=1}^2 \bar{\varepsilon}_j^2 \nu_j^2 \int_{I_{th}}^{\infty} dI \left(1 - \tilde{\mathfrak{D}}_j^{\|\nu_j\|}\right) J_{\nu_j}^2(z_j) \frac{\partial F_0}{\partial I}, \quad (3.74)$$

where we have defined the integral with respect to action to reflect the regions where stochasticity occurs and again made the approximation $\nu_j \approx \|\nu_j\|$ where appropriate. In this limit, we see that the \tilde{P}_{QL} term does not contribute since in the short time limit there are no poles. However, the stochastic term, which we assumed to average to zero in the quasilinear analysis actually has a finite contribution. Indeed, assuming sufficiently large amplitude such that the stochastic threshold extends to values for $\rho < \nu_j/\kappa_j$ and noting that $J_{\nu_j}^2(z_j) \rightarrow 0$ as $\rho \rightarrow 0$, we extend this integral to the entire domain in I to find

$$\tilde{P}_S = \frac{\tau_{ac}}{2} \left(1 - \frac{(\tau_{ac}\delta)^2}{6}\right) \sum_{j=1}^2 \bar{\varepsilon}_j^2 \nu_j^2 \int_0^{\infty} dI J_{\nu_j}^2(z_j) e^{-I}, \quad (3.75)$$

where again we have assumed a Maxwellian distribution for the ion ensemble. At last, allowing $\tau_{ac} \approx \pi$, i.e. the energetic particle in the stochastic region experiences interactions with the wave twice each orbit (when its velocity is close to the perpendicular phase velocity), we thus find the contribution to damping in the perpendicular limit as

$$\tilde{P}_S = \frac{\pi}{2} \left(1 - \frac{(\pi\delta)^2}{6} \right) \sum_{j=1}^2 \bar{\varepsilon}_j^2 \nu_j^2 \int_0^\infty dI J_{\nu_j}^2(z_j) e^{-I}. \quad (3.76)$$

This is the same form as derived by Karney [12] who found the power absorption term in the perpendicular limit by first deriving a diffusion equation. We, on the other hand, have implicitly recovered diffusion through the assumption of stochasticity in our kinetic formulation. Employing again our apt identity for Bessel functions from Watson [58], we can simplify the result further to yield

$$\tilde{P}_S = \frac{\pi}{2} \left(1 - \frac{(\pi\delta)^2}{6} \right) \sum_{j=1}^2 \bar{\varepsilon}_j^2 \nu_j^2 e^{-\bar{\kappa}_j^2} I_{\nu_j}(\bar{\kappa}_j). \quad (3.77)$$

We thus retain power absorption even in the limit of perpendicular propagation—provided there is a decorrelation mechanism to destroy orbit coherence.

We follow a similar treatment to evaluate the nonlinear term in the limit of perpendicular propagation, though we make special note that the filters exclude on-resonance terms $\nu_j = \|\nu_j\|$ from this formulation. Since we have already satisfied the beat criterion such that $\Delta\nu = 1$, the \tilde{P}_{SBEW} result for the case where we retain finite time effects is given by

$$\tilde{P}_{SBEW} = \frac{\pi}{8} \sum_{j=1}^2 \int dI \left(\bar{\varepsilon}_b^{(1)} + \bar{\varepsilon}_{nl}^{(1)} \right)^2 e^{-I}, \quad (3.78)$$

where we have only retained the dominant $p = 1$ term in P_{SBEW} . We thus find that power absorption does occur for both the beat waves as well in the perpendicular limit of propagation.

Quasilinear and nonlinear contributions to power absorption

In light of the results rigorously derived above, we now see that we can recover the same stochastic terms through a judicious choice of limits for the traditional QL term. In particular, we take the limit $\bar{\kappa}_{zi} \rightarrow 0$ after performing the integral with respect to P_Z in Eq. 3.60 to find

$$\tilde{P}_{QL} = -\pi^2 \sum_{j=1}^2 \sum_n \bar{\varepsilon}_j^2 \int dI n^2 J_n^2(z_j) \frac{\partial F_0}{\partial I} \delta(n - \nu_j). \quad (3.79)$$

Substituting in a Maxwellian distribution yields the result

$$\tilde{P}_{QL} = \frac{\pi}{2} \sum_{j=1}^2 \sum_n \bar{\varepsilon}_j^2 \nu_j^2 e^{-\bar{\kappa}_j^2} I_{\nu_j}(\bar{\kappa}_j^2) \delta(n - \nu_j), \quad (3.80)$$

which is the result we found by explicitly considering the stochastic effects in the perpendicular limit with the exception that in this case, the absorption only occurs exactly at *on-resonance*. From our explicit inclusion of the stochastic effects, we have introduced a broadening in this exact on-resonance condition. A similar treatment reveals that taking the appropriate limits allows us to recover $\tilde{P}_{SBEW} \approx \tilde{P}_{NL}$ within a constant factor.

3.3 Comparing descriptions

From our above analysis for the case of average kinetic energy in Sec. 3.1 as well as our estimate for power absorption in Sec. 3.2, we see that the effect of the BEW modes is to introduce additional energy absorption into a plasma by virtue of a nonlinear coupling. From the average kinetic energy description, we interpreted this effect in terms of individual particle orbits where the frequency coupling between the beat mode and the ion cyclotron frequency can lead to regular, coherent acceleration of low energy particles. From the power absorption description, we examined the beat effect as an induced virtual wave at the beat frequency and beat wavelength. We implicitly averaged over particle orbits by invoking a stochastic criterion and as such

we could not see the precise effect of the BEW waves. Ultimately, we recovered an approximation for the coherent acceleration of individual particles through the resonant interaction of the beat mode with the plasma.

Since both descriptions offer different insight into the energy exchange of BEW with the plasma ions and ultimately lead us to similar conclusions, we anticipate that the two descriptions should predict similar behavior under the same assumptions. With this in mind, we examine Eq. 3.59 subject to the restrictions we adopted for the average kinetic energy description, $\bar{\kappa}_1 = \bar{\kappa}_2 = \bar{\kappa}$, $\bar{\kappa}_{1z} = \bar{\kappa}_{2z} = 0$, and $\bar{\varepsilon}_1 = \bar{\varepsilon}_2 = \bar{\varepsilon}_0$. In this limit of perpendicular propagation, we substitute these assumptions into Eq. 3.77 from the previous section to find

$$\tilde{P}_S = \frac{\pi}{2} \left(1 - \frac{(\pi\delta)^2}{6} \right) \sum_{j=1}^2 \nu_j^2 \bar{\varepsilon}_j^2 e^{-\bar{\kappa}^2} I_{\nu_j}(\bar{\kappa}^2), \quad (3.81)$$

which is equivalent to our expression for Eq. 3.17 within a constant factor—bearing in mind that $\bar{\xi} = \bar{\kappa}\bar{\varepsilon}$. The constant 1 in Eq. 3.17 represents the initial average kinetic energy of the ensemble and does not appear in Eq. 3.81 since this term is the power absorption—the instantaneous change in kinetic energy over time. The effect of enhanced heating at on-resonance $\delta = 0$ also is also equivalent to Eq. 3.17 provided that $\delta_c^2 = 6/\pi^2$.

The beating wave contribution under the assumptions of our average kinetic energy formulation is given by Eq. 3.78 with the dielectric response amplitude $\bar{\varepsilon}_{nl} = 0$ and the amplitude term

$$\begin{aligned} \bar{\varepsilon}_b^{(1)} = \frac{\bar{\varepsilon}_1 \bar{\varepsilon}_2}{4} \sum_m m \left(J_m(z_1) J'_{1+m}(z_1) \left[\frac{1 - \tilde{\mathfrak{D}}_1^m}{\nu_1 - m} + \frac{1 - \tilde{\mathfrak{D}}_2^{1+m}}{\nu_2 - (1+m)} \right] \right. \\ \left. + J_m(z_1) J'_{m-1}(z_1) \left[\frac{1 - \tilde{\mathfrak{D}}_2^m}{\nu_2 - m} + \frac{1 - \tilde{\mathfrak{D}}_1^{m-1}}{\nu_1 - (m-1)} \right] \right). \end{aligned} \quad (3.82)$$

From this expression, we can immediately see that the effect of the nonlinear term is to enhance the power absorption. In this sense then, the average kinetic energy description from Eq. 3.20 and this power absorption formulation capture the same

essential feature. There is a significant difference, however, in that the nonlinear power absorption term is fourth order in amplitude while for the average kinetic energy case, the BEW effect was described to second order. We already alluded to this distinction in our previous discussion of the averaged kinetic energy where we noted that our expression for BEWH required an estimate for how the coherent acceleration and stochastic acceleration regimes interact. Our simplification that permitted a second-order estimate for this energy exchange was justified by the fact that we were approximating a steady-state distribution in a non self-consistent regime where particle orbits were allowed to evolve indefinitely. On the other hand, our more physical derivation for the power absorption indicates the *instantaneous* power absorption that occurs for a Maxwellian distribution of ions. This is a more valid description for most thermal plasmas where collisionality is sufficiently high to maintain a Maxwellian distribution. Of course, finding the true steady state distribution would require that we introduce collisionality as a loss term into our power absorption [12].

3.4 Dispersion relation

We can use the formalism from Sec. 3.2 to determine the self-consistent dispersion that constrains the relationship between the frequency and wavenumber of the individual modes. This was not possible with the average kinetic energy model since this description did not provide information on the kinetic response, f_1 , of the plasma to the waves. With the kinetic formalism, however, we can find such a relationship in physical coordinates (Appendix E):

$$D(\omega, \mathbf{k}) = k^2 \epsilon(\omega, \mathbf{k}) = 0, \quad (3.83)$$

where the dielectric tensor is given by

$$\epsilon(\omega, \mathbf{k}) = 1 + \sum_s \frac{\omega_{ps}^2}{k^2} 2\pi \int v_\perp dv_\perp dv_z \sum_n \frac{J_n^2(z_{(s)})}{\omega - n\Omega_s - k_z v_z} \left(k_z \frac{\partial f_{0(s)}}{\partial v_z} + \frac{n\Omega_s}{v_\perp} \frac{\partial f_{0(s)}}{\partial v_\perp} \right). \quad (3.84)$$

Here $z_{(s)} = v_\perp k_x / \Omega_s$, $f_{0(s)}$ denotes the three-dimensional velocity distribution of the species, and $\omega_{ps}^2 = q_s^2 n_0 / m_s \epsilon_0$ is the species plasma frequency. Allowing for background Maxwellian distributions with parallel drift velocities and isotropic temperature, we can integrate this relation to find [10]:

$$D(\omega, \mathbf{k}) = k_z^2 + k_x^2 + \sum_{s=e,i} k_{ds}^2 \left[1 + \sum_n e^{-a_s} I_n(a_s) Z(\zeta_n) \left(\zeta_n + \frac{n\Omega}{\sqrt{2}k_z v_{t(s)}} \right) \right], \quad (3.85)$$

where we have defined $k_{ds}^2 = n_0 q^2 / \epsilon_0 T_s$; $\zeta_n = (\omega - n\Omega_s - k_z v_{d(s)}) / \sqrt{2}k_z v_{t(s)}$; the thermal velocity, $v_{t(s)}^2 = T_s / m_s$; $a_s = (k_x \rho_s)^2$; the plasma dispersion function, $Z(\zeta_n) = 1/\sqrt{\pi} \int_{-\infty}^{\infty} [e^{-s^2} / (s - \zeta_n)] ds$; $\rho_s = v_{t(s)} / \Omega_s$; $v_{d(s)}$ is the drift velocity of the given species; and I_n is the modified Bessel function of the first kind.

3.5 Condition for superiority of BEWH

Armed with our expression for the power absorption that occurs in BEWH, we now are in a position to compare this process to SEWH. Indeed, while in our simplified calculation for the average kinetic energy in Sec. 3.1, we found that BEWH is superior for roughly equivalent input energy densities, we see that for the more general case of power absorption, the quartic dependence on amplitude of the nonlinear term suggests that there may be a regime where SEWH heating is the preferable process.

To identify this regime, we compare the SEW process with the BEW process under the condition that each has the same total wave energy density, W_T . From the electrostatic dispersion relation, we know that the energy density in a single mode is

given in unnormalized coordinates by [10]:

$$W_j = \epsilon_0 \frac{\omega_i}{4} \Phi_i^2 \frac{\partial}{\partial \omega} D(\mathbf{k}_j, \omega_j). \quad (3.86)$$

We thus see that the energy density for a single wave depends quadratically on the potential amplitude. For the case of two propagating modes then, the total energy density is

$$W_T = \beta_1 \Phi_1^2 + \beta_2 \Phi_2^2, \quad (3.87)$$

where β_j is the coupling coefficient that depends on the dispersion relation of the propagating mode. In order to simplify our analysis further, we define the fraction of the total energy in the first wave as

$$\eta = \frac{\beta_1 \Phi_1^2}{W_T}, \quad (3.88)$$

such that we have

$$\begin{aligned} \Phi_1^2 &= \frac{\eta}{\beta_1} W_T \\ \Phi_2^2 &= \frac{W_T}{\beta_2} (1 - \eta). \end{aligned} \quad (3.89)$$

Given these definitions, we can re-write our expression for power absorption as

$$P_d = \alpha_1 \Phi_1^2 + \alpha_2 \Phi_2^2 + \Phi_1^2 \Phi_2^2 \gamma_{12}, \quad (3.90)$$

where α_j corresponds to the single wave absorption process, and γ_{12} is the coefficient for the nonlinear term that arises from the beat mode at the difference frequency $\Delta\omega = \omega_2 - \omega_1$. Substituting our expressions for total energy density into Eq. 3.90, we thus find

$$P_d = W_T \left(\frac{\alpha_1}{\beta_1} \eta + \frac{\alpha_2}{\beta_2} (1 - \eta) + W_T \frac{\gamma_{12}}{\beta_1 \beta_2} \eta (1 - \eta) \right). \quad (3.91)$$

This result expresses the power deposition in the plasma due to the BEW effect as a function of fraction of the total energy density in the first mode. It permits us to formulate a simple criterion for the case where BEW is superior to SEW. Specifically, if BEW produces superior heating to SEW (where $\eta = 0$ or 1), then for the same total

energy density, there should be some combination of the two waves where the increase in ion temperature for BEW is greater than the equivalent temperature increase at either SEW frequency. More succinctly, if we define $F(\eta) = [T_i(\eta) - T_{i0}] / T_{i0}$, the fractional increase in ion temperature T_i due to wave heating, then if BEW is the more efficient process for fixed W_T , there exists a range of $\eta \in (0, 1)$ such that $F(\eta) > F(0), F(1)$.

Since P_d is a smoothly varying function, we see that this requirement for the superiority of BEW can be translated into calculating the optimal value of η :

$$\eta = \frac{1}{2} + \frac{\alpha_1 \alpha_2}{2\gamma_{12} W_T} \left(\frac{\beta_2}{\alpha_2} - \frac{\beta_1}{\alpha_1} \right). \quad (3.92)$$

This result is physically intuitive. For increasing total energy density or a larger nonlinear coupling term, we see that the optimal value approaches an equal split between the two density modes. We further can see from this criterion that in order for BEW to be the more efficient process (where $\eta \in (0, 1)$), it is necessary that

$$W_T > \left| \frac{\alpha_1 \alpha_2}{\gamma_{12}} \left(\frac{\beta_2}{\alpha_2} - \frac{\beta_1}{\alpha_1} \right) \right|. \quad (3.93)$$

In other words, there is a threshold value for total wave energy density for the BEW process to be superior to SEW. The interesting consequence of this expression is that while BEW is always the superior process for sufficiently large input energy (provided the perturbative expansion is still valid, i.e. $\bar{\epsilon}_j \leq 1$ at these values), at low wave energies this advantage can disappear. For experiments and applications where the input power to the waves is limited, it may be possible that it is preferable to employ SEW.

This formulation also provides insight into our results for the special case we examined in Sec. 3.1. In particular, we now see that implicit in our assumption for equating the equilibrated average energy terms $\langle I'_{eff} \rangle = \langle I_{eff} \rangle$, we effectively assumed $\alpha_1 = \alpha_2$. Furthermore, we did not include dispersion in our estimate for total wave energy densities, i.e. we assumed $\beta_j = 1$. Substituting these coefficients into our

expression for Eq. 3.93, we see that the criterion for BEW superiority is satisfied for arbitrarily small W_T . Our assertion for the superiority of BEWH to SEWH that we derived from our average kinetic energy description therefore is vindicated from our power absorption model.

As a final note, we determine the forms for the coefficients in Eq. 3.93. From Eq. 3.67 we find in physical coordinates that

$$\alpha_j = n_0 m_i \pi^2 k_{jz}^{-1} \left(\frac{\Omega_i}{B_0} \right)^2 \left(\frac{m_i}{2\pi T_i} \right)^{3/2} \omega_j (\omega_j - k_{jz} v_{di}) e^{-\lambda_j} \times \sum_n I_n(\lambda_j) e^{-m_i(\omega_j - n\Omega_i - k_{jz} v_{di})^2 / 2T_i k_{jz}^2}, \quad (3.94)$$

where we have defined $\lambda_j = (T_i/m_i) (k_{jz}/\Omega_i)^2$. The nonlinear term similarly is derived from Eq. 3.68:

$$\gamma_{12} = n_0 m_i \pi^2 (\Delta k_z)^{-1} \left(\frac{m_i}{2T_i} \right)^{3/2} \left(\frac{\Omega_i}{B_0} \right)^4 \Delta\omega (\Delta\omega - \Delta k_z V) e^{-m_i(\Delta\omega - \Delta k_z v_{di} - p\Omega_i)^2 / 2T_i (\Delta k_z)^2} \times \sum_{p,m} \int_{-\infty}^{\infty} \int_0^{\infty} v_{\perp} dv_{\perp} dv_z A_p^m A_p^n f_{(0)}^{\perp} \delta \left(v_z - \frac{\Delta\omega - p\Omega_i}{\Delta k_z} \right), \quad (3.95)$$

where we have defined $\Delta k_z = k_{z2} - k_{z1}$, $\Delta\omega = \omega_2 - \omega_1$, and

$$f_{(0)}^{\perp} = \left(\frac{m_i}{2\pi T_i} \right)^{3/2} e^{-m_i v_{\perp}^2 / 2T_i}. \quad (3.96)$$

The velocity-dependent terms are given by

$$\begin{aligned} A_p^m = & \frac{1}{4} \left[m \frac{\Omega_i}{v_{\perp}} \left(J_m(z_1) J_{p+m}'(z_2) \left[\frac{1 - \mathfrak{D}_1^m}{\omega_1 - m\Omega_i + v_z k_{1z}} + \frac{1 - \mathfrak{D}_2^{p+m}}{\omega_2 - (p+m)\Omega_i - v_z k_{2z}} \right] \right. \right. \\ & + J_m(z_2) J_{m-p}'(z_1) \left[\frac{1 - \mathfrak{D}_2^m}{\omega_2 - m\Omega_i - v_z k_{2z}} + \frac{1 - \mathfrak{D}_1^{m-p}}{\omega_1 - (m-p)\Omega_i - v_z k_{1z}} \right] \Big) \\ & + k_{1z} k_{2z} J_m(z_{1(s)}) J_{m+p}(z_2) \left(\frac{1 - \mathfrak{D}_1^m}{(m\Omega_i + v_z k_{1z} - \omega_1)^2} + \frac{1 - \mathfrak{D}_2^{m+p}}{((m+p)\Omega_s + v_z k_{2z} - \omega_2)^2} \right) \Big] \\ & - J_p(\Delta z) \frac{m_i}{q\Phi_1\Phi_2} [\epsilon(\Delta\omega, \Delta\mathbf{k})]^{-1} \left[\frac{\omega_{pi}^2}{(\Delta k)^2} \right] 2\pi \int v_{\perp} dv_{\perp} dv_z J_m(\Delta z_{(i)}) \\ & \times \left[\frac{\Phi_{b(i)}^{(m)}}{\Delta\omega - m\Omega_i - v_z \Delta k_z} \left(\Delta k_z \frac{\partial f_{0(i)}}{\partial v_z} + \frac{m\Omega_i}{v_{\perp}} \frac{\partial f_{0(i)}}{\partial v_{\perp}} \right) + D_i^{(m)} \right], \end{aligned} \quad (3.97)$$

where $\Phi_{b(i)}^{(m)}$ and D_i^m are given in Sec. F.2 and the derivatives are with respect to v_\perp . The coefficients β_j stem directly from our definition of the energy density and the unnormalized dispersion relation Eq. 3.85.

3.6 Chapter summary

In this analytical treatment, we set out with the goal of describing the heating of an ensemble of ions that occurs once the particle orbits have become decorrelated. This is a critical step for relating our understanding of the single particle dynamics to the physical heating of a plasma. As a first attempt toward this end, we started with an ensemble description that translated directly to the single particle description from Chapter 2. This model was based on an inspection of the Poincaré cross-section and a second-order estimate for the average increase in kinetic energy of particles. It provided direct insight into how the BEW effect can lead to enhanced heating, though ultimately it suffered from a lack of self-consistency, an overly restrictive assumption of perpendicular propagation, and a need to account for the BEW effect through a qualitatively modeled corrective term.

In order to more directly model the plasma heating then and allow for oblique propagation, we explored a second description based on examining the power absorbed by ions subject to BEW. We found that this approach not only produced traditional ion cyclotron damping due to individual waves but also provided a fourth-order term that accounted for the power deposited by the beat mode. On the other hand, this model did have a failing in that the averaging required to arrive at our expression for power absorption make it difficult to link our understanding of single particle orbits to this model.

The two descriptions ultimately illustrated the same behavior under the same assumptions, but since the power absorption approach allowed both for self-consistency

as well as oblique propagation, we chose this model as the basis for comparison between SEWH and BEWH. The interesting result we found is that there are some cases when the SEWH process may be superior to BEWH, and the condition for this superiority depends directly on the total wave energy density, the wave parameters, and the background temperature of the plasma.

We can combine this result with the conclusions from the last chapter. In particular, let us denote the threshold total energy density for when stochasticity first appears for the single wave case as W_T^* , i.e. the lower value of $W_{1(SEW)}$ and $W_{2(SEW)}$ from Eq. 2.25, and let us denote the total energy density for when stochasticity first appears for the BEW case as W_0 . Similarly, we label \overline{W}_T as the condition when Eq. 3.93 is an equality. The results from our analytical investigation thus suggest separable regions of behavior in terms of the input energy density:

| Total Energy Density | Superior Process |
|--------------------------------|------------------|
| $W_T < W_0$ | — |
| $W_0 < W_T < W_T^*$ | BEWH |
| $W_T^* < W_T < \overline{W}_T$ | SEWH |
| $\overline{W}_T < W_T$ | BEWH |

In the following chapters, we describe an experimental setup and procedure for examining these analytically predicted trends.

Chapter 4

Experimental setup and diagnostics

The goal of the experimental investigation is to explore the SEWH and BEWH processes over a wide range of wave energy densities and to compare the results with our theoretical predictions. We describe in this chapter the Beating Waves Experiment II (BWX II), the setup constructed to achieve this end. In Section 4.1, we provide a detailed schematic of the entire setup with a special emphasis on the vacuum chamber and magnetic field of BWX II. In Section 4.2, we present the plasma source along with typical plasma parameters. In Section 4.3, we describe the antenna geometry we adopted to launch electrostatic modes in the BWX II plasma. In Section 4.4, we include a discussion of the low frequency matching network we employed to couple two beating electrostatic modes to the antenna concurrently. And in Section 4.5, we describe the primary diagnostics in the experimental setup. These include a double Langmuir probe array for electron temperature and density measurements and a laser induced fluorescence system to examine ion temperature and wave properties.

4.1 Vacuum chamber and solenoid

We show a detailed schematic of BWX II in Fig. 4.1 along with a computer generated image and photograph in Fig. 4.2. In this configuration, the vacuum vessel is a Pyrex

cylinder 132 cm in length with a 16.5 cm inner diameter placed concentrically in a 122 cm long, 10 ring solenoid. A small window at the end of the chamber allows longitudinal optical access while argon gas can flow into the chamber through a feed in the cross at the opposite end of the vessel. The RF plasma source and plasma heating regions are located on opposite sides of the vacuum vessel in order minimize stray RF noise in the experimental region.

During experimental runs, a constant pressure of 0.1 mT is maintained in the vessel by a 140 l/s turbo pump backed with a roughing pump. Two klystron Varian 1955A magnets placed end to end provide a magnetic field in the experimental test region. Each magnet is calibrated experimentally as well as numerically modeled to produce a uniform field in this region with a magnitude of 525 G, corresponding to an ion cyclotron frequency of 20 kHz. We show in Fig. 4.3 a plot of the magnitude of this magnetic field along the central axis of the plasma as a function of position.

4.2 Plasma source

The plasma discharge in BWX II is produced by a Boswell-type saddle antenna with a 18.4 cm inner diameter placed around the vacuum chamber at one end of the solenoid. The antenna is powered by a 1.25 kW source operated at 13.56 MHz and matched to the plasma with an L network consisting of two Jennings 1000 pF 3kV variable vacuum capacitors. In order to minimize RF noise from this antenna as well as provide a low energy background for contrast to the heating, we operate this antenna in the inductive mode at 275 W.

Typical electron density and temperature radial profiles that were measured with an array of double probes (Sec. 4.5.1) are shown in Fig. 4.4. From these plots, we see that the electron temperature in BWX II is approximately uniform over the majority of the heating volume with $T_e \approx 3.5$ eV. The small increase in temperature at the

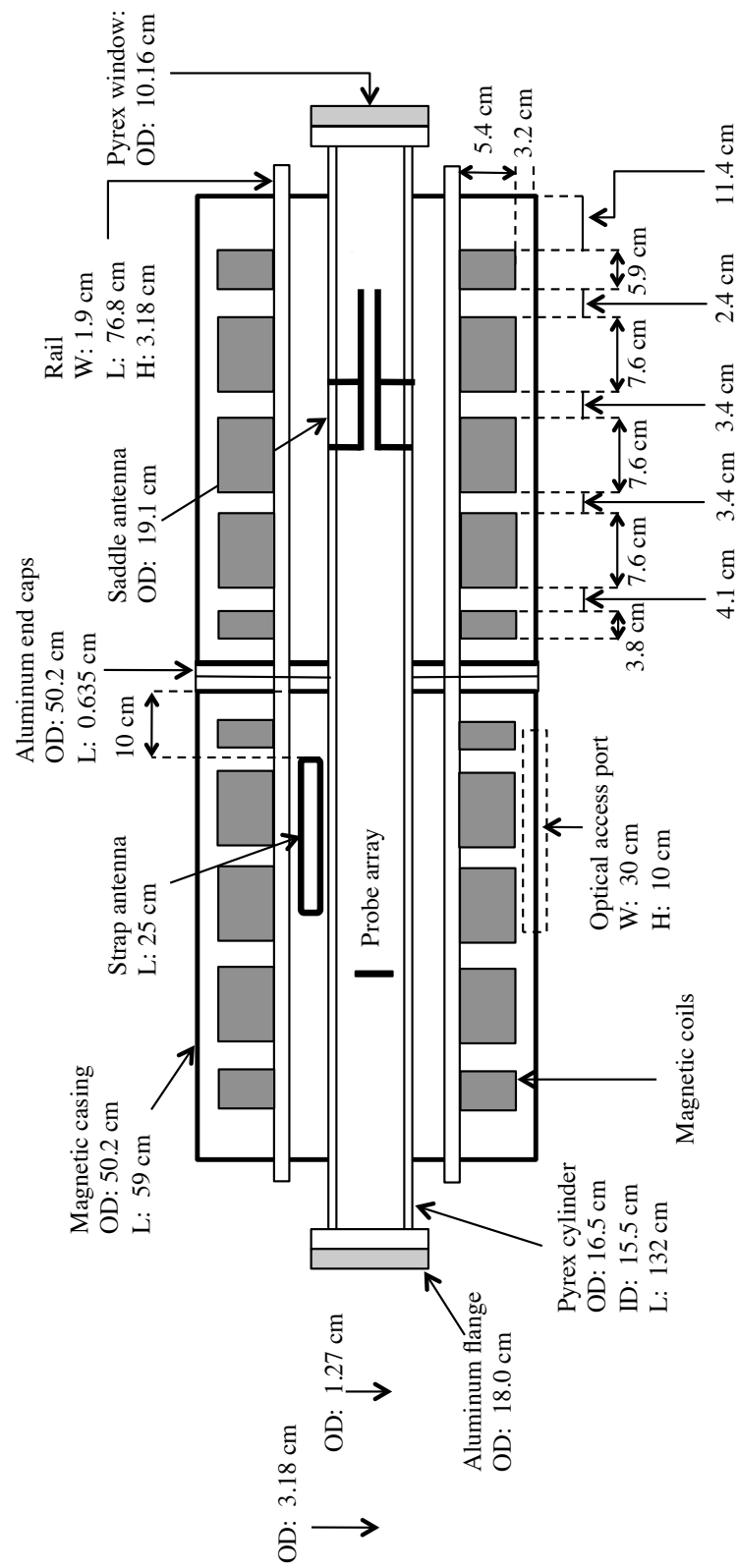
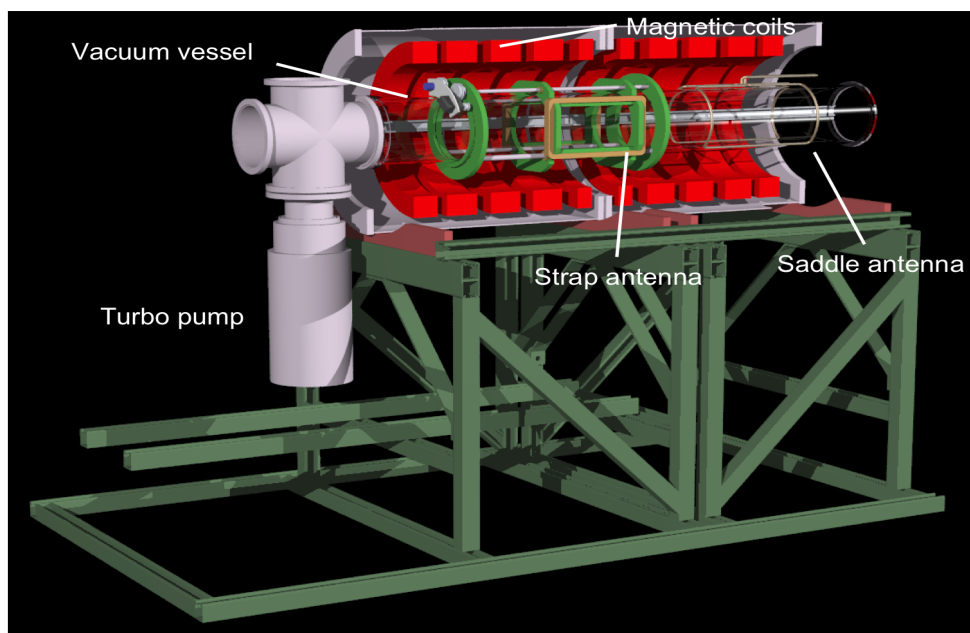
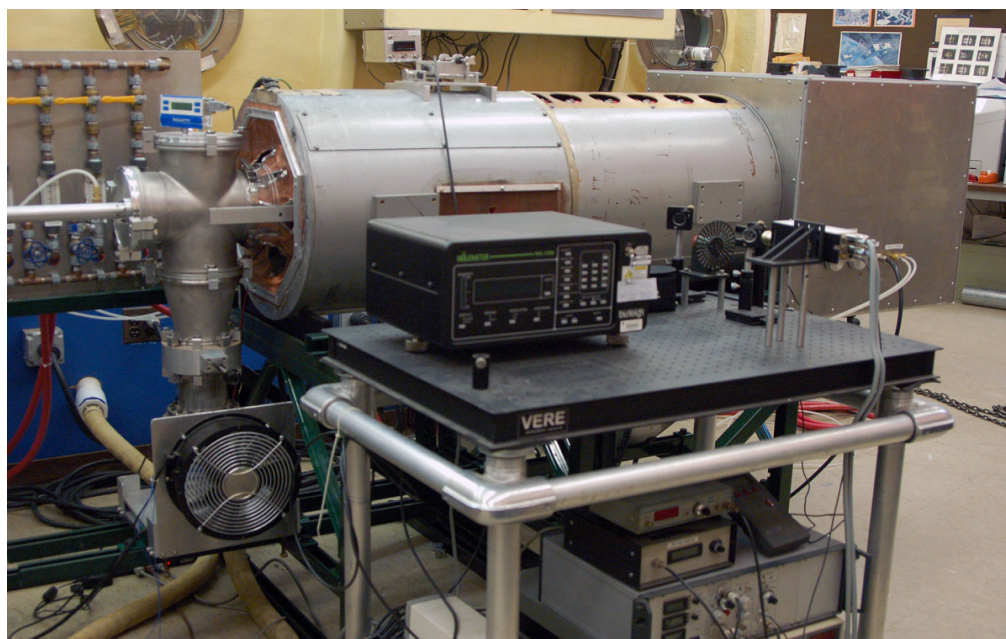


Figure 4.1: Schematic drawing of BWX II



(a) Computer generated schematic of the BWX II.



(b) Photograph of the experimental apparatus showing the LIF system in the foreground.

Figure 4.2: Experimental setup

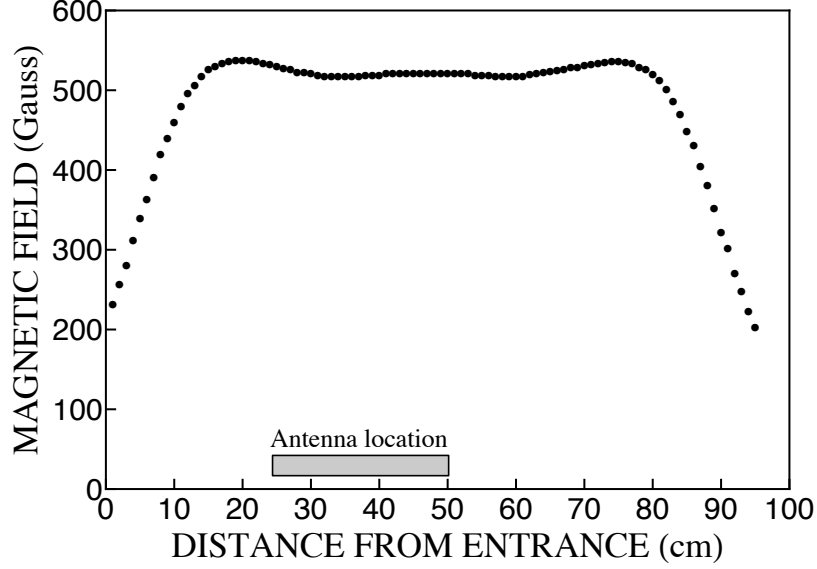
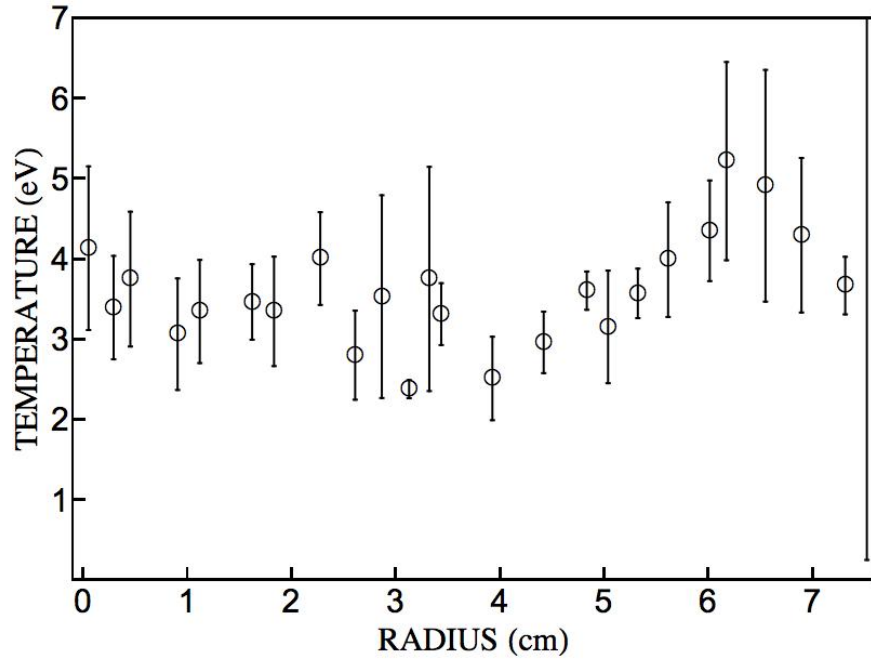


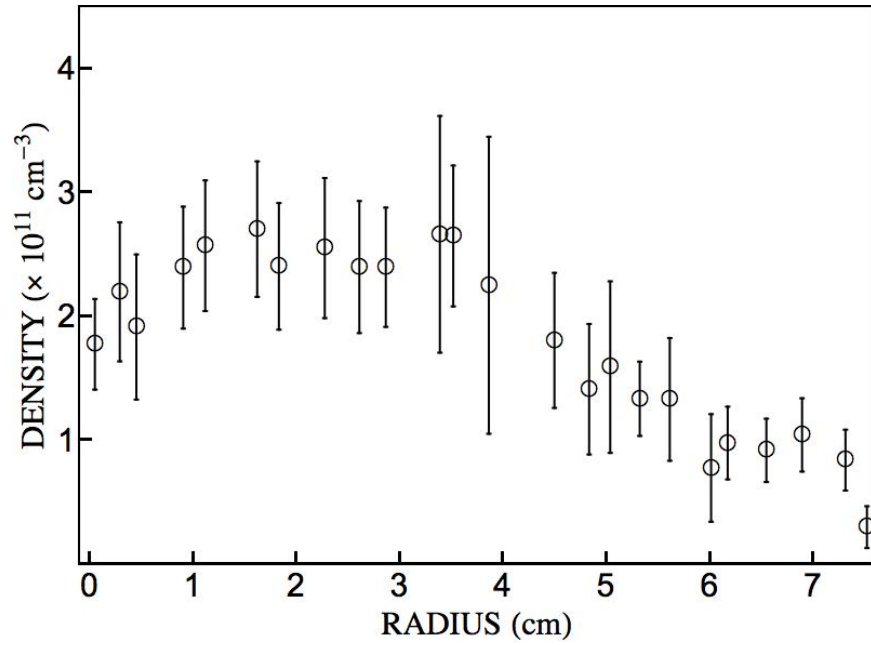
Figure 4.3: Plot of the magnetic field along the central axis of the plasma.

plasma edge is consistent with cylindrical inductively coupled sources [71]. As for the density, there is an approximately uniform region near the center of the plasma with a small dip at $r = 0$. This same trend has been reported for similar inductive discharges at low power [72]. The axial dependence of both temperature and density is uniform for the length of the heating volume.

The background ion temperature for our experimental conditions is approximately $T_i = 0.25$ eV, and we use this parameter in conjunction with the density and electron temperature measurements to show typical frequencies for BWX II in Fig. 4.5 [73]. The Hall parameter for ion-neutral collisions, $\Omega_i/\nu_{in} \gg 1$, is particularly important since it suggests that for our weakly ionized plasma ($< 5\%$) where these collisions are the dominant contributor to momentum transfer, we are in a regime where our collisionless model for ion heating has applicability.



(a) Typical radial profile for electron temperature.



(b) Characteristic radial profile for density in BWX II.

Figure 4.4: BWX II experimental parameters.

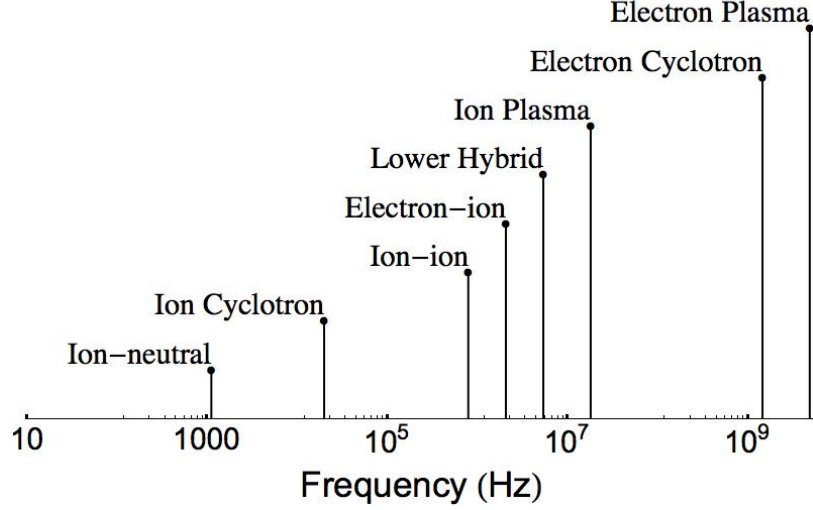


Figure 4.5: Characteristic frequencies for BWX II.

4.3 Antenna

While a number of studies have indicated electrostatic waves can be generated efficiently in a magnetized plasma by capacitive plates [74], capacitively coupled concentric rings [49], planar antenna [13, 48], and current-carrying wires along the axis of the plasma [75, 76], all of these methods subject the antenna to significant erosion. Since potential applications of the two-wave process depend on maintaining component integrity, BWX II employs a strap antenna placed outside the plasma for launching the electrostatic waves. In this configuration, the antenna generates a time-varying magnetic flux in the direction perpendicular to the ambient magnetic field. This in turn induces a substantial charge gradient in the plasma, which couples to both perpendicular and oblique electrostatic waves. The type of wave that is excited depends on the geometry of the inductive antenna. Two commonly employed configurations include the Nagoya III for coupling to the electric field component of helicon modes in a magnetized plasma [77] and a Helmholtz coil antenna that excites the electrostatic ion cyclotron wave [78].

The waves in the BWX II are launched by means of a simpler form of these two

configurations, a strap antenna 5.5 cm in width and 25 cm in length with 40 turns. The antenna is located outside the vacuum vessel with the longer dimension parallel to the magnetic field. The face of the antenna is pressed directly against the Pyrex vessel with the normal vector oriented parallel to the ground. We selected this geometry to launch near planar modes across the plasma in order to facilitate a comparison between the experimental results and theoretical predictions that we derived under the assumption of planar modes in a cartesian geometry.

Power is coupled into the two electrostatic waves launched concurrently from the antenna by means of an ENI 1140 LA amplifier that is matched to the antenna's inductive load with the variable dual frequency wave [79] launcher discussed in the next section. This provides near optimized matching over the frequency range of interest in this investigation, $f = f_{ci} - 5f_{ci} = 20 - 100$ kHz. The maximum current excited in each mode is 22 A—the value where excessive heating of the matching network by resistive losses significantly changes the matching characteristics. The power output from the amplifier at this point is 400 W.

4.4 Variable dual-frequency wave launcher

For a full parametric investigation of the BEW process, it is necessary to have the capability of easily and independently tuning the frequencies, f_1 and f_2 , of the concurrently launched waves. With this end in mind, we have designed the Variable Dual-frequency Wave Launcher (VDWL) — a system that (I) maximizes power into two waves simultaneously at the variable frequencies f_1, f_2 and (II) attenuates any undesired frequencies not equal to f_1 and f_2 . These criteria ensure that only the waves of interest are excited in the plasma while harmonic distortions that may arise from the non-ideal amplifier are blocked. In describing the VDWL, which we show in the context of BWX II in Fig 4.6, we first motivate the choice of the matching

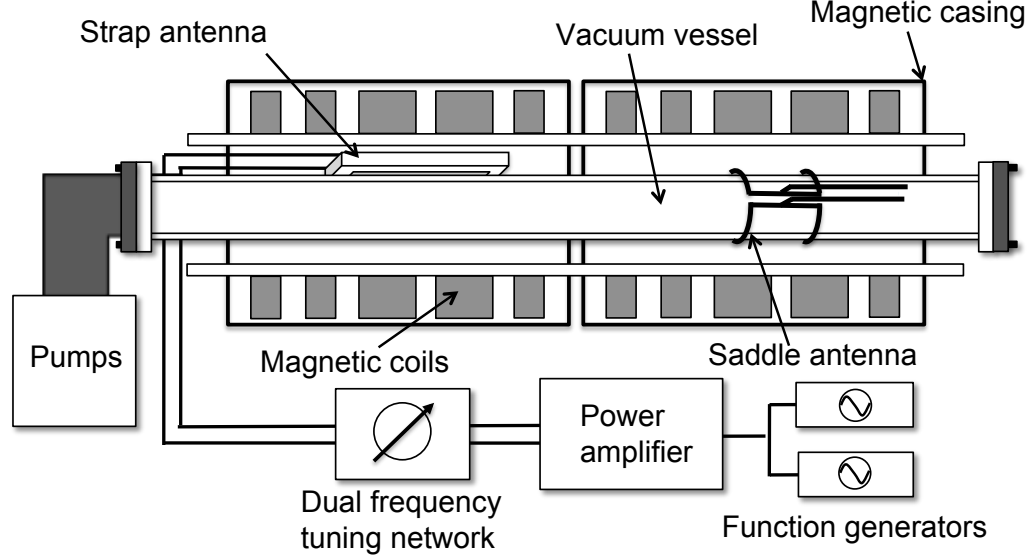


Figure 4.6: Representative drawing of the Variable Dual-frequency Wave launcher in relation to BWX II.

network as a means to tune to the strap antenna we employ in BWX II. We then evaluate the performance of the system with the BWX II antenna.

The strength of the coupling of the antenna we employ in BWX II depends on the magnetic flux through the plasma volume, which is a function of the antenna inductance. We model this inductance with an equivalent circuit for the antenna that consists of a series resistor, R_A , and inductor, L_A , in parallel with a parasitic capacitor, C_A . The real and imaginary components of the impedance of the strap antenna were measured directly at the leads by comparing the magnitude and phase of a sinusoidal signal from the ENI 1140LA at the indicated frequency. These measurements were verified with a low-frequency dual directional coupler. The results are shown in Fig. 4.7 for the case of an input power of 50 W and correspond to a small capacitance, $C_A = 66$ pF and inductance $L_A = 317$ μ H. The calculated series resistance, R_A , which is shown in Fig. 4.7, increases by a factor of four over our frequency range due to AC resistive losses.

As the wave coupling for the inductive antenna depends directly on the average magnetic flux density, the criteria outlined in I and II for our wave launching

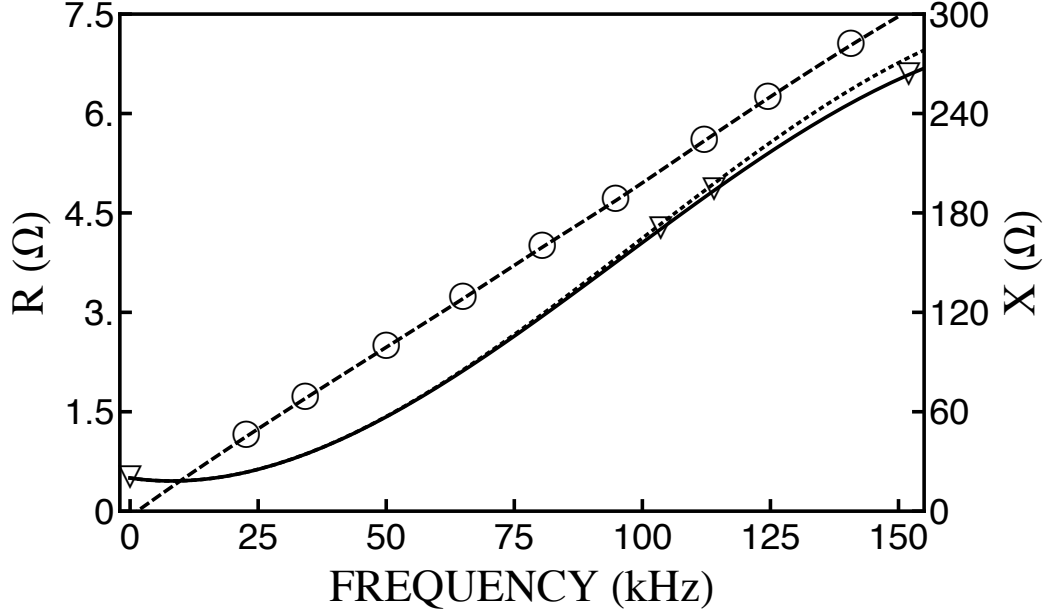


Figure 4.7: The measured impedance of the strap antenna with an interpolation fit. The dashed line corresponds to the reactance and the solid is the overall resistance. The dotted line is the calculated value of the resistor, R_A , for an equivalent circuit model of the antenna that is comprised of the series resistor and inductor ($L_A = 317\mu\text{H}$) in parallel with a capacitor ($C_A = 66\text{ pF}$).

system are now framed in the context of this physical parameter. Specifically, we need a matching network for the antenna that is capable of maximizing the magnetic flux density for two variable frequencies while simultaneously attenuating the flux at frequencies other than the selected values, f_1, f_2 . We note here that while this selectivity is necessary to block undesirable harmonic distortions from the wave source, this latter feature also has added value for experiments in which the plasma is initially created by radio frequency waves. The noise from such a process can induce voltage fluctuations on the heating antenna that unattenuated could produce harmful feedback into the signal amplifier.

The magnetic flux density for the strap antenna depends linearly on the current it carries. This leads to an expression for the average flux density in the plasma volume,

$$\langle B \rangle = \gamma_c N I_A, \quad (4.1)$$

where N is the number of turns in the antenna, I_A is the current per turn, and γ_c is a fixed constant that depends on the geometry. Since the number of turns and geometry of the strap antenna are constrained by the availability of space and the type of excited mode that is desired, the antenna current is the free parameter we manipulate to achieve the performance goals cited above. This is accomplished with the dual frequency network shown in Fig. 4.8 along with the equivalent circuit for the strap antenna.

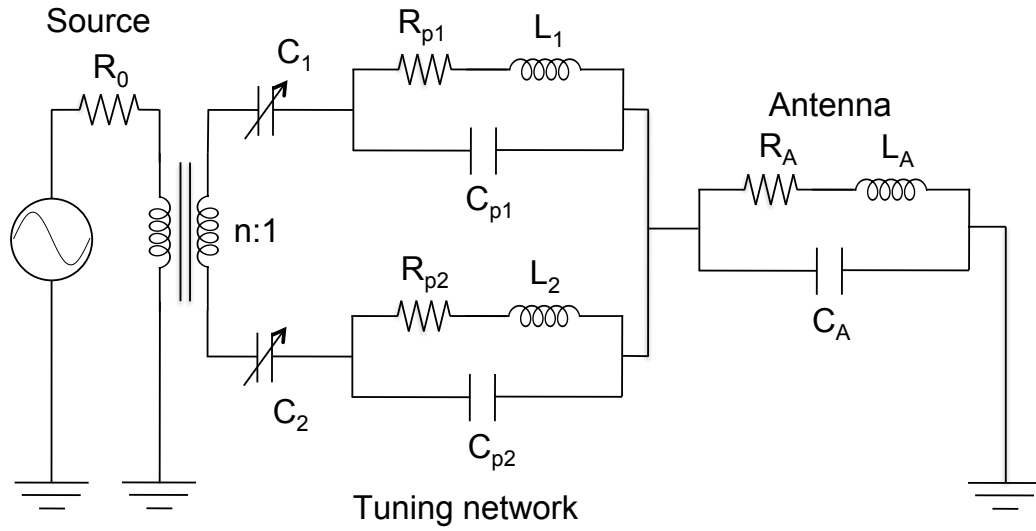


Figure 4.8: Dual frequency tuning circuit with equivalent circuit models for each component. The transformer has an $n:1$ turns ratio.

The tuning network consists of an $n:1$ step-down transformer between the source with impedance R_0 and two parallel LC traps connected in series with the antenna. The parasitic components (C_{p1} , R_{p1} , C_{p2} , R_{p2}) account for the non-ideal behavior of the inductors. During operation, the LC traps provide two separate and isolated paths for the waves from the source's combined signal. As a result, only one frequency f_1 is passed through the top arm, while the second frequency f_2 is passed through the bottom arm. By tuning the series resonance of the inductors L_1, L_2 and the variable capacitors C_1, C_2 , not only can the values of f_1, f_2 be changed, but the circuit will provide a conjugate match to the load at these values. The step down

transformer serves to match the residual resistance to the source impedance, which in turn multiplies the current through the antenna at the tuned frequencies. In this way, the circuit is capable of selectively passing two frequencies concurrently and attenuating the surrounding frequency spectrum.

We can quantify the performance of this system with an expression for the current through the antenna. For a fixed voltage V_S at the source, the current through L_A is given by,

$$I_A = nV_S \left| \frac{Z_A}{(R_A + j\omega L_A)(R_0 + n^2[Z_T + Z_A])} \right|, \quad (4.2)$$

where ω is the angular frequency and the factors of n and n^2 stem from the transformer. Z_T is the impedance of the tuning network which is given by

$$Z_T = \left(\sum_{i=1,2} \left[\left(\frac{1}{R_{pi} + j\omega L_i} + j\omega C_{pi} \right)^{-1} + \frac{1}{j\omega C_i} \right]^{-1} \right)^{-1}. \quad (4.3)$$

Z_A denotes the impedance of the antenna, which from the equivalent circuit model is

$$Z_A = \left(\frac{1}{R_A + j\omega L_A} + j\omega C_A \right)^{-1}. \quad (4.4)$$

It is evident from Eq. 4.2 that the LC traps introduce poles at two frequencies, which we denote f_1, f_2 . Moreover, since these resonant frequencies are functions of the component values, we can use Eq. 4.2 to calculate numerically the values necessary to produce resonances at arbitrary f_1 and f_2 . While this procedure will yield a wide range of valid component values for isolating f_1, f_2 , we choose to constrain our inductor values such that $L_1, L_2 \gg L_A$. We do this for two reasons. First, provided the parasitic resistances R_{p1}, R_{p2} are sufficiently small, this constraint yields simplified expressions for the resonant frequencies,

$$f_1 \approx \frac{1}{2\pi\sqrt{L_1 C_1}} \quad f_2 \approx \frac{1}{2\pi\sqrt{L_2 C_2}}. \quad (4.5)$$

This convenient relationship between the tuned frequencies and capacitances gives us a first-order approximation for how to tune our components. The second reason for

this restriction on inductance is that the strap antenna has a low inductance. As a consequence, for our low-frequency application, if we were to let $L_1, L_2 \approx L_A$, commercially available variable capacitors would be unable to produce sufficient capacitance for the LC traps to function. In order to continue to employ variable capacitors for effective tuning, we instead are forced to use large inductors $L_2, L_1 \gg L_A$.

With these considerations in mind, we use Eqs. 4.1 and 4.2 to find an approximation for the normalized magnetic flux density, β , produced by the antenna as a function of component values and frequency

$$\beta = \frac{\langle B \rangle}{\langle B_0 \rangle} = \left| \frac{2n (R_0 R_A)^{1/2} Z_A}{(R_A + j\omega L_A) (R_0 + n^2 [Z_T + Z_A])} \right|, \quad (4.6)$$

where we have normalized the flux density by the maximum magnetic flux density $\langle B_0 \rangle$ that can be generated through the antenna. This field occurs when the antenna current is $I_0 = V_s (4R_0 R_A)^{-1/2}$, i.e. the maximum amount of power from the amplifier is dissipated across the resistor R_A that is in series with the antenna inductor.

With Eq. 4.6 we have a metric—analogue to the transducer power gain [80] employed for power matching systems—that represents the relative performance of the tuning network in generating a magnetic flux density from a single source. With the goal in mind of maximizing β , we thus can use this equation to guide the choice of real circuit components in Fig. 4.8 and to gauge the efficacy of our chosen system in achieving (I) and (II).

Variable capacitors

Each LC trap of the circuit employs a 1-1000 pF vacuum variable Jennings capacitor. We used a set of fixed elements (four 1000 pF Mica capacitors and one 10,000 pF Mica capacitor) placed in parallel with the vacuum variable capacitors in order to yield a variable range of capacitance of C_1 from 1-10,000 pF and C_2 from 1- 5000 pF.

In general, we have found the parasitic inductance and resistance of the capacitors are small when compared to the parasitic elements of the inductors. This verifies our depiction in Fig. 4.8 of C_1, C_2 as ideal elements.

Inductors

We chose to use air-core, cylindrical inductors in order to avoid core losses [81] at the high inductances and powers required for BWX II. The disadvantage of this configuration is that a large number of turns are required, which can lead to large parasitic interwinding capacitance, AC series resistance, and stray capacitances. We minimized these effects by isolating the inductors from the surrounding environment and winding them in single layers with length to diameter ratios of approximately one [82]. In this way, we constructed two inductors from 14 AWG copper wire that measured 35.6 cm and 26.7 cm in diameter with inductances of $L_1 = 3.7$ mH and $L_2 = 1.7$ mH. The parasitic capacitances were found to be $C_{p1} = 90$ pF and $C_{p2} = 110$ pf. As with the case of the strap antenna, the values of R_{p1}, R_{p2} increased over the frequency range due to AC resistive effects. However, since the calculation of β in Eq. 4.6 only requires an estimate for the total impedance Z_T , instead of determining the explicit frequency dependencies of the equivalent circuit elements R_{p1}, R_{p2} , we used interpolation fits to the total measured impedances of each inductor in our calculations for the normalized flux density.

Transformer

For the BWX II application, we employ a 2:1 ($n = 2$) current transformer to provide an approximate match of the combined resistance from the non-ideal inductors and antenna to the 50Ω source impedance over the frequency range. Conventional power transformers, which employ ferrite or iron cores, are plagued by the same saturation effects and core losses in BWX II as the aforementioned inductors. This

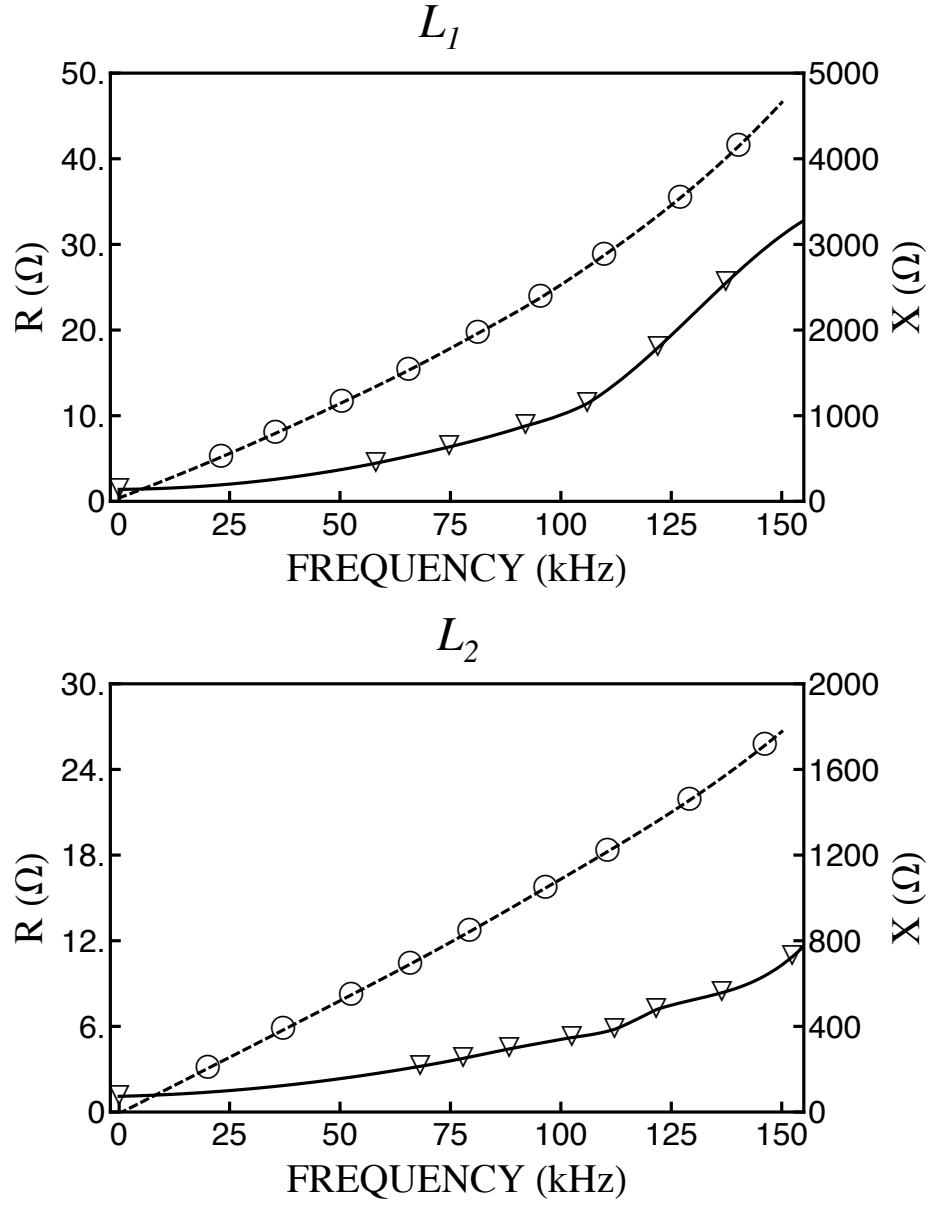


Figure 4.9: Impedance of the two air-core inductors employed in the matching network for an input power of 50 W. The solid line (∇) corresponds to the real component of the impedance while the dotted (\circ) represent the reactive component. $L_1 = 3.7$ mH and $L_2 = 1.7$ mH.

is a consequence of the core's primary role in transferring energy between primary and secondary windings. An air core transformer avoids saturation; however, the loss in magnetic coupling that results from the absent core significantly reduces the transformer's performance. Given these inherent difficulties with the conventional

configuration, we instead chose to employ a Ruthroff transmission line transformer [83] that consisted of several windings of $50\ \Omega$ coaxial cable around a toroidal magnetic core of type W-material. The advantage of this method is that instead of transferring energy, the core serves as a choke to prevent current imbalance between the center conductor and shield. We have found that the core performance is close to ideal over our ultrasonic frequency range when connected to effective resistive loads on both ends. It is for this reason that this type of transformer works particularly well with the VDWL shown in Fig. 4.8 as it is placed between the resistive source and a conjugately matched load at the frequencies of interest.

Antenna Flux density

Ignoring the small effects of plasma loading, we now examine the normalized flux density in our antenna as a function of wave frequency and capacitance by numerically evaluating Eq. 4.6 with the measured impedances of our components reported in the previous section. In order to illustrate the parameters we will investigate, we show in Fig. 4.10 a sample plot of the normalized magnetic flux density produced by the BWX II antenna in the heating region as a function of frequency for fixed capacitor values of $C_1 = 1640\ \text{pF}$ and $C_2 = 1770\ \text{pF}$. This figure shows two peaks at the frequencies $f_1(60\ \text{kHz})$ and $f_2(85\ \text{kHz})$ with values of $\beta_1(0.57)$ and $\beta_2(0.6)$. The full-width half maximum (FWHM) of each peak is denoted as $w_1(1.5\ \text{kHz})$ and $w_2(1.5\ \text{kHz})$ respectively. It is evident from this figure that the network is capable of producing magnetic flux densities at over 50% of the ideal case at two frequencies simultaneously. Moreover, the small width of each peak indicates that the network effectively attenuates the surrounding spectrum.

In order to gauge the success of the VDWL over the entire frequency spectrum, we devised a procedure to find a single term that could reflect the average tuning capability of the network. To this end, we fixed f_1 and f_2 in the frequency

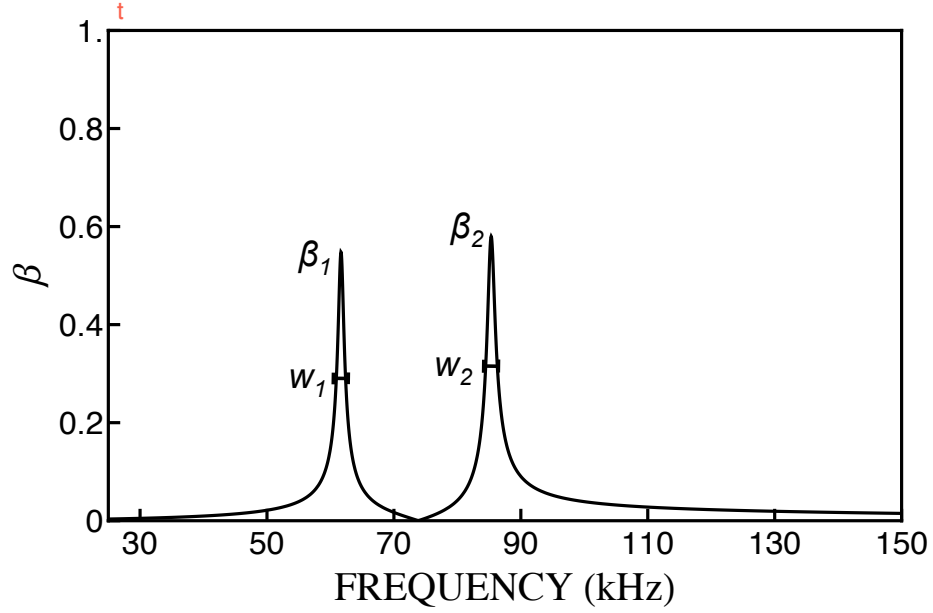


Figure 4.10: The normalized, magnetic flux density for the wave launching system as a function of frequency. The peaks occur at frequencies f_1 (60 kHz), f_2 (85 kHz); β_1 (0.57), β_2 (0.6) correspond to the values of the normalized flux density at the peaks; and w_1 (1.5 kHz), w_2 (1.5 kHz) are the FWHMs. $C_1 = 1640$ pF, $C_2 = 1770$ pF.

range and numerically determined from Eq. 4.6 the capacitor values that yielded the highest average value of the two peaks β_1, β_2 . We denote this as $\beta^*(f_1, f_2) = [(\beta_1(C_1, C_2) + \beta_2(C_1, C_2)) / 2]_{max} |_{f_1, f_2}$ where f_1, f_2 are constant and C_1, C_2 are the variables used to maximize the term. We then held f_1 constant and repeated this procedure for incremented values of f_2 in the frequency range. With this data set, we averaged over f_2 to yield $\bar{\beta}(f_1) = \langle \beta^*(f_1, f_2) \rangle_{f_2}$ as a function of f_1 . The process was then iterated for a new value of f_1 in order to arrive at the plot shown in Fig. 4.11a. Typical error bars are also shown.

Each point in this figure represents the average peak value that can be achieved when f_1 is fixed and f_2 is allowed to vary over $27.5 < f_2 < 150$ kHz. The figure is therefore an indication of the overall tuning capability of the network for almost all combinations of frequencies. There is one significant exception to this generalization: in our iteration procedure, all of our frequencies were chosen such that $|f_2 - f_1| > 10$ kHz. This is a restriction specific to BWX II, as in this experiment

we investigate waves whose frequencies differ by values larger than the cyclotron frequency. When $f_1 \rightarrow f_2$, however, the ability of the network to isolate peaks is drastically reduced. This would skew the results in Fig. 4.11a to values lower than would be achieved for our application. With this in mind, we see from this plot that provided $|f_2 - f_1| > 10$ kHz, we generally can tune the network such that the magnetic flux density generated at each desired frequency is greater than 50% of ideal. By comparison, we also show in Fig. 4.11a the dotted line that corresponds to the maximum normalized magnetic field that can be generated in the antenna without a tuning network or transformer. It is evident from this plot that the VDWL produces significantly improved results over the unmatched case.

In order to quantify the ability of the network to isolate dual, variable frequencies while attenuating the rest of the spectrum, we followed the same averaging procedure outlined above to determine $\overline{w}(f_1)$ for the optimized values of $\overline{\beta}$. This is shown in Fig. 4.11b where we see the average FWHM of each peak (< 2 kHz) corresponds to $|\overline{w}|/f_{ci} < 10\%$ for the BWX II experimental parameters. This excellent attenuation suits the careful tuning of frequencies required for the BWX II two-wave investigation. Moreover, this performance offers a vast improvement over the unmatched case where all frequencies are passed (w_1, w_1 are unbounded).

As an additional evaluation of this network, we consider the necessary capacitances to achieve the desired matched frequencies. Using the values of C_1, C_2 that optimized $\beta^*(f_1, f_2)$, we have plotted as markers in Fig. 4.12 the average values of C_1 that produced β_1 at f_1 and the average values of C_2 that yielded β_2 at f_2 . We also have included as dotted lines the ideal relations as given by Eq. 4.5. There is good agreement at the extremes of the frequency region where the larger inductor and capacitor series (L_1, C_1) follows the asymptotically derived equation for the low end of the spectrum and the smaller inductor-capacitor series (L_2, C_2) is successfully modeled for high frequencies. Eq. 4.5 thus serves as a reliable, first indicator of the range

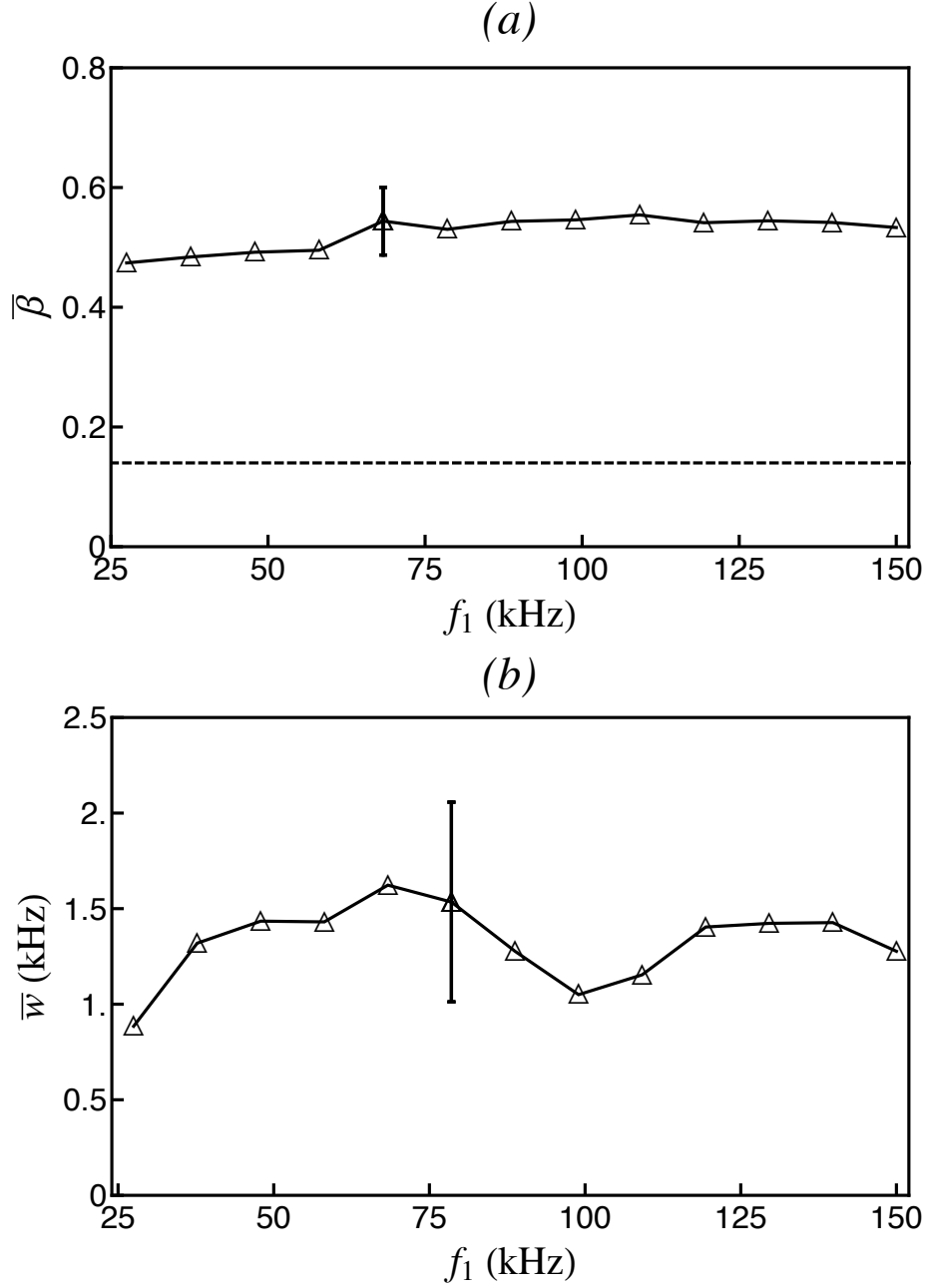


Figure 4.11: a) Each point is the average of the maximum, normalized magnetic flux density achieved simultaneously by the network at fixed frequency f_1 and frequency f_2 where the average is performed over $27.5 < f_2 < 150$ kHz. The dotted line corresponds to the maximum flux density for the antenna without a matching network. b) Values are the average of the FWHM of the optimized dual peaks that occur at the fixed frequency f_1 and frequency f_2 where the averaging is the same as in (a). In both cases, the averaging is performed such that $|f_2 - f_1| > 10$ kHz.

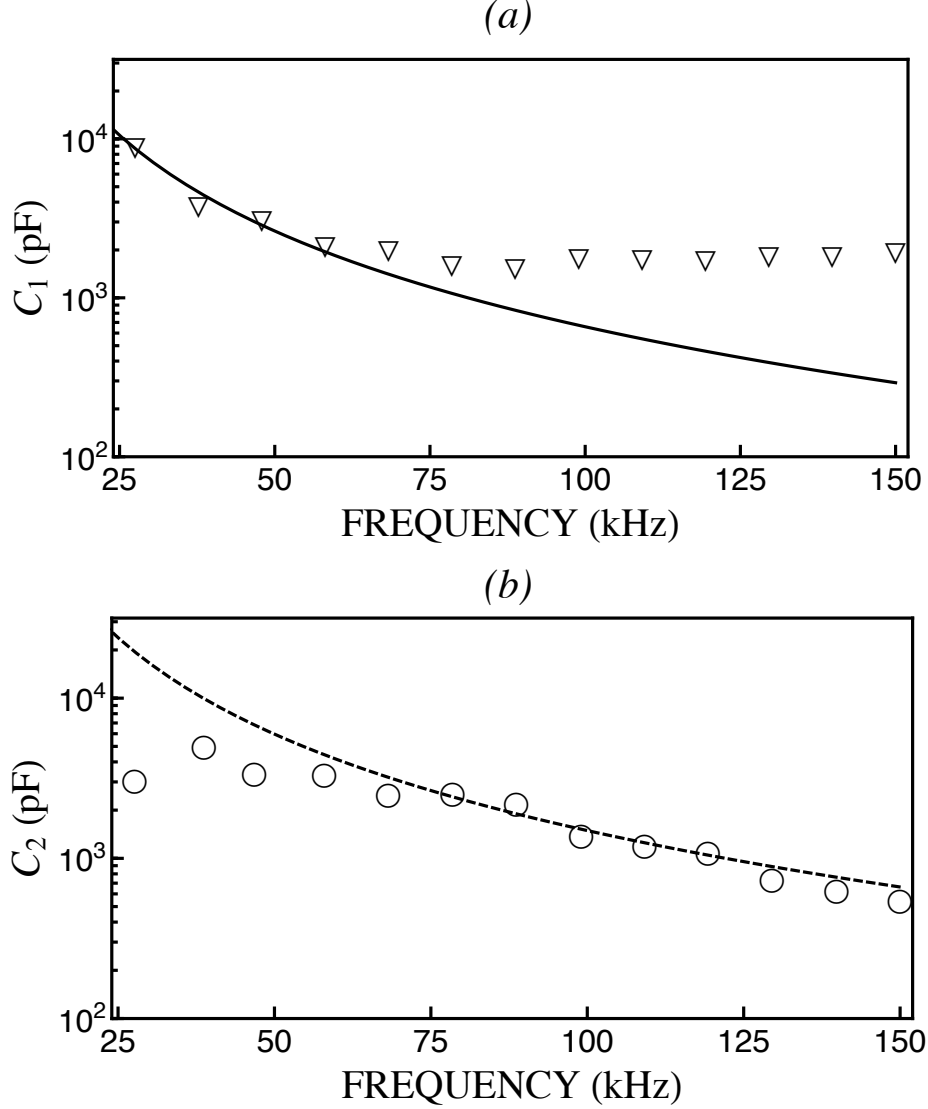


Figure 4.12: a) The average capacitance of C_1 (∇) that yields the optimized magnetic flux density at fixed f_1 and f_2 where an average is taken over all values of f_2 in the spectrum. b) The average capacitance of C_2 (\circ) that yields the optimized magnetic flux density at fixed f_1 and f_2 where the average is performed over all values of f_1 in the spectrum. In both cases, the averaging is performed such that $|f_2 - f_1| > 10$ kHz. The dotted line in each figure corresponds to the ideal tuning conditions represented by Eq. 4.5.

of capacitance to which we must tune in order to achieve the highest $\overline{\beta}$, and any deviations can be accounted for by using the data plots shown in Fig. 4.12. More importantly, we see that the matching conditions do not call for capacitances outside of our variable tuning range.

4.5 Diagnostics

4.5.1 Double Langmuir probe array

While the BWX II Pyrex vessel provides full optical access to the plasma and permits inductive coupling to BEW modes from an externally-mounted antenna, this setup precludes the insertion of probes through the walls. In order to determine the radial dependence of the density and electron temperatures in BWX II then, we employ the azimuthally swept double probe array shown schematically in Figs. 4.13 and 4.14. This configuration consists of a series of alumina tubes arrayed around a central support. Each tube holds two tungsten tips that are 0.254 mm in diameter and extend 1.5 mm in length from the end of the alumina support.

We choose to use double probes for this configuration since they provide a compact means for compensating for RF induced noise produced by the plasma source. Indeed, high frequency fluctuations from the RF source can induce significant perturbations in the plasma potential [84] which appear as oscillations in the I-V trace of a typical single Langmuir probe. Averaging over several probe sweeps can in part eliminate this noise; however, this technique is only reliable for estimating the steady-state ion saturation current (and therefore the density). For electron temperature measurements, the non-linear nature of the I-V probe trace where this parameter is measured leads to significant error in the estimates for this quantity even after linear averaging. RF compensated single probes can overcome this limitation [85] by forcing the probe tip to follow the RF fluctuations such that only the steady state potential is

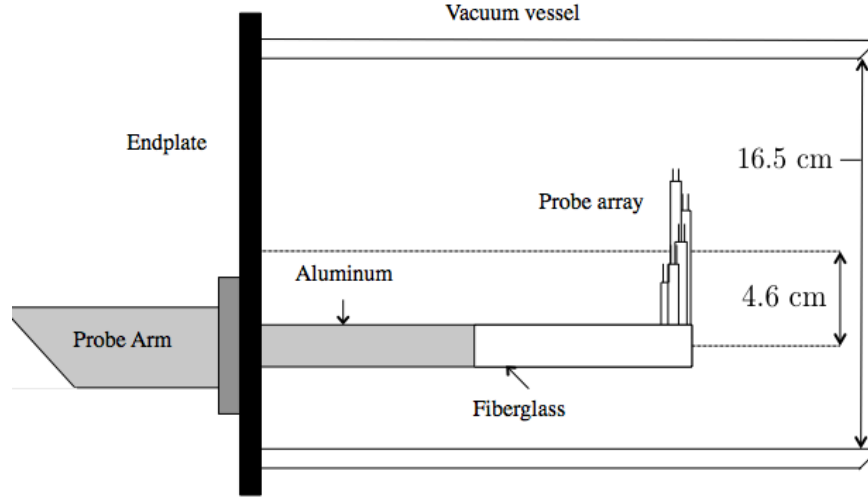


Figure 4.13: Schematic drawing of the probe array mounted on an arm in the plasma. The arm is capable of translating in the axial direction and rotating azimuthally.

observed. However, the implementation of this technique requires a careful use of RF chokes as well as an auxiliary electrode exposed to the plasma. The necessary space as well as the steady-state perturbation to the plasma induced by this setup are both problematic for implementation of a single probe array in BWX II.

It is for this reason that we turn to the use of double probes. Indeed, double probes are inherently floating and depend only on the relative potential between the probe tips such that they inherently follow the RF fluctuations in the plasma. Furthermore, since the measurements of the double probe system are differential, by twisting the leads from the two ends, any RF pick-up in the electrical circuit is eliminated through common mode rejection. The small space required for this system—effectively two wires insulated by alumina—further lends itself to implementation in the compact array configuration shown in Fig. 4.14.

Circuit

The successful implementation of a double probe requires that the probe tips float in the plasma. We accomplished this end with the circuit shown in Fig. 4.15. A voltage

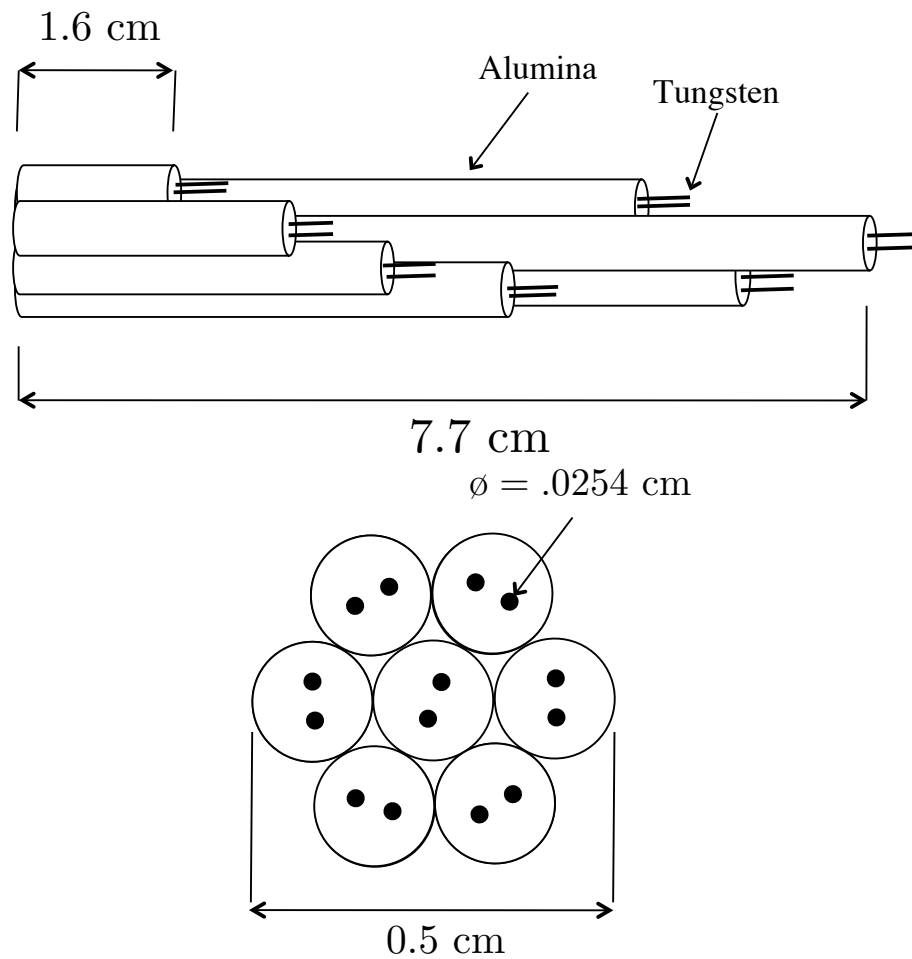


Figure 4.14: Array of double Langmuir probes with a side view (top) and a face on view of the probe tips (bottom).

bias is provided in this configuration by two floating amplifiers, and it is applied to the desired set of probe tips through a system of switches. A parallel capacitor inserted between the leads serves to short-circuit any high-frequency biases between the leads. In order to exploit the benefits of common mode rejection, we measure the double probe current as a function of voltage bias between the tips by subtracting the voltage drops across two matched resistors, R_{s1} and R_{s2} , placed near the probe tips.

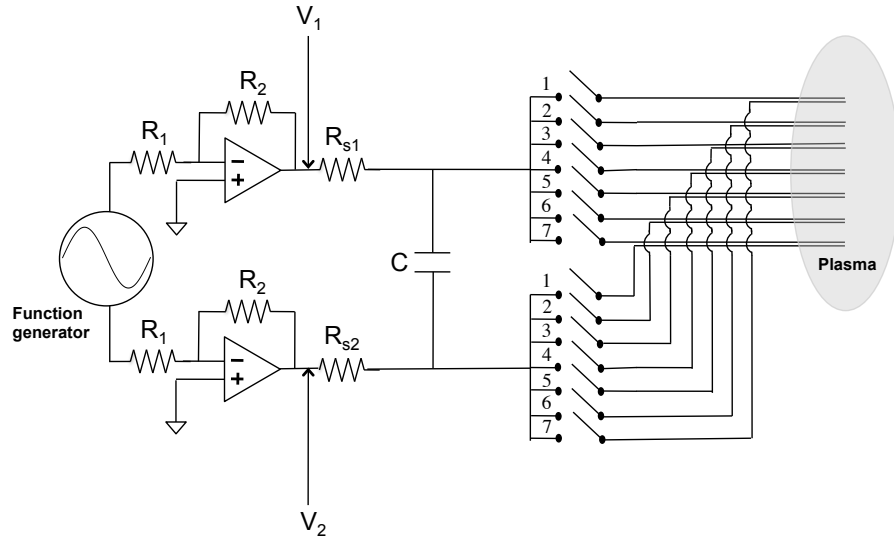


Figure 4.15: The circuit employed for the double probe array. The inverted triangles denote a floating common.

The one significant limitation for employing a double probe system in an RF coupled plasma is that the MHz fluctuations in the plasma can find paths to ground through small stray capacitances in the double probe circuit. This has the potential to destroy the ability of the probe tips to follow the plasma potential [86]. Castro et al. [87], however, compared the results from single probe analysis to double and RF compensated probe techniques in a dense RF discharge and found the double probe to be a precise measurement tool. The key to their success stemmed from their ability to effectively isolate the probe circuit from ground. We therefore attempted to follow this technique by taking the extra measures we outlined above to ensure our probe

circuit was floating.

Analysis

A typical I-V trace from a probe in the double probe array is shown in Fig. 4.16 where we plot the measured current I as a function of the applied voltage $V = V_2 - V_1$ between the probe tips. This plot was taken by one double probe from the array swept at 30 Hz and averaged over 200 cycles.

The symmetry with respect to the voltage axis ($I = 0$) reflects the equal area of the probe tips while the weak dependence of the ion saturation current on the biasing voltage results from the effective sheath expansion that occurs at large biases. There are several models for this weak dependence [84] that are applicable in different ranges of ionization, probe geometry, and plasma density. Instead of modeling this expansion in our investigation, however, we follow Owens [88] in his treatment of double probe traces by assuming approximate linearity for this trend. This enables us to employ a standardized numerical analysis for double probe traces—the procedure for which is as follows.

First, we fit linear trends to the ion saturation regions that occur for $|V| \gg 0$ and to the current trace at $V = 0$, i.e. where the entire system is at the floating potential. We denote the value of the voltage where the best fit lines intersect as V_{S2} and $-V_{S1}$, and we denote the current at these points as i_{S2} and $-i_{S1}$. The values where the ion saturation lines intercept the current axis ($V = 0$) are similarly labeled as $i_{S2} - \Delta i_2$ and $-i_{S1} + \Delta i_1$. From the symmetry of the traces, we see that $V_{S1} \approx V_{S2} = V_S$, $i_{S1} \approx i_{S2} = i_S$, and $\Delta i_1 \approx \Delta i_2 = \Delta i$ such that following the analysis of Owens, we have the following relationships between these quantities and the plasma parameters:

$$\frac{T_e}{q} = \frac{1}{2}V_S \quad n_e = .61 \frac{2}{A_p} i_S \frac{i_S - \Delta i}{2i_S - \Delta i} \left(q \sqrt{T_e/m_i} \right)^{-1} \quad (4.7)$$

where T_e is expressed in units of energy, A_p denotes the exposed area of each tip, q is the charge value (assuming singly ionized species), and m_i is the ion mass.

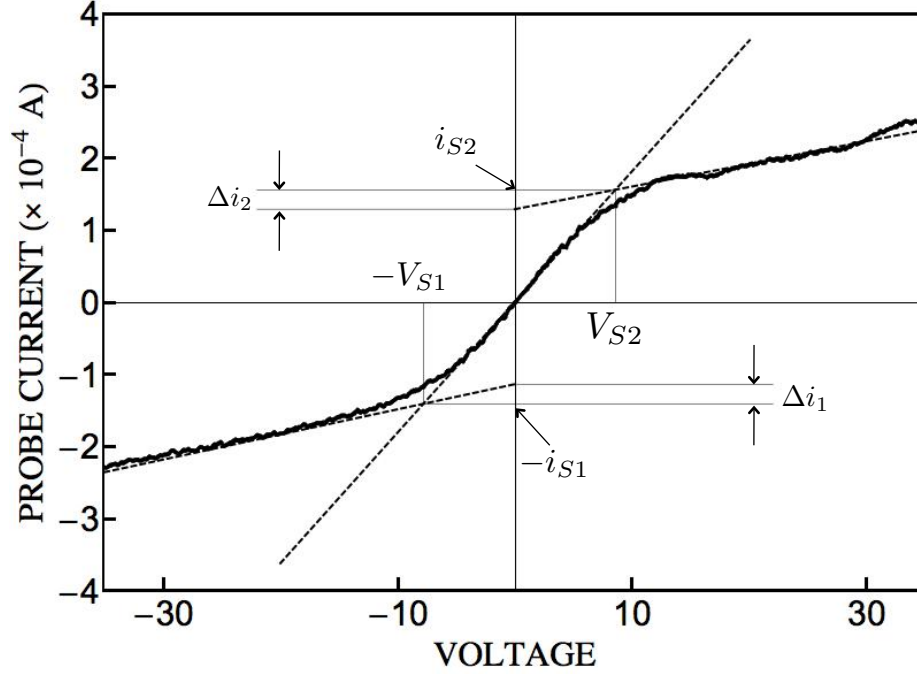


Figure 4.16: Typical IV trace for a double probe in BWX II.

Procedure

For our experimental investigation, each probe measurement consisted of the average of 200 sweeps performed at a rate of 30 Hz. This averaging served to eliminate any errant RF noise coupled into the leads. In order to estimate errors in our plasma parameters, we first included a 15% instrumental error characteristic of all Langmuir probe systems where erosion and sheath expansion leads to uncertainty in measurements [84]. We then estimated experimental error by repeating the 200 sweep cycle ten times and determining the 93% confidence interval from a t-distribution [89]. This uncertainty was added in quadrature with the instrumental error to yield the total error estimates. The measurements for density and electron temperature we presented in Fig. 4.4 in order to characterize the BWX II plasma source were made by following this procedure.

4.5.2 Laser induced fluorescence

The primary ion diagnostic for BWX II is a Laser Induced Fluorescence (LIF) system that is tuned to a metastable state of the Ar II ion. This tool probes the local velocity distribution of ions in the system and as such can provide information both on the ion temperature as well as the ion kinetic response to propagating plasma modes. Since the LIF technique also is inherently non-invasive, this diagnostic offers a significant advantage over probe measurements of ion temperature and wave properties where elements exposed to the plasma might perturb the BEW effect. The principle of operation for LIF as well as the setup for the BWX II system is presented below. The two modes of operation for temperature measurements and wave measurements are also discussed.

Principle of operation

For BWX II, the LIF system is based on two disparate atomic transitions in the Ar II ion shown schematically in Fig. 4.17. The first is an induced transition of a metastable state from $3d^4F_{7/2} - 4p^4D_{5/2}^0$, which occurs in the rest frame of the ion at $\lambda_0 = 668.6138$ nm [90]. The second transition is the resulting decay of the excited state to a lower energy level $4s^4P_{3/2}$ that produces light at 442.72 nm. The fluoresced light is the measured signal, which is more easily detected since it is distinct from the exciting mode wavelength.

In the BWX II argon plasma, a narrow band, collimated laser beam (Fig. 4.18) with frequency ν is injected into the plasma in an attempt to initiate this three level process. However, since ions in the plasma are characterized by a range of velocities with components v_x in the direction of the laser beam propagation, the frequency of the light ν_L encountered by the ion in its rest frame is Doppler shifted from the

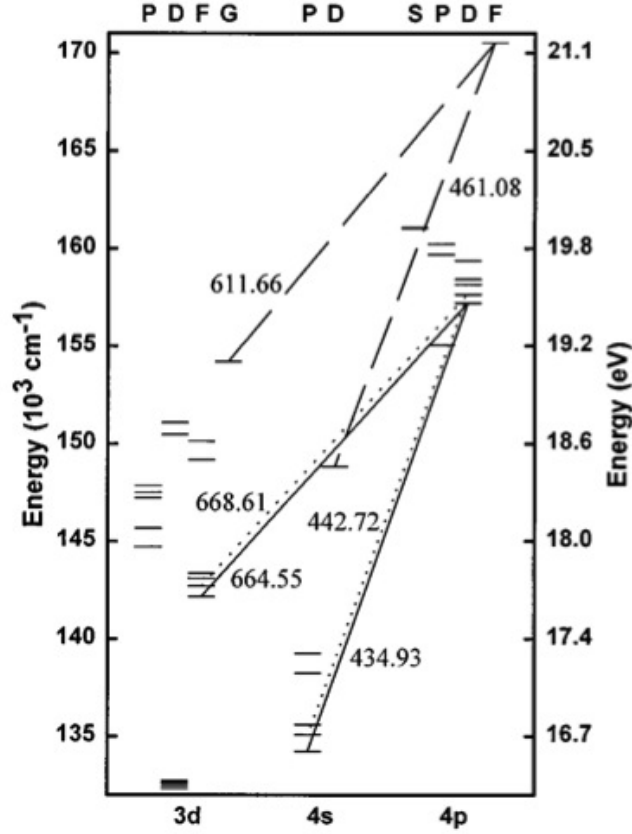


Figure 4.17: Partial Grotrian diagram for Ar II that includes the transition targeted in BWX II. Figure taken from Ref. [90].

laboratory frame frequency:

$$\nu_L = \nu \left(1 + \frac{v_x}{c} \right), \quad (4.8)$$

where c is the speed of light. For ions moving toward the laser source with v_x , the frequency of the beam as seen by the ion is shifted to higher values while the opposite effect occurs for the ions moving away from the beam. In order to excite the targeted transition for a moving ion, it therefore is necessary to tune the laser wavelength such that $\nu_L = \nu_0 = c/\lambda_0$. This yields in the non-relativistic limit ($|v_x|/c \ll 1$)

$$v_x = \frac{c}{\nu_0} (\nu_0 - \nu). \quad (4.9)$$

Provided we have a tunable laser, this relationship is a means to selectively excite a subset of the velocity population in the plasma. The intensity of the resulting

fluoresced light at 442 nm similarly provides a relative measurement of the number of particles with the selected velocity. We can localize this velocity measurement to a small volume in the plasma by only observing the fluoresced light from a small segment the beam. This is accomplished by employing a set of collection optics with a converging field of view that intersects the beam.

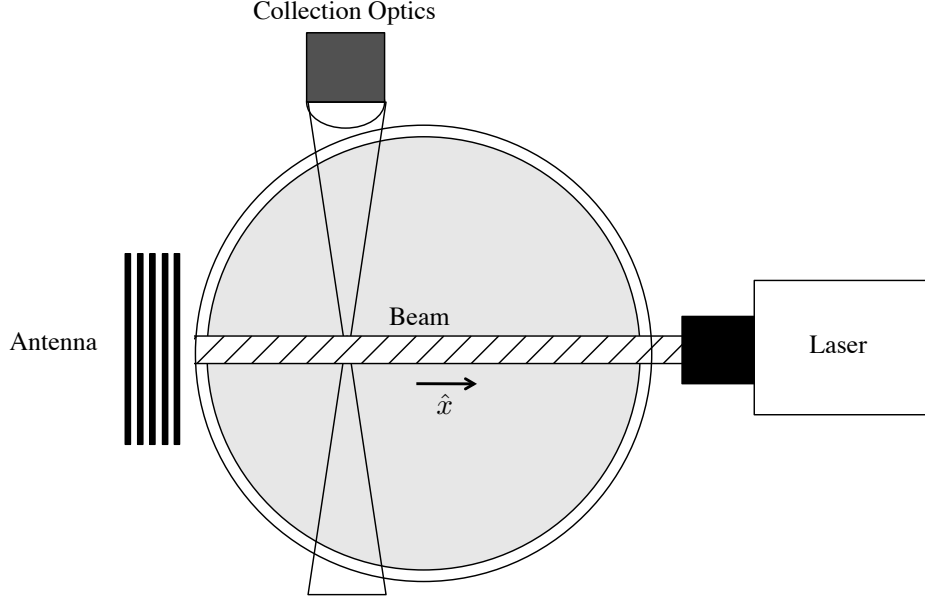


Figure 4.18: Conceptual view of the LIF system from the perspective along the axis of BWX II. The empty triangles indicate the field of view of the collection optics.

Broadening mechanisms

While Eq. 4.9 is valid assuming that the induced transition is constant at ν_0 and distinct, there are a number of mechanisms in a magnetized plasma—most notably Zeeman splitting—that can broaden the transition into a spectra of closely spaced wavelengths. Such effects introduce error in using Eq. 4.9 to calculate velocity. In Appendix G, we catalog these broadening processes and show that in the BWX II plasma the majority of them can be neglected when inferring the plasma temperature. On the other hand, when using LIF for wave measurements, we must incorporate these broadening effects into a systematic uncertainty $\Delta\nu_0$ in our estimates for the

rest frame frequency of the transition. We then proceed in our analysis under the assumption that Eq. 4.9 is approximately valid with error that stems from $\Delta\nu_0$.

Temperature measurements

For an ion population in local thermal equilibrium, the steady-state density distribution in a single direction is given by

$$f_0(v_x) = n_0 \left(\frac{m_i}{2\pi T_i} \right)^{1/2} e^{-m_i(v_x - v_{di})^2 / 2T_i}, \quad (4.10)$$

where n_0 is the background spatial density, T_i denotes the temperature expressed in units of energy and v_{di} is the drift velocity in the x direction. Using the Doppler relation from Eq. 4.9, we thus see that the LIF system tuned to frequency ν will produce fluoresced light at 442 nm with steady-state intensity given by

$$I_M(\nu) = I_0 e^{-(\nu - \bar{\nu}) / (2\sigma^2)}, \quad (4.11)$$

where we have defined the quantities

$$\bar{\nu} = \nu_0 \left(1 + \frac{v_{di}}{c} \right); \quad \sigma^2 = \frac{\nu_0^2 T_i}{c^2 m_i}; \quad I_0 = \alpha_c \left(\frac{m_i}{2\pi T_i} \right)^{1/2}. \quad (4.12)$$

Here we have assumed that the ion population has a linear correspondence with the metastable state targeted by the laser light and that α_c is a quantity that depends on the beam intensity, volume of intersection between the beam and collection optics field of view, and attenuation of the light through the collection optics. From Eq. 4.11, we thus see that by measuring the steady-state signal produced by the beam, we can infer both the local drift velocity v_{di} and temperature of the ion population.

Wave measurements

The LIF system also can yield information on coherent modes propagating in the plasma by measuring the time-dependent perturbation f_1 to the density distribution. We model this velocity dependent perturbation through an analysis of the Vlasov

equation for ion motion:

$$f + \mathbf{v} \cdot \frac{\partial f}{\partial \mathbf{x}} + \frac{q}{m_i} (\mathbf{E} + \mathbf{v} \times \mathbf{B}) \cdot \frac{\partial f}{\partial \mathbf{v}} = 0, \quad (4.13)$$

where \mathbf{E} denotes the electric field, \mathbf{B} is the magnetic field vector, and the plasma is assumed to be locally uniform such that $\int f d^3\mathbf{v} = n$ where n is the total ion density. We note that this general formulation for the evolution of the velocity density distribution space explicitly neglects collisions; however, the effect of weak collisionality on waves can be recovered through a judicious choice of wave frequency [91].

The strap antenna of our system is designed to couple primarily to electrostatic modes such that the form of the electric field is given by $\mathbf{E} = -i\mathbf{k}\Phi \exp[i(\mathbf{k} \cdot \mathbf{x} - \omega t)]$, where \mathbf{k} denotes the wave vector, ω is the wave frequency, and Φ is the potential amplitude of the mode. Similarly, since we assume the magnetic field is uniform in the axial direction and the time dependent contribution of the magnetic field for electrostatic modes is negligible, the magnetic field term in Eq. 4.13 is given by $\mathbf{B} = B_0 \hat{z}$.

In order to determine the kinetic response of the plasma to the electrostatic mode, we expand $f = f_0 + f_1$ and write the first order equation:

$$\frac{df_1}{dt} = i \frac{q}{m_i} \Phi \exp[i(\mathbf{k} \cdot \mathbf{x} - \omega t)] \mathbf{k} \cdot \frac{\partial f_0}{\partial \mathbf{v}}, \quad (4.14)$$

where we assume that the magnetized ions have the three-dimensional steady-state Maxwellian distribution:

$$f_0(\mathbf{v}) = n_0 \left(\frac{m_i}{2\pi T_{\parallel i}} \right)^{1/2} e^{-m_i(v_z - V)^2/2T_{\parallel i}} \left(\frac{m_i}{2\pi T_{\perp i}} \right) e^{-m(v_x^2 + v_y^2)^2/2T_{\perp i}}. \quad (4.15)$$

Here $T_{\parallel i}$ denotes the ion temperature parallel to the magnetic field, $T_{\perp i}$ is the temperature perpendicular to the field, and we have implicitly assumed that the bulk velocity in the plane orthogonal to the magnetic field is small. Substituting this expression into Eq. 4.14 and employing the method of characteristics, it is possible to integrate this equation with respect to time (c.f Ref. [10], Chapter 10) to solve for

$f_1(v_x, v_y, v_z)$, i.e. the perturbed density distribution as a function of all three velocity components.

The LIF system can only scan in one direction (\hat{x}), however, so we integrate over the other two velocities, $f_1(v_x) = \int f_1(v_x, v_y, v_z) dv_y dv_z$. This was done in Refs. [78, 91, 92] to yield $f_1 = \bar{f}_1(v_x) \exp i(\mathbf{k} \cdot \mathbf{x} - \omega t)$ where

$$\begin{aligned} \bar{f}_1(v_x) = & \left(\frac{q\Phi}{\pi m_i v_{ti\perp}^2} \right) f_0(v_x) \sum_{n,m} \left(1 + Z(\zeta_{n+m}) \left[\zeta_0 \frac{T_{\parallel}}{T_{\perp}} + \left(1 - \frac{T_{\parallel}}{T_{\perp}} \right) Z(\zeta_{n+m}) \right] \right) \\ & \times J_m(k_{\perp} v_y / \Omega_i) e^{-im\pi/2} e^{i(m+n)\pi} e^{ik_y v_x / \Omega_i} e^{-a^2/8} e^{-c^2/4} \\ & \times \sum_k I_{(n+k)/2} \left(\frac{a^2}{8} \right) I_k \left(\frac{ac}{2} \right) e^{ik\pi/2}. \end{aligned} \quad (4.16)$$

Here Z denotes the plasma function; $f_0(v_x)$ is given by Eq. 4.10 with $T_i \rightarrow T_{i\perp}$ and $v_{di} \rightarrow 0$; $\zeta_n = (\omega - n\Omega_i - k_z v_{di}) / v_{ti\parallel} k_z$; $a = \sqrt{2} k_{\perp} v_{ti\perp} / \Omega_i$; $k_{\perp} = \sqrt{k_x^2 + k_y^2}$; and $c = \sqrt{2} k_x v_{ti\perp} / \Omega_i$. Here we have $\tan^{-1}(k_x/k_y)$ such that θ is the angle the wavevector makes with respect to the \hat{y} axis in the transverse plane.

With this kinetic description, we thus see that there is a time-dependent model for the kinetic response of the ions to electrostatic waves in the plasma. This suggests that on top of the steady-state distribution, the observed intensity of the fluoresced light from the plasma will have two components that oscillate at wave frequency ω . The first signal is in phase with the wave with magnitude given by

$$I_{IP}(\nu) = \alpha_c \text{Re} \left[\bar{f}_1 \left(\frac{c}{\nu_0} (\nu_0 - \nu) \right) \right], \quad (4.17)$$

where α_c is the same scaling constant discussed previously. The second component is 90° out of phase with magnitude

$$I_Q(\nu) = \alpha_c \text{Im} \left[\bar{f}_1 \left(\frac{c}{\nu_0} (\nu_0 - \nu) \right) \right], \quad (4.18)$$

where I_Q denotes the quadrature component. By locking in on the wave frequency, we can scan over the laser frequency range to produce the perturbed velocity profile. Fitting the above model to the profile then yields information on the three dimen-

sional wavevector and amplitude of the propagating mode. This is contrasted with traditional, invasive probe techniques where it is necessary to employ a three-axis probe that examines the phase difference between the spatially separated signals in order to estimate the wave number.

LIF setup and implementation

The LIF system employed in BWX II is shown from a top-down perspective in Fig. 4.19. A Littrow configuration tunable diode laser from Sacher Laser provides a 2 mm diameter, linearly polarized beam at 7 mW. This beam can be scanned in a mode-hop free range of 668.6020 – 668.6240 nm around the vacuum transition wavelength $\lambda_0 = 668.6138$. From the laser head, the beam passes through a 90/10 beam splitter with the weaker component directed through a Burleigh 1500 wavemeter that is accurate to 0.2 ppm. The remaining portion of the beam passes through a series of mirrors to either traverse the plasma in the direction perpendicular to the uniform magnetic field or to enter the plasma in the axial direction. In each case, the beam is parallel to the ground and in the same plane as the exciting strap antenna. For perpendicular measurements, the beam’s linear polarization is oriented parallel to the uniform magnetic field so as to selectively excite the π transition induced by Zeeman splitting (Fig. G.1 in Appendix G) while for parallel wave measurements, the linearly polarized beam is passed through a $1/4$ wave plate. The resulting circularly polarized light selectively excites only one of the σ bands induced by Zeeman splitting. In order to collect the fluoresced light from the induced transition in the Ar II ions, we employ a set of optics comprised of two convex lenses separated by a light-baffling collimating tube (Fig. 4.18). The focal point of the lens facing the plasma intersects the laser beam such that the collected light from this region passes through the collimating tube. The width of the collection optics field of view at the focal length is ~ 2 mm, which accordingly limits the resolution of the system. The light passing

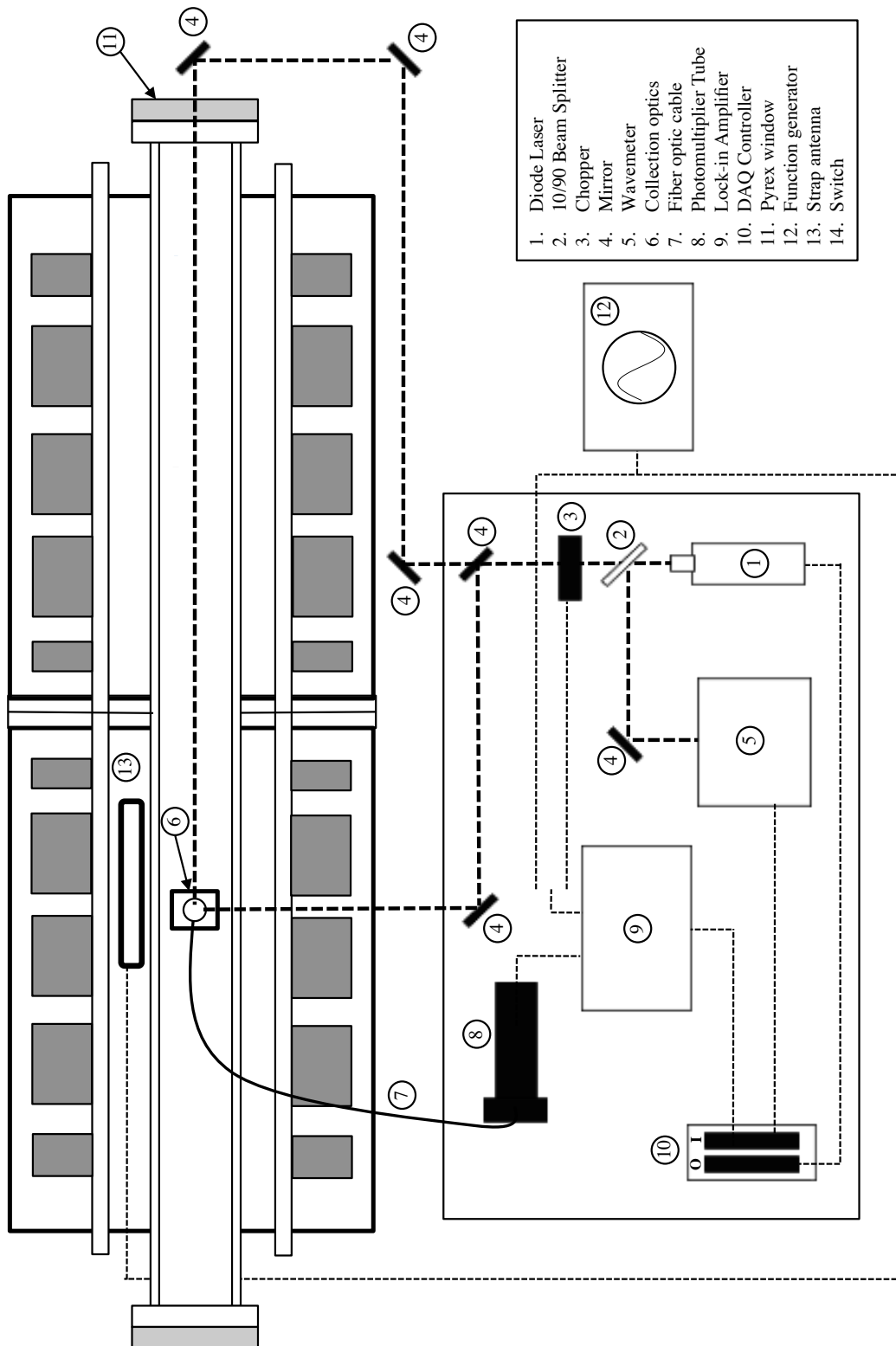


Figure 4.19: Schematic for the LIF system. The thick dotted lines indicate the two possible beam paths.

through the collimating tube is refocused onto the tip of a fiber optic cable where it is then directed through a narrow band 442 nm filter and into a Hamamatsu HC124-06MOD photomultiplier tube (PMT). The entire collection optics assembly is capable of translating across the plasma (perpendicular to the magnetic field). However, the measurements reported for this dissertation were performed at $r = 3$ cm where the plasma was observed to be uniform. This experimental uniformity is necessary both to align our measurements with the analytical predictions from Chapters 2 and 3 as well as to employ the theoretical model for the ion's kinetic response to the wave we discussed in the previous section.

During our experimental trials, we found that at our chosen position, in spite of the narrow filter on the PMT, the fluoresced signal from the metastable transition was overwhelmed by ambient radiation emitted from the plasma. For measurements of the steady-state distribution then, we chopped the laser beam at 3 kHz before it passed into the plasma and used this chopping frequency as a reference in a Stanford 830 lock-in amplifier (LIA). The fluoresced signal from the PMT, now pulsed at 3 kHz, was then fed into the LIA that subsequently isolated and increased the signal to noise ratio. While the Stanford 830 was capable of retaining both the magnitude of the detected signal as well as its phase with respect to the reference signal, for temperature measurements we only monitored the magnitude of the signal.

With this LIF setup, we measured the steady-state intensity profile by scanning the frequency of the laser over the specified range and simultaneously recording the wavelength of the beam and the amplitude of the fluoresced signal as indicated by the PMT. The laser power, monitored by a photodiode internal to the laser head, remained approximately constant over the frequency range. Each full wavelength scan consisted of 50 data points sampled over a 10 second interval, and we repeated this measurement five times to yield a total of 250 points. The wavelengths were then converted to frequency, and we performed a fit of the data to the model provided

by Eq. 4.11. Since the signal to noise was high ($S/N > 20$) for these measurements, we weighted each data point equally. The fit was evaluated through a Mathematica algorithm that employed the LevenbergMarquardt fitting scheme. The error of the best fit parameters were estimated through an evaluation of the diagonal terms of the covariant matrix at the best fit point [89] scaled by the average of the measurement errors. Following this procedure, we show in Fig. 4.20 a sample T_i plot for a scan performed in the perpendicular direction at $r = 3$ cm along with the best fit line from Eq. 4.11.

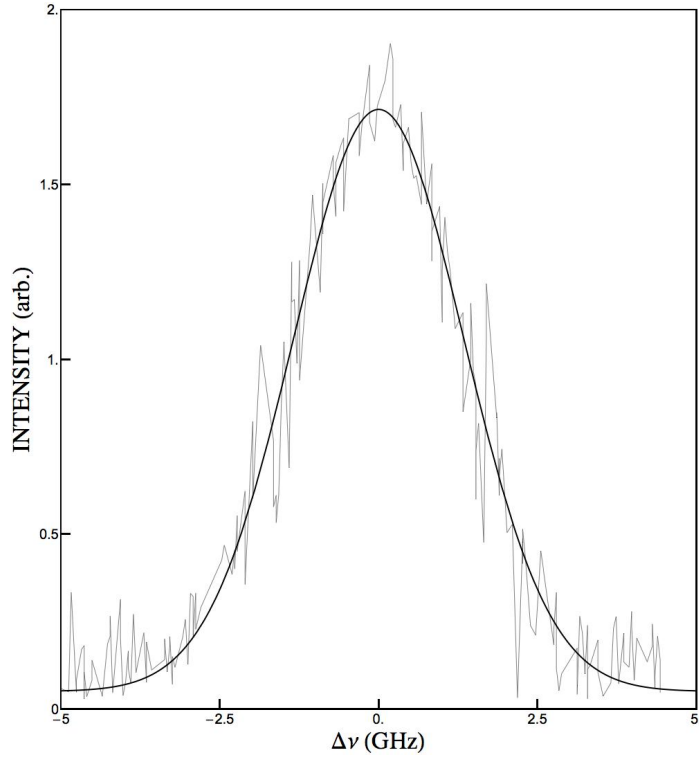


Figure 4.20: Characteristic profile at $r = 3$ cm for the steady-state perpendicular velocity distribution in the BWX II plasma. The best fit Maxwellian is also indicated. $v_{di} = 0$ and $T_i = 0.25$ eV.

For wave measurements, it was necessary to isolate the time dependent variations in the velocity distribution profile. We accomplished this by removing the beam chopper from the system and toggling the switch in Fig. 4.19 to use the targeted wave frequency from the signal generator as the reference in the LIA [91, 93, 78]. The

LIA subsequently produced in phase and quadrature measurements, I_{IP}^m and I_Q^m , of the wave's velocity distribution function shifted by the difference in phase φ between the reference signal from the source and the wave at the locally measured point in the plasma:

$$\begin{aligned} I_{IP}^m(\nu) &= \alpha_c \text{Re} \left[e^{i\varphi} f_1 \left(\frac{c}{\nu_0} (\nu_0 - \nu) \right) \right] \\ I_Q^m(\nu) &= \alpha_c \text{Im} \left[e^{i\varphi} f_1 \left(\frac{c}{\nu_0} (\nu_0 - \nu) \right) \right]. \end{aligned} \quad (4.19)$$

In order to apply the theoretically indicated fits to these profiles, it was necessary to eliminate the phase dependence φ in the data. To this end, we followed Ref. [91] in noting that for electrostatic waves, the Poisson equation indicates that the perturbed plasma density, $n_1 = \int f_1(v_x) dv_x$, is in phase with the wave potential. Since we have

$$f_1(v_x) = e^{i(\mathbf{k} \cdot \mathbf{x} - \omega t)} [f_{1R}(v_x) + i f_{1I}(v_x)] \quad (4.20)$$

$$\Phi(t) \propto e^{i(\mathbf{k} \cdot \mathbf{x} - \omega t)}, \quad (4.21)$$

the in-phase requirement demands that

$$\int f_{1I}(v_x) dv_x = 0. \quad (4.22)$$

For the measured intensity profiles, we have

$$\begin{aligned} \int I_{IP}^m d\nu &= \alpha_c \frac{\nu_0}{c} \left[\cos \varphi \int f_{1R}(v_x) dv_x + \sin \varphi \int f_{1I}(v_x) dv_x \right] \\ \int I_Q^m d\nu &= \alpha_c \frac{\nu_0}{c} \left[-\sin \varphi \int f_{1R}(v_x) dv_x + \cos \varphi \int f_{1I}(v_x) dv_x \right]. \end{aligned} \quad (4.23)$$

The condition stipulated by Eq. 4.22 thus requires

$$\varphi = -\tan^{-1} \left(\frac{\int I_Q^m d\nu}{\int I_{IP}^m d\nu} \right). \quad (4.24)$$

This permits us with our measured profile to correct the data in such a way that we can employ Eq. 4.16.

Before we apply this model to the phase-corrected, however, we note that in order to overprescribing the fit, it is necessary to reduce the number of free parameters, $k_\perp, k_z, \theta, \Phi$ [91, 78]. To this end, we eliminate Φ by identifying the value ν_{max}

where the corrected phase data is maximized and normalizing the two data sets by $I_{IP}^m(\nu_{max})$. The model to fit then becomes

$$\hat{f}_1(v_x) = f_1(v_x) / f_1(v_{max}), \quad (4.25)$$

where v_{max} is related to ν_{max} through Eq. 4.9. Next, we employ the electrostatic dispersion relation Eq. 3.85 to determine k_z as a function of the perpendicular wave parameter k_\perp . This leaves only two free parameters, k_\perp and θ , to fit our experimentally measured data.

With this in mind, we show as solid lines in Fig. 4.21 theoretical fits to the measured in-phase and quadrature components of the ion kinetic response to a wave with frequency 40 kHz that we excited in BWX II's locally isotropic ($T_{i\perp} = T_{i\parallel}$) plasma with ion temperature, $T_i = 0.25$ eV, electron temperature, $T_e = 3.5$ eV, and parallel drift velocity, $v_{di} = 100$ m/s. The data in these plots is comprised of sixty points from a thirty second scan performed with the LIF system. The best fit lines were found through a χ^2 analysis of Eq. 4.16 applied to the data [89] in which we numerically calculate χ^2 and plot the inverse quantity $1/\chi^2$ as a function of the free parameters, θ and k_\perp (Fig. 4.22). The best fit parameters correspond to the maximum value while we gauge the uncertainty as the full width half max (FWHM) of this fit [91].

Employing this method, we were able to determine non-invasively the wave vector and angle of propagation of the waves. The wave amplitudes in turn were calculated [91, 78] by considering the linearized Boltzmann relation for low frequency electrostatic waves

$$\frac{n_1}{n_0} = \frac{q\Phi}{T_e}. \quad (4.26)$$

Since intensity measurements exhibit the same scaling constant α_c , we calculated the ratio of densities by dividing the integral of the intensity profile we measured from

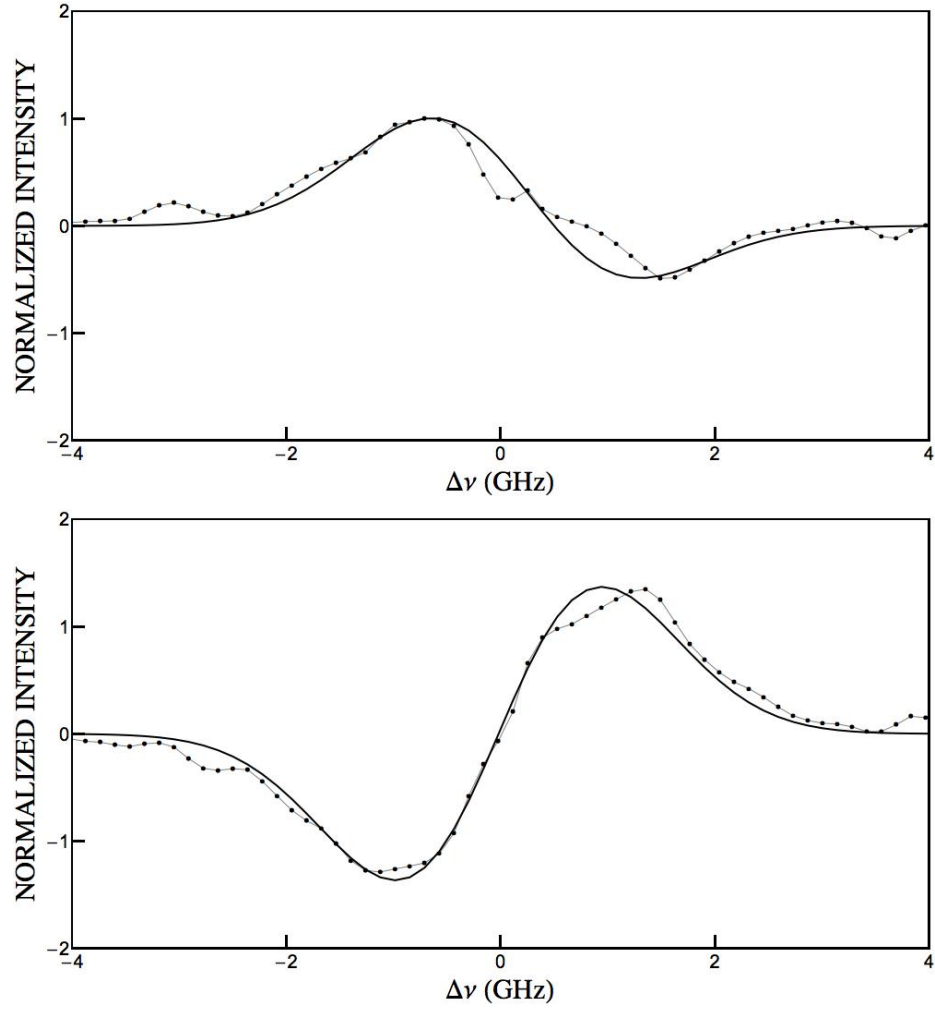


Figure 4.21: In phase (top) and quadrature (bottom) measurements for the ion kinetic response to an electrostatic wave at 40 kHz. The solid lines are theoretical fits from Eq. 4.16. $T_i = 0.25$ eV; $T_e = 3.5$ eV; $v_{di} = 100$ m/s.

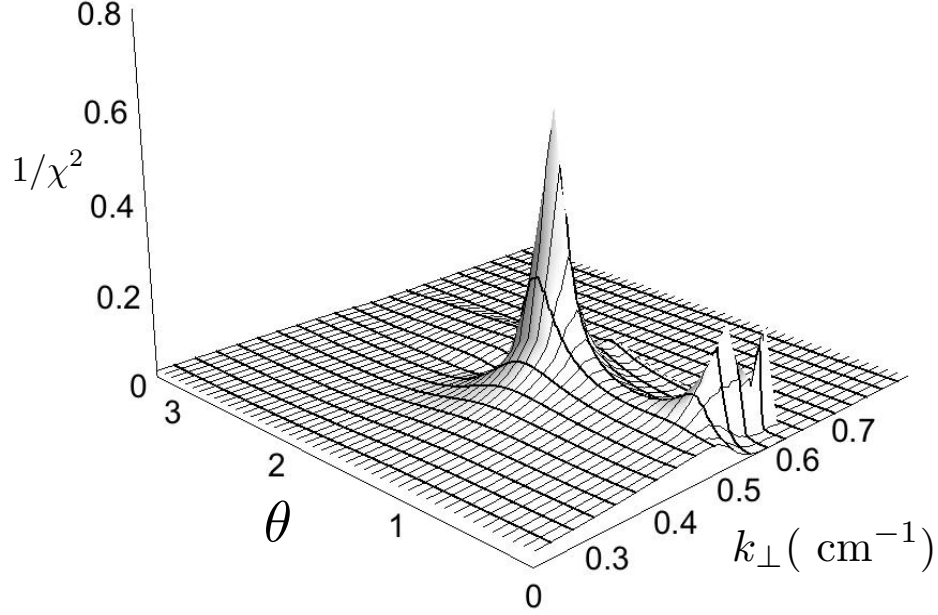


Figure 4.22: Inverse χ^2 plot for Eq. 4.16 as applied to the data in Fig. 4.21.

the waves to the integral of the intensity profile of the steady state distribution:

$$\frac{n_1}{n_0} = \frac{\sqrt{[\int I_{IP}(\nu) d\nu]^2 + [\int I_Q(\nu) d\nu]^2}}{|\int I_M(\nu) d\nu|}. \quad (4.27)$$

Substituting this relation into Eq. 4.26, we thus were able to infer the wave potential amplitude.

We note here that while the formalism is present in our analysis to allow for weak collisionality by introducing a third free parameter ν_c such that $\omega \rightarrow \omega + i\nu_c$, the error in our fits was sufficiently small that we chose to neglect these effects. Also, while we assumed only a single wave was present in the plasma for the fitting procedure outlined above, the same relations still can be employed when two waves are present by setting the reference frequency, f_1 or f_2 , of the LIA to the mode of interest.

4.6 Conclusion

We have outlined the experimental setup in this chapter for our systematic investigation of the BEW effect. We have described the framework of the system, identified the typical plasma parameters, and determined the local point where the assumptions for our analytical models are valid. In addition, we have presented the two major diagnostics of BWX II—a double Langmuir probe array and a laser induced fluorescence system. In the next chapter, we describe how we applied these diagnostics along with the procedures outlined above in an effort to examine the analytically predicted trends we identified in Chapters 2 and 3.

Chapter 5

Experimental results and analysis

The goal of this chapter is to investigate experimentally SEWH and BEWH in the BWX II plasma. To this end, we examine the two processes over the entire range of available input energy densities for our system and interpret the results in the context of our analytical predictions for power absorption and the onset of heating. In the first section, we establish the baseline for the investigation by reporting the measured dispersion relation of the electrostatic modes launched in the plasma and the measured SEW heating as a function of frequency. In the second section, we explore the onset of heating for SEWH and BEWH as a function of wave amplitude and energy density. In the third and final section, we examine the regime of higher energy density where heating has onset by comparing the increase in ion temperature produced by SEWH and BEWH.

5.1 SEW results

5.1.1 Dispersion relation

Using the prescription in Sec. 4.5.2 for employing LIF to perform wave measurements, we generated the dispersion relation shown in Fig. 5.1 for the electrostatic modes in

the plasma. These measurements were made at $r = 3$ cm where the plasma properties were observed to be approximately uniform and isotropic with ion temperature $T_i = 0.25$ eV, electron temperature $T_e = 3.5$ eV, and parallel ion drift velocity, $v_{di} = 100$ m/s. The input power to the antenna was 100 W for the reported values.

The near acoustic relationship in Fig. 5.1 with a cutoff at the cyclotron frequency suggests that the propagating mode is the electrostatic ion cyclotron wave (EICW). Indeed, while two modes exist in this low frequency regime [13]—the forward-propagating EICW and the backward-propagating neutralized ion Bernstein wave (NIBW)—the EICW is less susceptible to the charge-exchange collisions characteristic of the low temperature BWX II plasma [24]. It thus is not surprising the EICW is the observed mode. From our LIF wave measurements, we also have plotted in Fig. 5.2 the angle θ the perpendicular component of the vector makes with respect to the direction perpendicular to the laser beam and magnetic field, i.e. \hat{y} in the formalism of Chapters 2 and 3. This plot suggests that for $f \geq 2f_{ci}$, the transverse component of the wave vector is oriented normal to the antenna loop. Coupled with the observation that the antenna cross-section presented to the plasma is large, we use this angle of propagation to assert that the modes are approximately planar at the local point of observation. This facilitates a comparison of theory with the analytical model.

5.1.2 Frequency dependence of heating

In order to inform our decision as to what frequency set f_1, f_2 to employ for our comparison of the SEWH and BEWH processes, we first performed a parametric analysis of the frequency dependence of ion heating with a single electrostatic mode. To this end, we input 300 W into the VDWL system at each frequency and recorded the increase in perpendicular ion temperature over background at $r = 3$ cm. The resulting plot is shown in Fig. 5.3. As we can see, there is a clear dependence of the ion temperature on the frequency with an optimum at the second harmonic $\omega = 2\Omega_i$.

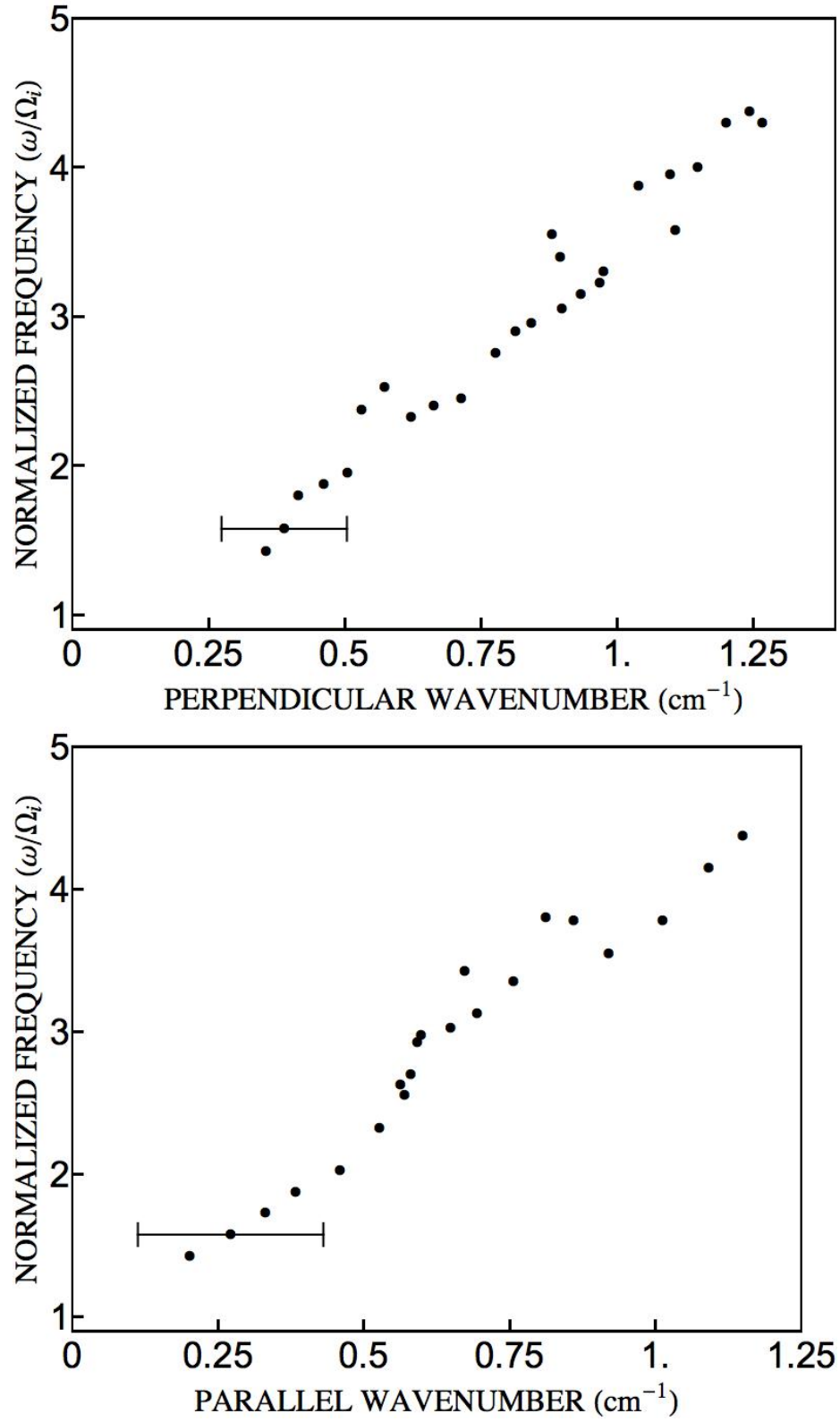


Figure 5.1: Experimentally determined dispersion relation for the perpendicular (top) and parallel (bottom) components of the wavevector. A representative error bar is also shown.

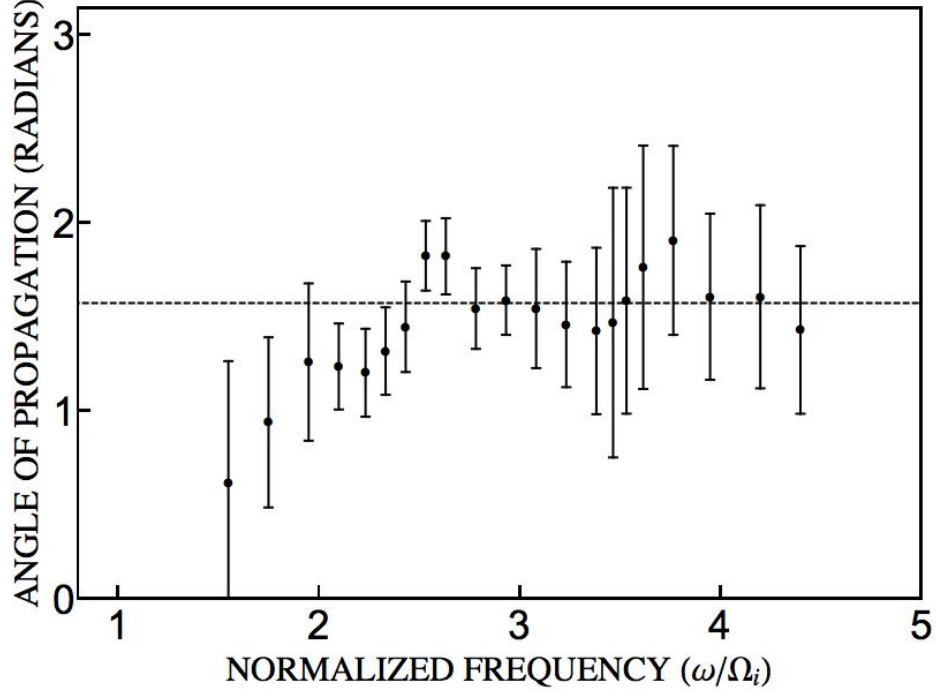


Figure 5.2: Plot of the angle of propagation as a function of wave frequency. The dotted line corresponds to $\theta = \pi/2$ where the direction of propagating is normal to the antenna.

This optimum lends support to the notion that the SEWH heating primarily results from ion cyclotron harmonic damping since this process exhibits maximal heating at a cyclotron harmonic. We note that there is no peak at the fundamental frequency as the dispersion relation experiences a cutoff at this value.

In light of the results from Fig. 5.3, we chose to employ the frequency combination $f_1 = 2f_{ci}$ and $f_2 = 3f_{ci}$ for our parametric comparison of BEWH and SEWH. The reasoning for this is two fold. First, the larger magnitude of heating allows us to more easily distinguish increases in ion temperature over background. This is particularly important in the next section where we identify the threshold value for the onset of heating. Second, since one of the goals of this chapter is to establish experimentally if BEWH can improve upon SEWH, we set the standard as high as possible by using the best heating results from SEWH as the baseline for comparison.

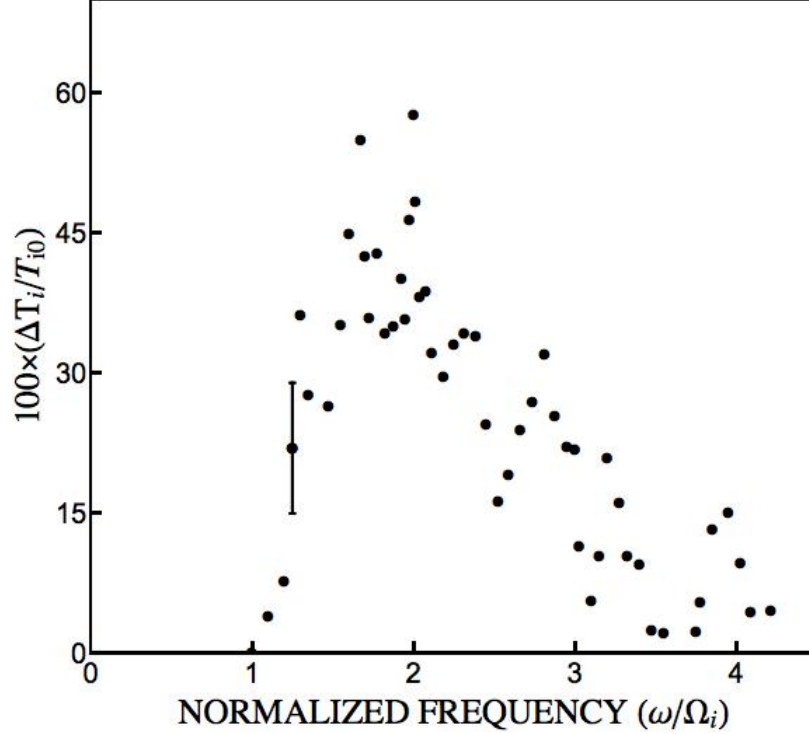


Figure 5.3: The maximum change in perpendicular ion temperature achieved at each frequency for the SEW case. A representative error bar is shown as well.

5.2 BEW heating onset

In order to identify experimentally the onset of heating, it is necessary to develop a metric for when the increase in ion temperature first occurs above background. With this in mind, for our parametric investigation of BEW and SEW we coupled two waves into the plasma at frequencies $f_1 = 2f_{ci}$, $f_2 = 3f_{ci}$ and monitored the increase in temperature T_i as a function of the current, I_1, I_2 , delivered to the antenna at each frequency. Three representative data sets are shown in Fig. 5.4 where each trend corresponds to a different fixed value of I_2 . It is evident from these plots, similar to those reported in Refs. [49, 48], that there is a threshold value where a jump in temperature above background occurs. This is followed by a rapid temperature increase with antenna current that ultimately gives way to saturation for sufficiently large values—a result that likely stems from self-consistent effects in the plasma preventing further energy exchange of the mode with the ions. As is intuitively expected from Chapter

2's discussion, we can see from Fig 5.4 that the threshold value I_1 decreases with larger values of I_2 .

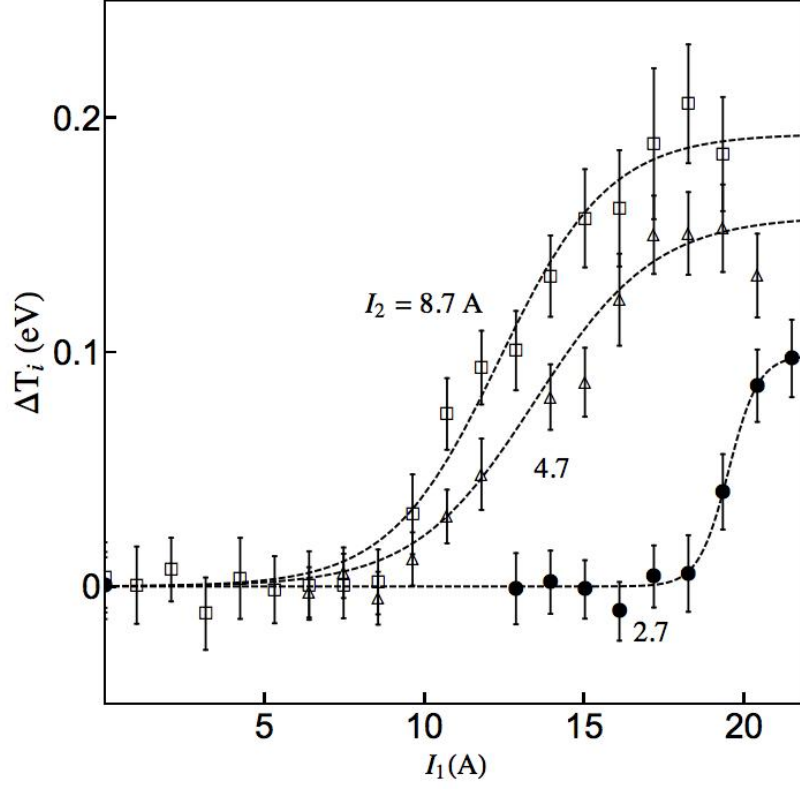


Figure 5.4: Change in ion temperature as a function of antenna current I_1 to the lower frequency mode. Each data set corresponds to a case where the antenna current at the second frequency I_2 is constant. The dotted lines are best fits from Eq. 5.1, a phenomenological model for the heating.

In order to quantify the value where the onset of heating occurs, we numerically applied the following phenomenological trend to the increase in temperature over background:

$$\Delta T_i = T_i - T_{i0} = \Delta T_s (\tanh [AI_1 + I_0] + 1), \quad (5.1)$$

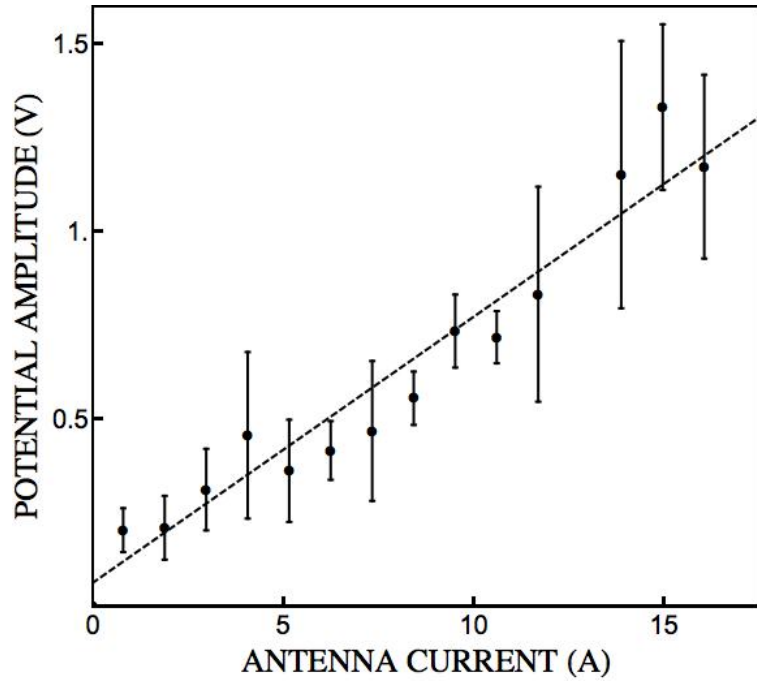
where ΔT_s , A , and I_0 are free parameters. We subsequently identified the threshold for heating as the current value where according to Eq. 5.1 the temperature is 10% of the saturated value, i.e. where $(T_i - T_{i0}) / \Delta T_s = 0.1$. This is an appropriate metric

as it accounts for the fact that the magnitude of temperature increase—once heating has onset—is also heavily dependent on the antenna current. In order to relate this measured current to wave potential amplitude, we generated the calibration curves shown in Fig. 5.5. These relationships are linear, and we observed the same linear relationship even for the case where the other mode was also present in the plasma.

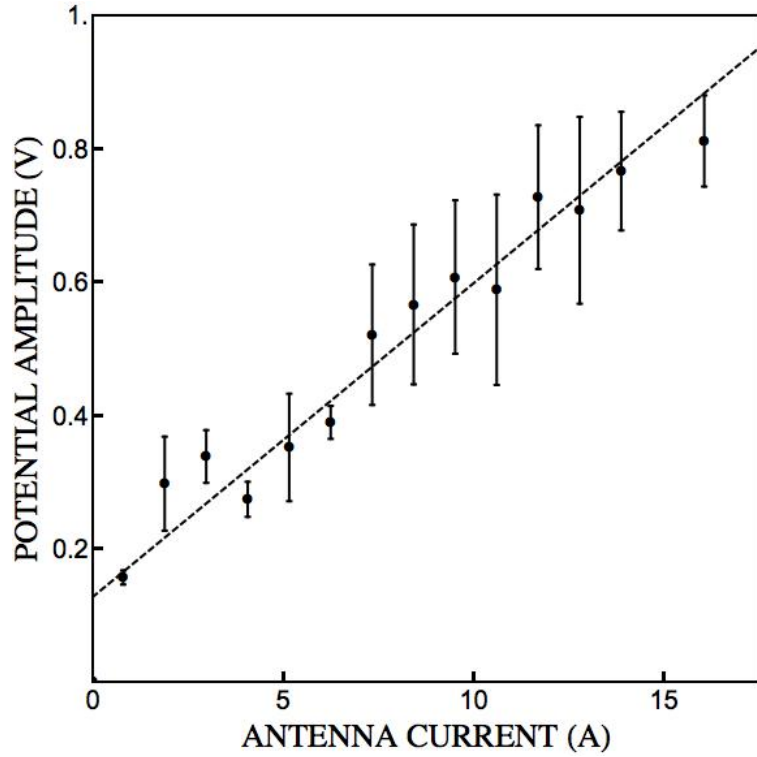
Using the 10% metric as the criterion for heating onset, we show in Fig. 5.6 the threshold value as a function of the potential amplitudes Φ_1, Φ_2 where the error in these plots reflects the uncertainty in relating the current to the measured wave amplitudes. As we have assumed that the threshold for heating is correlated with the appearance of stochasticity in ion orbits, the linearity of this data confirms two characteristics for the onset of stochasticity we found in Chapter 2. First, the requisite amplitudes for producing stochasticity is lower than that for SEW heating with individual waves, i.e. where $\Phi_1 \rightarrow 0$ or $\Phi_2 \rightarrow 0$. Second, the linearity suggests that the onset of heating can be achieved for a lower total energy density than in the SEW case. We can confirm this second observation explicitly by estimating the total energy density in the system and comparing it to the onset condition for SEW. To this end, we take the formula for the energy density for the acoustic-like mode observed in BWX II to be [10]

$$W_j = \epsilon_0 \frac{\omega_j}{4} \Phi_j^2 \frac{\partial}{\partial \omega_j} D(\omega_j, \mathbf{k}_j). \quad (5.2)$$

Employing the dispersion relation for the electrostatic modes given by Eq. 3.85 and our observed amplitudes in Fig. 5.6, we use this expression to show in Fig. 5.7 the total energy density required for heating onset in the BEW case, $W_1 + W_2 = W_{BEW}$, where the error bars stem from uncertainty both in the wave amplitudes and wave vectors. In this plot, the energy densities have been normalized by the required energy density $W_{1(SEW)}$ for onset with a SEW at f_1 (the same parameter as W_T^* from Sec. 3.6). For the independent variable, we use $\eta = W_1/W_{BEW}$, i.e. the fraction of the total BEW power in the first mode.



(a) $f = 40$ kHz, $k_{\perp} = 60$ m⁻¹, and $k_{\parallel} = 43$ m⁻¹



(b) $f = 60$ kHz, $k_{\perp} = 85$ m⁻¹, and $k_{\parallel} = 56$ m⁻¹.

Figure 5.5: Linear relationship between potential amplitude and antenna current for each of the BEW. The dashed line is a best fit regression.

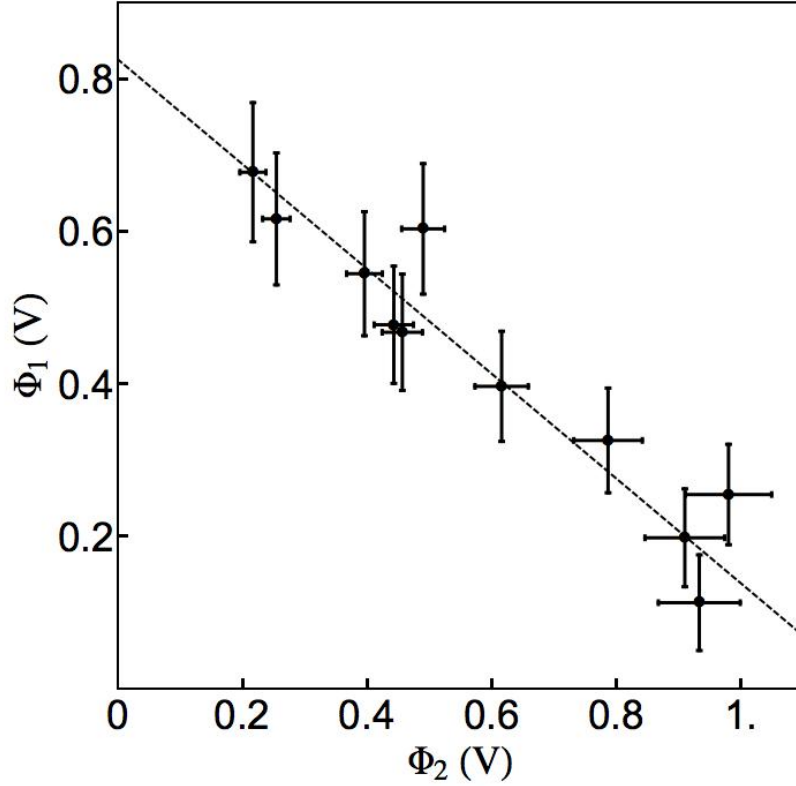


Figure 5.6: Potential amplitudes of the two waves where the threshold for ion heating is observed to occur. The dotted line is a best fit linear trend.

From Fig 5.7, it is evident that there exists a range of wave parameters $\eta \in (0.25, 1)$ where the threshold for the onset of heating is lower than that exhibited by either SEW case ($\eta = 0, 1$). This result confirms our earlier statement and theoretical prediction that BEWH is a more efficient process than SEWH for low energy density.

The results from Figs. 5.6 and 5.7 thus lend support to our conclusions from Chapter 2, and we now are in a position to explicitly compare these results with the analytical predictions. To this end, we restate from Eq. 2.32 that the threshold for BEW stochastic acceleration for an ion with initial velocity v_\perp, v_z is given in physical coordinates by

$$\alpha = \frac{\omega_1 - k_z v_z}{\Omega_i B_0 v_\perp} k_{1x} \left(\Phi_1 |H_{\mu_1}^{(1)'}(z_1)| + \Phi_2 |H_{\mu_2}^{(1)'}(z_2)| \right), \quad (5.3)$$

where $H_{\mu_j}^{(1)}$ is the Hankel function of the first kind, B_0 denotes the background mag-

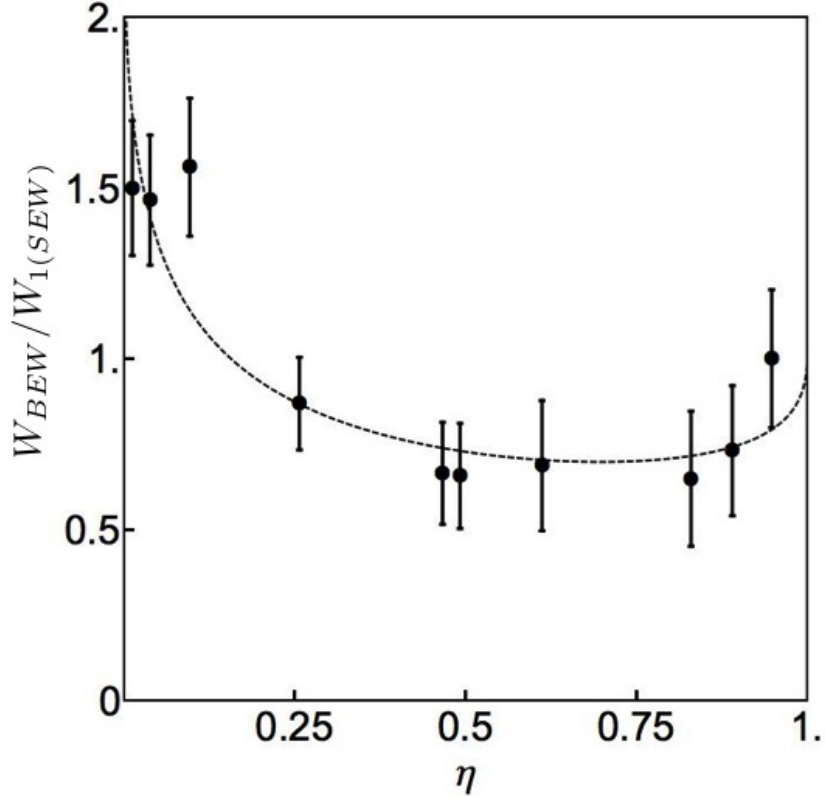


Figure 5.7: Calculated total energy density where the threshold for ion heating is observed to occur as a function of the fraction of energy density in the first mode $\eta = W_1/W_{BEW}$. The energy density is normalized by the total energy density required for stochastic heating by a single mode at the lower frequency, f_1 . The dotted line represents a best fit according to model Eq. 5.6

netic field magnitude, $\mu_j = (\omega_j - k_z v_z) / \Omega_i$, and $z_j = k_{jx} v_\perp / \Omega_i$. This relationship was shown to be valid under the assumption that the perpendicular components of the two modes k_{1x}, k_{2x} are collinear and that the parallel components satisfy $k_{1z} \approx k_{2z}$. Both of these assumptions, as can be seen from the dispersion relation in Fig. 5.1 and the angles in Fig. 5.2 are approximately valid for the two modes at $\omega_1 = 2\Omega_i$ and $\omega_2 = 3\Omega_i$. Similarly, since $\omega_1/k_{1z}/\bar{v}_z > 4$ where $\bar{v}_z = (2T_i/m_i)^{1/2}$ for our experimental configuration, we further make the simplifying assumption $\mu_j \approx \omega_j/\Omega_i$. Coupled with the fact that $\omega_1/k_{1x} \approx \omega_2/k_{2x}$ for our two modes, this approximation allows us to use

Eq. 2.22, the reduced form of Eq. 2.20 in estimating the onset of stochasticity:

$$\alpha = \frac{k_{1x}^2}{\omega_1 B_0} \left[\Phi_1 \left(\frac{\omega_1}{\Omega_i} \right)^{1/3} + \Phi_2 \left(\frac{\omega_2}{\Omega_i} \right)^{1/3} \right]. \quad (5.4)$$

In order to compare this to the results from Fig. 5.6, we solve for Φ_1 as a function of Φ_2 to find

$$\Phi_1 = -\Phi_2 \left[\frac{\omega_2}{\omega_1} \right]^{1/3} + \frac{\alpha B_0 \omega_1}{k_{1x}^2} \left(\frac{\Omega_i}{\omega_1} \right)^{1/3}. \quad (5.5)$$

Substituting in for the wavenumbers k_{1x}, k_{2x} as well as the average value $\alpha = 0.17 \pm 0.1$ from Chapter 2, we find the coefficients for the linear trend in Eq. 5.5. These results are listed in Table 5.1 with uncertainties that stem from the errors in the wavenumbers and α . For comparison, we include the coefficients for the best fit linear trend to the experimental data shown in Fig. 5.6.

$$\Phi_1 = a\Phi_2 + b$$

| | a | b |
|--------------|------|--------------|
| Analytical | -1.1 | $1. \pm 0.4$ |
| Experimental | -0.7 | 0.8 |

Table 5.1: Analytical (from Eq. 5.5) and experimental coefficients for the linear trend shown in Fig. 5.6.

In spite of the assumptions we have made to place Eq. 5.5 in its simplified form, we can see that the observed values correspond closely to the predicted coefficients. The relative agreement of the analytically predicted trends thus lends experimental weight to our theoretical analysis from Chapter 2 and supports the notion that the beat effect is an important contributing factor to the onset of stochasticity in this case.

The experimental agreement theory extends to our energy density analysis as well. We can see this by inverting the first equation in Eq. 2.26 to find

$$\frac{W_{BEW}}{W_{1(SEW)}} = \left[\sqrt{\eta} + \gamma \sqrt{1 - \eta} \right]^{-2}, \quad (5.6)$$

where under the same the same assumptions we employed to derive Eq. 5.5, γ is given by

$$\gamma = \left(\frac{\omega_2}{\omega_1}\right)^{1/3} \left(\frac{\beta_1}{\beta_2}\right)^{1/2} \quad (5.7)$$

with $\beta_j = W_j/\Phi_j^2$. From our experimental values, we use this relation to find the theoretical value $\gamma = 0.91 \pm 0.3$. We then fit Eq. 5.6 to the data in Fig. 5.7 to yield the dotted line shown and the coefficient $\gamma = 0.64$. Once again, we find the model and experimental data agree to within error bars, which lends support to the theoretical predictions from Chapter 2.

In sum, we have showed experimentally in the low energy density regime that the threshold for the onset of stochasticity is linear with respect to the perturbation amplitudes for the case of two obliquely-propagating electrostatic modes that satisfy the beat criterion. The BEW waves further were shown to exhibit a lower requisite total energy density to produce stochasticity than SEW propagating modes at the same frequencies. We compared our experimental results to analytically predicted trends and found a reasonable agreement. This correspondence suggests that the BEW effect is indeed a contributor to the observed dependence of the stochastic threshold on wave amplitude.

5.3 BEW power absorption after onset

In order to investigate the power absorption of BEWH and SEWH, we assume that the temperature values we report represent an equilibrium between losses in the plasma and the power absorption. Higher power absorption rates therefore correspond to higher equilibrium temperatures. In addition, we assume that the dominant contributor to ion heating is direct power absorption from the wave. It is possible, for example, that electrons absorb the wave energy and then in turn deliver this energy to the ions. However, during our heating measurements, increases to the electron

temperature as monitored in near real time by the double probe array were small. Similarly, the analytically predicted ion cyclotron absorption from electrons due to the waves is a factor of 15 less than the predicted absorption for ions. We arrived at this ratio by comparing the electron absorption term (derived from the ion terms in Chapter 3 with the appropriate transformation to physical coordinates) to the ion absorption term.

Assuming then that the ions absorb the wave energy, we used the calibration curves from Fig. 5.5 in conjunction with a parametric set of current traces such as those reported in Fig. 5.4 to determine the ion temperature as a function of potential amplitudes Φ_1, Φ_2 in each mode. We then employed the canonical definition of energy density in Eq. 5.2 with the dispersion relation in Fig. 5.1 to convert these wave potentials to energy density. Following this technique, we show in Fig. 5.8 the percentage increase in ion temperature over background as a function of the fraction η of the total wave energy density in the first mode. Each curve corresponds to a different value of total energy density that has been normalized by the analytically predicted value where BEWH superiority is anticipated, \overline{W}_T (see Eq. 3.93). We similarly ensure that for each curve heating has onset for all values of η such that we are above the energy density regime discussed in the previous section. The top curve represents the maximum available energy density we could impart into the plasma with our current configuration. The cases where $\eta = 0, 1$ correspond to SEW heating.

From these results, we identify two classes of behavior. First, for intermediate values of total wave energy density, $0 < W_T/\overline{W}_T < 0.1$, the relationship of heating efficiency with fraction of energy is approximately linear—increasing from $\eta = 0$ to a maximum at $\eta = 1$. This trend reflects the fact that greater absorption occurs for the lower frequency wave ω_1 . Second, for higher values of wave energy density $W_T/\overline{W}_T > 0.1$, the plotted profile changes until it is almost uniform for all fractional combinations of wave energy densities.

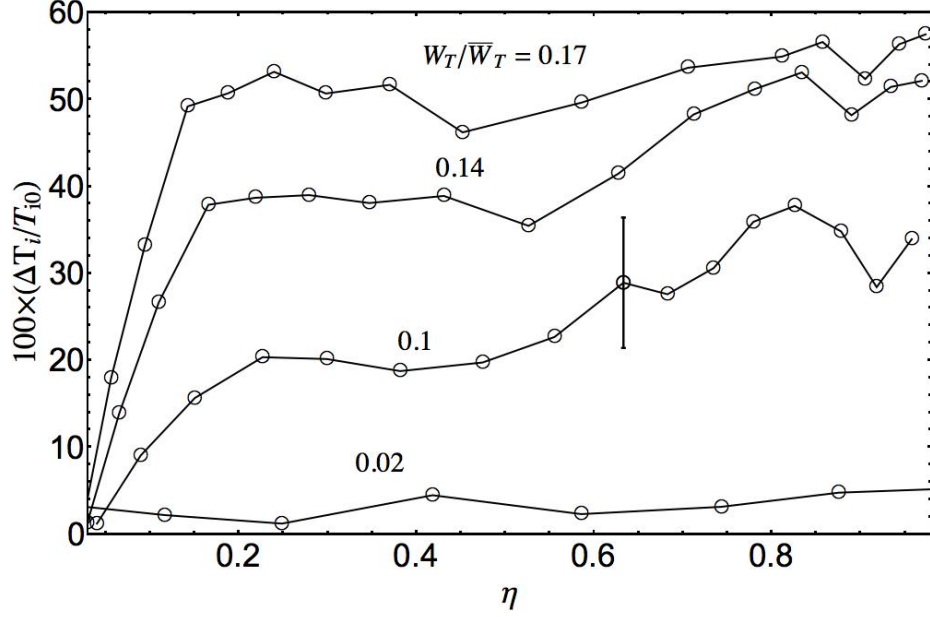


Figure 5.8: Fractional increase in ion temperature as a function of the fraction of total energy density in the first mode at ω_1 . Each curve represents a case where the total wave energy density W_T is constant.

The first trend is consistent with our analytical understanding of the BEWH process in the case where the condition for BEWH superiority has not been achieved, $W_T < \bar{W}_T$. In this event, the SEW terms dominate in Eq. 3.91 such that we anticipate a linear relationship between power absorption (heating efficiency) and the fraction of energy density. Indeed, we can see that this equation also predicts the increase in slope of this linear relationship with total wave energy density.

There are two possible explanations for the second observed trend with increasing input energy density. The first is that the input energy approaches the limit $W_T = \bar{W}_T$, in which case this plateau is a precursor to the emergence of an optimal frequency $\eta \in (0, 1)$ such that BEW is the superior process. However, our maximum available energy density is well below the analytically predicted threshold for the superiority of BEWH, and even if this threshold value is overestimated, pursuant to Eq. 3.92 with our experimental values for β_j and α_j , we would anticipate that the BEW optimum first appear with increasing input energy density near $\eta = 1$. This is not consistent

with the asymptotic approach to the plateau exhibited in Fig. 5.8.

On the other hand, this observed plateau could be the result of saturation effects. This is a strong possibility since we already have noted from Fig. 5.4 that saturation does occur for each combination of input current. Moreover, if we still fall in the regime where SEW is dominant ($W_T < \overline{W}_T$), we can understand the profile shown in Fig. 5.8 exclusively in terms of the independent single wave absorption of the propagating modes (the α_j terms in Eq. 3.91). To see how this is the case, we note that if the power delivered to the plasma is the result of two, independent SEW interactions, we would anticipate from our parametric analysis that the temperature should asymptote first at the SEW conditions, i.e. $\eta = 0, 1$. As the total power increases, however, each wave mode can contribute its saturated value to the total power absorption at intermediate values of $\eta \in (0, 1)$. For sufficiently large total energy density, this effect will lead to the same saturated power being delivered to the plasma for all BEW combinations. With the same input power and the same plasma losses, we correspondingly would anticipate a uniform plateau in temperature increase with sharp drops at $\eta = 0, 1$. Such a precipitous drop does appear to begin to form near $\eta = 0$ in Fig. 5.8. There is no equivalent drop at $\eta = 1$, though this could result from our inability to achieve an energy density sufficiently large for the saturation effects from ω_2 to contribute significantly to heating at larger values of η . The nascent plateau therefore still could be consistent with a saturation effect on the individual waves. Thus while we can conclude that for $W_T/\overline{W}_T \ll 1$, our results are consistent with the energy density regime we identified in Chapter 3 ($W_T^* < W_T < \overline{W}_T$) where we anticipate SEWH to be dominant, due to limitations in available energy density as well as unanticipated saturation effects, we cannot draw any experimental conclusions about the regime $W_T > \overline{W}_T$.

We should note that our results contradict previously reported investigations of BEWH versus SEWH heating in a plasma similar to the configuration reported here

[24, 94]. In these studies, there was an effort made to control for the same total power to the antenna in both the SEWH and BEWH cases; however, the energy density of the modes propagating in the plasma was not directly measured. The coupling to the plasma from the individual waves thus was not taken into the account—rendering the assumption of equal wave energy density invalid. For example, in the case of BEWH, it is possible that the second introduced mode couples to the plasma more efficiently by virtue of its higher frequency and longer parallel wavenumber. In this event, the total energy introduced into the plasma would be greater than the SEWH case—even though the input power from the wave amplifier to the antenna is the same. It also should be pointed out that these previous investigations examined only a small range of input power values and did not parametrically explore the effect of fractional content of each mode. Our results presented here are more general.

5.4 Chapter summary

In this chapter, we have compared SEWH to BEWH over the range of available input energy densities from the VDWL system in BWX II. By using the optimal SEWH case to inform our choice of BEW frequencies, we have been able to explore two of the predicted regimes from Table 1 in Chapter 3. This has yielded the following conclusions:

- For $W_0 < W_T < W_T^*$ where W_T^* denotes the lower SEW threshold for the onset of heating, we have confirmed experimentally that BEWH is the superior process. The close fit of our experimental results with the model lends support to our interpretation that the ability of BEW to facilitate the onset of stochasticity in this regime leads to the onset of heating at lower energy density values.
- For $W_T^* < W_T < \overline{W}_T$, we have examined the lower energy density part of this regime and confirmed that SEWH is the superior process. The qualitative agree-

ment of ion temperature with our model for power absorption lends credibility to our analysis.

- At higher values of W_T , saturation effects in concert with a limited availability in the VDWL system have prevented a thorough investigation of the threshold value \overline{W}_T . The saturation effects are particularly important as they occur for values of $W_T/\overline{W}_T \ll 1$. This suggests that saturation may prevent us from observing the transition to the regime of BEWH superiority—even if we could access higher energy levels with our system.

Chapter 6

Conclusions

In this dissertation, we have presented an investigation into plasma heating with beating electrostatic waves—a nonlinear process that by virtue of its ability to energize low energy ions has potential applications in a number of different plasma processes. While a number of investigations have focussed on characterizing the BEW process and contrasting its unique properties to the energization produced by a traditional, single electrostatic wave [14, 15, 19, 16, 20, 17, 21, 22, 23, 24, 25], there is still a need to compare the two processes systematically when applied to heating an ion ensemble. In this dissertation, we have addressed this shortcoming through an analytical, numerical, and experimental investigation with the specific goals in mind of

- Deriving the condition for the onset of heating for both SEWH and BEWH as a function of wave amplitude and input energy density.
- Comparing the power absorbed by ions subject to both processes SEWH and BEWH once the onset of heating has occurred.
- Analytically deriving criteria for when one process is preferred over another.
- Performing an experimental investigation to explore our analytical conclusions.

6.1 Summary of major findings

6.1.1 Analytical findings

In our analytical treatment of the BEWH and SEWH problem, we have identified three regimes of input energy density where the relative performance of SEWH and BEWH differ. For low input wave energy densities, the BEWH process leads to the onset of ion heating at lower input values than the SEWH process. This is because the formation of stochasticity in particle orbits depends on the development of resonances between the ion orbits and the propagating wave frequencies. For the case of SEW, the formation of these resonances requires significant finite-amplitude perturbations to the precession frequency of the ion, while for BEW where $\omega_2 - \omega_1 = \Omega_i$, there is already a natural resonance between the beat frequency of the waves and the ion motion. Resonances therefore occur at significantly lower values of wave amplitude, which in turn translates to a lower input energy density necessary for the BEW to achieve stochastic onset.

Once phase space has become stochastic, however, we have showed that there is an intermediate regime of input energy density where the SEWH leads to higher power absorption than the case of BEWH. This is because the amplitude of the virtual beat mode at $\Delta\omega$ and $\Delta\mathbf{k}$ driven by the two BEW is itself second-order—suggesting that the diffusion resulting from this mode is fourth order. The SEWH process, on the other hand, as per traditional ion cyclotron damping is second order in amplitude. We thus find that at intermediate energy densities, the SEWH process is dominant.

Finally, for sufficiently high energy densities, we have showed that the BEWH process once again becomes superior to SEWH. The threshold value for when this occurs depends both on the plasma parameters and the wave parameters of the BEW.

6.1.2 Experimental findings

With the BWX II and the associated diagnostics, we have performed a systematic comparison between SEWH and BEWH. In contrast to the previous experimental investigation into BEWH [24], we were able both to identify the optimal frequency combination for comparing the two processes as well as perform a full parametric analysis as a function of the fraction of input energy density into each mode.

Employing electrostatic ion cyclotron waves in a collisional plasma, we have found direct confirmation for our collisionless, analytical prediction that the onset of BEWH does occur at lower energy density levels than SEWH. Our analytical work also accurately predicted the trends exhibited by the experimental data, which lends further support to the notion that the onset of heating is linked to the onset of stochastic particle orbits.

At an intermediate energy density range where heating has onset for both BEWH and SEWH processes, we have found trends that are consistent with an input energy density that is below the threshold for the superiority of BEWH. Most notably, we confirmed experimentally that SEWH was the superior process. The onset of saturation effects—likely due to loss processes as well as trapping effects—in concert with an upper bound on the available energy density in our experiment, however, prevented us from exploring the high energy density regime where BEWH is predicted to be the superior process.

6.2 Recommendations for future work

Our systematic treatment of the problem has provided new insight into this BEW plasma heating process, yet there are a number of questions that remain. From the analytical perspective, one of the most significant questions concerns the role of collisions as a loss process in the plasma. Indeed, while collisions can be folded

into our assumptions of a randomizing element to justify the phase-averaged power absorption description we have employed in this work, they also are an important loss mechanism for the power introduced by the waves. This loss in conjunction with other processes in the plasma must be modeled in order to accurately estimate changes in ion temperature. A full kinetic, numerical simulation [95, 50] could achieve this end by providing insight into how collisions impact energy transport. Such a model also could shed light on the saturation processes that were beyond the scope of our power absorption model. In that same vein, the framework is in place from our above discussion in conjunction with previous nonlinear models [15, 19] to develop a kinetic wave equation for the spatial damping of the BEW in the plasma. Combined with a numerical model, this description for wave damping would be useful for optimizing BEW coupling to the plasma.

Experimentally, in order to explore the last regime of high energy density we identified, it is necessary to introduce more power to the plasma while minimizing saturation effects. A different antenna geometry may facilitate this. Indeed, while we employed in our setup a simple strap antenna located outside the vacuum vessel, with the optimized VDWL system it may be possible to employ a capacitive antenna inside the plasma (as was done by Spektor [24]) sufficiently separated from the heating zone that the antenna is non perturbative in the region of temperature measurements. Through its direct contact with the plasma, this configuration might couple more strongly to electrostatic modes. Additionally, with higher wave energy, higher heating levels are possible such that it would be possible to explore frequency combinations that we neglected in this investigation due to the low observed heating levels.

Finally, with our improved understanding of the BEW mechanism, we can start to turn our attention to real applications of this two-wave process. In particular, we have outlined in previous reports [5, 6, 96] two plasma propulsion concepts that depend on the efficient power absorption facilitated by BEW. These thruster ideas

merit further attention—both from a modeling and experimental perspective— in light of the results we have presented in this work.

Appendix A

Derivation of the Hamiltonian

Here we derive the Hamiltonians employed in Chapters 2 and 3. This treatment follows the action-angle formulation first outlined by Karney [12] and expanded upon in detail by Spektor [24].

A.1 Single particle Hamiltonian

The equation of motion for an ion subject to two, perpendicularly-propagating electrostatic waves in a uniform magnetic field is given by [22]

$$m_i \frac{d^2 \mathbf{x}}{dt^2} = q \sum_{j=1}^2 \Phi_j k_{jx} \sin(k_{jx}x - \omega_j t + \alpha_j) + q \mathbf{v} \times \mathbf{B}, \quad (\text{A.1})$$

where m_i denotes the ion mass, q is the charge, Φ_j is the potential amplitude, k_{jx} is the wave vector where we have denoted the direction of propagation as \hat{x} , ω_j is the wave frequency, $\mathbf{B}_0 = B_0 \hat{z}$ denotes the background magnetic field, and α_j is the phase of the wave.

We denote the kinetic energy and potential energy for this system as

$$\begin{aligned} T &= \frac{m_i}{2} (\dot{x}^2 + \dot{y}^2) \\ U &= q (\Phi - \mathbf{v} \cdot \mathbf{A}), \end{aligned} \quad (\text{A.2})$$

where we have defined $\Phi = \sum_j \Phi_j \cos(k_{jx}x - \omega_j t + \varphi_j)$ and the magnetic vector

potential $\mathbf{B} = \nabla \times \mathbf{A}$. Letting $\mathbf{A} = xB_0\hat{y}$ and recognizing that the Lagrangian is given by $L = T - U$, we can express the dynamical system in a Hamiltonian formulation [46]:

$$h = \frac{1}{2} ([p_y - qx B_0]^2 + p_x^2) + q \sum_{j=1,2} \Phi_j \cos(k_{jx}x - \omega_j t + \alpha_j), \quad (\text{A.3})$$

where $p_y = m_i \dot{x} + qx B_0$ and $p_x = m_i \dot{x}$. We normalize this expression such that

$$\bar{H} = \frac{1}{2m_i} ([P_Y - X]^2 + P_X^2) + \sum_{j=1,2} \varepsilon_j \cos(\kappa_j X - \nu_j \tau + \alpha_j), \quad (\text{A.4})$$

where we have defined

$$\begin{aligned} \tau &= \Omega_i t & \nu_j &= \omega_j / \Omega_i & \kappa_j &= k_{jx} / k_{1x} & X &= k_{1x} x \\ P_X &= \frac{k_{1x}}{m_i \Omega_i} p_x & P_Y &= \frac{k_{1x}}{m_i \Omega_i} p_y & \varepsilon_j &= (q k_{1x}^2 \Phi_j / m_i \Omega_i^2) & \bar{H} &= \frac{k_{1x}^2}{\Omega_i^2 m_i} h. \end{aligned} \quad (\text{A.5})$$

Now, in order to transform this to an action-angle formulation, we employ a generating function of the first kind [46] with $F_1(X, Y, \theta_1, \theta_2) = 1/2 (X - \theta_2)^2 \cot \theta_1 + Y \theta_2$. This yields the Hamiltonian:

$$H = I_1 + \sum_{j=1,2} \varepsilon_j \cos(\kappa_j \sqrt{2I_1} \sin \theta_1 + \kappa_j \theta_2 - \nu_j \tau + \alpha_j), \quad (\text{A.6})$$

with the transformations given by

$$\begin{aligned} X &= \sqrt{2I_1} \sin \theta_1 + \theta_2 & Y &= \sqrt{2I_1} \sin \theta_1 - I_2 \\ V_X &= \sqrt{2I_1} \cos \theta_1 & V_Y &= -\sqrt{2I_1} \sin \theta_1. \end{aligned} \quad (\text{A.7})$$

Physically, we see that $I_1 = (V_X^2 + V_Y^2) / 2$ is the normalized kinetic energy of an ion, θ_1 is the angle of Larmor precession, θ_2 is the position of the guiding center in the \hat{x} direction, and $-I_2$ is the position of the guiding center in the \hat{y} direction.

It is evident from this formulation that the guiding center in the \hat{x} direction is a constant of motion. While this is significant when considering a distribution of particles, for our single particle analysis we fold this constant into the wave phase φ_j . Letting $I_1 \rightarrow I$ and $\theta_1 \rightarrow \theta$, the resulting Hamiltonian is given by

$$H = I + \sum_{j=1,2} \varepsilon_j \cos(\kappa_j \rho \sin \theta - \nu_j \tau + \varphi_j), \quad (\text{A.8})$$

where we have defined $\rho = \sqrt{2I}$ and $\varphi_j = \alpha_j + \kappa_j \theta_2$.

A.2 Ensemble Hamiltonian

For our formulation of the ensemble Hamiltonian in Chapter 3, we include the parallel direction and normalize variables with respect to average thermal quantities. With this in mind, the governing equations of motion are given by

$$\frac{d^2 \mathbf{x}}{dt^2} = \frac{q}{m_i} \left[\sum_{j=1}^2 \mathbf{k}_j \Phi_j \sin(\mathbf{k}_j \cdot \mathbf{x} - \omega_j t + \alpha_j) + \Delta \mathbf{k} \Phi_{nl} \sin(\Delta \mathbf{k} \cdot \mathbf{x} - \Delta \omega t + \Delta \alpha) + \mathbf{v} \times \mathbf{B} \right], \quad (\text{A.9})$$

where $\Delta \mathbf{k} = \mathbf{k}_2 - \mathbf{k}_1$, $\Delta \omega = \omega_2 - \omega_1$, $\Delta \alpha = \alpha_2 - \alpha_1$, and Φ_{nl} is the amplitude of the dielectric response to the driven mode. For the Hamiltonian formulation in this case we use the modified forms

$$T = \frac{m_i}{2} (\dot{x}^2 + \dot{y}^2 + \dot{z}^2) \quad (\text{A.10})$$

$$U = q(\Phi - \mathbf{v} \cdot \mathbf{A}),$$

where the magnetic vector potential remains the same as in Sec. A.1 and we now have defined $\Phi = \sum_{j=1}^2 \Phi_j \cos(\mathbf{k}_j \cdot \mathbf{x} - \omega_j t + \alpha_j) + \Phi_{nl} \cos(\Delta \mathbf{k} \cdot \mathbf{x} - \Delta \omega t + \Delta \alpha)$. The Hamiltonian thus is given by

$$h = \frac{1}{2m_i} ([p_y - qx B_0]^2 + p_x^2 + p_z^2) + q \left[\sum_{j=1}^2 \Phi_j \cos(\mathbf{k}_j \cdot \mathbf{x} - \omega_j t + \alpha_j) \right. \quad (\text{A.11})$$

$$\left. + \Phi_{nl} \cos(\Delta \mathbf{k} \cdot \mathbf{x} - \Delta \omega t + \Delta \alpha) \right]. \quad (\text{A.12})$$

We normalize this Hamiltonian in terms of the thermal quantities of the distribution such that

$$\begin{aligned}\tilde{H} = \frac{1}{2} [P_X^2 + (P_Y - X)^2] + \frac{1}{2} P_Z^2 + \sum_{j=1}^2 \bar{\varepsilon}_j \cos(\bar{\kappa}_j X + \bar{\kappa}_{jz} Z - \nu_j \tau + \alpha_j) \\ + \bar{\varepsilon}_{nl} \cos(\Delta \bar{\kappa} X + \Delta \bar{\kappa}_z Z - \Delta \nu \tau + \Delta \alpha).\end{aligned}\quad (\text{A.13})$$

The normalization terms in this scheme are given by

$$\begin{aligned}X = x/\bar{r}_L \quad V_{X,Y} = v_{x,y}/v_{ti} \quad \nu_j = \omega_j/\Omega_i \\ \tau = \Omega_i t \quad \bar{\varepsilon}_j = (q\Phi_j)/(m_i \bar{r}_L^2 \Omega_i^2) \quad \bar{\kappa}_j = k_j \bar{r}_L.\end{aligned}\quad (\text{A.14})$$

where $v_{ti} = \sqrt{T_i/m_i}$ and $\bar{r}_L = v_{ti}/\Omega_i$. Employing the same generating function of the first kind as in the previous section, we thus find the transformed action-angle formulation:

$$\begin{aligned}H = I + \frac{1}{2} P_z^2 + \sum_{i=1}^2 \bar{\varepsilon}_j \cos(\bar{\kappa}_j \rho \sin \theta + \bar{\kappa}_{jz} Z - \nu_j \tau + \bar{\varphi}_j) \\ + \bar{\varepsilon}_{nl} \cos(\Delta \bar{\kappa} \rho \sin \theta + \Delta \bar{\kappa}_z Z - \Delta \nu \tau + \Delta \bar{\varphi}),\end{aligned}\quad (\text{A.15})$$

where we have let $I_1 \rightarrow I$, $\theta_1 \rightarrow \theta$, $\rho = \sqrt{2I}$, and defined $\bar{\varphi}_j = \alpha_j + \bar{\kappa}_j \theta_2$. This is the Hamiltonian we employ in Sec. 3.2. In the perpendicular limit and with the substitution $\bar{\varepsilon}_j \rightarrow \bar{\xi}_j/\bar{\kappa}_j$, however, we recover Eq. 3.6 from Sec. 3.1. Similarly, by eliminating the $\bar{\varepsilon}_{nl}$ term and employing the normalization scheme from A.1, we arrive at the Hamiltonian for Sec. 2.6.

Appendix B

Lie transform analysis

B.1 General theory

Since the nonlinearity of the action-angle Hamiltonians we have outlined in Eqs. 2.2, 3.6, and 3.26 preclude any integrable solution, we seek a canonical transformation to a new coordinate system where the transformed Hamiltonian is more tractable. We first establish the general formalism to achieve this end and then discuss the special cases in Chapters 2 and 3.

For the initial coordinates and momenta (\mathbf{q}, \mathbf{p}) with Hamiltonian H , let us represent the canonical transformation with the operator T such that the transformed coordinates (\mathbf{Q}, \mathbf{P}) with Hamiltonian K are given by

$$\mathbf{Q} = T[\mathbf{q}] \tag{B.1}$$

$$\mathbf{P} = T[\mathbf{p}]. \tag{B.2}$$

Finding a closed form for T that accurately portrays the dynamics of a nonlinear system while allowing for a simplified analysis is extremely difficult and often impossible. Therefore, for a system such as ours where the integrable motion $H = I$ is modified by a small nonlinear term ε , we use a perturbation analysis in order to approximate a transformation.

There are a number of perturbation methods available to achieve this end [38]; however, one of the most formulaic is the method Lie transforms. This technique consists of expanding the transformation operator in a series [63, 64]. A concise and enlightening review of this analysis is provided in Ref. [65], and we use this reference to guide the discussion here. In particular, we assume T can be expressed in Poisson bracket notation such that

$$T = e^{-L}, \quad (\text{B.3})$$

where $L = \{w, ..\}$ is the Poisson operator and w is a generating function that is related to the transformed Hamiltonian through the equation

$$\frac{\partial w}{\partial \tau} = \frac{\partial K}{\partial \varepsilon} - LK - T^{-1} \frac{\partial H}{\partial \varepsilon}. \quad (\text{B.4})$$

Here $T^{-1} = e^L$ denotes the inverse operator, and we note that both T and T^{-1} are canonical and commute with functions [65].

We solve Eq. B.4 through perturbation analysis by expanding K , H , T , and w as series with respect to the small parameter:

$$\begin{aligned} H &= \sum_{n=0}^{\infty} H_n \\ K &= \sum_{n=0}^{\infty} K_n \\ T &= \sum_{n=0}^{\infty} T_n \\ w &= \sum_{n=0}^{\infty} w_{n+1}. \end{aligned} \quad (\text{B.5})$$

Expanding the exponentials in T and T^{-1} and then substituting in these series rela-

tions yields the first and second order components of the transformation

$$\begin{aligned}
T_0 &= I \\
T_1 &= -L_1 \\
T_2 &= -\frac{1}{2}L_2 + \frac{1}{2}L_1^2 \\
T_0^{-1} &= I \\
T_1^{-1} &= L_1 \\
T_2^{-1} &= -\frac{1}{2}L_2 + \frac{1}{2}L_1^2,
\end{aligned} \tag{B.6}$$

where $L_n = \{w_n, ..\}$. Similarly, we find from Eq. B.4 to second order that

$$\begin{aligned}
K_0 &= H_0 \\
\frac{\partial w_1}{\partial \tau} + \{w_1, H_0\} &= K_1 - H_1 \\
\frac{\partial w_2}{\partial \tau} + \{w_2, H_0\} &= 2(K_2 - H_2) - L_1(K_1 + H_1).
\end{aligned} \tag{B.7}$$

Ideally we would be able to find a transformation where $K_1, ..., K_n = 0$ since then the equations of motion under the Hamiltonian are extremely tractable. However, we can see from these relations that if the right hand side has any terms that are independent of time, the solution w_n will have secular components that are divergent with time. The typical goal for the transformation then is to keep K as simple as possible while at the same time defining its components in such a way to prevent the appearance of secular terms in the generating functions.

With this in mind, we now discuss the specific Hamiltonians outlined in the text.

B.2 Hamiltonian in Eq. 2.2

Here we have the Hamiltonian in action-angle coordinates given by

$$H = I + \sum_{j=1,2} \varepsilon_j \cos(\kappa_j \sqrt{2I} \sin \theta - \nu_j \tau + \varphi_j). \tag{B.8}$$

The higher order components thus are $H_2, \dots, H_n = 0$ while we have for the zeroth and first order terms

$$\begin{aligned} H_0 &= I \\ H_1 &= \sum_{j=1,2} \varepsilon_j \cos(\kappa_j \sqrt{2I} \sin \theta - \nu_j \tau + \varphi_j). \end{aligned} \quad (\text{B.9})$$

We rewrite H_1 as a series expansion in terms of the Bessel function of the first kind to find [11]:

$$H_1 = \frac{1}{2} \sum_{j=1,2} \varepsilon_j \sum_m J_m \left(\kappa_j \sqrt{2I} \right) \left[e^{i(m\theta - \nu_j \tau + \varphi_j)} + e^{-i(m\theta - \nu_j \tau + \varphi_j)} \right]. \quad (\text{B.10})$$

Substituting this into the second line of Eq. B.7, we immediately see that if $\nu_j \neq \|\nu_j\|$, there are no secular terms such that we can let $K_1 = 0$. Employing the method of characteristics to solve for w_1 , we thus find

$$w_1 = \frac{i}{2} \sum_{j=1}^2 \sum_m \varepsilon_j J_m \left(\kappa_j \sqrt{2I} \right) \frac{\left[e^{i(m\theta - \nu_j \tau + \varphi_j)} - e^{-i(m\theta - \nu_j \tau + \varphi_j)} \right]}{m - \nu_j}. \quad (\text{B.11})$$

We note here that we have eliminated the dependence of w_1 on the initial condition τ_0 following the precedent for single particle analysis set by Spektor [24], Chia [20], and Benisti [17]. With this in mind, we can generate the second-order transformed Hamiltonian, K_2 , by substituting Eq. B.11 into the third line of Eq. B.7 and eliminating the secular terms. Examining the cross-terms that arise from $L_1 H_1 = \{w_1, H_1\}$ reveals secular terms that arise when $m = n$, $\nu_2 - \nu_1 = n$, $\nu_2 + \nu_1 = n$, and $2\nu_j = m + n$ where n is an integer. However, following Ref. [22], since we are interested primarily in the dynamical effects of the beat resonance at $\nu_2 - \nu_1 = 1$, we assume that the other resonant conditions are not satisfied by the frequencies, i.e. we do not explicitly include half harmonics in our analysis. We thus can recover Eq. 2.3.

B.3 Analysis in Sec. 3.1

For the formulation of the average kinetic energy in Sec. 3.1, we follow the Lie transform analysis of Latham et al. [57]. The idea here is to solve for the average kinetic

energy as a function of time and initial action I_0 but averaged over the initial position $\langle I(I_0, \theta_0, \tau) \rangle_{\theta_0}$. To this end, we seek a transformation $T(\theta, I)[I] = \tilde{I}$ where in the new coordinate system with Hamiltonian K the equations of motion are simpler. Then, in order to find $I(\tau)$, we transform the initial condition I_0 to \tilde{I}_0 , solve the equations of motion in the new coordinate system until time τ , and then invert the transformation $I(\tau) = T^{-1}(\tilde{\theta}, \tilde{I})[\tilde{I}(\tau)]$.

If we denote the time-propagating operator in the tilde reference frame as $S_K(\tau, \tau_0)$, we can use this indirect technique to relate the action at time τ to the initial conditions I_0 without ever calculating the transformed coordinates (Sec. II of Ref. [57]):

$$I(\tau) = T(\theta, I) S_K(\tau, \tau_0) T^{-1}(\theta, I) I_0. \quad (\text{B.12})$$

Using the prescription from Sec. B.1, to second order this expression yields

$$I(\tau) = \left[S_K + S_K L_1 - L_1 S_K + \frac{1}{2} (S_K L_2 - L_2 S_K) + \frac{1}{2} (L_1^2 S_K - 2 L_1 S_K L_1 + S_K L_1^2) \right] I_0. \quad (\text{B.13})$$

Since the Hamiltonian in Sec. 3.1 has the same form as that discussed in Sec. B.2, we employ the same assumptions to assert that $K_1 = 0$, and thus we can approximate $S_K(I_0) = I_0$ and $S_K(\theta_0) = \theta_0 + \tau$. The second order approximation for $I(\tau)$ then becomes

$$I(\tau)_2 = I_0 + \{\Delta w_1, I_0\} + \frac{1}{2} \{\Delta w_2, I_0\} + \frac{1}{2} \{\Delta w_1, \{\Delta w_1, I_0\}\} \quad (\text{B.14})$$

$$+ \frac{1}{2} \{w_1(\theta_0 + \tau, I_0, \tau), w_1(\theta_0, I_0, \tau_0)\}, I_0\}, \quad (\text{B.15})$$

where we have defined $\Delta w_j = w_j(\theta_0 + \tau, I_0, \tau) - w_j(\theta_0, I_0, \tau_0)$ and

$$w_1(\theta, I, \tau) = \frac{i}{2} \sum_{j=1}^2 \sum_m \frac{\xi_j}{\kappa_j} J_m(\kappa_j \sqrt{2I}) \frac{[e^{i(m\theta - \nu_j \tau + \varphi_j)} - e^{-i(m\theta - \nu_j \tau + \varphi_j)}]}{m - \nu_j}. \quad (\text{B.16})$$

Now, we can see that w_1 is periodic with respect to θ and since we design our transformation to eliminate secular terms, we can assume the same is true for w_2 . Thus

we can simplify Eq. B.14 by averaging with respect to the initial angles to yield

$$I(\tau)_2 = I_0 + \frac{1}{2} \langle \{ \Delta w_1, \{ \Delta w_1, I_0 \} \} \rangle_{\theta_0}, \quad (\text{B.17})$$

where the other terms have been eliminated due to their periodicity. Finally, expanding out the Poisson brackets, and integrating with respect to θ_0 we recover Eq. 3.11.

B.4 Analysis in Sec. 3.2

For this section, instead of concentrating on the time dependence of the action I as a function of initial conditions, we follow Cary [66] in considering the local density distribution function $f(\theta, I)$. Since we seek a canonical transformation, we know that the density distribution function for the oscillation center is related to the distribution in physical coordinates by

$$f(\theta, I) = F(\tilde{\theta}(\theta, I), \tilde{I}(\theta, I)), \quad (\text{B.18})$$

where $\tilde{\theta} = T[\theta]$, $\tilde{I} = T[I]$. Employing the fact that T commutes with functions, we thus see

$$f(\theta, I) = T[F(\theta, I)]. \quad (\text{B.19})$$

Expanding T in series to fourth order yields

$$f(\theta, I) = F + T_1 + T_2 F + T_3 F + T_4 F, \quad (\text{B.20})$$

where T_1, T_2 are given by Eq. B.6 and the higher order terms are

$$T_3 = -\frac{1}{3}L_3 + \frac{1}{6}L_2L_1 + \frac{1}{3}L_1L_2 - \frac{1}{6}L_1^3 \quad (\text{B.21})$$

$$T_4 = -\frac{1}{4}L_4 + \frac{1}{12}L_3L_1 + \frac{1}{8}L_2^2 + \frac{1}{4}L_1L_3 - \frac{1}{24}L_2L_1^2 - \frac{1}{12}L_1L_2L_1 - \frac{1}{8}L_1^2L_2 + \frac{1}{24}L_1^4. \quad (\text{B.22})$$

While there are several terms in this expansion, we only retain the one that has the same form as the non-periodic, second-order contribution to T , i.e. we approximate

$$\begin{aligned} T_3 &\approx 0 \\ T_4 &\approx \frac{1}{8} L_2^2. \end{aligned} \tag{B.23}$$

We justify this approximation by noting that many of terms in Eq. B.21 are ultimately eliminated through the phase averaging we perform to arrive at the power absorption term. However, the T_4 term remains and provides fourth-order stochastic damping in directly analogy to the second-order stochastic term that arises from $L_1^2 F$. The fourth-order transformation between f and F that we employ is thus given by

$$f = F - \{w_1, F\} + \frac{1}{2} \{w_1, \{w_1, F\}\} - \frac{1}{2} \{w_2, F\} + \frac{1}{8} \{w_2, \{w_2, F_0\}\}. \tag{B.24}$$

Appendix C

Simplification of terms from Chapter 2

C.1 Simplification of F

For these considerations, we employ the asymptotic approximation for the Bessel function in the $x \gg m + (\frac{1}{2}m)^{1/3}$ [11] limit:

$$J_m(x) = \left(\frac{2}{\pi}\right)^{1/2} \frac{\cos \left[(x^2 - m^2)^{1/2} - m \cos^{-1} \left(\frac{m}{x} \right) - \frac{\pi}{4} \right]}{(x^2 - m^2)^{1/4}}. \quad (\text{C.1})$$

With this expression, we see that the cross-term in F becomes to leading order

$$\frac{1}{\rho} \frac{\partial S_6(\rho)}{\partial \rho} = \frac{1}{2\pi\rho^4} (S_6^A(\rho) + S_6^B(\rho)), \quad (\text{C.2})$$

where we have defined

$$\begin{aligned} S_6^A(\rho) = & - \sum_m \left(\frac{(\kappa_2\rho)^2 - (m+1)^2}{(\kappa_1\rho)^2 - m^2} \right)^{1/4} \frac{m}{\nu_1 - m} \times \\ & \left[\left([(\kappa_2\rho)^2 - (m+1)^2]^{1/2} + [(\kappa_1\rho)^2 - m^2]^{1/2} \right) \cos C_1 + \right. \\ & \left. \left([(\kappa_2\rho)^2 - (m+1)^2]^{1/2} - [(\kappa_1\rho)^2 - m^2]^{1/2} \right) \cos C_2 \right] \end{aligned} \quad (\text{C.3})$$

$$\begin{aligned}
S_6^B(\rho) = & - \sum_m \left(\frac{(\kappa_1 \rho)^2 - (m-1)^2}{(\kappa_2 \rho)^2 - m^2} \right)^{1/4} \frac{m}{\nu_2 - m} \times \\
& \left[\left([(\kappa_1 \rho)^2 - (m-1)^2]^{1/2} + [(\kappa_2 \rho)^2 - m^2]^{1/2} \right) \cos D_1 + \right. \\
& \left. \left([(\kappa_1 \rho)^2 - (m-1)^2]^{1/2} - [(\kappa_2 \rho)^2 - m^2]^{1/2} \right) \cos D_2 \right]
\end{aligned} \tag{C.4}$$

and condensed the arguments of the cosine functions to

$$\begin{aligned}
C_1 = & ((\kappa_2 \rho)^2 - (m+1)^2)^{1/2} + ((\kappa_1 \rho)^2 - m^2)^{1/2} \\
& - m \cos^{-1} \left(\frac{m}{\kappa_1 \rho} \right) - (m+1) \cos^{-1} \left(\frac{m+1}{\kappa_2 \rho} \right) - \frac{\pi}{2}
\end{aligned} \tag{C.5}$$

$$\begin{aligned}
C_2 = & ((\kappa_1 \rho)^2 - m^2)^{1/2} - ((\kappa_2 \rho)^2 - (m+1)^2)^{1/2} \\
& - m \cos^{-1} \left(\frac{m}{\kappa_1 \rho} \right) + (m+1) \cos^{-1} \left(\frac{m+1}{\kappa_2 \rho} \right) \\
D_1 = & ((\kappa_2 \rho)^2 - (m-1)^2)^{1/2} + ((\kappa_1 \rho)^2 - m^2)^{1/2} \\
& - (m-1) \cos^{-1} \left(\frac{m-1}{\kappa_1 \rho} \right) - m \cos^{-1} \left(\frac{m}{\kappa_2 \rho} \right) - \frac{\pi}{2}
\end{aligned} \tag{C.6}$$

$$\begin{aligned}
D_2 = & ((\kappa_1 \rho)^2 - (m-1)^2)^{1/2} - ((\kappa_2 \rho)^2 - m^2)^{1/2} \\
& - (m-1) \cos^{-1} \left(\frac{m-1}{\kappa_1 \rho} \right) + m \cos^{-1} \left(\frac{m}{\kappa_2 \rho} \right).
\end{aligned}$$

In order to evaluate the expressions in C.3 and C.4, we follow Ref. [12] in expanding the coefficients of the rapidly varying, sinusoidal terms about $m = \nu_1$ in S_6^A and $m = \nu_2$ in S_6^B :

$$\begin{aligned}
S_6^A = & -\nu_1 \frac{\Gamma_2}{\Gamma_1} \left[(\Gamma_2^2 + \Gamma_1^2) \sum_m \frac{\cos C_1}{\nu_1 - m} + (\Gamma_2^2 - \Gamma_1^2) \sum_m \frac{\cos C_2}{\nu_1 - m} \right] \\
S_6^B = & -\nu_2 \frac{\Gamma_1}{\Gamma_2} \left[(\Gamma_2^2 + \Gamma_1^2) \sum_m \frac{\cos D_1}{\nu_2 - m} + (\Gamma_1^2 - \Gamma_2^2) \sum_m \frac{\cos D_2}{\nu_2 - m} \right],
\end{aligned} \tag{C.7}$$

where we have defined

$$\Gamma_i^2 = [(\kappa_i \rho)^2 - \nu_i^2]^{1/2}. \quad (\text{C.8})$$

We similarly expand the arguments of the cosine functions. For example,

$$\sum_m \frac{\cos C_1}{\nu_1 - m} = \text{Re} \left[\exp \left[i \left(\Gamma_1^2 + \Gamma_2^2 - \nu_1 b_1 - \nu_2 b_2 - \frac{\pi}{2} \right) \right] \sum_m \frac{\exp [i (b_1 + b_2) (\nu_1 - m)]}{\nu_1 - m} \right] \quad (\text{C.9})$$

where we have defined $b_1 = \cos^{-1} \left(\frac{\nu_1}{\kappa_1 \rho} \right)$ and $b_2 = \cos^{-1} \left(\frac{\nu_2}{\kappa_2 \rho} \right)$. We can evaluate this summation for the case of $\kappa_1 \rho \gg \nu_1$ [12, 11]

$$\sum_m \frac{\cos C_1}{\nu_1 - m} = \pi \frac{\sin [\Gamma_1^2 + \Gamma_2^2 - \nu_1 b_1 - \nu_2 b_2 + \pi \delta]}{\sin (\pi \delta)}. \quad (\text{C.10})$$

We follow a similar treatment for the additional terms in C.7

$$\begin{aligned} \sum_m \frac{\cos C_2}{\nu_1 - m} &= \pi \frac{\cos [\Gamma_1^2 - \Gamma_2^2 - \nu_1 b_1 + \nu_2 b_2 + \pi \delta]}{\sin (\pi \delta)} \\ \sum_m \frac{\cos D_1}{\nu_2 - m} &= \pi \frac{\sin [\Gamma_1^2 + \Gamma_2^2 - \nu_1 b_1 - \nu_2 b_2 + \pi \delta]}{\sin (\pi \delta)} \\ \sum_m \frac{\cos D_2}{\nu_2 - m} &= \pi \frac{\cos [\Gamma_1^2 - \Gamma_2^2 - \nu_1 b_1 + \nu_2 b_2 + \pi \delta]}{\sin (\pi \delta)}. \end{aligned} \quad (\text{C.11})$$

We can express these as functions of the variable α_i defined in Eq. 2.14:

$$\begin{aligned} \sum_m \frac{\cos C_1}{\nu_1 - m} &= \pi \frac{\cos [\alpha_1 + \alpha_2]}{\sin (\pi \delta)} \\ \sum_m \frac{\cos C_2}{\nu_1 - m} &= \pi \frac{\cos [\alpha_2 - \alpha_1 + \pi \delta]}{\sin (\pi \delta)} \\ \sum_m \frac{\cos D_1}{\nu_2 - m} &= \pi \frac{\cos [\alpha_1 + \alpha_2]}{\sin (\pi \delta)} \\ \sum_m \frac{\cos D_2}{\nu_2 - m} &= \pi \frac{\cos [\alpha_2 - \alpha_1 + \pi \delta]}{\sin (\pi \delta)}. \end{aligned} \quad (\text{C.12})$$

Under the assumption that $\nu_1, \nu_2 \gg 1$ such that $\nu_1 \sim \nu_2$, we use these expressions along with C.7 to write C.2 as

$$\frac{1}{\rho} \frac{\partial S_6(\rho)}{\partial \rho} = -\frac{\nu_1 (\Gamma_1 \Gamma_2)^{-1}}{2 \sin (\pi \delta) \rho^4} \left[(\Gamma_1^2 + \Gamma_2^2)^2 \cos (\alpha_1 + \alpha_2) + (\Gamma_2^2 - \Gamma_1^2)^2 \cos (\alpha_2 - \alpha_1 + \pi \delta) \right]. \quad (\text{C.13})$$

We now make the simplifying assumption, valid for small δ , that $\cos(\alpha_2 - \alpha_1) \approx \cos(\alpha_2 - \alpha_1 + \pi\delta)$. Through the addition and sum trigonometric identities, this assumption permits us to write

$$\frac{1}{\rho} \frac{\partial S_6(\rho)}{\partial \rho} = -\frac{\nu_1 (\Gamma_1 \Gamma_2)^{-1}}{\sin(\pi\delta) \rho^4} [(\Gamma_1^4 + \Gamma_2^4) \cos \alpha_1 \cos \alpha_2 - 2\Gamma_1^2 \Gamma_2^2 \sin \alpha_1 \sin \alpha_2]. \quad (\text{C.14})$$

We can follow the same expansion procedure outlined above to find the single wave contributions to Eq. 2.11:

$$\frac{1}{\rho} \frac{\partial S_1^{\nu_i}(\rho)}{\partial \rho} = -\frac{\nu_1}{\sin(\delta\pi) \rho^4} \Gamma_i^2 (\cos^2 \alpha_i - \sin^2 \alpha_i). \quad (\text{C.15})$$

This expression along with that in C.13 allows us to write Eq. 2.11 in the factored form

$$F(\varepsilon, \nu_1, \nu_2) = \frac{\nu_1^2}{\sin(\pi\delta) \rho^4} [(\varepsilon_1 \Gamma_1 \sin \alpha_1 + \varepsilon_2 \Gamma_2 \sin \alpha_2)^2 - (\varepsilon_1 \Gamma_1 \cos \alpha_1)^2 - (\varepsilon_2 \Gamma_2 \cos \alpha_2)^2 - \varepsilon_1 \varepsilon_2 \frac{(\Gamma_1^4 + \Gamma_2^4)}{\Gamma_1 \Gamma_2} \cos \alpha_1 \cos \alpha_2]. \quad (\text{C.16})$$

Finally, in order to avoid the singularity at $\kappa_i \rho = \nu_i$, facilitate comparison to previous SEW results [12], and lay the ground work for examining the $\rho < \nu_i / \kappa_i$ limit, we make the substitution that is valid for $\kappa_i \rho > \nu_i + (\frac{1}{2}\nu_i)^{1/3}$ that

$$\left(\frac{2}{\pi}\right)^{1/2} \frac{[(\kappa_i \rho)^2 - \nu_i^2]^{1/4}}{\rho} \rightarrow |H_{\nu_i}^{1'}(\kappa_i \rho)|, \quad (\text{C.17})$$

where the derivative of the Hankel function is with respect to ρ . Substituting this result into the expression for F , we recover Eq. 2.13.

C.2 Completing the square

In order to simplify the second term of Eq. 2.13, the goal is to factor the remaining cross-term:

$$\varepsilon_1 \varepsilon_2 \frac{(A_1^4(\rho) + A_2^4(\rho))}{A_1(\rho) A_2(\rho)} \cos \alpha_1 \cos \alpha_2. \quad (\text{C.18})$$

We re-write this as

$$\varepsilon_1 \varepsilon_2 A_1 A_2 \left(\left(\frac{A_1}{A_2} \right)^2 + \left(\frac{A_2}{A_1} \right)^2 \right) \cos \alpha_1 \cos \alpha_2. \quad (\text{C.19})$$

Using the forms of A_1, A_2 from Appendix A, we can write the ratio

$$\frac{A_1}{A_2} = \left(\frac{(\kappa_1 \rho)^2 - \nu_1^2}{(\kappa_2 \rho)^2 - \nu_2^2} \right)^{1/2}. \quad (\text{C.20})$$

For the large $\rho \kappa_i \gg \nu_i$ case, we see that this term approaches

$$\frac{A_1}{A_2} \approx \frac{\kappa_1}{\kappa_2}. \quad (\text{C.21})$$

Therefore, in the event that the ratio of the wave numbers is on the order of unity $\kappa_1/\kappa_2 \sim 1$, we can express the cross-term from C.18 as

$$2\varepsilon_1 \varepsilon_2 A_1 A_2 \cos \alpha_1 \cos \alpha_2. \quad (\text{C.22})$$

This allows us to factor the terms in Eq. 2.13 to yield the simplified form Eq. 2.17.

Appendix D

Estimating the maximum Lyapunov exponent

We present here a brief formulation for determining the Maximum Lyapunov Exponent (MLE). We reserve mathematical rigor for the more detailed treatments of the subject [97] and instead focus on providing a concise description for the algorithm we employ. The analysis presented here is largely guided by the summary from Sandri [98], who wrote the integrator we adopted for our calculations.

With that in mind, for a continuous dynamical system, let us assume that the equations of motion are given by

$$\dot{\mathbf{x}} = F(\mathbf{x}), \tag{D.1}$$

where F is a function of the state vector \mathbf{x} , and $\dot{\mathbf{x}}$ denotes the derivative with respect to time. We write the solution of these equations of motion for some initial condition \mathbf{x}_0 as $\mathbf{x}(t) = f^t(\mathbf{x}_0)$ where f^t is a vector. Now, let us consider the separation in phase space, denoted \mathbf{u}^t between two trajectories whose initial conditions are only separated by a small initial displacement \mathbf{u}_0 :

$$\mathbf{u}_t = f^t(\mathbf{x}_0 + \mathbf{u}_0) - f^t(\mathbf{x}_0). \tag{D.2}$$

Since the displacement is in fact small, we can Taylor expand this quantity to find

$$\mathbf{u}_t = D_{\mathbf{x}_0} f^t(\mathbf{x}_0) \cdot \mathbf{u}_0, \quad (\text{D.3})$$

where $D_{\mathbf{x}_0}$ denotes the spatial derivative. Ultimately, we want to characterize how this separation evolves in time, and the key to determining this is to assume that over a sufficiently long time interval $t \rightarrow \infty$, the separation can be described as exponential:

$$\lim_{t \rightarrow \infty} \|\mathbf{u}_t\| = \|\mathbf{u}_0\| e^{\lambda t}, \quad (\text{D.4})$$

where $\|\cdot\|$ denotes the magnitude of the vector and λ is the maximum Lyapunov exponent (MLE). We note here that the modifier “maximum” stems from the fact that there are actually multiple exponents that characterize the separation in phase space—one for each degree of freedom. It is logical to assume though that with increasing time the largest of these exponents and the corresponding expansion in that direction of phase space will be the dominant factor, and indeed, a more rigorous treatment reveals that the separation between trajectories is dictated by the MLE [99].

This exponent thus captures the three possible behaviors for a dynamical system. For $\lambda > 0$, the separation continually grows, and the orbits become stochastic. For $\lambda < 0$, the orbits converge to a single trajectory. And for $\lambda = 0$, the separation remains constant—indicating a possibly oscillatory system.

In order to find an estimate for the MLE, we begin by solving Eq. D.4 for λ such that

$$\begin{aligned} \lambda &= \lim_{t \rightarrow \infty} \frac{1}{t} \ln \frac{\|\mathbf{u}_t\|}{\|\mathbf{u}_0\|} \\ &= \lim_{t \rightarrow \infty} \frac{1}{t} \ln \|\mathbf{u}_t\|. \end{aligned} \quad (\text{D.5})$$

Evaluating λ now can be accomplished by determining \mathbf{u}_t . To this end, let us denote

the tensor element $\Phi = D_{\mathbf{x}_0} f^t(\mathbf{x}_0)$. Rewriting Eq. D.3, we find

$$\mathbf{u}_t = \Phi \cdot \mathbf{u}_0. \quad (\text{D.6})$$

If we can evaluate Φ as a function of time, then we should be able to determine \mathbf{u}_t .

From Eq. D.1, we have that

$$\dot{f}^t(\mathbf{x}_0) = F(f^t(\mathbf{x}_0)). \quad (\text{D.7})$$

Differentiating with respect to \mathbf{x}_0 yields

$$D_{\mathbf{x}_0} \dot{f}^t(\mathbf{x}_0) = D_{\mathbf{x}} F(f^t(\mathbf{x}_0)) D_{\mathbf{x}_0} f^t(\mathbf{x}_0), \quad (\text{D.8})$$

where we have employed the chain rule. Using our definition for Φ , this result can be written as

$$\dot{\Phi} = D_{\mathbf{x}} F(f^t(\mathbf{x}_0)) \Phi. \quad (\text{D.9})$$

With Eqs. D.7 and D.9, we thus have a series of equations that we can solve numerically to determine Φ as a function of time. The last step then is to let tensor Φ operate on an initial displacement vector \mathbf{u}_0 . The evaluation of the MLE thus becomes

$$\lambda = \lim_{t \rightarrow \infty} \frac{1}{t} \ln \|\Phi \cdot \mathbf{u}_0\|. \quad (\text{D.10})$$

There is some ambiguity as to what initial displacement vector we should choose; however, Oseledec [99] showed that the MLE will converge to the same value for almost any choice of small initial displacement. This theory is valid provided that the trajectories dictated by the equations of motion are bounded in phase space and that the initial displacement falls within this bounded region. Thus, any randomly generated initial displacement within this region will lead to the same value of MLE.

In order to evaluate the MLE for the Hamiltonian H in Eq. 2.2 with the above relations, we define $\mathbf{x} = (\theta, I, \tau)$ in canonical coordinates where time τ is also treated as a degree of freedom. The function F correspondingly is given by

$$\mathbf{F} = \begin{pmatrix} \frac{\partial H}{\partial I} \\ -\frac{\partial H}{\partial \theta} \\ 1 \end{pmatrix}. \quad (\text{D.11})$$

Similarly, we have

$$D_{\mathbf{x}}F(f^t(\mathbf{x}_0)) = \begin{pmatrix} \frac{\partial^2 H}{\partial^2 I} & \frac{\partial^2 H}{\partial I \partial \theta} & \frac{\partial^2 H}{\partial I \partial \tau} \\ \frac{\partial^2 H}{\partial \theta \partial I} & \frac{\partial^2 H}{\partial^2 \theta} & \frac{\partial^2 H}{\partial \theta \partial \tau} \\ \frac{\partial^2 H}{\partial \tau \partial I} & \frac{\partial^2 H}{\partial \tau \partial \theta} & \frac{\partial^2 H}{\partial^2 \tau} \end{pmatrix}. \quad (\text{D.12})$$

With Φ as a 3×3 matrix of free variables and our state vector \mathbf{x} , we were able to employ Eqs. D.7 and D.9 in conjunction with the above relations to find a set of twelve differential equations for twelve variables. To evaluate these for our analysis, we implemented a numerical integrator from Sandri [98] written in Mathematica. We then determined the MLE for a given initial condition by multiplying by a randomly generated initial displacement and substituting this along with our time dependent result for Φ into Eq. D.10. Since we used the MLE as a metric for the local stochasticity of phase space—which implicitly assumes the degree of stochasticity is largely localized to that region—we were careful to limit our initial displacements to be smaller than the spacing between sampled initial conditions (θ_0, ρ_0) . Following this procedure, we found in Chapter 2 that the values of λ were convergent for times $\tau < 150$.

Appendix E

Electrostatic dispersion relation

We evaluate here the electrostatic dispersion relation through the Lie transform formalism. To this end, we consider the first-order component of the Poisson equation:

$$-k^2\Phi_1 = \frac{1}{\epsilon_0} \sum_s q_s \int d^3\mathbf{v} f_{1(s)}, \quad (\text{E.1})$$

where s denotes the sum over species and we have defined

$$\Phi_1 = \frac{1}{2} \Phi_0 e^{i(\mathbf{k} \cdot \mathbf{x} - \omega t + \alpha)} + \text{c.c.} \quad (\text{E.2})$$

We see that in normalized coordinates we have

$$f_1 = F_1 - \{w_1, F_0\}, \quad (\text{E.3})$$

where we employ the first-order generating function from Eq. 3.36 in the long-time limit with only one amplitude term such that

$$f_1 = \frac{\bar{\epsilon}_0}{2} \sum_n \frac{J_n(z)}{\nu - n - \bar{\kappa}_z P_Z} \left(\bar{\kappa}_z \frac{\partial F_0}{\partial P_Z} + n \frac{\partial F_0}{\partial I} \right) e^{i(n\theta + \bar{\kappa}_z Z - \nu\tau + \bar{\varphi})} + \text{c.c.}, \quad (\text{E.4})$$

where $z = \bar{\kappa}\rho$. Recalling from Appendix A that we have

$$\begin{aligned} \bar{\varphi} &= \alpha + \bar{\kappa}\theta_2 \\ &= \alpha + \bar{\kappa}X - z \sin \theta, \end{aligned} \quad (\text{E.5})$$

we can substitute into Eq. E.4 and integrate over the normalized variables to find

$$\int f_1 dI dP_Z d\theta = \frac{\bar{\epsilon}_0}{2} e^{i(\bar{\kappa}X + \bar{\kappa}_z Z - \nu\tau + \alpha)} \quad (\text{E.6})$$

$$\times \int dI dP_Z d\theta \sum_{n,p} \frac{J_n(z) J_p(z)}{\nu - n - \bar{\kappa}_z P_Z} \left(\bar{\kappa}_z \frac{\partial F_0}{\partial P_Z} + n \frac{\partial F_0}{\partial I} \right) e^{i(n-p)\theta} + \text{c.c.} \quad (\text{E.7})$$

We thus see after integrating with respect to the angle that

$$\int f_1 dI dP_Z d\theta = \frac{\bar{\epsilon}_0}{2} e^{i(\bar{\kappa}X + \bar{\kappa}_z Z - \nu\tau + \alpha)} \quad (\text{E.8})$$

$$\times 2\pi \int dI dP_Z \sum_n \frac{J_n^2(z)}{\nu - n - \bar{\kappa}_z P_Z} \left(\bar{\kappa}_z \frac{\partial F_0}{\partial P_Z} + n \frac{\partial F_0}{\partial I} \right) + \text{c.c.} \quad (\text{E.9})$$

We now convert to physical coordinates to recover the species dependence:

$$\int f_{1(s)} d^3\mathbf{v} = \frac{qn_0\Phi_0}{2m_s} e^{i(\mathbf{k}\cdot\mathbf{x} - \omega t + \alpha)} \quad (\text{E.10})$$

$$\times 2\pi \int v_\perp dv_\perp dv_z \sum_n \frac{J_n^2(z_{(s)})}{\omega - n\Omega_s - k_z v_z} \left(k_z \frac{\partial f_{0(s)}}{\partial v_z} + \frac{n\Omega_s}{v_\perp} \frac{\partial f_{0(s)}}{\partial v_\perp} \right) + \text{c.c.}, \quad (\text{E.11})$$

where $z_{(s)} = v_\perp k_x / \Omega_s$, and $f_{0(s)}$ denotes the three-dimensional velocity distribution of the species. Substituting into Eq. E.2 we eliminate Φ_0 to find the dispersion relation

$$k^2 \epsilon(\omega, \mathbf{k}) = 0, \quad (\text{E.12})$$

where we have

$$\epsilon(\omega, \mathbf{k}) = 1 + \sum_s \frac{\omega_{ps}^2}{k^2} \sum_s 2\pi \int v_\perp dv_\perp dv_z \sum_n \frac{J_n^2(z_{(s)})}{\omega - n\Omega_s - k_z v_z} \left(k_z \frac{\partial f_{0(s)}}{\partial v_z} + \frac{n\Omega_s}{v_\perp} \frac{\partial f_{0(s)}}{\partial v_\perp} \right), \quad (\text{E.13})$$

with the species plasma frequency given by $\omega_{ps}^2 = q_s^2 n_0 / m_s \epsilon_0$.

Appendix F

Fourth-order beating contribution

F.1 Unshielded term

In order to find the amplitude term $\bar{\varepsilon}_b^{(p)}$ from Eq. 3.37, we derive explicitly here the full form for K_2 from the third line of Eq. B.7. To this end, we first evaluate $L_1 H_1$ with the arguments given in the long term time limit by

$$\begin{aligned}
 H_1 &= \frac{1}{2} \sum_{j=1}^2 \sum_n \bar{\varepsilon}_j J_n(z_j) e^{i(\bar{\kappa}_j \rho \sin \theta + \bar{\kappa}_{jz} Z - \nu_j \tau + \bar{\varphi}_j)} + \text{c.c.} \\
 w_1 &= -\frac{i}{2} \sum_{j=1}^2 \sum_n \bar{\varepsilon}_j [1 - \mathfrak{D}(\nu_j - n - \bar{\kappa}_{jz} P_Z)] J_n(z_j) \frac{e^{i(\bar{\kappa}_j \rho \sin \theta + \bar{\kappa}_{jz} Z - \nu_j \tau + \bar{\varphi}_j)}}{\nu_j - n - \bar{\kappa}_{jz} P_Z} + \text{c.c.}
 \end{aligned}
 \tag{F.1}$$

We have

$$L_1 H_1 = \frac{\partial w_1}{\partial \theta} \frac{\partial H_1}{\partial I} - \frac{\partial w_1}{\partial I} \frac{\partial H_1}{\partial \theta} + \frac{\partial w_1}{\partial Z} \frac{\partial H_1}{\partial P_Z} - \frac{\partial w_1}{\partial P_Z} \frac{\partial H_1}{\partial Z},
 \tag{F.2}$$

such that we find

$$\begin{aligned}
L_1 H_1 = & \sum_{\substack{j=1,2 \\ k=1,2}} \sum_{n,m} \frac{1}{2} \bar{\varepsilon}_j \bar{\varepsilon}_k m J_m(z_j) J'_n(z_k) \\
& \times [\cos[(m-n)\theta + (\bar{\kappa}_{jz} - \bar{\kappa}_{kz})X - (\nu_j - \nu_k)\tau + \bar{\varphi}_j - \bar{\varphi}_k] \\
& \times \left(\frac{1 - \mathfrak{D}_j^m}{\nu_j - m - P_Z \bar{\kappa}_{jz}} + \frac{1 - \mathfrak{D}_k^n}{\nu_k - n - P_Z \bar{\kappa}_{kz}} \right) \\
& + \cos[(m+n)\theta + (\bar{\kappa}_{jz} + \bar{\kappa}_{kz})X - (\nu_j + \nu_k)\tau + \bar{\varphi}_j + \bar{\varphi}_k] \\
& \times \left(\frac{1 - \mathfrak{D}_j^m}{\nu_j - m - P_Z \bar{\kappa}_{jz}} - \frac{1 - \mathfrak{D}_k^n}{\nu_k - n - P_Z \bar{\kappa}_{kz}} \right)] \\
& + \frac{1}{2} \bar{\varepsilon}_j \bar{\varepsilon}_k \bar{\kappa}_{kz} \bar{\kappa}_{jz} \frac{J_m(z_j) J_n(z_k)}{(m + P_Z \bar{\kappa}_{jz} - \nu_j)^2} [1 - \mathfrak{D}_j^m] \\
& \times (\cos[(m-n)\theta + (\bar{\kappa}_{jz} - \bar{\kappa}_{kz})X - (\nu_j - \nu_k)\tau + \bar{\varphi}_j - \bar{\varphi}_k] \\
& - \cos[(m+n)\theta + (\bar{\kappa}_{jz} + \bar{\kappa}_{kz})X - (\nu_j + \nu_k)\tau + \bar{\varphi}_j + \bar{\varphi}_k]) ,
\end{aligned} \tag{F.3}$$

where we have condensed

$$\mathfrak{D}_j^n = \mathfrak{D}(\nu_j - n - \bar{\kappa}_{jz} P_Z). \tag{F.4}$$

From this collection of terms and H_2 , we retain the potential BEW contributions to our expression for K_2 from Eq. B.7:

$$\begin{aligned}
K_2 = & - \sum_{\substack{j=1,2 \\ i=1,2}} \sum_{n,m} \frac{1}{4} \bar{\varepsilon}_j \bar{\varepsilon}_k \cos[(m-n)\theta + (\bar{\kappa}_{jz} - \bar{\kappa}_{kz})X - (\nu_j - \nu_k)\tau + \bar{\varphi}_j - \bar{\varphi}_k] \\
& \times \left[m J_m(z_j) J'_n(z_k) \left(\frac{1 - \mathfrak{D}_j^m}{\nu_j - m - P_Z \bar{\kappa}_{jz}} + \frac{1 - \mathfrak{D}_k^n}{\nu_k - n + P_Z \bar{\kappa}_{kz}} \right) \right. \\
& \left. + \bar{\kappa}_{kz} \bar{\kappa}_{jz} \frac{J_m(z_j) J_n(z_k)}{(m + P_Z \bar{\kappa}_{jz} - \nu_j)^2} [1 - \mathfrak{D}_j^m] \right] \\
& + \sum_p \bar{\varepsilon}_{nl}^{(p)} \cos(p\theta + \Delta \bar{\kappa}_z Z - \Delta \nu t + \Delta \bar{\varphi}).
\end{aligned} \tag{F.5}$$

Now, through our power absorption analysis, we want to isolate and examine the impact of the BEW driven mode with frequency at $\Delta \nu = \nu_2 - \nu_1$. This justifies our use of the long-term limit approximation and further permits us to retain only the

BEW terms ($\nu_2 - \nu_1 = p$) in our approximation for the transformed Hamiltonian:

$$\begin{aligned}
K_2 = & \frac{1}{4} \sum_{m,p} \bar{\varepsilon}_1 \bar{\varepsilon}_2 \left[m \left(J_m(z_1) J'_{p+m}(z_2) \left[\frac{1 - \mathfrak{D}_1^m}{\nu_1 - m - P_Z \bar{\kappa}_{1z}} + \frac{1 - \mathfrak{D}_2^{p+m}}{\nu_2 - (p+m) - P_Z \bar{\kappa}_{2z}} \right] \right. \right. \\
& + J_m(z_2) J'_{m-p}(z_1) \left[\frac{1 - \mathfrak{D}_2^m}{\nu_2 - m - P_Z \bar{\kappa}_{2z}} + \frac{1 - \mathfrak{D}_1^{m-p}}{\nu_1 - (m-p) - P_Z \bar{\kappa}_{1z}} \right] \Big) \\
& + \bar{\kappa}_{1z} \bar{\kappa}_{2z} J_m(z_1) J_{m+p}(z_k) \left(\frac{1 - \mathfrak{D}_1^m}{(m + P_Z \bar{\kappa}_{1z} - \nu_1)^2} + \frac{1 - \mathfrak{D}_2^{m+p}}{(m + p + P_Z \bar{\kappa}_{2z} - \nu_2)^2} \right) + \frac{4\bar{\varepsilon}_{nl}^{(p)}}{\bar{\varepsilon}_1 \bar{\varepsilon}_2} \Big] \\
& \times \cos[p\theta + \Delta \bar{\kappa}_z Z - \Delta \nu \tau + \Delta \bar{\varphi}].
\end{aligned} \tag{F.6}$$

We thus find the unshielded contribution from the driven mode:

$$\begin{aligned}
\bar{\varepsilon}_b^{(p)} = & \frac{\bar{\varepsilon}_1 \bar{\varepsilon}_2}{4} \sum_m \left[m \left(J_m(z_1) J'_{p+m}(z_2) \left[\frac{1 - \mathfrak{D}_1^m}{\nu_1 - m - P_Z \bar{\kappa}_{1z}} + \frac{1 - \mathfrak{D}_2^{p+m}}{\nu_2 - (p+m) - P_Z \bar{\kappa}_{2z}} \right] \right. \right. \\
& + J_m(z_2) J'_{m-p}(z_1) \left[\frac{1 - \mathfrak{D}_2^m}{\nu_2 - m - P_Z \bar{\kappa}_{2z}} + \frac{1 - \mathfrak{D}_1^{m-p}}{\nu_1 - (m-p) - P_Z \bar{\kappa}_{1z}} \right] \Big) \\
& + \bar{\kappa}_{1z} \bar{\kappa}_{2z} J_m(z_1) J_{m+p}(z_k) \left(\frac{1 - \mathfrak{D}_1^m}{(m + P_Z \bar{\kappa}_{1z} - \nu_1)^2} + \frac{1 - \mathfrak{D}_2^{m+p}}{(m + p + P_Z \bar{\kappa}_{2z} - \nu_2)^2} \right) \Big].
\end{aligned} \tag{F.7}$$

F.2 Shielded term

In order to evaluate the self-consistent contribution, $\bar{\varepsilon}_{nl}^{(p)}$, we employ the Poisson equation

$$\nabla^2 \Phi = \frac{1}{\epsilon_0} \sum_s q_s \int f_s d^3 \mathbf{v}, \tag{F.8}$$

where s denotes the species. We consider that the second-order contribution to this equation stems from the dielectric response of the plasma to the driven mode such that we have

$$\Phi_2 = \frac{\Phi_{nl}}{2} e^{i(\Delta k_z z + \Delta k_x x - \Delta \omega t + \Delta \alpha)} + \text{c.c.}, \tag{F.9}$$

which we have expressed in physical coordinates. To second order then, we have

$$-(\Delta k)^2 \Phi_2 = \frac{1}{\epsilon_0} \sum_s q_s \int f_{2s} d^3 \mathbf{v}, \tag{F.10}$$

where f_2 has the same sinusoidal time dependence as Φ_2 . To evaluate the integral on the RHS, we consider in normalized coordinates that

$$f_2 = F_2 - \{w_2, F_0\} + \frac{1}{2}\{w_1, \{w_1, F_0\}\}, \quad (\text{F.11})$$

where in F_2 and w_2 we only retain the long-term time contributions

$$\begin{aligned} F_2 &= \frac{1}{2} \sum_p \left(\bar{\varepsilon}_{nl}^{(p)} + \bar{\varepsilon}_b^{(p)} \right) \mathfrak{D}_\Delta^p \left(\Delta \bar{\kappa}_z \frac{\partial F_0}{\partial P_Z} + p \frac{\partial F_0}{\partial I} \right) \frac{e^{i(p\theta + \Delta \bar{\kappa}_z z - \Delta \nu \tau + \Delta \bar{\varphi})}}{\Delta \nu - p - P_Z \Delta \bar{\kappa}} + \text{c.c.} \\ w_2 &= -\frac{i}{2} \sum_p \left(\bar{\varepsilon}_{nl}^{(p)} + \bar{\varepsilon}_b^{(p)} \right) [1 - \mathfrak{D}_\Delta^p] \frac{e^{i(p\theta + \Delta \bar{\kappa}_z z - \Delta \nu \tau + \Delta \bar{\varphi})}}{\Delta \nu - n - \Delta \kappa_Z P_z} + \text{c.c.} \end{aligned} \quad (\text{F.12})$$

Here $\bar{\varepsilon}_b^{(p)}$ is given by Eq. F.7, and we can relate the components of the self-consistent contribution to $\bar{\varepsilon}_{nl}$ by considering

$$\bar{\varepsilon}_{nl} e^{i(\Delta \bar{\kappa}_z Z + \Delta \bar{\kappa} X - \Delta \nu t + \Delta \bar{\alpha})} + \text{c.c.} = \bar{\varepsilon}_{nl} J_p(\Delta z) e^{i(p\theta + \Delta \bar{\kappa}_z Z - \Delta \nu \tau + \Delta \bar{\varphi})} + \text{c.c.} \quad (\text{F.13})$$

such that

$$\bar{\varepsilon}_{nl}^{(p)} = \bar{\varepsilon}_{nl} J_p(\Delta z). \quad (\text{F.14})$$

Now, since the sum $F_2 - \{w_2, F_0\}$ eliminates the filter functions, we find

$$F_2 - \{w_2, F_0\} = \quad (\text{F.15})$$

$$\frac{1}{2} \sum_p \left(\bar{\varepsilon}_{nl} J_p(\Delta z) + \bar{\varepsilon}_b^{(p)} \right) \left(\Delta \bar{\kappa}_z \frac{\partial F_0}{\partial P_Z} + p \frac{\partial F_0}{\partial I} \right) \frac{e^{i(p\theta + \Delta \bar{\kappa}_z z - \Delta \nu \tau + \Delta \bar{\varphi})}}{\Delta \nu - p - P_Z \Delta \bar{\kappa}} + \text{c.c.} \quad (\text{F.16})$$

In order to relate our normalized formulation to the physical coordinates, we integrate with respect to action and phase to yield the result

$$\begin{aligned} \int f_2 dP_Z dI d\theta &= \int dP_Z dI d\theta \sum_p e^{i(p\theta + \Delta \bar{\kappa}_z z - \Delta \nu \tau + \Delta \bar{\varphi})} \\ &\times \frac{1}{2} \left[\frac{\bar{\varepsilon}_{nl} J_p(\Delta z) + \bar{\varepsilon}_b^{(p)}}{\Delta \nu - p - P_Z \Delta \bar{\kappa}} \left(\Delta \bar{\kappa}_z \frac{\partial F_0}{\partial P_Z} + p \frac{\partial F_0}{\partial I} \right) + D^{(p)} \right] + \text{c.c.}, \end{aligned} \quad (\text{F.17})$$

where $D^{(p)}$ contains the polarization correction from $\frac{1}{2}\{w_1, \{w_1, F_0\}\}$. To evaluate this term, we can use the periodicity with respect to θ as well as integration by parts

with respect to P_Z to write

$$\int \frac{1}{2} \{w_1, \{w_1, F_0\}\} dP_Z dI d\theta = - \int dP_Z dI d\theta \frac{1}{2} \frac{\partial}{\partial Z} \left[\left(\frac{\partial w_1}{\partial \theta} \frac{\partial F_0}{\partial I} + \frac{\partial w_1}{\partial Z} \frac{\partial F_0}{\partial P_Z} \right) \frac{\partial w_1}{\partial P_Z} \right]. \quad (\text{F.18})$$

Only retaining the beat terms at $\nu_2 - \nu_1 = p$ yields the result

$$\int \frac{1}{2} \{w_1, \{w_1, F_0\}\} dP_Z dI d\theta = - \int dP_Z dI d\theta D^{(p)} e^{i(p\theta + \Delta \bar{\kappa}_z z - \Delta \nu \tau + \Delta \bar{\varphi})} + \text{c.c.}, \quad (\text{F.19})$$

where we denote

$$D^{(p)} = \frac{\varepsilon_1 \varepsilon_2}{4} \Delta \bar{\kappa} \sum_m J_m(z_1) J_{m+p}(z_2) \mathfrak{D}_2^{m+p} \mathfrak{D}_1^m \times \left[\frac{\bar{\kappa}_{1z} \left[(m+p) \frac{\partial F_0}{\partial I} + \bar{\kappa}_{2z} \frac{\partial F_0}{\partial P_Z} \right]}{(m+p + P_Z \bar{\kappa}_{2z} - \nu_2) (m + P_Z \bar{\kappa}_{1z} - \nu_1)^2} - \frac{\bar{\kappa}_{2z} \left[m \frac{\partial F_0}{\partial I} + \bar{\kappa}_{1z} \frac{\partial F_0}{\partial P_Z} \right]}{(m + P_Z \bar{\kappa}_{1z} - \nu_1) (m+p + P_Z \bar{\kappa}_{2z} - \nu_2)^2} \right]. \quad (\text{F.20})$$

With this result in mind, we now recall from Appendix A that

$$\begin{aligned} \bar{\varphi}_j &= \alpha_j + \bar{\kappa}_j \theta_2 \\ &= \alpha_j + \bar{\kappa}_j X - z_j \sin \theta. \end{aligned} \quad (\text{F.21})$$

Substituting into Eq. F.17, we thus find

$$\begin{aligned} \int f_2 dP_Z dI d\theta &= e^{i(\bar{\kappa} X + \Delta \bar{\kappa}_z Z - \Delta \nu \tau + \Delta \alpha)} 2\pi \int dP_Z dI \sum_p J_p(\Delta z) \\ &\times \frac{1}{2} \left[\frac{\bar{\varepsilon}_{nl} J_p(\Delta z) + \bar{\varepsilon}_b^{(p)}}{\Delta \nu - p - P_Z \Delta \bar{\kappa}} \left(\Delta \bar{\kappa}_z \frac{\partial F_0}{\partial P_Z} + p \frac{\partial F_0}{\partial I} \right) + D^{(p)} \right]. \end{aligned} \quad (\text{F.22})$$

Finally, we convert back to physical coordinates in order to recover the species dependence of the density distribution function:

$$\begin{aligned} \int f_{2(s)} v_\perp dv_\perp dv_z d\theta &= e^{i(k_x x + \Delta k_z z - \Delta \omega t + \Delta \alpha)} \frac{q n_0}{m_s} 2\pi \int v_\perp dv_\perp dv_z \sum_p J_p(\Delta z_{(s)}) \\ &\times \frac{1}{2} \left[\frac{\Phi_{nl} J_p(\Delta z_{(s)}) + \Phi_{b(s)}^{(p)}}{\Delta \omega - p \Omega_s - v_z \Delta k_z} \left(\Delta k_z \frac{\partial f_{0(s)}}{\partial v_z} + \frac{p \Omega_s}{v_\perp} \frac{\partial f_{0(s)}}{\partial v_\perp} \right) + D_s^{(p)} \right] + \text{c.c.} \end{aligned} \quad (\text{F.23})$$

Here we have

$$D_s^{(p)} = \frac{q}{m_s} \frac{\Phi_1 \Phi_2}{4} \sum_m J_m(z_{1(s)}) J_{m+p}(z_{2(s)}) \Delta k_z \mathfrak{D}_2^{m+p} \mathfrak{D}_1^m \left[\frac{k_{1z} \left[\frac{(m+p)\Omega_s}{v_\perp} \frac{\partial f_0}{\partial v_\perp} + k_{2z} \frac{\partial f_0}{\partial v_z} \right]}{((m+p)\Omega_s + v_z k_{2z} - \omega_2)(m\Omega_s + v_z k_{1z} - \omega_1)^2} - \frac{k_{2z} \left[\frac{m\Omega_s}{v_\perp} \frac{\partial f_0}{\partial v_\perp} + k_{1z} \frac{\partial f_0}{\partial v_z} \right]}{(m\Omega_s + v_z k_{1z} - \omega_1)((m+p)\Omega_s + v_z k_{2z} - \omega_2)^2} \right], \quad (\text{F.24})$$

where n_0 is the background density of the species, $f_{0(s)}$ is the three-dimensional Maxwellian expressed in physical coordinates, and $\Delta z_{(s)} = z_{2(s)} - z_{1(s)} = v_\perp (k_{2x} - k_{1x}) / \Omega_s$.

Similarly, we have for the beating contribution:

$$\Phi_{b(s)}^{(p)} = \frac{q}{m_s} \frac{\Phi_1 \Phi_2}{4} \sum_m \left[m \frac{\Omega_s}{v_\perp} \left(J_m(z_{1(s)}) J'_{p+m}(z_{2(s)}) \left[\frac{1 - \mathfrak{D}_1^m}{\omega_1 - m\Omega_s + v_z k_{1z}} + \frac{1 - \mathfrak{D}_2^{p+m}}{\omega_2 - (p+m)\Omega_s - v_z k_{2z}} \right] + J_m(z_{2(s)}) J'_{m-p}(z_{1(s)}) \left[\frac{1 - \mathfrak{D}_2^m}{\omega_2 - m\Omega_s - v_z k_{2z}} + \frac{1 - \mathfrak{D}_1^{m-p}}{\omega_1 - (m-p)\Omega_s - v_z k_{1z}} \right] \right) + k_{1z} k_{2z} J_m(z_{1(s)}) J_{m+p}(z_{2(s)}) \left(\frac{1 - \mathfrak{D}_1^m}{(m\Omega_s + v_z k_{1z} - \omega_1)^2} + \frac{1 - \mathfrak{D}_2^{m+p}}{((m+p)\Omega_s + v_z k_{2z} - \omega_2)^2} \right) \right], \quad (\text{F.25})$$

where the derivatives are now with respect to v_\perp .

In our formulation, we assume that $\Phi_{b(e)}^{(p)} = D_e^{(p)} = 0$ since the driven mode at the ion cyclotron frequency does not form a resonance with the electron cyclotron frequency. This permits us to substitute a simplified form of Eq. F.23 back into Eq. F.10 and solve for the nonlinear amplitude to find

$$\Phi_{nl} = -[\epsilon(\Delta\omega, \Delta\mathbf{k})]^{-1} \left[\frac{\omega_{pi}^2}{(\Delta k)^2} \right] \sum_p 2\pi \int v_\perp dv_\perp dv_z J_p(\Delta z_{(i)}) \times \left[\frac{\Phi_{b(i)}^{(p)}}{\Delta\omega - p\Omega_i - v_z \Delta k_z} \left(\Delta k_z \frac{\partial f_{0(i)}}{\partial v_z} + \frac{p\Omega_i}{v_\perp} \frac{\partial f_{0(i)}}{\partial v_\perp} \right) + D_i^{(p)} \right], \quad (\text{F.26})$$

where we have denoted the ion plasma frequency $\omega_{pi}^2 = (q^2 n_0) (\epsilon_0 m_i)$ and $\epsilon(\Delta\omega, \Delta\mathbf{k})$ is the dielectric tensor derived in Appendix E. We see this result corresponds to Eq. 32 in Ref. [19]; however, unlike in this reference, we have explicitly evaluated through

our formalism the polarization response, $D_i^{(p)}$. Physically, Φ_{nl} represents the dielectric response to the beat wave, and it is well-defined since the beat wave is not a natural mode of the plasma ($\epsilon(\Delta\omega, \Delta\mathbf{k}) \neq 0$).

Appendix G

LIF broadening effects for BWX II

In order to arrive at Eq. 4.9, we have assumed that ν_0 , the frequency for excitation, is fixed for an ion in the reference frame. However, there are a number of plasma-based processes that can broaden this frequency. These fall into five categories: natural broadening, Stark/pressure broadening, saturation broadening, instrument broadening, and Zeeman broadening [100, 101, 102, 103, 104, 105, 106]. In each of these cases, plasma or quantum mechanical effects lead to a range of ν_0 in the reference frame that can excite the transition. For the most precise treatment, it therefore is necessary to convolve the broadening mechanisms with the theoretical model for the velocity response in order to arrive at the true LIF intensity profile.

When the spread in frequency anticipated from the theoretical model for velocity response is large compared to the variation in ν_0 generated by one of the aforementioned broadening mechanisms, however, it is standard to simply neglect that broadening process. For example, for an inductive plasma configuration similar to ours and for the same metastable transition, Boivin et al. [107] demonstrated that Stark broadening and natural broadening of ν_0 are negligible when compared to the spread in frequency produced by thermal effects. Similarly, they observed that the power saturation effects, which arise from large power density in the laser beam, were

small for their 10 mW diode laser. As our configuration employs a 7 mW laser with a comparable beam width, we can conclude that power saturation effects similarly can be neglected for our experiment. The instrument broadening, which arises in our situation from the spread in the laser frequency is also small for our narrowband Littrow configuration diode laser. We thus are justified in following the precedent of Refs. [107], [78], and [24] in ignoring most broadening effects when performing LIF measurements of the temperature broadened profile.

The case of Zeeman splitting, however, requires special consideration for moderate magnetic field intensity. Zeeman splitting occurs in the presence of a magnetic field when the interaction of the magnetic moment of the atom with the ambient field breaks the degeneracy of the transition. This effect was examined in significant detail in Refs. [108, 109] where it was noted that for our $J_1 = 5/2$ to $J_2 = 7/2$ transition, where J denotes the total angular momentum, the allowable Zeeman transitions fall into two categories: π and σ transitions. The former of these, π , occur where the magnetic quantum number M is conserved while the latter are characterized by a change of unity: $M_2 - M_1 = \pm 1$. The magnetic quantum number for the two quantum states can assume the quantities $M = -J, -J + 1 \dots J - 1, J$. As a consequence of this constraint, we can see in contrast to the case with no magnetic field, Zeeman splitting yields 18 allowable transitions between the metastable and excited states of Ar II.

The frequencies of the photons emitted by each of these transitions are given by small deviations from ν_0 [108, 109]:

$$\Delta\nu = \beta B h^{-1} (g_1 M_1 - g_2 M_2), \quad (\text{G.1})$$

where β is the Bohr magneton and g_j is the Landé factor. It is important to note that this effect is linearly dependent on the magnetic field, B . On the other hand, some transitions have greater probabilities than others, and the relative weight of each transition w is independent of magnetic field. These weights were reported in Ref. [107] along with the *wavelength* shifts produced by the Zeeman effect at 1000

kG. Since we know that $\Delta\nu = \Delta\lambda\lambda^{-2}c$ and that the Zeeman effect is linearly related to magnetic field strength, we can scale down these the results of Ref. [107] to our case of $B = 525$ G. The resulting changes in frequency and weights for the transitions are shown graphically Fig. G.1 .

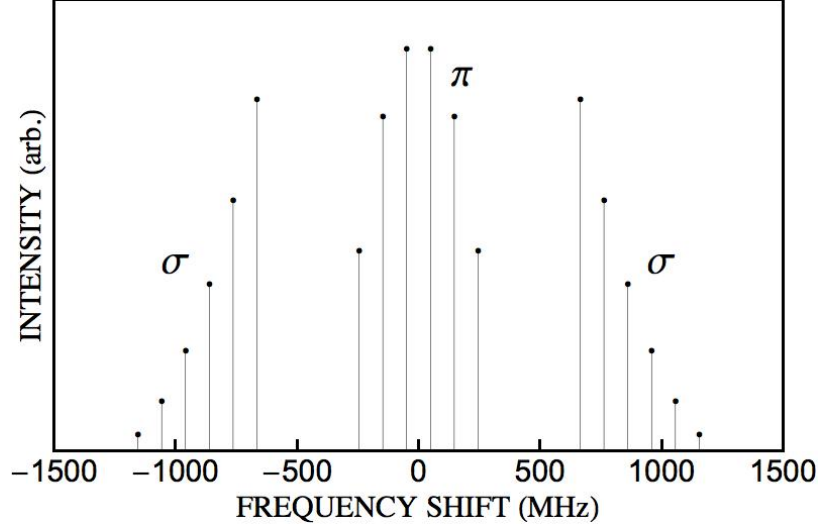


Figure G.1: This figure illustrates the Zeeman splitting around the rest frame frequency of the targeted transition for $B_0 = 525$ G. The two groups correspond to the $\Delta M = 0$ (π) and $\Delta M = \pm 1$ (σ) clusters.

The most distinguishing aspect of this plot is that while both categories of transitions are symmetric with respect to ν_0 , the σ transitions have a wider offset and are locally asymmetric. We also note that both types of transitions are polarized. The π transitions are polarized in the direction parallel to the magnetic field while the σ transitions are circularly polarized. By a judicious use of a linearized laser beam oriented along the magnetic field then, we are able to selectively target the π transitions. On the other hand, by injecting this polarized light through a quarter wavelength, we can produce circularly polarized light that will target only one of the σ groups.

Once we have targeted a certain transition, we can determine the impact Zeeman broadening has on temperature measurements. Given that the ions have some characteristic thermal velocity distribution $f_0(v_x)$, the actual observed intensity profile is

a convolution of the Zeeman lines:

$$I(\nu) = \alpha_c \sum_{i=1}^n w_i (\nu_0 + \Delta\nu_i) f_0 \left[\frac{c}{\nu_0} (\nu_0 + \Delta\nu - \nu) \right], \quad (\text{G.2})$$

where α_c is constant dependent on geometry and collection volume, I denotes the intensity of light emitted, w_i is the weight of each transition in the targeted group (π or σ), and the summation is over the number of lines in each group, $n = 6$. Implicit in this expression is that $(\Delta\nu_j + \nu_0)/\nu_0 \approx 1$.

While we can produce the most accurate estimate for the velocity distributions by using Eq. G.2 to deconvolve an intensity profile, we can forgo this computationally expensive step if the average Zeeman splitting is small compared to the characteristic spread in frequency produced by the velocity distribution [109]. For a thermalized ion distribution without Zeeman splitting, the standard deviation in frequency of the intensity profile is given by

$$\Delta\nu_{T_i} = \left(\frac{2T_i\nu_0^2}{m_i c^2} \right)^{1/2}. \quad (\text{G.3})$$

By comparison, we can approximate the effective Zeeman splitting of a given transition as normally distributed in frequency space with a standard deviation given by

$$\Delta\nu_s = \left(\frac{\sum_{i=1}^n w_i (\overline{\Delta\nu_s} - \Delta\nu_i)^2}{\sum_{i=1}^n w_i} \right)^{1/2}, \quad (\text{G.4})$$

where $s = \sigma, \pi$ and

$$\overline{\Delta\nu_s} = \frac{\sum_{i=1}^n w_i \Delta\nu_i}{\sum_{i=1}^n w_i}, \quad (\text{G.5})$$

denotes the average displacement due to the Zeeman effect.

For our typical background temperatures of $T_i = 0.25$ eV with magnetic field strength of $B_0 = 525$ G we see that $\Delta\nu_\pi/\Delta\nu_{T_i} = 0.1$, $\Delta\nu_\sigma/\Delta\nu_{T_i} = 0.09$. Since the difference in standard deviation for the two processes is $\Delta\nu_s/\Delta\nu_{T_i} < 0.1$, we can approximate the Zeeman effect for our temperature measurements in a simplified way [106]. In particular, we assume that the measured standard deviation of the intensity

profile is given approximately by [109]:

$$\Delta\nu_{obs} \approx \Delta\nu_s + \Delta\nu_{T_i}, \quad (\text{G.6})$$

such that the temperature is

$$T_i = \frac{m_i c^2}{2\nu_0^2} (\Delta\nu_{obs} - \Delta\nu_s)^2. \quad (\text{G.7})$$

Calculating the temperature with the uncorrected form $\Delta\nu_s \rightarrow 0$ leads to errors in the temperature $< 10\%$. For our analysis then, we assume the measured intensity profile yields the correct temperature and add the 10% Zeeman error in quadrature with the statistically determined error from the fitting algorithm.

We can align the linear polarization of the laser beam to be parallel to the magnetic in such a way to target the π cluster when we take measurements perpendicular to the magnetic field. This is not possible for measuring the parallel ion temperature since the beam polarization is transverse to the magnetic field. Left unchecked, this linearly polarized light would excite both σ transitions. We thus employ a quarter wave plate to target only one of the clusters. The resulting impact of the Zeeman splitting on the spread of the intensity profile is approximately the same as for the perpendicular case. Since the σ cluster is off-center, however, the measured intensity profile is offset by the constant velocity

$$v_{off} = c \frac{\overline{\Delta\nu_\sigma}}{\nu_0} = 526 \text{ m/s}. \quad (\text{G.8})$$

For our parallel temperature measurements, we correct the velocity values according to this offset.

Finally, we note that all of the measurements of the dielectric response of the plasma to the wave, $f_1(v_x)$, are performed in the direction perpendicular to the magnetic field such that only the π cluster is excited. Furthermore, since the velocity response profiles have a similar spread to the thermal distribution (indeed, the two are directly related), we assume that the error introduced by the broadening processes

outlined above are small with Zeeman spreading as the dominant effect. We then incorporate the Zeeman splitting as an intrinsic error $\Delta\nu_\pi$ in our measurements of frequency ν . For discretized measurements $\nu_1, \nu_2, \nu_3, \dots$ with associated values I_1, I_2, I_3, \dots , this error translates to uncertainty in the intensity measurements:

$$\Delta I_p \approx \Delta\nu_\pi \left| \frac{I_{p+1} - I_p}{\nu_{p+1} - \nu_p} \right|. \quad (\text{G.9})$$

This estimate allows us to weight points when performing fits of our model for the dielectric response to data and provides a means to estimate the average variance of the data. However, given that we found that fluctuations in the profile produced by the ambient noise were much greater than this estimate, we typically assumed that the points in the intensity distribution were equally weighted and used the average variance in our χ^2 analysis to estimate uncertainty in the best-fit parameters.

Bibliography

- [1] R.A. Cairns. Radiofrequency Heating of Plasmas. A. Hilger, 1991.
- [2] M.A. Lieberman and A.J. Lichtenberg. Principles of Plasma Discharges and Materials Processing. Wiley, 2005.
- [3] G. Emsellem. Electrodeless plasma thruster design. In 41st AIAA/ASME/SAE/ASEE Joint Propulsion Conference and Exhibit, Tucson, Arizona, AIAA-2005-3855, 2005.
- [4] E.A. Bering, F.R. Chang-Diaz, J.P. Squire, M. Brukardt, T.W. Glover, R.D. Bengtson, V.T. Jacobson, G.E. McCaskill, and L. Cassady. Electromagnetic ion cyclotron resonance heating in the VASIMR. Advances in Space Research, 42(1):192–205, Jan. 2008.
- [5] B. Jorns and E.Y. Choueiri. A plasma propulsion concept based on direct ion acceleration with beating electrostatic waves. In 46th AIAA/ASME/SAE/ASEE Joint Propulsion Conference and Exhibit, Nashville, TN, AIAA-2010-7107, 2010.
- [6] B. Jorns and E.Y. Choueiri. Thruster concept for transverse acceleration by the beating electrostatic waves ponderomotive force. In 32nd International Electric Propulsion Conference, Wiesbaden, Germany, IEPC-214, 2011.

- [7] D.G. Swanson. Plasma Waves, 2nd Edition. Series in Plasma Physics. Taylor & Francis, 2003.
- [8] F. Skiff, M. Ono, and L.K. Wong. Excitation of ion Bernstein waves from loop antennas. Physics of Fluids, 31(7):2030–2036, 1988.
- [9] M. Ono. Ion Bernstein wave heating research. Physics of Fluids B: Plasma Physics, 5(2):241–280, 1993.
- [10] T.H. Stix. Waves in Plasmas. American Institute of Physics, New York, 1992.
- [11] M. Abramowitz and I.A. Stegun. Handbook of Mathematical Functions: With Formulas, Graphs, and Mathematical Tables. Applied mathematics series. Dover Publications, 1964.
- [12] C.F.F Karney. Stochastic ion heating by a lower hybrid wave. Phys. Fluids, 21(9):1584–1599, 1978.
- [13] J. Goree, M. Ono, and L.K. Wong. Observation of the backward electrostatic ion-cyclotron wave. Phys. of Fluids, 28(9):2845, 1985.
- [14] M.N. Rosenbluth, B. Coppi, and R.N. Sudan. Nonlinear interactions of positive and negative energy modes in rarefied plasmas (II). Annals of Physics, 55(2):248 – 270, 1969.
- [15] M. Porkolab and R. P. H. Chang. Instabilities and induced scattering due to nonlinear Landau damping of longitudinal plasma waves in a magnetic field. Physics of Fluids, 15(2):283–296, 1972.
- [16] A. K. Ram, A. Bers, and D. Benisti. Ionospheric ion acceleration by multiple electrostatic waves. J. Geophys. Res., 103:9431, 1998.

- [17] D. Benisti, A.K. Ram, and A. Bers. Ion dynamics in multiple electrostatic waves in a magnetized plasma. I. Coherent acceleration. Phys. Plasmas, 5(9):3224–3232, 1998.
- [18] R.Z. Sagdeev and A. Galeev. Nonlinear Plasma Theory. Frontiers in physics. W. A. Benjamin, 1969.
- [19] S. Johnston. Oscillation-center formulation of the classical theory of induced scattering in plasma. Physics of Fluids, 19(1):93–107, 1976.
- [20] P.K. Chia, L. Schmitz, and R.W. Conn. Stochastic ion behavior in subharmonic and superharmonic electrostatic waves. Phys. Plasmas, 3(5):1545, May 1996.
- [21] D. Benisti, A.K. Ram, and A. Bers. Ion dynamics in multiple electrostatic waves in a magnetized plasma. II. Enhancement of the acceleration. Phys. Plasmas, 5(9):3233–3241, 1998.
- [22] D. J. Strozzi, A. K. Ram, and A. Bers. Coherent acceleration of magnetized ions by electrostatic waves with arbitrary wavenumbers. Phys. Plasmas, 10(7):2722–2731, July 2003.
- [23] R. Spektor and E. Y. Choueiri. Ion acceleration by beating electrostatic waves: Domain of allowed acceleration. Phys. Rev. E, 69(4):046402, 2004.
- [24] R. Spektor. Ion Acceleration by Beating Electrostatic Waves. Ph.D Thesis. Princeton University, Princeton, NJ, 2006.
- [25] B. Jorns and E. Y. Choueiri. Ion heating with beating electrostatic waves. Phys. Rev. Lett., 106(8):085002, Feb. 2011.
- [26] M. Ono, T. Watari, R. Ando, J. Fujita, Y. Hirokura, K. Ida, E. Kako, K. Kawahata, Y. Kawasumi, K. Matsuoka, A. Nishizawa, N. Noda, I. Ogawa, K. Ohkubo, M. Okamoto, K. Sato, S. Tanahashi, Y. Taniguchi, T. Tetsuka,

- K. Toi, and K. Yamazaki. Ion-Bernstein-wave heating in the JIPPT-II-U tokamak plasma. Phys. Rev. Lett., 54:2339–2342, May 1985.
- [27] J. D. Moody, M. Porkolab, C. L. Fiore, F. S. McDermott, Y. Takase, J. Terry, and S. M. Wolfe. Ion-Bernstein-wave heating and improved confinement in the Alcator C tokamak. Phys. Rev. Lett., 60:298–301, Jan. 1988.
- [28] Y. Yasaka, H. Takeno, M. Sakka, O. Sakai, R. Itatani, T. Fujimoto, H. Suemitsu, K. Takahata, M. Fukao, S. Tanaka, and Y. Terumichi. Nonlinear ion Bernstein wave heating experiment in the WT-3 tokamak. Plasma Physics and Controlled Fusion, 35(3):379, 1993.
- [29] R. Sugaya. Ion heating by nonlinear Landau damping of ion Bernstein waves. Physics of Fluids, 30(6):1730–1733, 1987.
- [30] M. Sugawa. Numerical study of self-interaction of Bernstein waves by nonlinear Landau damping. Journal of Plasma Physics, 48(03):465–476, 1992.
- [31] R. Sugaya. Velocity space diffusion due to nonlinear wave-particle scattering of electromagnetic and electrostatic waves in a magnetized plasma. Journal of the Physical Society of Japan, 63:1775, May 1994.
- [32] P. W. Schuck, J. W. Bonnell, and P. M. Kintner. A review of lower hybrid solitary structures. IEEE Transactions on Plasma Science, 31(6):1125 – 1177, Dec. 2003.
- [33] K. A. Lynch, R. L. Arnoldy, P. M. Kintner, P. Schuck, J. W. Bonnell, and V. Coffey. Auroral ion acceleration from lower hybrid solitary structures: A summary of sounding rocket observations. Journal of Geophysical Research-Space Physics, 104(A12):28515–28534, Dec. 1999.

- [34] D.E. Baldwin and G. Rowlands. Plasma oscillations perpendicular to a weak magnetic field. Physics of Fluids, 9(12):2444–2453, 1966.
- [35] C. Karney and A. Bers. Stochastic ion heating by a perpendicularly propagating electrostatic wave. Phys. Rev. Lett., 39(9):550, 1977.
- [36] Charles F. F. Karney. Stochastic ion heating by a lower hybrid wave: II. Physics of Fluids, 22(11):2188–2209, 1979.
- [37] A. Fukuyama, H. Momota, R. Itatani, and T. Takizuka. Stochastic acceleration by an electrostatic wave near ion cyclotron harmonics. Phys. Rev. Lett., 38:701–704, Mar. 1977.
- [38] A. J. Lichtenberg and M. A. Lieberman. Regular and Chaotic Dynamics. Applied mathematical sciences. Springer-Verlag, 1992.
- [39] R. Sugaya. Plasma heating by nonlinear Landau damping of lower-hybrid waves. Journal of the Physical Society of Japan, 59(9):3227–3236, 1990.
- [40] M. Sugawa. Observation of self-interaction of Bernstein waves by nonlinear Landau damping. Phys. Rev. Lett., 61:543–546, Aug. 1988.
- [41] R. P. H. Chang and M. Porkolab. Experimental observation of nonlinear Landau damping of plasma waves in a magnetic field. Phys. Rev. Lett., 25:1262–1266, Nov. 1970.
- [42] R.P.H. Chang and M. Porkolab. Experimental studies of nonlinear Landau damping and growth of plasma waves in a magnetic field. Physics of Fluids, 15(2):297–303, 1972.
- [43] R. Spektor and E.Y. Choueiri. Design of an experiment for studying ion acceleration by beating waves. In 38th AIAA/ASME/SAE/ASEE Joint Propulsion Conference, Indianapolis, IN, AIAA-2002-3801, 2002.

- [44] R. Spektor and E.Y. Choueiri. Measurements of ion energization by a pair of beating electrostatic ion cyclotron waves. In 29th International Electric Propulsion Conference in Princeton, NJ, IEPC-2005-289, 2005.
- [45] Z. Sheng, L. Yu, G. Hao, and R. White. Nonlinear interaction between ions and multiple electrostatic waves. Phys. Plasmas, 16(7), 2009.
- [46] H. Goldstein. Classical Mechanics. Addison-Wesley, Cambridge, MA, 1951.
- [47] B.V. Chirikov. A universal instability of many-dimensional oscillator systems. Physics Reports, 52(5):263 – 379, 1979.
- [48] F. Skiff, F. Anderegg, and M. Q. Tran. Stochastic particle acceleration in an electrostatic wave. Phys. Rev. Lett, 58(14):1430, Apr. 1987.
- [49] A. Fasoli, F. Skiff, R. Kleiber, M.Q. Tran, and P.J. Paris. Dynamical chaos of plasma ions in electrostatic waves. Phys. Rev. Lett., 70(3):303–306, Jan. 1993.
- [50] L. Gibelli, B.D. Shizgal, and A.W. Yau. Ion energization by wave-particle interactions: Comparison of spectral and particle simulation solutions of the Vlasov equation. Comp. and Math. App., 59:2566–2581, 2010.
- [51] M. Fivaz, A. Fasoli, K. Appert, F. Skiff, T.M. Tran, and M.Q. Tran. Stochastic plasma-heating by electrostatic-waves - a comparison between a particle-in-cell simulation and a laboratory experiment. Physics Letters A, 182(4-6):426–432, 1993.
- [52] R. Spektor and E.Y. Choueiri. Ion acceleration by beating electrostatic waves: Domain of allowed acceleration. In 27th International Electric Propulsion Conference in Pasadena, CA, IEPC-01-209, 2001.
- [53] C.K. Birdsall and A.B. Langdon. Plasma Physics via Computer Simulation. Adam Hilger, Philadelphia, PA, 1991.

- [54] R. Marchand. Test-particle simulation of space plasmas. Comm. Comp. Phys., 8:471–483, 2010.
- [55] G.E. Box and M. E. Muller. A note on the generation of random normal deviates. Ann. Math. Stat., 29:610–611, 1958.
- [56] J. Candy and W. Rozmus. A symplectic integration algorithm for separable Hamiltonian functions. J. Comp. Phys., 92:230–256, 1992.
- [57] P. E. Latham, S. M. Miller, and C. D. Striffler. Use of Lie transforms to generalize Madey’s theorem for computing the gain in microwave devices. Phys. Rev. A, 45(2):1197, 1992.
- [58] G.N. Watson. A Treatise on the Theory of Bessel Functions. Cambridge University Press, New York, 1996.
- [59] I. B. Bernstein, J.M. Greene, and M.D. Kruskal. Exact nonlinear plasma oscillations. Phys. Rev., 108:546, 1957.
- [60] T. O’Neil. Collisionless damping of nonlinear plasma oscillations. Physics of Fluids, 8(12):2255–2262, 1965.
- [61] R.C. Davidson. Methods in Nonlinear Plasma Theory. Academic Press, New York, NY, 1972.
- [62] R.L. Dewar. Oscillation center quasilinear theory. Physics of Fluids, 16(7):1102–1107, 1973.
- [63] A. Deprit. Canonical transformations depending on a small parameter. Celestial Mechanics and Dynamical Astronomy, 1(1):12–30, Mar. 1969.
- [64] R.L. Dewar. Renormalized Canonical Perturbation-theory for Stochastic Propagators. Journal of Physics A-Mathematical and General, 9(12):2043–2057, 1976.

- [65] J. Cary. Lie transform perturbation theory for Hamiltonian systems. Physics Reports, 79(2):129–159, May 1981.
- [66] J.R. Cary and A. Kaufman. Ponderomotive effects in collisionless plasma: A Lie transform approach. Physics of Fluids, 24(7):1238–1250, 1981.
- [67] C.W. Gardiner. Handbook of stochastic methods for physics, chemistry, and the natural sciences. Springer series in synergetics. Springer, 1985.
- [68] N.G. van Kampen. Stochastic Processes in Physics and Chemistry. North-Holland Personal Library. Elsevier, 2007.
- [69] N.G. van Kampen and B.U. Felderhof. Theoretical methods in plasma physics. North-Holland, 1967.
- [70] J. Plemelj. Problems in the Sense of Riemann and Klein. Interscience tracts in pure and applied mathematics. Interscience Publishers, 1964.
- [71] F.F. Chen and J.P. Chang. Lecture notes on principles of plasma processing. Kluwer Academic/Plenum Publishers, 2003.
- [72] Lieberman, M. A. and Boswell, R. W. Modeling the transitions from capacitive to inductive to wave-sustained rf discharges. J. Phys. IV France, 08(PR7):Pr7–145–Pr7–164, 1998.
- [73] J. D. Huba. NRL Plasma Formulary. Naval Research Laboratory, Washington, D.C., 2006.
- [74] W. M. Hooke and S. Bernabei. Direct observation of waves propagating near the lower-hybrid-resonance frequency. Phys. Rev. Lett., 28(7):407, 1972.
- [75] J. P. M. Schmitt. Dispersion and cyclotron damping of pure ion Bernstein waves. Phys. Rev. Lett., 31(16):982, 1973.

- [76] R. L. Stenzel and W. Gekelman. Electrostatic waves near the lower hybrid frequency. Phys. Rev. A, 11(6):2057, 1975.
- [77] M. Light and F. F. Chen. Helicon wave excitation with helical antennas. Physics of Plasmas, 2(4):1084–1093, 1995.
- [78] J. L. Kline, E. E. Scime, P. A. Keiter, M. M. Balkey, and R. F. Boivin. Ion heating in the HELIX helicon plasma source. Physics of Plasmas, 6(12):4767–4772, Dec. 1999.
- [79] B. Jorns, R. Sorenson, and E. Choueiri. Variable dual-frequency electrostatic wave launcher for plasma applications. Review of Scientific Instruments, 82(12), 2011.
- [80] B.S. Yarman. Design of ultra wideband power transfer networks. John Wiley, Chichester, West Sussex, UK, 2010.
- [81] W. H. Mclyman. Transformer and Inductor Design Book. Marcel Dekker, New York, NY, 2004.
- [82] F.E. Terman. Electronic and Radio Engineering. McGraw-Hill, New York, NY, 1955.
- [83] J. Seveck. Transmission Line Transformers, 4th ed. Noble Publishing, Atlanta, GA, 2001.
- [84] F.F. Chen. Lecture notes on Langmuir probe diagnostics. In Mini-Course on Plasma Diagnostics, IEEE-ICOPS, 2003.
- [85] R. Sudit and F. F. Chen. RF compensated probes for high-density discharges. Plasma Sources Science and Technology, 3:162–168, 1994.

- [86] M.B. Hopkins. Gaseous Electronics Conference RF Reference Cell. Journal of research of the National Institute of Standards and Technology. U.S. Department of Commerce, National Institute of Standards and Technology, 1996.
- [87] R.M. Castro, G.A. Cirino, P. Verdonck, H.S. Maciel, M. Massi, M.B. Pisani, and R.D. Mansano. A comparative study of single and double Langmuir probe techniques for RF plasma characterization. Contributions to Plasma Physics, 39(3):235–246, 1999.
- [88] D.K Owens. Lecture IV: Langmuir probes. Technical report, Princeton Plasma Physics Laboratory, Princeton, NJ, 2000.
- [89] P.R. Bevington and D.K. Robinson. Data Reduction and Error Analysis for the Physical Sciences. McGraw-Hill, 2003.
- [90] G. D. Severn, D. A. Edrich, and R. McWilliams. Argon ion laser-induced fluorescence with diode lasers. Review of Scientific Instruments, 69(1):10–15, 1998.
- [91] M. Sarfaty, S. de Souza-Machado, and F. Skiff. Direct determination of ion wave fields in a hot magnetized and weakly collisional plasma. Physics of Plasmas, 3(12):4316–4324, 1996.
- [92] J. Kline, C. Franck, and R. Spangler. First order perturbed velocity distribution theory and measurement. Technical Report PL-047, Plasma Physics Group, West Virginia University, 2000.
- [93] F. Skiff and F. Anderegg. Direct observation of plasma dielectric motion. Phys. Rev. Lett., 59:896–899, Aug. 1987.

- [94] B. Jorns and E.Y. Choueiri. Experiment for plasma energization with beating electrostatic waves. In 31st International Electric Propulsion Conference Proceedings, Ann Arbor, MI, IEPC-199, 2009.
- [95] Charles F.F. Karney. Fokker-Planck and quasilinear codes. Computer Physics Reports, 4(34):183 – 244, 1986.
- [96] B. Gardineer, B. Jorns, and E.Y. Choueiri. Simulations of direct ion acceleration with beating electrostatic waves. In 32nd International Electric Propulsion Conference, Wiesbaden, Germany, IEPC-2011-212, 2011.
- [97] J. P. Eckmann and D. Ruelle. Ergodic theory of chaos and strange attractors. Rev. Mod. Phys., 57:617–656, Jul 1985.
- [98] M. Sandri. Numerical calculation of Lyapunov exponents. The Mathematica Journal, 6(3):78–84, 1996.
- [99] V.I. Oseledec. A multiplicative ergodic theorem: Lyapunov characteristic numbers for dynamical systems. Trans. Moscow Math. Soc., 19:197–231, 1968.
- [100] H.R. Griem. Plasma Spectroscopy. McGraw-Hill, New York, 1964.
- [101] I. Corney. Atomic and Laser Spectroscopy. Clarendon, Oxford, 1977, 1977.
- [102] W.L. Wiese. Plasma Diagnostic Techniques. Academic, New York, 1965.
- [103] H.R. Griem. Spectral Line Broadening by Plasmas. Academic, New York, 1974.
- [104] M.J. Goeckner and J. Goree. Laser-induced fluorescence measurement of plasma ion temperatures: Corrections for power saturation. Journal of Vacuum Science & Technology A: Vacuum, Surfaces, and Films, 7(3):977–981, 1989.

- [105] M.J. Goeckner, J. Goree, and T.E. Sheridan. Saturation broadening of laser-induced fluorescence from plasma ions. Review of Scientific Instruments, 64(4):996–1000, 1993.
- [106] R.F. Boivin. Study of the different line broadening mechanisms for the laser induced fluorescence diagnostic of the HELIX and LEIA plasmas. Technical Report PL-039, Plasma Physics Group, West Virginia University, 2000.
- [107] R.F. Boivin and E.E. Scime. Laser induced fluorescence in Ar and He plasmas with a tunable diode laser. Review of Scientific Instruments, 74(10):4352–4360, 2003.
- [108] G. Marr. Plasma Spectroscopy. Elsevier, New York, NY, 1968.
- [109] R.F. Boivin. Zeeman splitting for LIF transitions and de-convolution technique to extract ion temperature. Technical Report PL-050, Plasma Physics Group, West Virginia University, 2001.